The structure of the atmospheric surface layer subject to local advection

N.J.Bink

The structure of the atmospheric surface layer subject to local advection

Proefschrift

ter verkrijging van de graad van doctor
in de landbouw- en milieuwetenschappen
op gezag van de rector magnificus
dr. C.M. Karssen
in het openbaar te verdedigen op
woensdag 3 april 1996
des namiddags te vier uur
in de Aula van de Landbouwuniversiteit te Wageningen.

BIBLIOTHEEK
LANDBOUWUNIVERSITEIT
WAGENINGEN

Cover page (design: Nico Schaefers)

The cover shows the dry Crau surface (photo: J.G. van der Vliet) and three photos of the
experiment (top right: mast with profile and eddy correlation measuring equipment above
the dry terrain; top left: masts with profile and eddy correlation measuring equipment above
the grass terrain). bottom: aerial overview of experimental site and its surroundings looking
to the west (photo: A. van Dijken).

Financial support

Stellingen

1. Bij het bepalen van het verschil tussen de Bowen-verhouding op enige hoogte boven het oppervlak en die aan het oppervlak dient zowel de fluxdivergentie als de ongelijke turbulente diffusiviteit van warmte en waterdamp in rekening gebracht te worden.

   Dit proefschrift

2. De dikte van de zogenaamde aangepaste grenslaag na een terreinovergang hangt sterk af van het gehanteerde kriterium om aangepast van niet aangepast te onderscheiden en verschilt dan nog afhankelijk van de grootheid waarop dit kriterium wordt toegepast.

   Dit proefschrift

3. De transportefficiëntie van vocht vanaf het aardoppervlak onder droge omstandigheden wordt bepaald door de verhouding van vochtentrainment aan de top van de planetaire grenslaag en de vochtflux aan het oppervlak en niet, zoals verondersteld door McBean, door de transportefficiëntie van voelbare warmte.

   McBean, G., 1973, Comparison of the turbulent transfer processes near the surface, Bound.Layer Meteor. 4, 265-274.

4. Het is in een handomdraai aan te tonen dat de door Katul *et al.* afgeleide relatie voor het verband tussen de correlaties van temperatuur- en vocht-, verticale wind- en temperatuur- en verticale wind- en vochtfluctuaties, $R_{tq} = R_{wt}/R_{wq}$, alleen geldt als $R_{tq} = \pm 1$, hetgeen een triviaal resultaat is.

   Katul, G., Golts, S.M., Hsieh,C-I, Cheng, Y., Mowry, F. and Sigmon, J., 1995, Estimation of surface heat and momentum fluxes using the flux-variance method above uniform and non-uniform terrain, Bound.Layer Meteor. 74, 237-260.

5. Bij de berekening van het waterverbruik van irrigatieprojecten middels de FAO-methode wordt onvoldoende rekening gehouden met de verandering van het microklimaat ten gevolge van de veranderde terreinomstandigheden in het projectgebied.

   Wartena, L., 1959, Het klimaat en de verdamping van een meer in Centraal-Irak, Proefschrift Landbouwuniversiteit Wageningen.

   De Bruin, H.A.R., 1996, FAO overschat waterbehoefte van irrigatieprojecten, Wagenings Universiteitsblad, 15 februari 1996.

6. Om de warmteopslag in de bomen van een bos te bepalen kan men volstaan met het meten van de luchttemperatuur en de windsnelheid in dat bos.

   Meesters, A.G.C.A. and Vugts, H.F., 1996, Heat storage in stems, accepted for publication, Agricultural and Forest Meteorology.

7. Onder bepaalde omstandigheden, zoals boven sterk reflecterende oppervlakken ten tijde van hoge instraling en kleine voelbare warmtefluxen, kan de fout in de voelbare warmteflux ten gevolge van de correlatie tussen de stralingsfout in de thermokoppel-temperatuur en de windsnelheidsfluctuaties even groot zijn als de voelbare warmteflux zelf.

   Jacobs, A.F.G. and McNaughton, K.G., 1994, The excess temperature of a rigid fast-response thermometer and its effects on measured heat flux, J.Atm.Ocean.Tech., 11, no.3, 680-686.

8. Universitaire studieprogrammas die onvoldoende zijn aangepast aan de verkorte studieduur in combinatie met het zogenaamde onderwijs in blokken leidt tot taferelen die zich ook voordoen binnen de ganzeleverindustrie.

9. Bij de voorlichting aan leerlingen van het VWO gedragen de universiteiten zich vaak als kinderlokkers.

10. Lineaire extrapolatie bij de berekening van toekomstige hardlooprecords, zoals gebruikt door Ryder *et al.*, bevestigt al te zeer het beeld dat hardlopers doodlopers zijn.

    Ryder, H.W., Carr, H.J and Herget, P., 1976, Future performance in footracing, Scientific American, 234, 108-119.

11. Bij de berekening van het aantal caramboles dat een speler moet maken in de competitie van de Biljartbond Wageningen en omstreken dient de relatieve grootte van het biljart van de eigen vereniging in rekening gebracht te worden.

12. Gezien de steeds verder gereduceerde zitruimte per treinreiziger verdient het aanbeveling om het formaat van de dagbladen te halveren.

Stellingen behorend bij het proefschrift: "**The structure of the atmospheric surface layer subject to local advection**", N.J. Bink, Wageningen, 3 april 1996.

Abstract

For many applications in agriculture, hydrology and meteorology simple methods are needed to determine the surface-atmosphere exchange of momentum, heat and water vapour, *i.e* to determine the fluxes of momentum, heat and water vapour. Most methods to calculate these fluxes are only valid for horizontal, homogeneous terrain with sufficient large dimensions. It is thus assumed that so-called advective effects can be neglected because wind speed, temperature and humidity do not change in the horizontal direction. In practice, the surface is hardly ever homogeneous. It was the objective of this study to investigate the effects of advection of heat and moisture on the fluxes. It appeared that only a few sets related to advection were available, and the available sets yielded contradictive results. Therefore an experiment was carried out in La Crau, France around a step-change from a dry and bare terrain to irrigated grass in order to measure the influence of advection on the structure of the flow and the exchange processes near the earth's surface.

Before this study there was confusion about the behaviour of the flux-gradient ratios or eddy diffusivities under conditions of local advection. The flux-gradient ratios or eddy diffusivities were estimated using the calculated surface fluxes and the gradients from the profile measurements. It was found that the flux-gradient ratio for heat was smaller than that for water vapour in the lower part of the surface layer after the step-change. This was in agreement with the ratio of the observed transfer efficiencies. Higher up in the surface layer after the step-change and for weak advective conditions it was found that the flux-gradient ratio for heat was larger than that for water vapour.

Also, flux determination methods were tested using a second-order closure model which was found to compare favourably with the measurements. It was found that for situations similar to that in the Crau, the so-called gradient Bowen ratio can be used at fetch-to-height ratios up to $z/x = 0.02$ which is high compared to what was accepted untill now. It was also found that the difference between the Bowen ratio at the surface and at some level above the surface is compensated for by the ratio of the eddy diffusivities at the height where the gradient is measured. For the Bowen ratio from standard deviations in the thermally stable surface layer the error was found to be below 10%, up to $z/x = 0.02$. The ratio of the transfer efficiencies was below unity which compensated the error due to the flux divergence. For the unstable surface layer z/x must be below 0.008 to achieve the same accuracy because now the ratio of the transfer efficiencies amplifies the error due to flux divergence. For the cases studied here, a number of factors may have cooperated in a favourable manner due to which the error sources cancel out. However, it is significant to note that the model can be used to forecast which conditions are favourable and which are not for the application of micro-meteorological methods to determine the surface fluxes under conditions of local advection.

Keywords: local advection, surface energy balance, Bowen ratio method, eddy diffusivities, transfer efficiencies, second-order closure.

'Good morning!' said Bilbo, and he meant it. The sun was shining, and the grass was very green. But Gandalf looked at him from under long bushy eyebrows that stuck out further than the brim of his shady hat.

'What do you mean?' he said. 'Do you wish me a good morning, or mean that it is a good morning whether I want it or not; or that you feel good this morning; or that it is a morning to be good on?'

'All of them at once,' said Bilbo. 'And a very fine morning for a pipe of tobacco out of doors, into the bargain. If you have a pipe about you, sit down and have a fill of mine! There is no hurry, we have all the day before us!'

The Hobbit, J.R.R. Tolkien (1937).

Voor mijn ouders

Voorwoord

"Maak nou eens je proefwerk af" (Fleur Bakker, 1995).

Na jaren en jaren en nog eens jaren is het dan zover. Mijn proefwerk is af. En dat is zeker niet alleen mijn verdienste. Zeer velen hebben er aan bijgedragen dat het nu zo ver is.

Het begon allemaal in 1985. Bert Wartena, mijn promotor, riep vanuit zijn raam op de eerste verdieping van Duivendaal 2 over de parkeerplaats, telefoon nog in de hand, "je bent aangenomen" en vervolgde zijn telefoongesprek. Bert, alleen al daarvoor bedankt maar ook voor je adequate ondersteuning bij de afronding van dit werk.

Leo Kroon, mijn co-promotor, heeft nooit harde woorden laten vallen als weer eens een deadline werd overschreden. Hij is al die jaren trouw blijven wachten op de brokken en stukken van dit werk om ze steeds weer rood terug te sturen. Verder heeft hij zeer veel werk verricht bij het modelleren. Zijn bijdrage kan alleen maar onderschat worden.

Na de nat-nat overgang van Ganzegouw had Henk de Bruin al snel gezien dat wij het zuidelijker moesten zoeken. Hij bood mij de mogelijkheid om mee te gaan naar de Crau in Frankrijk om daar een geschikte terreinovergang te vinden. Die vonden we. Henk heeft al die jaren een overvloed van ideeën en plannen aangebracht waarvan we er ook een aantal daadwerkelijk uitgevoerd hebben en een aantal nog voltooid dienen te worden. Henk, bedankt voor je cruciale bijdrage.

"Met verhalen in het achterhoofd gaan we naar de Crau, een stukje steenwoestijn aan de voet van de Alpilles, kleine alpjes. Het ruikt er intensief naar tijm. Het is er bijna Spaans, zo heet, zo kaal en winderig, zo droog en distelig." (Koos van Zomeren, Vandaag of morgen, NRC van 5/7/93). Gelukkig vonden we te midden van deze steenwoestijn een kleine oase (zie voorkant) alwaar de meetopstelling opgebouwd kon worden. C'est avec plaisir que je remercie mr.Py pour la permission d'exécuter nos mesurages sur sa propriété. J'exprime egalement ma gratitude envers Bernard Seguin et mr.Verbrugge de l'INRA pour l'hospitalité et la coopération sur place. Merci pour tout!

De expeditie naar de Crau was alleen mogelijk door de geweldige inzet van een grote groep mensen van diverse instituten. Onze apparatuur en de meetopstelling werd op deskundige wijze verzorgd door Antoon Jansen, Teun Jansen, Peter Jansen, Willy Hillen, Dick Welgraven en Cees van Asselt.

Onder leiding van mijn tweede promotor Hans Vugts vormden Fred Cannemeijer, Frits Tesselaar, Niekie van Harlingen, Jan Vink, Kees Groen en Johan de Lange terplaatse het team van de VU dat met een indrukwekkende hoeveelheid apparatuur voor de dag kwam. Wim Kohsiek, Gerard van der Vliet en Wim Monna verzorgden de metingen voor het KNMI waar wij ook dankbaar gebruik van hebben gemaakt. Niet alleen verliep de samenwerking fantastisch, ook 'les nuits de bowling' mochten er wezen.

John van Boxel, mijn kamergenoot in Wageningen, verzorgde de programmatuur bij het mobiele meteorologische meetsysteem en heeft zijn grote spierkracht ingezet bij het boren van de gaten in de Crau. Verder leerde ik veel van hem over computeren en veldwerk. Met Addo van Pul, mijn andere kamergenoot, heb ik menig harinkje verschalkt. We luisterden altijd met verwondering naar de conversaties die John met zijn computer voerde. Aan de discussies die wij met z'n drieën vaak hadden heb ik goede herinneringen. Bij de metingen in Frankrijk werd ik ook nog bijgestaan door dr. Cor Jacobs, toen bezig met zijn afstudeervak meteo. Hij hield ondermeer het weer bij en van hem is de volgende objectieve waarneming te vinden in het weerschrift: "Synops 7.45 GMT: Hollands Pokkenweer".

After the experiment appraisal in France, I had the opportunity to work at the CSIRO division of Environmental Mechanics in Canberra, Australia. I lived at Giles and Heathers place and we had a real good time, thanks guys. Frank Bradley, John Finnigan, Mike Raupach, Dick Lang and all the others, I must thank you for the good time I had at the institute. Even when I blew up a whole computer and some apparatus you remained friendly. The Bungendore lake experiment, visiting Kangaroo Valley, wild-water rafting, doing triathlons and discussing the Navier-Stokes equations with John while running are also unforgettable events.

Terug in Nederland kon ik aan de VU bij Hans Vugts komen werken. Ik had, zoals werd vereist, uitzicht op promotie. Gelukkig was er blijkbaar goed zicht (minstens synopscode VV=89). Ik ben Hans Vugts en Fred Cannemeijer en onze decaan, Theo Levelt, en alle anderen collegas van de VU dankbaar voor hun geduld en het in mij gestelde vertrouwen. Mijn huidige kamergenoot bij de VU, Antoon Meesters, heeft diverse hoofdstukken gelezen en met zijn kritische instelling veel waardevolle bijdragen aan dit proefschrift geleverd. Ook Edwin Henneken heeft mij een aantal keren waar ik dat vroeg geholpen. Verder bedank ik nog in het bijzonder Ernie Weijers die toen dat nodig was mij onderdak verschafte in Amsterdam.

Aan het einde van de rit wordt nog een inspanning geleverd door, naar ik vernam, de commissie: Jon Wieringa, Bert Holtslag, Frans Nieuwstadt en Wim Kohsiek dank hiervoor. Verder word ik bijgestaan door Menno Bartlema en Gerard Swinkels. Ik ben benieuwd hoe het rokkostuum jullie staat!

Kort maar krachtig, uit het diepst van mijn hart, bedank ik tenslotte mijn vrienden en familie die allen op hun manier hebben bijgedragen aan de totstandkoming van dit proefwerk.

Table of Contents

1 INTRODUCTION AND STUDY DESCRIPTION

1.1 General background

For many applications in agriculture, hydrology and meteorology simple methods are needed to quantify the exchange at the surface of momentum, heat and water vapour per unit area and unit time, *i.e* to determine the flux densities (from here on abbreviated to fluxes) of momentum, heat, water vapour and other atmospheric constituents such as CO_2 and ozone.

A widely used method applies the flux-profile relations which are based on the Monin-Obukhov similarity theory (MO theory) as formulated by Obukhov (1946, 1971). Vertical profiles of mean temperature, humidity and wind can be readily measured from which subsequently the fluxes can be calculated. The method can only be applied under homogeneous conditions as MO theory is valid for an infinite homogeneous plane surface. Therefore, the first measurements to be used for the verification and further development of the flux-profile method took place at desolate sites in Kansas and Minnesota (Kaimal and Wyngaard, 1990) or in the outback of Australia (Garrat and Hicks, 1990). However, we have to live with the fact that conditions found there are exceptional. The common landscape is a patchwork quilt of farmland where different crops are grown, cities, lakes, forests, desserts etc. on flat land, hills and in mountains.

It is, as yet, not feasible to consider all aspects of terrain heterogeneity together in one study. For a review of the state of the art one should consult Kaimal and Finnigan (1994). The variation of natural terrain at a variety of length scales causes advection: the transport of energy or mass in the downwind direction. This study deals with 'local' advection and is restricted to a single step-change from arid to irrigated, flat land. The adjective 'local' points at the location of the source of the advected properties and at the scale of influence of the process. It is assumed that the effects of local advection are confined to the Atmospheric Surface Layer (ASL), the first 10-100 m above the surface in which turbulent exchange controls the exchange of heat, momentum and mass at the surface. The ASL is the lowest part of the Atmospheric Boundary Layer, the ABL which on its turn is the lowest layer of the atmosphere having a thickness of typically 100 m at night-time to 2 km during day-time depending on wind speed, the surface flux and the entrainment flux at the top of the ABL.

In literature we may find a subdivision into three effects of local advection. These are the 'clothesline' effect, the 'oasis' effect and the 'leading-edge' or 'fetch'-effect (Oke, 1987). The clothesline effect is caused by the horizontal flow of locally unadapted air through a vegetative canopy. Warm, dry air entering a stand border enhances evaporation close to the edge due to heat supply and an increased humidity deficit. The oasis effect prevails where an isolated humid area, like an oasis, a small lake, a small irrigated plot or a Class-A evaporation pan is embedded in warm air. Temperature above the humid area is low due to evaporative cooling and a sensible heat flux towards the humid area can be used to increase evaporation above the available net radiation energy as long as sufficient water is available. The process of the adapting mean flow and turbulence properties, downwind of a step-change or leading-edge, can be summarized as the leading-edge or fetch effect (Oke, 1987). Consider the air-flow over a step-change of surface properties which is, at first, in equilibrium with the surface so that the profiles of wind, temperature, humidity and the characteristics of the surface are adapted to each other. The result is that the fluxes in the upwind ASL are, to a close approximation, constant with height. Air passing from one surface to another must adapt itself to the new surface conditions whereas surface and crop conditions like canopy temperature, available moisture and stomatal aperture will also react on the changing air properties. After the step-change the flow adapts to the new surface conditions and vice versa in a complicated process with several feedback processes. First the lowest layers will adapt and at a certain distance downwind the whole Surface-ASL system will be in equilibrium again. This can also be understood as the formation of an Internal Boundary Layer (IBL). The IBL itself is usually thought to be divided into an adapted layer, the Internal Adapted Layer (IAL) in which flux divergence is negligible and the profiles are adapted to the underlying surface, and a transition zone in which the flow is partly influenced by the downwind terrain and in which the flux divergence is large.

1.2 Local advection and evapotranspiration

The step-change from arid land to an irrigated crop, considered in this study seems a somewhat selective case in view of the broader range of step-changes that could be studied. However, from a practical point of view it is a significant case. Water use of irrigated crops may increase due to local advection depending on the arrangement of dry and wet terrains

and wind direction. One can imagine that this is an important problem in areas where water supply is limited and where the irrigated area is (going to be) implemented in dry and hot areas with little precipitation. Or as Philip (1987) puts it 'To dwellers in the green and pleasant lands of well-watered England, much of Europe and the Eastern U.S., concern with horizontally non-uniform, advective processes may well seem academic. People involved with irrigation and water storage in arid areas, e.g. in the Western U.S., Australia and Israel, are, however, confronted with irrigated areas and reservoirs surrounded by hot dry land-scapes'. They are therefore interested in methods with which the transpiration E_c (kgm^{-2}s^{-1}) can be calculated under these conditions.

Transpiration, as a part of evapotranspiration, is the evaporation of water from dry plants and plant parts. Other components of evapotranspiration are bare soil evaporation and evaporation of intercepted water by the canopy. Evapotranspiration influences the dynamics of atmospheric flow due to large magnitude of the latent heat of vaporization, $\lambda = 2.47 \times 10^6$ J kg^{-1} (at 10°C). At a modest evapotranspiration rate of 3.5 mm/day for a day-length of 12 hours an average energy flow of 200 Wm^{-2} is needed to maintain the evapotranspiration λE, which is a considerable portion of the incoming solar radiation.

One of the most widely used methods to evaluate evapotranspiration is the Bowen ratio energy balance method (BREB method, see for example Rosenberg *et al.*, 1983). The surface energy balance

$$R_n = G + H + \lambda E \qquad\qquad 1.1$$

between respectively net radiation (positive when directed to the surface), heat storage into the soil (negative when directed to the surface) or the canopy, the surface sensible heat flux and surface latent heat flux (both positive when directed away from the surface) is then combined with the Bowen ratio

$$\beta = \frac{H}{\lambda E} \qquad\qquad 1.2$$

to calculate the fluxes. The value for β can be obtained from the ratio of the vertical temperature gradient and the vertical humidity gradient when measured in the IAL and

providing the eddy diffusivities (the ratio between the flux and the gradient) for sensible heat and water vapour are equal. The behaviour of β in the IAL, under conditions of local advection, is now considered.

For well-watered crops in semi-arid regions λE may exceed the net radiation considerably resulting in negative Bowen ratios during day-time. For example, advected energy, assumed to be $\lambda E - (R_n + G)$ (when positive), contributed 15-50% to the evapotranspiration of irrigated alfalfa in Nebraska (Brakke *et al.*, 1978), 22% to the evapotranspiration of cotton grown in Arizona (Gay and Bernhofer 1991) and 40% to the evapotranspiration of irrigated rice (Evans, 1971). Extreme values for the ratio of the energy consumed by evaporation and net radiation of 2.5 (equal to an advective contribution of 60%) have been observed over irrigated cotton (Lemon *et al.*, 1957). Some insight in the effect of crop and weather conditions leading to these results can be given by using a well-known evaporation model.

The 'big-leaf model' represented by the Penman-Monteith equation (Monteith, 1981) considers a vegetated surface as a single, flat, big leaf, having the same properties as the vegetation it represents. The model combines the surface energy balance (Eq.1.1) with resistance formulations for the surface fluxes of latent and sensible heat, respectively

$$\lambda E = \frac{\rho\lambda[Q_s(\Theta(0)) - Q(z)]}{r_s + r_a} \qquad\qquad 1.3$$

and

$$H = \rho c_p \frac{[\Theta(0) - \Theta(z)]}{r_a} \qquad\qquad 1.4$$

in which r_a is the bulk aerodynamic resistance of both heat and water vapour assuming these are equal and r_s is the bulk surface or canopy resistance, the area integrated value of the stomatal resistance.

The Penman-Monteith equation (PME) then becomes

$$\lambda E = \frac{\Delta(R_n - G) + \gamma\rho\lambda D/r_a}{(1 + r_s/r_a)\gamma + \Delta} \qquad\qquad 1.5$$

in which Δ is the slope of the temperature-saturation specific humidity curve and $\gamma = c_p/\lambda$. The specific saturation deficit $D = Q_s(\Theta(z)) - Q(z)$ where $Q_s(\Theta(z))$ is the saturation specific humidity for the temperature $\Theta(z)$ at level z and $Q(z)$ is the actual specific humidity at z.

In order to characterize conditions over an evaporating terrain it is useful to rewrite the PME and to consider the ratio of the latent heat flux and available energy. Following Thom (1975), Eq.1.5 can be written as

$$\alpha = \frac{\lambda E}{R_n - G} = \frac{\Delta r_a + \gamma r_i}{\gamma r_a + \Delta r_a + \gamma r_s} \qquad 1.6$$

and the Bowen ratio β can be written as

$$\beta = \frac{\gamma(r_a + r_s - r_i)}{\Delta r_a + \gamma r_i} \qquad 1.7$$

in which

$$r_i = \frac{\rho \lambda D}{R_n - G} \quad . \qquad 1.8$$

With the introduction of this 'isothermal' resistance (Monteith, 1965) several weather variables which govern the evaporation process are combined in a clever way. It is seen that, during day-time, r_i is large in dry air during cloudy conditions or at low solar elevations.

A noteworthy feature of Eq.1.7 is that it shows that the Bowen ratio is negative when $r_a + r_s < r_i$ as can be the case in advective conditions. In this situation, the air temperature in the IAL will be above the surface temperature and heat is drawn from the air to feed evapotranspiration. Provided the stratification upwind of the step-change is unstable, this stable temperature stratification is referred to as an 'advective inversion'. The presence of such an inversion is a clear sign that advection is important but it is not a prerequisite since r_i may increase due to advection but not necessarily be larger than $r_a + r_s$.

Using Eqs.1.6 and 1.7, the influence of local advection for different atmospheric conditions and plant-water status may be divided into three cases.

1. $r_i \gg r_s + r_a$

In this case $\beta \rightarrow -1$ and $\alpha \gg 1$. The energy for evapotranspiration is partly supplied by a downward sensible heat flux and the temperature of the air above the surface decreases in time. The magnitude of the fluxes depends on the heat supply by advection and the dynamics of the turbulent transport in the atmosphere.

2. $r_i \approx r_s + r_a$.

It is seen that now $\alpha \approx 1$ and $\beta \approx 0$ i.e. $H \approx 0$. All available energy $R_n - G$ is used for evapotranspiration.

3. $r_i < r_s + r_a$

The Bowen ratio is positive and air in the unstably stratified IAL is heated from the surface as is the case in the day-time homogeneous surface layer.

These three cases can be used to give some characteristics of the development of the ASL after the dry to wet step-change as a function of time or at a fixed moment as function of fetch. For a **fixed location** in the IBL and starting with conditions described by case 1 (i.e just after irrigation), the influence of advection decreases in the course of time mainly because r_s increases due to the depletion of available moisture. At a **fixed moment**, the influence of advection decreases, roughly speaking, with fetch because the water vapour deficit decreases and surface temperature increases. Several nonlinear interactions complicate this situation considerably. For instance, because of the stable temperature stratification of the IAL in case 1, the flow is less turbulent, i.e r_a is higher thus weakening the advective inversion due to which r_a would increase. Furthermore, both r_s and r_i will vary with downwind distance. Surface resistance is a function of D and Θ (among other factors) and r_i changes because D changes but also because R_n may change because of a possible change of albedo and surface temperature. Early models of the dry to wet step-change predict a large overshoot of the evaporation rate just after a dry to wet step-change (Philip, 1959). A less than expected overshoot, as observed by Millar (1964), was probably caused by a relatively large r_s close to the edge (Monteith, 1965). Just recently, the feedback between atmosphere properties and surface resistance was implemented in a model for local advection (Kroon and De Bruin, 1993) and it was found that the overshoot may even disappear completely.

The different weather conditions to which a crop is exposed, in cooperation with the plant physiological characteristics, may not only increase water-use of a crop. It makes it also difficult to predict its crop water-use throughout the growing season. This problem is more serious if local advection is important since the range of possible Bowen ratios is larger then. The procedure to predict crop-water use as discussed in Doorenbos and Pruitt (1975) does account for local advection but in a fully empirical way and only for maize, grass and deciduous forest. It shows that at that time the knowledge was lacking to provide the irrigation engineer with more precise advice. Until now, this practice has not been improved as can also be seen in more recent FAO-publications (Smith, 1992).

1.3 Objectives

The above shows the conditions under which the contribution of advected energy become important and some of the mechanisms which control advection. However, there are several aspects of local advection which need further study. In the above discussion (section 1.2) it was tacitly assumed that simple meteorological methods, like the BREB, are applicable under conditions of local advection. The requirements to use this method together with gradient measurements seemed simple: put up the instruments close enough to the surface to ensure that flux divergence can be neglected, and assume that the eddy diffusivities for water vapour and sensible heat fluxes are equal. In two studies (Verma *et al.*, 1978, Lang *et al.*, 1983a) only the latter assumption was tested as it was assumed that the measurements were performed at large enough fetch-to-height ratios to be in the IAL. It was not verified whether this was actually the case and no clear subdivision between the IAL and the IBL was defined. The two studies gave seemingly contradicting results concerning the transfer mechanisms of water vapour and heat after a dry-to-wet step-change and the relation between fluxes and profiles subject to advection.

Also for other methods to measure the Bowen ratio, assumptions concerning the transfer mechanisms of water vapour and sensible heat are needed. For instance, to obtain the Bowen ratio using the ratio of the standard deviations (Tillman, 1972) of the temperature fluctuations and humidity fluctuations, it is required that the correlation between the vertical wind

fluctuations and temperature fluctuations and the correlation between the vertical wind
fluctuations and humidity fluctuations are equal. It is not known whether this is the case in
the IAL or IBL.

Kroon (1985) attacked the problem of flux-determination under conditions of local advec-
tion using the second-order closure model of Rao *et al.* (1974b). It was concluded from this
study that the model still suffered from shortcomings concerning the closure assumptions
and the description of the lower boundary conditions. Until now, a comparison between the
model simulations involving a step-change and experimental data was limited to mean pro-
files of wind, temperature and moisture because of the lack of turbulence data obtained
under conditions of local advection. Still it would be useful to have a model which can be
used in cooperation with the measurements. It may lessen the confusion if the model which
resolves the second-order moments could be used to study the turbulence structure of the
Internal Boundary Layer and the flux-profile relations under these conditions. But before
further work with the model can be undertaken, it first needs validation.

Therefore, in general, the goals of this study are

-   to collect a data-set from a micro-meteorological experiment in which mean profiles and
    turbulence flow properties around a dry-to-wet step-change are measured which can be
    used to verify a second-order closure model.

-   to improve our understanding of the transfer mechanisms of heat and water vapour under
    conditions of local advection in order to be able to predict how these transfer mechan-
    isms differ from the homogeneous situation.

To this purpose an experiment was carried out in the South of France in 1987 in the Crau
plain: the CRAU experiment (De Bruin *et al.*, 1991). The data-set from the CRAU-experi-
ment and the model will be used to

1.- Compare measured data and modelling results in order to validate the model and to rec-
    ognize its shortcomings and potential for further research.

2.- Study the downwind evolution of the surface fluxes and the interaction between the IBL
    temperature and humidity field and surface properties like surface temperature and sur-
    face resistance.

3.- Study the behaviour of turbulence quantities and the relation with mean field quantities in the IBL.

4.- Study the performance of micro-meteorological methods to determine the surface fluxes under conditions of local advection also in relation to a clearly defined IAL.

1.4 Structure of the thesis

In Chapter 2 theoretical aspects of local advection are discussed as far as they are relevant to this study.

The experiment, its location and set-up together with data processing methods are given in Chapter 3. In the last section of Chapter 3, section 3.6, the weather during the experiment is described and a data set of 81 runs is selected for this study.

The CRAU-experiment was set up around a step-change from a sparsely vegetated, dry and hot terrain to a vegetated wet and cooler surface. The data set consists of runs when the dry terrain was the upwind terrain. In Chapter 4, the experimental results from the upwind terrain and the radiation measurements over both terrains are given and discussed. These data are needed to compile the input for the second-order model used in this study and to check whether the modelling assumptions concerning the upwind conditions are valid for this experiment.

The mean flow characteristics and the fluxes over the downwind terrain are presented in Chapter 5 where in section 5.3 the surface roughness of the downwind terrain is calculated and in section 5.4 a simple parameterization to calculate the surface resistance is tested. These two quantities are also needed to run the second-order model used in this study.

In Chapter 6 both modelling and experimental results are used to explore the structure of the IBL and in particular the transfer mechanisms of heat and water vapour under advective conditions. In the section 6.1 the experimental results are compared with the model calculations. The performance of the model for homogeneous conditions is tested. To this purpose, flux-profile and flux-variance relations for homogeneous conditions as produced by the model are compared with the MO-relations. Then, observed and calculated mean

profiles of temperature, water vapour and wind and the observed and calculated fluxes of sensible heat, latent heat and momentum after the step-change are compared. Sections 6.2 to 6.4 deal with the flux-variance relations and the flux-profile relations in the IBL.

In Chapter 7 the applicability of the Bowen ratio methods using mean gradients or standard deviations above inhomogeneous terrain is studied. Using the model, the differences between the fluxes obtained with these methods and the surface fluxes are calculated. Furthermore, the IAL height will be studied and the confusion concerning the findings in the experiments mentioned in section 1.3, is discussed.

In Chapter 8 the summary and conclusions are given of which the dutch translation is given in Chapter 9.

2 THEORETICAL BACKGROUND

In this Chapter several theoretical aspects of local advection are introduced which are needed in the following chapters. The co-ordinate system and definitions of turbulent fluxes are given in section 2.1. In section 2.2 the MO theory is introduced and in section 2.3 the diffusion equation for some scalar C (or S) is used to compare flux divergence due to the daily cycle and the flux divergence caused by advection. In section 2.4 a calculation method for IBL height is discussed. Section 2.5 considers the second-order closure model to be used in this study. Finally, in section 2.6 the eddy diffusivity and the so-called transfer efficiency of scalars are considered.

2.1 Definitions of the co-ordinate system and some important quantities

The Cartesian co-ordinate system x, y, z is being used throughout the thesis for the analysis of the measured data and model results. The x-axis is taken in the direction of the mean horizontal wind $\overline{U}$; z is the vertical axis and y is the horizontal axis perpendicular to the mean wind direction.

The instantaneous components of the wind are U, V and W in respectively the x, y and z direction (positive upward). An overbar indicates an ensemble average and a lowercase symbol denotes the deviation from the mean so that, for example, the instantaneous horizontal wind can be written, using Reynolds'decomposition, as $U = \overline{U} + u$. An exception is made for density which is written as $\rho = \overline{\rho} + \rho'$.

The covariance of one the three wind components u, v and w with a fluctuating quantity s is the turbulent kinematic flux of S in the x, y or z-direction, for example the kinematic sensible heat flux $\overline{w\theta}$ or the momentum flux $\overline{uw}$. The vertical turbulent fluxes of interest for this study are the vertical turbulent flux of horizontal momentum, or shear stress

$$\tau = -\rho\overline{uw}, \tag{2.1}$$

with air density ρ;

the vertical turbulent flux of sensible heat

$$H = \rho c_p \overline{w\theta}, \tag{2.2}$$

in which c_p is the specific heat of dry air at constant pressure;

the vertical turbulent flux of water vapour

$$E = \rho \overline{wq} \qquad\qquad 2.3$$

or, in energy units, λE where λ is the latent heat of vaporisation;

and finally the buoyancy flux or virtual kinematic heat flux (neglecting some minor terms)

$$\overline{w\theta_v} = \overline{w\theta} + \overline{\Theta}0.61\overline{wq} \qquad\qquad 2.4$$

2.2 The Monin-Obukhov similarity relations

There are several reasons why MO-similarity theory is needed for this study. Firstly, the upwind measurements are verified using the MO-relations. Secondly, in the model MO-similarity is applied for its upper and lower boundary conditions. Thirdly, a modified form of MO-theory using so-called local scaling will be tested for the IBL using the measurements taken there.

MO-theory assumes that the non-dimensional first and second moments in the ASL are functions of only

$$\frac{z}{L} = \zeta = -\frac{kgz}{\Theta_v}\frac{\overline{w\theta_v}}{u_*^3} = \frac{kgz}{\Theta_v}\frac{\theta_{v,*}}{u_*^2} \qquad\qquad 2.5$$

in which L is the Obukhov length (Obukhov, 1971) and

$$\theta_{v,*} = \theta_* + 0.61\overline{\Theta}q_* \qquad\qquad 2.6$$

where

$$\theta_* = -\frac{\overline{w\theta}}{u_*} \qquad\qquad 2.7$$

and

$$q_* = -\frac{\overline{wq}}{u_*}. \qquad\qquad 2.8$$

The universal relations between the non-dimensional first and second moments and ζ have been determined in many experiments. The semi-empirical forms used in this study are given below; some of which can also be compared with the data from the experiment (Chapter 4). For the non-dimensional vertical gradients

$$\phi_m = \frac{kz}{u_*}\frac{\partial \overline{U}}{\partial z}, \quad \phi_\theta = \frac{kz}{\theta_*}\frac{\partial \overline{\Theta}}{\partial z} \quad \text{and} \quad \phi_q = \frac{kz}{q_*}\frac{\partial \overline{Q}}{\partial z} \qquad\qquad 2.9$$

results from several experiments indicate that

$$\phi_\theta = \phi_q = \phi_m^2 = (1 - 16\zeta)^{-0.5}. \qquad\qquad 2.10$$

The non-dimensional velocity variances or, as we propose to name these ratios of vertical fluxes and variances, the flux-variance relations for wind are

$$\varphi_u^2 = \frac{\sigma_u^2}{u_*^2} = 4.00 + 0.2(-\zeta/k)^{2/3} \qquad\qquad 2.11$$

$$\varphi_v^2 = \frac{\sigma_v^2}{u_*^2} = 1.94 + 0.2(-\zeta/k)^{2/3}$$

$$\varphi_w^2 = \frac{\sigma_w^2}{u_*^2} = 1.56(1 - 3\zeta)^{2/3}$$

although it is doubtful whether $\varphi_{u,v}$ are 'MO-quantities' depending on z/z_i, where z_i is the height of the PBL, rather than ζ (De Bruin $et\ al$, 1993, Kaimal and Finnigan, 1994). The neutral value of 1.94 for φ_v^2 follows from

$$\varphi_u^2 + \varphi_v^2 + \varphi_w^2 = 7.5. \qquad\qquad 2.12$$

at $\zeta = 0$. The value of 7.5, twice the amount of turbulent kinetic energy at neutral conditions, is within the range of values which have been reported in literature (Stull, 1988).

The non-dimensional scalar variances or flux-variance relations for scalars are written as

$$\varphi_c^2 = \frac{\sigma_c^2}{c_*^2} = a_c(1 - b_c\zeta)^{-2/3} \qquad\qquad 2.13$$

for $c = \theta$ or q in which $a_c = 8.4$ and $b_c = 28.4$ according De Bruin *et al.* (1993) whereas $a_c = 4$ and $b_c = 9.5$ according Kaimal and Finnigan (1994). For all scalar quantities answering to MO-theory, so-called MO-scalars, a_c and b_c should be the same for each C (Hill, 1989).

A parameterization for the non-dimensional horizontal heat and moisture fluxes can be found following Wyngaard *et al.* (1971). They argue that $\overline{uc}$ should vanish when either $\partial \overline{C}/\partial z$ or $\partial \overline{U}/\partial z$ are zero. Furthermore, they expect the sign of $\overline{uc}$ to change when the sign of either gradient changes. To cover these features they formulated that

$$\frac{\overline{u\theta}}{u_*\theta_*} = 4\phi_m\phi_\theta \qquad\qquad 2.14$$

$$\frac{\overline{uq}}{u_*q_*} = 4\phi_m\phi_q$$

where the constant is obtained from measurements which also validated these scaling relations (Wyngaard *et al.*, 1971, Bradley *et al.*, 1981b).

The flux-profile method applies MO theory and uses the integrated form of the flux-profile relations (Paulson, 1970) given in Eqs.2.9 and 2.10 for homogeneous and steady state conditions. These equations are

$$u(z) = \frac{u_*}{k}\left(\ln\left(\frac{z}{z_o}\right) - \psi_m(\zeta(z)) + \psi_m(\zeta(z_o)) \right) \qquad\qquad 2.15$$

$$\Theta(z) = \frac{\Theta_*}{k}\left(\ln\left(\frac{z}{z_o}\right) - \psi_\theta(\zeta(z)) + \psi_\theta(\zeta(z_o)) \right) + \Theta(z_o)$$

$$Q(z) = \frac{q_*}{k}\left(\ln\left(\frac{z}{z_o}\right) - \psi_q(\zeta(z)) + \psi_q(\zeta(z_o)) \right) + Q(z_o)$$

in which

$$\psi_m = 2\ln\left(\frac{1+X}{2}\right) + \ln\left(\frac{(1+X^2)}{2}\right) - 2\arctan(X) + \frac{\pi}{2} \qquad\qquad 2.16$$

$$\psi_{\theta,q} = 2\ln\left(\frac{1+Y^2}{2}\right)$$

and

$$X = (1 - x\zeta)^{0.25}$$

$$Y = (1 - y\zeta)^{0.25}$$

2.17

with $x = 16$ and $y = 16$ for $-2 \leq z/L \leq 0$. Since these relations are to be used preferably for $z_o \ll z$, $\psi_{m,h,q}(\zeta(z_o))$ can be neglected.

2.3 The diffusion equation for concentration

The budget equation for a conserved scalar C reads

$$\frac{\partial \overline{C}}{\partial t} + \overline{U}_j \frac{\partial \overline{C}}{\partial x_j} = -\frac{\overline{\partial u_j c}}{\partial x_j}$$

2.18

neglecting sources and sinks for concentration and radiation divergence in case of temperature. For temperature and moisture under steady state and horizontally homogeneous conditions all terms are small. This defines the one-dimensional case with a so-called constant flux layer. Because of the daily cycle of temperature the constant flux layer does not actually exist but the resulting flux divergence is relatively small in the ASL (see section 2.3.1).

With significant advection of C and for the two-dimensional case, the budget becomes

$$+\overline{U} \frac{\partial \overline{C}}{\partial x} = -\frac{\partial \overline{wc}}{\partial z}$$

2.19

considering a location in the IBL far enough from the step-change and therefore neglecting the horizontal flux divergence. This seems justified, considering for example the calculations of Philip (1987) which showed that in the first ten meters after a hot-cold step-change $\rho c_p \partial \overline{w\theta}/\partial x \approx 10 W/m^{-3}$, the next 100 meters it is already one order of magnitude smaller. Furthermore it is also assumed that $\overline{W} = 0$ as only moderate roughness changes and fetches above, say, 50 m over horizontal terrain are considered. The resulting budget together with a eddy diffusivity formulation for $\overline{wc}$,

$$\overline{wc} = -K_c \frac{\partial \overline{C}}{\partial z}$$

2.20

are being used in first-order closure models for studies on local advection (Philip, 1959, and see also Munn, 1966 and Brutsaert, 1982 for overviews). First-order closure models offer analytical solutions to the advection problem and are able to reproduce mean profiles of C in the IBL. Furthermore, they provide insight in the rate of IBL-growth from which fetch requirements have been defined. The main objection against these kind of models is the use of the mixing length hypothesis (Kroon, 1985) to solve the closure problem, a method that should only be used for flows with a constant mixing length or one that depends in a simple way on the geometry of the flow (Tennekes and Lumley, 1972). This is not to be expected in case of a step-change of surface conditions.

2.3.1 The magnitude of the flux divergence

Following Eq.2.19 the effect of local advection can be observed by measuring profiles of mean properties downstream of the step-change and by measuring vertical gradients of the turbulent fluxes. In order to get a feeling for the orders of magnitude that have to be dealt with, simple estimates are made for the vertical heat flux divergence due to the daily course of temperature in the homogeneous ASL and the divergence caused by a horizontal temperature gradient using an integrated form of Eq.2.19.

Typical values for the divergence with height of the sensible heat flux because of non-stationary conditions in the surface layer above homogeneous terrain and during day-time can be obtained using a simple estimate for the daily temperature course. It is assumed that temperature $\Theta(t)$ is a cosine function of time with day-length *day* and a daily temperature amplitude A_T K,

$$\Theta(t) = \Theta_{max} - A_T \cos\left(\frac{2\pi t}{day}\right)$$
                                                                                                    2.21

where t is the time elapsed since sunrise. This formulation can be used to estimate the flux-divergence that would be the result of heating or cooling of a column of air of height z. Integrating Eq.2.18 with $C = \Theta$ and neglecting advection gives the flux difference between two heights as a result of temperature change in time:

$$\int_0^{\bar{z}} \frac{\partial \Theta}{\partial t} dz = -\int_0^{\bar{z}} \frac{\partial}{\partial z}(\overline{w\theta})dz.$$

2.22

Together with Eq.2.21 it is then found that

$$\rho c_p[\overline{w\theta}_z - \overline{w\theta}_0] = -\rho c_p \frac{2\pi}{day} z A_T \sin\frac{2\pi t}{day}$$

2.23

For $day = 13$ hr and $A_T = 10$ K the magnitude of the flux divergence would then approximately be 1.6 W/m^3 at $t = 0.25 day$ and $t = 0.75 day$, when the divergence is maximal.

In the inhomogeneous ASL after a dry-to-wet step-change there is a horizontal gradient of the mean temperature. To estimate the effect of the horizontal temperature gradient Eq.2.19 is integrated between $z = z_o$ and z,

$$\int_{z_o}^{\bar{z}} \overline{U} \frac{\partial \overline{\Theta}}{\partial x} dz = -\int_{z_o}^{\bar{z}} \frac{\partial \overline{w\theta}}{\partial z} dz$$

2.24

which gives to a useful approximation for the flux difference between two levels

$$D_H = -\rho c_p \hat{U} \frac{\partial \hat{\Theta}}{\partial x} z_r$$

2.25

in which $\hat{U}$ and $\hat{\Theta}$ are the average wind speed and temperature in the layer below z_r and

$$D_H = H(z) - H(0).$$

As a rough estimate, to get a vertical sensible heat flux difference of 100 Wm^{-2} between the surface and $z = 4$ m it suffices to have a mean horizontal temperature gradient of 0.01 °C m^{-1} at $\hat{U} = 2$ ms^{-1}. These numbers indicate that, at least, flux divergence is often more likely to be neglected because of measuring problems than because it is actually negligible.

To conclude, it is found that a weak horizontal temperature gradient causes a flux divergence which is one to two orders of magnitude larger than the flux divergence owing to non-stationarity. A practical consequence for advection studies is that it is more feasible to measure flux divergences instead of measuring the almost intractable mean horizontal gradients.

2.4 IBL height

The IBL-height δ is defined as the height where the downwind vertical flux or concentration of some quantity attain a fixed fraction, say 99% percent, of their upwind value at the same height. Knowledge of the IBL-growth rate under local advection is restricted mainly to step-changes of surface roughness. For near-neutral conditions the thickness of the momentum-IBL after a surface roughness step-change was estimated to be proportional to $x^{0.8}$ where x is the downwind distance from the leading edge (Elliott, 1958). However, the growth rate of the IBL depends both on the character of the step-change (rough-to-smooth or vice-versa , Antonia and Luxton, 1971, 1972) and stability (Rao, 1975).

A method which relies more on the physics of IBL-formation was formulated by Miyake (1965). His approach to calculate the IBL-height is based on the diffusion of passive scalar quantities from ground sources and applies to all types of step-changes under neutral conditions. In the case of a surface roughness change, δ can be interpretated as a length scale for the thickness of the accelerated region after the step-change. The starting point for this method is the assumption that

$$\frac{d\delta}{dx} = \frac{B u_{*,2}}{\overline{U}} \qquad\qquad 2.26$$

i.e. the growth rate $d\delta/dx$ is supposed to be proportional to $u_{*,2}/U$ where the downwind friction velocity $u_{*,2}$ is taken as a characteristic velocity for the vertical diffusion process and the mean wind $\overline{U}$ represents the characteristic velocity for horizontal transport; $B \approx 1$ is a constant. For neutral conditions (when the wind profile is logarithmic function of height), integration leads to

$$B k = \frac{\delta}{x}\left(\ln\left(\frac{\delta}{z_{o2}} \right) - 1 \right) \qquad\qquad 2.27$$

where $z_{o,2}$ is the downwind surface roughness and $\delta = z_{o,2}$ at $x = 0$. For a surface roughness change under neutral conditions it was found that this length scale compares favourably with measurements of the momentum flux IBL-height, better than for example the power law formulas (Walmsley, 1989). It is therefore considered as a good estimate for a length scale

of vertical perturbation of the surface layer after a change of surface properties. In our case, the approach can only be considered as a rough estimate since (changing) stability is not accounted for.

2.5 The second-order closure model

An extensive description of the model employed in this thesis, together with an overview of all used equations, assumptions and initial conditions, was given by Kroon (1985). At this point only a short description of the model will be given. The set of equations, solved by the model, together with the applied parameterizations are summarized in Appendix A1.

The model simulates the flow structure of the ASL subject to local advection of momentum, heat and moisture. The air is assumed to flow at right angles across a surface discontinuity, restricting the description to two dimensions. To this end it solves the equations of the steady-state 2-dimensional field in the ASL using second-order closure.

Owing to the interaction between the mean, first-order flow field and the turbulence, second-order, flow field there are more unknowns than variables in the transport equations of U, W, Θ and Q. This well-known closure problem cannot be solved simply by introducing the explicit equations of the higher order terms since each equation of an ith-order term contains terms of the $i+1^{th}$-order. A solution is, to parameterize $i+1^{th}$-order terms, thus obtaining an ith-order closure model. First-order closure or K-models assume that there is a known relation between mean gradients and the fluxes. This so-called mixing length assumption is expected to break down under conditions of local advection. Therefore, if one it interested in the dynamics of the eddy diffusivity, it is necessary to take on at least second-order closure. The model used in this study employs second-order closure in which third-order terms are approximated by 'an ad-hoc gradient-transport model' (Rao *et al.*, 1974b),

$$\overline{Mu_i} = -K_M \partial \overline{M}/\partial x_i \qquad\qquad 2.28$$

where M can be $\overline{u_i s}(s = \theta, q)$, $\overline{\theta q}$, $\overline{\theta \theta}$ or $\overline{qq}$ and K_M is an eddy diffusivity for the gradient transport of M. Furthermore, pressure covariances and dissipation terms are parameterized following Wyngaard *et al.* (1974). A scheme of the model together with the closure approximations is given in Appendix A1.

Using these parameterizations, the transport equations of 16 dependent variables ($\overline{U}$, $\overline{W}$, $\overline{\Theta}$, $\overline{Q}$, σ_u, σ_v, σ_w, σ_q, σ_θ, $\overline{uw}$, $\overline{w\theta}$, $\overline{u\theta}$, $\overline{wq}$, $\overline{uq}$, $\overline{\theta q}$ and the dissipation of Turbulent Kinetic Energy (TKE), ε) are solved for $x \leq 0$ and $x > 0$. In the first part of the model , for $x \leq 0$, the advection terms are assumed zero and an initial equilibrium distribution with height of all first and second moments is calculated. These distributions should comply to the Monin-Obukhov similarity theory which is used in the model to calculate the lower ($z = z_o$) and upper boundary ($z = 50$ m) conditions.

In order to calculate the upwind structure of the ASL the model needs the upwind friction velocity $u_{*,1}$, the upwind characteristic temperature $\theta_{*,1}$ and the upwind characteristic specific humidity $q_{*,1}$. Furthermore, the upwind surface roughness $z_{o,1}$ and the upwind temperature and specific humidity at the level of the downwind surface roughness $z_{o,2}$ are needed. Note that a subscript "1" refers to the upwind terrain and "2" to the downwind terrain. The measurement results and calculations of these components are discussed in section 4.1.

A further input variable is the amount of available energy for the sensible and latent heat surface fluxes. The available energy is by definition

$$A = R_n - G. \qquad\qquad 2.29$$

The measurement results of radiation for both the up- and downwind terrains are discussed in section 4.2 together with the assumptions in the model concerning the behaviour of A.

The model also needs downwind surface parameters like the surface resistance r_s and the surface roughness $z_{o,2}$. The calculation of both these quantities is given in Chapter 5 where the downwind measuring results are discussed. Finally, dissipation ε is taken from the TKE-budget neglecting transport of TKE and applying MO-scaling,

$$\frac{kz}{u_*^3}\varepsilon = \phi_m - \zeta.$$
<div align="right">2.30</div>

The lower boundary conditions are calculated at $z = z_o$. The upper boundary conditions are calculated using the maximum height of the model grid, $z = 50$ m and the upwind Obukhov length. It is assumed that the fluxes decrease linearly with height from z_o to the height of the PBL, set at 1000 m.

2.6 Eddy diffusivities and transfer efficiencies of sensible heat and water vapour

The Bowen ratio energy balance method given in section 1.2 is, as said, a method to determine evapotranspiration. In the field, β can be obtained from simple measuring methods. One of these methods is the gradient method, it relies on the relation between the flux $\overline{wc}(z,x)$ and the gradient $\partial\overline{C}/\partial z$ of some concentration C. The ratio of these two quantities is referred to as the eddy diffusivity

$$K_c = -\frac{\overline{wc}(z,x)}{\partial\overline{C}/\partial z}.$$
<div align="right">2.31</div>

Since this study deals with an ASL in which the flux varies with height, it is important to note that, strictly speaking, eddy diffusivity should be evaluated using the flux measured at the height for which the gradient is evaluated. If the eddy diffusivities for sensible heat, K_θ and latent heat, K_q are equal, then (in its finite difference form)

$$\beta_g = \frac{c_p}{\lambda}\frac{\overline{\Theta}(z_2) - \overline{\Theta}(z_1)}{\overline{Q}(z_2) - \overline{Q}(z_1)} = \frac{c_p}{\lambda}\frac{\Delta\overline{\Theta}}{\Delta\overline{Q}} \quad .$$
<div align="right">2.32</div>

is the Bowen ratio obtained from mean gradients. The second method is the standard deviation method and it uses the relation between the flux $\overline{wc}$ and $\sigma_w\sigma_c$ of which the ratio is the correlation

$$R_{wc} = \frac{\overline{wc}}{\sigma_w\sigma_c}.$$
<div align="right">2.33</div>

This correlation is also referred to as the transfer efficiency of C (McBean and Miyake, 1972) since it is a measure of the net transfer of C by turbulent motions. If the transfer efficiencies for sensible heat, $R_{w\theta}$, and for latent heat, R_{wq}, have equal magnitudes it follows that

$$\beta_\sigma = \pm \frac{c_p}{\lambda} \frac{\sigma_\theta}{\sigma_q} \qquad\qquad 2.34$$

which is the Bowen ratio obtained from standard deviations; it is negative when $\overline{\theta q} < 0$ and positive when $\overline{\theta q} > 0$.

Here, both assumptions are looked at in somewhat more detail by considering the budget equations for the variances of temperature and water vapour. It will be shown that the transfer efficiency and the eddy diffusivity of C are closely related in the homogeneous ASL.

Qualitative insight in the dynamical behaviour of the eddy diffusivity and the transfer efficiency for vertical transport of a scalar quantity can be gained by considering the Reynolds equations of the second moments. For eddy diffusivity this was already done by Warhaft (1976) who used the $\overline{wc}$-budget and parameterizations from second-order modelling to arrive at an analytical expression for K_θ/K_q. It was concluded that for horizontally homogeneous conditions $K_\theta \geq K_q$ depending on the correlation between water vapour fluctuations and temperature fluctuations, $R_{\theta q}$. The standard deviation method requires that

$$|R_{w\theta}| = |R_{wq}| \qquad\qquad 2.35$$

which only holds when $q = a\theta$ and therefore $|R_{\theta q}| = 1$. It follows that both the requirements for the gradient method and the standard deviation method can be summarized in the condition that $|R_{\theta q}| = 1$.

Further insight in the relation between transfer efficiency and eddy diffusivity can be gained by considering the variance budget of C. For homogeneous conditions, the variance budget can be used to obtain a relation between φ_c and ϕ_c.

The C-variance budget for the steady, one-dimensional case, reads

$$0 = -2\overline{wc}\frac{\partial \overline{C}}{\partial z} - \frac{\partial \overline{c^2 w}}{\partial z} - 2N_c. \qquad 2.36$$

The right hand side terms from left to right are vertical gradient production, transport in the vertical and the dissipation of $\overline{c^2}$. The dissipation of c-fluctuations can be parameterized as is done in the second-order model used in this study,

$$N_c = \frac{\overline{c^2}}{\tau_c}. \qquad 2.37$$

Next, it is assumed that the relaxation time scale

$$\tau_c = \frac{kz}{A_c \sigma_w} \qquad 2.38$$

which is a parameterization thought to represent the stable, neutral and unstable conditions in the ASL because for stable and neutral conditions $\sigma_w \approx 1.25u_*$. For $\zeta \to -\infty$ u_* no longer is a governing velocity scale and $\sigma_w \approx (-kgz/\Theta\ \overline{w\theta})^{1/3}$, the velocity scale for local free convection (Wyngaard et al., 1971, De Bruin and Bink, 1994).

Furthermore, recall that

$$\phi_c = \frac{kz}{c_*}\frac{\partial \overline{C}}{\partial z} \text{ so } K_c = \frac{kzu_*}{\phi_c}. \qquad 2.39$$

For the homogeneous, stationary case it was shown that transport of $\overline{c^2}$ can be neglected (Wyngaard and Coté, 1971, Bradley et al., 1981a). Then it follows, also using Eqs.2.10, 2.11 and 2.13, that

$$\phi_c = A_c\varphi_w\varphi_c^2 \qquad 2.40$$

where A_c is a constant which follows from the values of ϕ_c, φ_c and φ_w for $\zeta = 0$.

The result of Eq.2.40 is given in Fig.2.1 for some scalar C. The observed relation for ϕ_c (Eq.2.10) is compared with the calculated ϕ_c using φ_w (Eq.2.11) and φ_c (Eq.2.13 with $a_c = 5.29$, $b_c = 14.2$ taken from Eq.4.7) with $A_c = 0.15$.
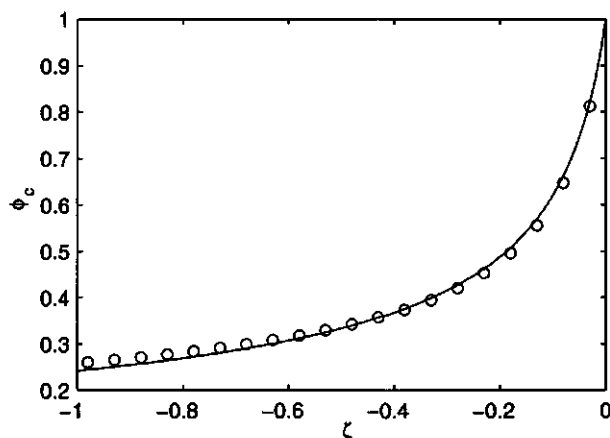
Fig.2.1 The non-dimensional gradient of C calculated using Eq.2.40 (open circles) compared with the observed relation for ϕ_c (Eq.2.10, solid line).

It can be seen that the product of the observed φ_w and φ_c^2 coincides almost exactly with the observed relation for ϕ_c. This is also interesting because this may explain why the free convective limit of the flux-profile relations (Eq.2.10) seems to be $\zeta^{-1/2}$ whereas this is $\zeta^{-1/3}$ for the flux-variance relation of C (Eq.2.13) which is in fact the expected limit for both relations (Monin and Yaglom, 1971). Using u_* in the relaxation time scale,

$$\tau_c = \frac{kz}{A_c u_*}$$

would lead to

$$\phi_c = A_c \varphi_c^2$$

which must be wrong since the free convective limit for ϕ_θ would then become $\zeta^{-2/3}$.

From Eqs.2.33, 2.39 and 2.40 it follows that

$$\frac{K_\theta}{K_q} = \frac{\varphi_q^2}{\varphi_\theta^2} = \frac{R_{w\theta}^2}{R_{wq}^2} \qquad\qquad 2.41$$

assuming that $A_\theta = A_q$ which can be expected considering the behaviour under neutral conditions when temperature and water vapour both can be considered as passive scalars.

It has been observed that over land, for horizontally homogeneous conditions when $R_{\theta q} < 1$, $R_{w\theta}$ is somewhat larger than R_{wq} (McBean and Miyake, 1972). There are two reasons for this which are often mentioned in literature. Firstly, the larger contribution of sensible heat fluctuations to air density fluctuations and therefore to vertical motions implies a higher correlation between w and θ compared to w and q. In other words, both parcels of relatively warm, humid air and parcels of relatively warm, dry air are sufficiently buoyant compared to their environment whereas humid, cool parcels may be not. It seems therefore that sensible heat has better mixing properties than water vapour and one would then expect that, for unstable conditions, $K_\theta > K_q$ which is in accordance with $R_{w\theta}^2 > R_{wq}^2$ and the earlier mentioned results of Warhaft (1976). Secondly, a more uniform surface temperature compared to the uniformity of the surface humidity must also play a role in connection with the mechanism given above. Otherwise, any parcel leaving the surface would be either wet and cool or dry and warm. Observations taken in a stable IAL (fetch 300 m, measuring height 1.5 m) after a dry, warm to cool, wet step-change (Lang et al., 1983a) also seem to agree, at least qualitatively, with Eq.2.41. For measurements in the stable IAL it was observed that, on average, $R_{w\theta}^2$ was smaller than R_{wq}^2 (Bink and Kroon, 1990) while for the same set of runs it was observed that $K_\theta < K_q$ (Lang et al., 1983a). Furthermore, from the data discussed in Motha et al. (1979) it can be deduced that K_θ/K_q and $R_{w\theta}/R_{wq}$ are correlated rather well.

To conclude, it was shown that eddy diffusivity and transfer efficiency in the homogeneous ASL are strongly related. Using the equation of the scalar variance budget, and with the help of a simple parameterization of scalar variance dissipation, a relation between these two flow properties was derived. With this result some insight is gained in the behaviour of the ratio K_θ/K_q. The analysis gives some guide-lines to study the structure of the flow in the IAL since the assumptions used to arrive at Eq.2.40 should also hold there. This is not the case for the IBL, because the one-dimensional form of the budgets was used, and the transport term in the variance budget (Eq.2.36) was neglected also. It remains to be seen where the IBL ends and the IAL begins.

3 DESCRIPTION OF THE 1987 CRAU EXPERIMENT

In June 1987 an experiment was carried out in order to study the airflow over an abrupt change from a dry and almost bare terrain to an irrigated grass field. The experiment was initiated to study the turbulence structure of the ASL that formed over the wet, cool grass terrain if warm, dry air was advected. For this purpose eddy-correlation and vertical profile measurements were performed at different heights and distances down- and upwind from the step-change. The experiment was carried out from June 2 to June 25, 1987 in close cooperation with the Department of Meteorology from the Vrije Universiteit of Amsterdam (VUA). Their contribution was described by Vugts *et al.* (1988).

3.1 Location of the experiment site

The location of the experiment site was about 10 km west of Salon-de-Provence at Mas[1] Capellan, France (43°38′*N* and 4°59′E) in the Crau plain (Fig.3.1) at the border of the Petite or Wet Crau and the Grande or Dry Crau[2]. The Crau plain measures about 500 km^2 with the Rhône at its west side, the Alpilles mountains to the north and the Mediterranean Sea in the south.

The Petite Crau is situated at the foot of the Alpilles and major agricultural activities are found several kilometres north-west from the experiment site. There, the Crau plain is mainly covered with orchards and fields with all kinds of crops. Most of these are surrounded by windbreaks. The area is very suitable for agriculture as it profits from the proximity of the mountains (favourable south slope, protection from the mistral and water availability). The Grande Crau is a bare stone-desert covered with stones, pebbles, some herbs and isolated, low shrubs.

---

1 Mas: homestead in S.France

2 Note that throughout the thesis, the used time standard is Universal Time (UTC). For the experimental location the sun reaches its heighest position around 11:40 UTC.
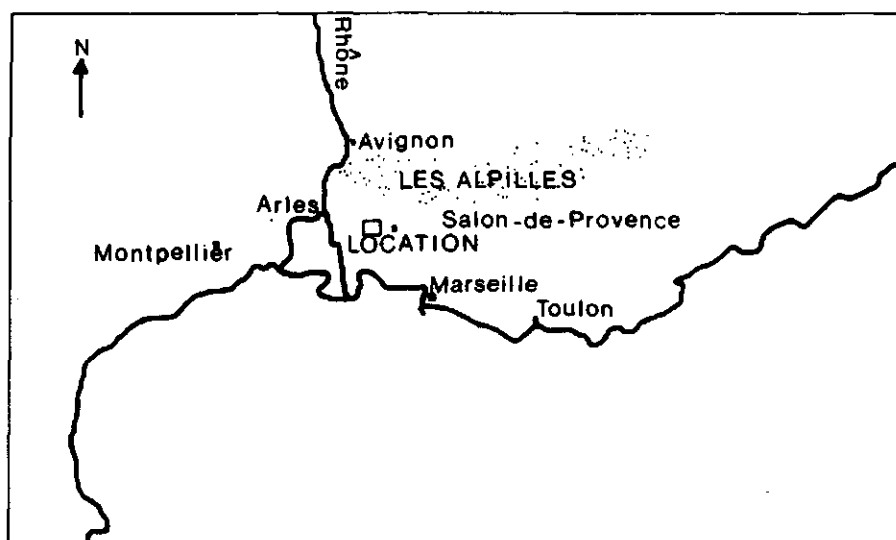
Fig.3.1 The location of the experiment site in the South of France.

3.2 Soil properties

The soil profile of the experiment site is an intergrade between Red and Brown Mediterra-
nean soils and Lithosols (Geze *et al.*, 1966, Aubert, 1968). Red and Brown Mediterranean
soils are formed in sub-tropical regions with a prolonged dry season and belong to a class of
soils which are rich in clay. The reddish colour is caused by dehydratation of iron com-
pounds (Buringh, 1970). Lithosols are shallow, stony soils where erosion removes soil so
rapidly that only a thin layer remains over weathered rock (Webster and Wilson, 1980).

The soil material is a mixture of colluvial (weathered material transported by gravity) and
alluvial (material transported and deposited by rivers) deposits. The soil is formed on lime-
stone with karst (denudation in limestone causing large cracks). Irrigation water at the site is
pumped up from a sub-surface river formed by karst. The profile of the dry terrain had a
high content of stones and rocks and was low on organic material. The top layer of the soil
profile of the wet terrain contained less stones as they have been removed by manual labour.
It also had a higher content of organic material due to the agricultural activities.

3.3 Description of the experiment site and its surroundings

A map of the site and its surroundings is given in Fig.3.2 and an aerial photo of the terrain can be found on the front cover of this thesis.

Fig.3.2 The experiment site and its direct surroundings. The 57.5 dm contour line is crossing the experiment site. Other contour lines (dashed) are given at 1.25 m intervals.

The experiment was set up around the leading edge between a strip of grass land (west of the edge) and the neighbouring uncultivated, dry and bare terrain (east, Fig.3.2). Two ways of referring to location with respect to the leading edge are employed in this thesis: dry, warm and wet, cool terrain (referring to the condition of soil moisture availability up- and down-wind of the leading edge and the surface temperature) and upwind and downwind terrain (with respect to the leading edge, assuming a wind direction from the dry to the wet terrain). Between the dry terrain and the wet terrain a somewhat elevated road was situated with a ditch to its west side. The dry terrain was partly covered with pebbles, low shrubs and some herbs, mostly thyme (see cover). The wet terrain had a maximum ground cover of grass which is irrigated from time to time (but not during this experiment) and grown for hay-making. The leading edge runs from the north-west to the south-east (310°). The grass terrain was made up of plots of approximately 500×100 m separated by ditches of 2 m width. The instruments above the wet terrain were placed in two neighbouring plots at the south-east end of Capellan.
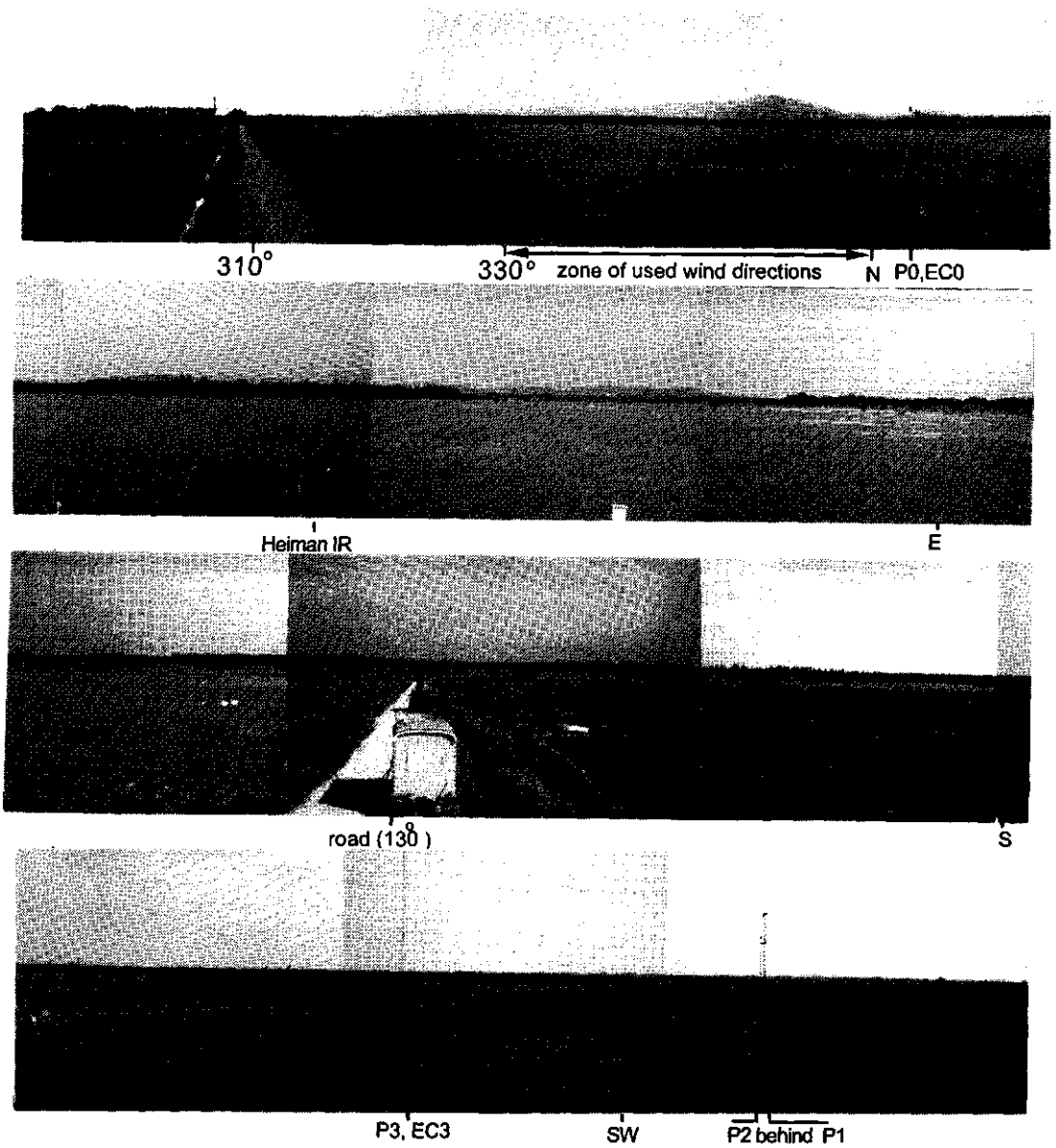
Fig.3.3 A panoramic view of the surroundings of the experiment site. Compass directions are indicated as well as some of the locations also indicated in Fig.3.4 and Table 3.1.

It can be seen in Fig.3.2 that the terrain slopes to the south-west. The slope of the Crau area is 0.0017 to 0.0034 radians. The slope in the direct surroundings of the experiment site is 0.0033 radians.

Fig.3.3 shows a panoramic view of the environment as seen from the top of the van containing the data-acquisition equipment. The van is also indicated in Fig.3.2 and was placed on the road at the east side of the grass terrain.

In Fig.3.4 a detailed map is presented of the experiment site and the location of the instruments. The zone of used wind directions or 'acceptance angle' for this study is indicated in Fig.3.4.
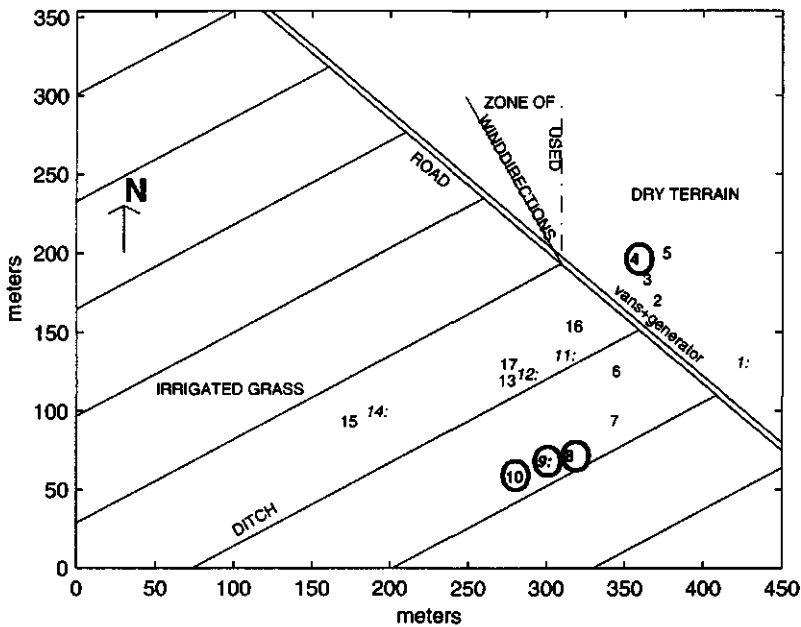
Fig.3.4 The experimental set up. The numbers in the figure refer to Table 3.1a,b. The zone of used wind directions refers to wind directions during runs which are used in this study. Bold, encircled numbers indicate Eddy Correlation stations and in italic print ending with ':' are locations with wind, temperature and humidity profile measurements.

Suitable wind directions for a dry-to-wet step-change are between 330° and 360° and between 45° and 90°. The region between 0° and 45° is somewhat less suitable due to a farm (Fontange) indicated in Fig.3.2 and visible on the panoramic view (Fig.3.3). The east limit

of the acceptance angle is dictated by the direction of the step-change and the set-up of the instruments. The actual wind directions during the experiment limited the acceptance angle to the zone of used wind directions. A wind break at about 700 m north-west from the location could influence measurements when the wind direction is around 320 °. Also, the largest concentration of orchards and irrigated crops is in the north-west and more to the west of the experiment site. The mountains that are indicated in Fig.3.1 and visible on the panoramic view are at about 9 km to the north. The preferred (and available) wind direction was therefore between 330° and 360°, also indicated in Fig.3.4. Between those directions from the mountains to the experiment site there is little agricultural activity. The nearest plot is 1.5 km north of the site. Farther away to the mountains there are some isolated plots with irrigated grass, wheat or fruit trees.

3.4 Instrumentation and data acquisition

In this section the measurements of mean profiles (3.4.1), radiation (3.4.2), wind direction (3.4.3) and soil heat flux (3.4.4) will be described. Where necessary, methods of data processing used for these measurements are given together with the instrument descriptions. Some further elaboration is needed on methods and corrections of the turbulence signals and direct flux measurements, these will be given in section 3.5. Finally, some general characteristics of the data-set and the weather during the experiment are given in section 3.6 together with run-selection criteria.

In Fig.3.4 the locations of the instruments are indicated and in Table 3.1.a and b, lists of the instruments installed at the dry and wet terrain are given. Throughout this thesis the numbers in Fig.3.4 and Table 3.1 are used to point to the instruments and their location (loc.) in the field.

A further convention will be used to refer to the locations of height-to-fetch dependent quantities, such as profiles of temperature, and to the turbulence measurements. A two-dimensional view at the array of masts and $\underline{E}$ddy $\underline{C}$orrelation stations EC in the $x - z$ plane is given in Fig.3.5. For the profile masts, the upwind mast is referred to as P0. The first mast after the step-change with profile equipment is referred to as P1 and so forth to P4. With these masts profiles of wind, temperature and humidity were collected, numbered P0 to P4. Eddy correlation observations were performed at one upwind station and at three downwind

stations. The downwind stations were set up to measure at different heights at approximately the same downwind distance. So we have EC station EC0 to EC3 where EC0 (top photo on the front cover) is the upwind station and EC1 is the station with the lowest height to fetch ratio (but the largest fetch), followed by EC2 and EC3 (lower photo on the front cover). This information can also be found in Fig.3.4 and Table 3.1. Note that the equipment of EC3 was installed in P3. The other EC stations were mounted on the top of separate masts.
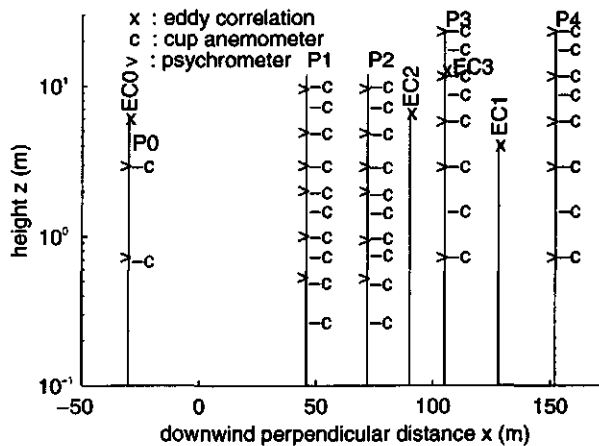
Fig.3.5 A two-dimensional view at the array of masts and EC stations in the $x - z$ plane. The perpendicular distance from the step-change is used on the x-axis. EC0 is drawn above P0 although P0 was placed at loc.1 and EC0 at loc.4 (see Fig.3.4).

The sampling process was controlled with a PDP 11-24 mini computer installed in a measuring-van. All samples were stored on magnetic tape. The data acquisition software can handle 2000 samples per second from a maximum of 200 channels. All incoming signals were filtered at 23 Hz with a first order filter to prevent aliasing of the power supply frequency (50 Hz).

The data were further processed in the laboratory. The sampled signals were reduced to 30-minute averages. The standard deviation and relevant correlation products of the signals with and without the removal of a linear trend were calculated (Van Boxel, 1987). The reduced signals were converted to obtain engineering values. The raw data remain stored on tape and optical disk.

The registration and calibration of data from the cup anemometers and psychrometers at P0 (loc.1), P3 (loc.9) and P4 (loc.14) and the net pyrradiometer at loc.7 were performed by the group of the VUA (Vugts *et al.*, 1988). The signals from all other instruments were recorded in the measuring van of Wageningen Agricultural University (WAU).

DRY TERRAIN			
Name	Loc.	Instrument (Section)	Level(s)
P0	1	2 Psychrometers (VUA)	3, 0.75 m
		2 Cup Anemometers (VUA)	3, 0.75 m
	2	Stevenson screen (thermohygrograph, min. and max. thermometer)	1.8 m
	3	Net pyrradiometer (3.4.2.2)	1.4 m
		Soil heat flux transducer (3.4.4)	$\approx$ -0.05 m
		Heimann KT24 infrared thermometer (3.4.2.3)	2.65 m
EC0	4	Eddy correlation system (1-component sonic, thermocouple, Lyman-α humidity fluctuation meter) (3.5)	6.1 m
		Inverted Pyranometer Kipp CN27. Reflected shortwave radiation (3.4.2.1)	1.5 m
		2 Psychrometers (3.4.1.1)	3.05, 0.75 m
	5	Net pyrradiometer (3.4.2.2)	1.4 m
		Soil heat flux transducer (3.4.4)	$\approx$ -0.05 m.
		Soil thermometers (3.4.1.3)	-0.38, -0.20, -0.10, -0.05 m.

Table 3.1.a The instruments and their location as indicated in Fig.3.4 at the dry terrain. Between brackets in the second column the relevant section is indicated, VUA: discussed in Vugts et al., 1988.

WET TERRAIN

	Loc.	Instrument	Level(s)
	6	Net pyrradiometer (3.4.2.2)	≈ 1 m
		Soil heat flux transducer (3.4.4)	≈ -0.02 m
	7	Net pyrradiometer (VUA)	≈ 1 m
		Stevenson screen (VUA)	2 m
EC2	8	Eddy correlation system (3-component sonic, thermocouple, Lyman-α humidity fluctuation meter) (3.5)	6.7 m
		Inverted Pyranometer (3.4.2.1)	1.5 m
P3	9	7 Cup anemometers (VUA, 3.4.1.2)	24, 18, 12, 6, 3, 1.5, 0.75 m
		5 Psychrometers (VUA)	24, 12, 6, 3, 0.75 m
EC3		Eddy correlation system (like 8 but without thermocouple) (3.5)	13 m
EC1	10	Eddy correlation system (see 8) (3.5)	4.1 m
P1	11	10 Cup anemometers (3.4.1.2)	10.15, 7.45, 4.90, 2.95, 1.95, 1.45, 0.95, 0.75, 0.45, 0.25 m
		6 Psychrometers (3.4.1.1)	9.95, 5.05, 3.05, 2.10, 1.05, 0.55 m
		Wind vane (3.4.3)	10.5 m
P2	12	10 Cup anemometers (3.4.1.2)	10.20, 7.45, 4.90, 2.95, 1.95, 1.50, 1.00, 0.75, 0.50, 0.25 m
		Pyranometer Kipp CN27 (3.4.2.1)	10 m
		6 Psychrometers (3.4.1.1)	9.95, 5.05, 3.00, 2.05, 1.00, 0.55 m
	13	Heimann KT24 infra red radiation thermometer (3.4.2.3)	2.05 m
		Soil heat flux transducer (3.4.4)	≈ -0.05 m
		Net pyrradiometer (3.4.2.2)	1.55 m
P4	14	7 Cup anemometers (VUA, 3.4.1.2)	24, 18, 12, 6, 3, 1.5, 0.75 m
		5 Psychrometers (VUA)	24, 12, 6, 3, 0.75 m
	15	Stevenson screen (VUA)	1.8 m
	16	4 Soil thermometers (3.4.1.3)	-0.50, -0.25, -0.10, -0.02 m
	17	4 Soil thermometers (3.4.1.3)	-0.50, -0.25, -0.10, -0.02 m

Table 3.1.b Same as 3.1.a but for the wet terrain.

3.4.1 Mean profile instrumentation

With the profile instrumentation mean soil- and air temperature, wind speed and humidity at different levels were measured. The standard deviation was mainly used to check instrumental performance. The sampling rate of these measurements was 1 Hz.

3.4.1.1 Psychrometers

Mean temperature and humidity were measured with two psychrometers in a mast (P0) at the dry terrain. Two masts at the grass terrain had six psychrometers up to 10 m (P0 and P1 at loc.11 and 12 at $x_p = 46$ and 75 m respectively, where x_p is the perpendicular distance from the step-change). Also at the grass terrain, two additional masts (VUA) contained five psychrometers up to 24 m (P3 and P4 at loc.9 and 14 at $x_p = 105$ and 152 m)

The psychrometer consists of two Pt-100 resistance elements. Each element is glued into the bottom of a stainless steel tube with a high heat conductive glue. The stainless steel tube is fixed in a plastic holder. They are surrounded by aluminium pipes and ventilated at a speed of at least 4 m s^{-1}. The complete system of ventilated sensors is surrounded by a radiation screen consisting of stacked white pans (polyester). A cotton wick covers the wet-bulb Pt-element. A constant flow of distiled water to the wet-bulb is maintained by a superseding pump. The wick is sufficiently long to ensure that the water is at the wet-bulb temperature when it reaches the sensor. There is a hole in the bottom plate of the psychrometer, just under the wet-bulb sensor, to ensure drainage of excess water.

All Pt-100 elements were calibrated in the laboratory with a precision of 0.02 K. The absolute error in temperature measurements with a Pt-100 is estimated to be $\Delta T = 0.09$ K (Bottemanne, 1982). From a comparison in the field comprising 8 out of the 14 psychrometers it was concluded that $\Delta T = 0.1$ K and $\Delta T_{wet} = 0.15$ K after the removal of systematic offsets.

The following relations are used to calculate the moisture variables. The vapour pressure e in Pa is calculated using the psychrometer equation

$$e = e_s(T_{wet}) - \gamma \frac{P}{\varepsilon_w}(T - T_{wet}) \qquad \qquad 3.1$$

where T and T_{wet} are the dry and wet-bulb temperature in °C. The isenthalpic psychrometer constant is

$$\gamma = \frac{c_p}{\lambda} \qquad\qquad 3.2$$

and P (Pa) is the air pressure, $\lambda = 2.43 \times 10^6$ J kg^{-1}, is the latent heat of vaporisation and $\varepsilon_w = 0.622$ the ratio of the molecular masses of water vapour ($M_w = 18.01$ kg kmol^{-1}) and dry air ($M_d = 28.96$ kg kmol^{-1}).

The saturated water vapour pressure $e_s(T)$ at T °C is obtained using Tetens'equation

$$e_s(T) = 611e^{17.27T/(T+237)} \qquad\qquad 3.3$$

(Monteith and Unsworth, 1990). The absolute humidity ρ_v (in kg m^{-3}) can be calculated from the equation of state for water vapour:

$$\rho_v = \frac{M_w e}{R(T+273.15)} \qquad\qquad 3.4$$

where $R = 8314$ J kmol^{-1} K^{-1} is the universal gas constant.

3.4.1.2 Cup anemometers

Wind speed profiles were measured at five different locations with self-manufactured lightweight 3-cup anemometers. These locations are P0 (loc.1, upwind) with measurements up to 3 m, P1 (loc.11) and P2 (loc.12) up to 10 m, P3 (at loc.9) and P4 (at loc.14) with measurements up to 24 m.

The first order response length D_r of the WAU cup anemometers is between 1 and 2 m and the starting speed is less than 0.3 m s^{-1}. All cups were calibrated in a wind tunnel at WAU. The response length of the WAU-cups was verified by Kohsiek et al., (1987). For the VUA-cups the response length is probably larger because of their higher starting speed compared to the WAU-cups.

The cup anemometers were mounted on rectangular booms pointing north, which were fitted to open triangular masts with sides of 20 cm. The booms were approximately 1 m long in order to avoid mast interferences.

A well-known problem is overspeeding of cup anemometers. A correction can be important since the error is height dependent and thus influences the vertical gradient and surface roughness calculations. Overspeeding is caused by the non-linear response of cup anemometers to fluctuating winds as they respond more quickly to an increase of wind speed than to a decrease. The relative overspeeding error can be calculated from

$$\frac{\overline{U}_m - \overline{U}}{\overline{U}} = \frac{\sigma_u^2}{\overline{U}^2} J_o + c_o \frac{\sigma_w^2}{\overline{U}^2} + d_o \frac{\sigma_v^2}{\overline{U}^2} \qquad\qquad 3.5$$

where $c_o \approx 0.67$ and $d_o = 0.5$ (Zhang, 1988) and the index m refers to the measured wind speed. The non-dimensional factor J_o is a function of the response length of the anemometer and a length scale for horizontal turbulence. As a first estimate for J_o we may use (Busch and Kristensen, 1976)

$$J_o = \left(1 + \frac{z}{D_r f_o}\right)^{-1}. \qquad\qquad 3.6$$

where $f_o = n_o z / \overline{U}$, the non-dimensional peak frequency of the horizontal velocity variance spectrum and n_o is the natural peak frequency (s^{-1}) of the horizontal velocity variance spectrum. The frequency f_o is a function of stability (Panofsky and Dutton, 1984),

$$f_o = 0.183 \qquad\qquad\qquad \left(\frac{z}{L} < -0.7\right) \qquad\qquad 3.7$$

$$f_o = 0.482 + 0.437\frac{z}{L} \qquad\qquad \left(-0.7 \leq \frac{z}{L} \leq 0\right)$$

$$f_o = 0.482 + 0.82\frac{z}{L} \qquad\qquad \left(\frac{z}{L} > 0\right).$$

The overspeeding error can be considered as a function of the four non-dimensional numbers z/z_o, z/L, D_r/z f_o. The stability z/L enters the problem through the dependence of

overspeeding on the non-dimensional standard deviations $\sigma_{u,v,w}/u_*$ which are functions of z/L as was discussed in section 2.2. Overspeeding also depends on $\overline{U}/u_*$, which is a function of z/L and z/z_o.

The Monin-Obukhov similarity formulations given in section 2.2 were used to calculate the non-dimensional standard deviations and the logarithmic wind profile corrected for stability. The roughness lengths were estimated from near-neutral wind profiles. The roughness lengths used to apply the overspeeding correction of the dry and wet terrain were estimated to be respectively 1×10^{-2} m and 7×10^{-2} m (see sections 4.1.1 and 5.3). Note that this method in fact requires an independent estimate for the surface roughness or an iterative procedure but the latter was found to be not necessary.

With these values it is possible to estimate relative overspeeding. It is found that the relative error for neutral to unstable conditions depends most strongly on z/z_o and less on z/L as can be seen in Fig.3.6.
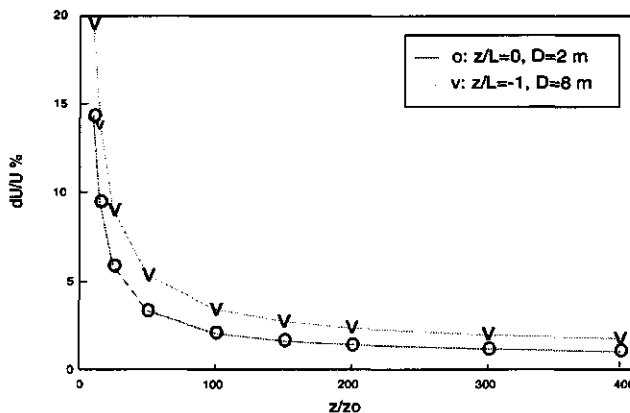

Fig.3.6 The relative overspeeding error as a function of z/z_o and stability for cup anemometers with $D_r = 2$ m at $z/L = 0$ and with $D_r = 8$ m at $z/L = -1$, representing two extreme cases.

The corrections for the cup anemometers were calculated using $D_r = 2$ m for the cups at P1 and P2 and $D_r = 8$ m for the cups at P3 and P4. The resulting corrections were below 10 %

(9% for 0.5 m down to 1 % at 24 m) for all levels except for the measurements at 0.25 m, which are not used in the analysis (also because the relative large error in the estimate of the height above the surface and incidental blocking of the cup rotation by the vegetation).

3.4.1.3 Soil thermometers

Soil temperature profiles of the grass terrain were measured using Pt-100 elements. The Pt-elements were installed sideways in an undisturbed soil profile. The Pt-100's were installed at four depths: 2, 10, 25 and 50 cm below the surface (loc.16, 17). Soil temperature profile measurements at the dry terrain were carried out by the VUA using NTC's (resistance temperature sensors with a Negative Temperature Coefficient, Van Boxel, 1986). The depths there were 5, 10, 20 and 38 cm below the surface.

The temperature profiles are used to calculate the thermal diffusity of the soil and the damping depth of the temperature wave going into the soil. Furthermore, soil heat fluxes can be calculated (Chapter 4).

3.4.2 Radiation

The incoming or global shortwave radiation and the reflected shortwave radiation were measured at both terrains (3.4.2.1). Above each of the two terrain types duplicate measurements of net radiation were performed (3.4.2.2). The radiation temperature for both terrains was also measured (3.4.2.3). The main use for these measurements was to get reliable data on the available energy for both terrains which is an important input parameter in models. The internal consistency of the radiation measurements can be tested by comparing observed net radiation with the calculated net radiation, i.e the sum of short and longwave radiation components. The sampling rate of all radiation measurements was 1 Hz.

3.4.2.1 Global radiation and reflected shortwave radiation

The global radiation and reflected shortwave radiation were measured using Kipp CN27 pyranometers. Above the dry terrain (no.4) and the grass terrain (no.8) two Kipps were facing the surface in order to measure the reflected shortwave radiation. The night-time readings were used to calculate the offset which was < 3 Wm^{-2}. Their calibration precision is estimated to be 5%.

3.4.2.2 Net radiation

The net radiation measurements (locs.3,5,6 and 13) were performed with (unventilated) Funk net pyrradiometers. The polyethylene domes were pressurized and dried with nitrogen.

Results of instrument comparisons have shown that large differences between net radiometers are possible in the field due to the characteristics of the dome and due to a different sensitivity for long and shortwave radiation of the instruments (Oliver and Wright, 1991; Halldin and Lindroth, 1991).

A check of the calibration as given by the manufacturer was carried out in the field with the radiometers installed close to each other above the grass terrain at a height of 1.5 m. It is tacitly assumed that the observed differences are not due to the location of the instruments during the field calibration. The set-up of the calibration trial ensured that the area covered by the net radiometers mutually coincided for a large part. The underlying surface was fully covered with fresh green grass. The measurements were taken at the end of the experiment on June 25. Results of 17 half hour runs were compared, 7 night-time runs and 10 day-time runs. The results are given in Table 3.2. The measured values are given as well as normalized values using instrument no.5 as the reference (again the number refers to its original location during the experiment). Instrument no.5 was chosen as the reference since its difference with the mean result showed the smallest trend (implicitly assuming that the mean of the 4 measurements is the best estimate for the actual net radiation).

Time (start)	loc.3 $W\ m^{-2}$	5 $W\ m^{-2}$	13 $W\ m^{-2}$	6 $W\ m^{-2}$	3 R_{n3}/R_{n5}	5 ref.	13 R_{n13}/R_{n5}	6 R_{n6}/R_{n5}
19.00	-72	-68	-74	-64	1.07	1.00	1.09	0.95
19.30	-76	-71	-78	-67	1.07	1.00	1.10	0.95
20.00	-74	-70	-76	-66	1.07	1.00	1.10	0.95
20.30	-73	-68	-75	-64	1.07	1.00	1.10	0.95
21.00	-73	-69	-75	-65	1.07	1.00	1.10	0.95
21.30	-75	-70	-77	-66	1.07	1.00	1.10	0.95
22.00	-75	-70	-77	-67	1.07	1.00	1.10	0.95
mean	-74	-69	-76	-66	1.069	1.000	1.096	0.947
st.dev	1	1	1	1	0.001	0	0.002	0.001

Table 3.2.a A comparison of net radiometers above grass terrain. Night-time measurements. 30 minute averages. The last four columns contain results normalized with the results from net radiometer 5.

Time (start)	loc.3 W m^{-2}	5 W m^{-2}	13 W m^{-2}	6 W m^{-2}	3 R_{n3}/R_{n5}	5 ref.	13 R_{n13}/R_{n5}	6 R_{n6}/R_{n5}
8.00	408	392	380	389	1.04	1.00	0.97	0.99
8.30	469	452	454	447	1.04	1.00	1.00	0.99
9.00	519	502	509	496	1.03	1.00	1.01	0.99
9.30	561	543	555	537	1.03	1.00	1.02	0.99
10.00	595	576	593	570	1.03	1.00	1.03	0.99
10.30	618	601	621	594	1.03	1.00	1.03	0.99
11.00	630	615	638	607	1.02	1.00	1.04	0.99
11.30	630	617	642	608	1.02	1.00	1.04	0.99
12.00	623	612	639	603	1.02	1.00	1.04	0.99
12.30	605	596	624	586	1.02	1.00	1.05	0.98
mean	566	551	566	544	1.028	1.000	1.024	0.988
st.dev	73	74	86	72	0.008	0.000	0.022	0.002

Table 3.2.b As 3.2.a but for the day-time measurements.

The results of the instruments originally used at loc.3, 5 and 6 compare well (within an offset of 15 W m^{-2}) whereas the pyrradiometer from loc.13 seems to have a different sensitivity for the shortwave component. The night-time differences were constant for all instruments, the largest difference being 11 Wm^{-2}. Based on these results individual corrections were applied to the measured net radiation during the experiment. The applied corrections are given in Table 3.3.

$R_n < 100$ W m^{-2}	$R_n > 100$ W m^{-2}
$R_{n3} := R_{n3} + 5$	$R_{n3} := R_{n3} - 15$
$R_{n13} := R_{n13} + 6$	$R_{n13} := R_{n13} - 0.13R_{n5} + 61$
$R_{n6} := R_{n6} - 3$	$R_{n6} := R_{n6} + 7$

Table 3.3 The corrections applied to the net radiation measurements at the different locations based on the field calibration (: = should be read as "becomes".)

It should be realized that these corrections are somewhat ad hoc. The duration of the field calibration does not justify further conclusions but to state the obvious: further research on the reliability and reproducibility of net radiation measurements is needed.

3.4.2.3 Surface temperature and outgoing longwave radiation

Radiation or infrared temperature at both terrains was observed with Heimann infrared thermometers (type KT24, locs.3 and 13). The instruments were calibrated at the WAU above a water-bath for which an emissivity $\varepsilon_r = 1$ is assumed. The instrument has an accuracy of about 0.5 K. The thermometers with a 8° field-of-view were mounted at 2.65 m above the dry terrain and at 2.05 m above the wet terrain under an angle of 45°.

The radiation temperature is an apparent surface temperature which accounts for the longwave radiation emitted as a function of the real surface temperature and the reflected incoming longwave radiation. No explicit knowledge of the emissivity of the surface and of the incoming longwave radiation is needed this way and the outgoing longwave radiation L_{out} can be calculated using

$$L_{out} = \sigma T_{s,m}^4 \qquad\qquad 3.8$$

where $T_{s,m}$ K is the measured Heimann temperature. However, in order to obtain surface temperatures for surface flux calculations, measurements need to be corrected for the emissivity of the natural terrain and for the reflected part of the downward longwave radiation flux (Muller *et al.*, 1990).

The emissivity of the grass terrain is taken as 0.92 and that of the dry terrain is estimated to be 0.96 (Oke, 1987). The length of the grass increased during the experiment which might have led to a decreasing emissivity (Oke, 1987). The humidity of the terrain also influences emissivity. The plots were not irrigated during the period under consideration. Rain was observed on several occasions but all rainfall occurred before June 19 which is just before the period of June 20 to June 24 from which the runs for further analysis were selected (see section 3.6).

To obtain a correction for the reflected incoming longwave radiation , the incoming or downward longwave radiation L_{in} has to be estimated. This was done using a simple estimate which is valid for cloudless skies and a temperature range between 10 and 40 °C: $L_{in} = 213 + 5.5T_a$ W m^{-2} (Monteith and Unsworth, 1990). This estimate does not consider air humidity. The air temperature T_a is the temperature at $z = 3$ m.

Finally, the real surface temperature is obtained from the measured infra-red temperature using

$$T_s = \left(\frac{T_{s,m}^4}{\varepsilon_r} - \frac{(213 + 5.5T)(1 - \varepsilon_r)}{\varepsilon_r \sigma} \right)^{0.25}$$

3.9

in which σ is the Stefan Boltzmann constant, 5.67×10^{-8} W m^{-2} K^{-4}. Note that all temperatures in Eq.3.9 are in K except T which has to be given in °C. The results of the correction are sensitive to the choice of the emissivity of the soil surface. E.g. a difference in the emissivity between 0.96 and 0.97 gives a change of approximately 0.3 K at a longwave radiation of 300 Wm^{-2}. However, since we are mainly interested in the difference between the up- and downwind surface temperature this error is relatively small.

3.4.3 Wind direction

The wind-vane (gray-code, 4 bit, i.e. 16 directions) was installed at 10 m height above the grass terrain. The wind direction is used to calculate the distance from the step-change of all instruments at the grass terrain. The distance x of some location at the grass terrain is calculated using

$$x = \frac{x_p}{\sin(50° + \overline{dd})}$$

3.10

where $\overline{dd}$ is the 30-minute mean wind direction (1800 samples) and x_p is the perpendicular distance to the step-change.

3.4.4 Soil heat flux

The soil heat flux was measured with soil heat flux transducers and can also be calculated using the measured soil temperature profiles. In section 4.2.2 the resulting soil heat flux will be compared with the soil heat flux calculated using the so-called integration method and the gradient method. Corrections to the transducer measurements are discussed below.

The soil heat flux transducers are 0.5 cm thick and have a diameter of 10 cm. Two transducers were used at each terrain. The transducers have been calibrated by the manufacturer (TNO-Delft, the Netherlands).

The transducers cannot be placed exactly at the surface but have to be buried under the soil surface. The estimated thickness of the soil layer above the transducer is 5 cm for the dry terrain and 2 cm for the wet terrain. Therefore, the soil heat fluxes measured with the transducers have to be corrected for heat-storage change in the layer (which can be considerable also depending on the time-averaging interval) above the transducers.

The heat-storage change above the transducer is calculated from

$$S_s = \int_0^h C_s \frac{\partial T}{\partial t} dh' \qquad\qquad 3.11$$

in which C_s is the volumetric heat capacity in J K^{-1} m^{-3} of the soil and h (m) is the thickness of the soil layer above the transducer. The temperature change $\partial T/\partial t$ of the layer above the transducer is estimated using the soil temperature at -0.05 m at the dry terrain and at -0.02 m at the wet terrain.

A further correction is needed for the difference in thermal conductivity of the transducers and the surrounding medium. This correction is evaluated as the ratio of the actual soil heat flux density G and G_p, the heat flux density across the central plane of the transducer normal to the direction of the heat flux at large distances from the meter (Philip, 1961, Overgaard-Mogensen, 1970)

$$\frac{G}{G_p} = 1 - b \frac{d_p}{A^{0.5}} \left(1 - \frac{\lambda_s}{\lambda_p}\right). \qquad\qquad 3.12$$

where b is an instrumental constant, for which the poor man's estimate is used: $b = 1$. The thickness d_p of the soil heat flux transducer is 0.005 m and A is the surface area of the transducer, λ_s and λ_p are respectively the thermal conductivity (W m^{-1} K^{-1}) of the soil and the transducer.

To calculate these corrections values for the volumetric heat capacity, thermal diffusity and thermal conductivity of the soil have to be estimated. These quantities can be calculated from observations of soil temperature and soil moisture as will be shown below.

3.4.4.1 Estimates of the thermal properties of the soil

The (volumetric) heat capacity of the soil is, neglecting the contribution of air,

$$C_s = x_{q,c}\rho_{q,c}c_{q,c} + x_w\rho_w c_w \qquad\qquad 3.13$$

in which x is the volume fraction of quartz and clay (q,c) and of water (w), ρ is density and c is specific heat capacity.

The solid fraction is $x_{q,c} = 1 - P_s$ where P_s is the porosity of the soil. Soil samples from just below the surface were taken at the dry and wet terrain once a day (at least) in the period from June 4 to June 21 by the VU. These samples were weighed, dried and weighed again. The samples with the lowest dry mass - total mass ratio were used to calculate the porosity of the soil. This way, the porosity for the wet terrain soil was estimated to be 0.47 and for the dry terrain 0.23 (assuming a density of 2600 kg m^{-3} for $\rho_{q,c}$ and 1000 kg m^{-3} for ρ_w). Calculations of C_s are performed using a fixed vol% H$_2$O of 30% for the wet terrain profile and 9% for the dry terrain based on the soil moisture measurements. With $c_{q,c} = 850$ J K^{-1} kg^{-1} for the solid phase and $c_w = 4180$ J K^{-1} kg^{-1}, the dry terrain volumetric heat capacity becomes $C_{s,1} = 2.08 \times 10^6$ and for the wet terrain $C_{s,2} = 2.43 \times 10^6$ J K^{-1} m^{-3}.

The thermal diffusity a m^2 s^{-1} of the soil is needed together with C_s to calculate the thermal conductivity $\lambda_s = aC_s$ W m^{-1} K^{-1}. For a homogeneous soil profile the thermal diffusity can be determined graphically from the relation between the amplitude of the soil temperature wave and the depth z. The relation reads (Van Wijk and De Vries, 1966, Van Boxel, 1986)

$$\ln A_z = -\frac{z}{D_d} + \ln A_o \qquad\qquad 3.14$$

where $A_{o,z}$ are the amplitudes of the temperature wave at the surface and at depth z. The damping depth D_d m, is the depth where $A_z = \frac{1}{e}A_o$. The thermal diffusity is

$$a = \frac{D_d^2 \pi}{P_t}, \qquad\qquad 3.15$$

$P_t = 86400$ s. In Fig.3.7 the results are given for the two different terrains based on the temperature profiles of June 20 to 24, 1987.
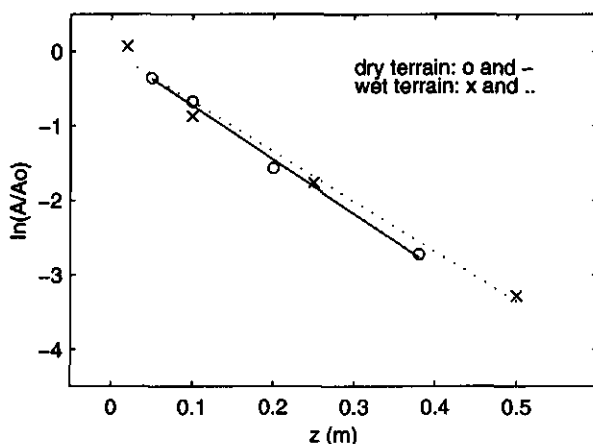
Fig.3.7 *The relation between the (normalized) amplitude of the soil temperature wave and depth. The slope of the line is* $-1/D_d$.

The damping depth for the dry terrain is thus found to be 0.14 m and for the wet terrain 0.15 m. This gives thermal diffusities of 0.69×10^{-6} (dry) and 0.81×10^{-6} m^2 s^{-1} (wet) resulting in thermal conductivities of 1.43 (dry) and 1.96 W m^{-1} K^{-1} (wet). A study to calculate thermal conductivities for the dry Crau using different methods (Van der Hurk, 1990) produced values which agree with our findings and with results from others for moderately dry soils (Ten Berge, 1986) but with a large scatter.

In Table 3.4 the results of the calculations of soil properties are summarized and given together with the probable errors in C_s and λ_s based on estimated errors in P_s, x_w and a.

	wet terrain	dry terrain	
P_s	0.47±0.05	0.23±0.05	
$x_{q,c}$	0.53±0.05	0.77±0.05	
x_w	0.30±0.05	0.09±0.05	
ρ_s	1680±140	2090±140	kg m^{-3}
C_s	2.43±0.11	2.08±0.11	10^6 J m^{-3} K^{-1}
D_d	0.15±0.01	0.14±0.01	m
a	0.81±0.10	0.69±0.10	10^{-6} m^2 s^{-1}
k	1.96±0.35	1.43±0.27	W K^{-1} m^{-1}

Table 3.4 Soil properties for the wet and dry terrain. The given quantities are porosity P_s, volume fractions of water and solid phase x_w and $x_{q,c}$, total soil density ρ_s, volumetric heat capacity C_s, damping depth D_d, thermal diffusity a and thermal conductivity k. The margins are probable errors based on estimated errors in P_s, a and x_w.

3.4.4.2 Corrections to the soil heat fluxes measured with the transducers

The storage correction is needed here because half hour means are being used. The correction depends on the time of day, it was 7 ± 10 % for the wet terrain and 12 ± 29 % for the dry terrain. It is a relatively large, positive correction in the morning (relative to the actual heat flux), approximately 0 around noon and becoming negative in the afternoon.

The thermal conductivity of the transducers is estimated to be 0.25 W m^{-1} K^{-1}. Together with the thermal conductivities of the soil and application of Eq.3.12 leads to $G/G_p = 1.27$ for the dry terrain and $G/G_p = 1.39$ for the wet terrain where there is a larger difference between the thermal conductivity of the transducer and the soil.

3.5 The turbulence measurements

The turbulence structure and turbulent fluxes were measured at three different stations after the step-change and at one upwind station of the step-change. The sample frequency for all these measurements was 10 Hz. At each station a combination of fast-response equipment was installed to obtain (co-)variances of the fluctuating wind, temperature and humidity fields.

At EC0, above the dry terrain, a Kaijo Denki one-component sonic anemometer, a Lyman-α humidity fluctuation meter and a thermocouple were mounted at 6.1 m height. At the EC1, 2 and 3 stations 3-component sonics, Kaijo Denki DAT310, and Lyman-α's were installed. Fast-responding thermocouples designed and constructed at the WAU (Van Asselt *et al.*, 1991) were mounted at the EC1 and EC2 whereas at EC3 the sonic temperature was used. When necessary levelling of the sonic array was performed. The sonic at EC3 (loc no.9) could only be levelled at the start of the experiment.

At EC2 (loc.8) the instruments were mounted 6.7 m above the ground, at EC3 (loc.9) the measuring height was 13 m and at EC1 (no.10) $z = 4.1$ m. The sonics of EC1 and 2 were placed on the top of their mast, at EC3 (no.9) the sonic was mounted on a 1.5 m boom pointing north. The Lyman-α's and thermocouples were positioned downwind of the sonics and the downwind separation between the vertical wind sensor and these instruments was < 0.5 m. The Lyman-α's are home-built, except for the source and the detector which are constructed by Glass Technologists, Maryland, USA. The thermocouples and Lyman-α's are used only for temperature and humidity fluctuation measurements as the mean values were not calibrated with sufficient precision.

In the next sections short descriptions will be given of the measuring principle of the applied instruments. Extensive descriptions are given in textbooks on experimental meteorology (Lenschow, 1986)

3.5.1 The sonic anemometer

The three-component sonic has three pairs of probe heads with combined ultra-sonic trans-mitter-receiver probes. With this system, the travel time of transmitted sound pulses is measured in 2×3 directions. From the difference in travel time of two pulses, transmitted in opposite directions along a fixed path, the wind speed along the path can be calculated. From the average travel time the sonic temperature can be obtained but this temperature is also sensitive to humidity and the wind component normal to the path (see 3.5.1.2). The path-lengths of both the one- and three-component sonics are 0.2 m. They are accurate to within 1% according to the manufacturer. This is also confirmed by calibration in a wind tunnel if the wind is not along the line of two opposite probe heads (Van Boxel, 1986).

3.5.1.1 Distortion of the flow through the sonic-array

Distortion of the flow due to the presence of the sonic itself, other instruments and (parts of) masts can be serious (Wyngaard, 1991). In this section, a simple correction method is given to estimate the influence of distortion. For homogeneous conditions and above non-sloping terrain it is reasonable to assume that $\overline{W} = 0$ in the surface layer and when a mean vertical velocity is observed it may be due to flow distortion or tilt of the instrument[3]. To start, the latter two possibilities are looked into and the magnitude of $\overline{W}$ they induce will be discussed.

The actual tilt (the deviation from a level position) of the sonics was checked throughout the experiment and was always smaller than 0.0087 radians (thus corresponding with $\overline{W} = 0.08$ m s^{-1} when $\overline{U} = 10$ m s^{-1}). Sloping terrain is in effect the same as a tilted sonic. The terrain slope (see section 3.3) was too small and cannot account for the observed mean vertical velocity, also supported by the fact that the expected sign is opposite of what was observed.

As a consequence of continuity, a roughness step-change gives rise to a vertical wind component. A simple estimate of $\overline{W}$ can be obtained through integration of the continuity equation

$$\frac{\partial \overline{U}}{\partial x} + \frac{\partial \overline{W}}{\partial z} = 0 \qquad\qquad 3.16$$

between z and z_o, neglecting the $\overline{V}$-gradient in the y-direction. This gives (in finite difference form)

$$\overline{W}(z) = -z \frac{\Delta \hat{U}}{\Delta x} \qquad\qquad 3.17$$

in which

$$\hat{U} = \frac{1}{z} \int_{z_o}^{z} U(z) dz . \qquad\qquad 3.18$$

---

3 A further possibility for a (small) mean vertical velocity is discussed in section 3.5.2.3 and is due to the presence of a vertical heat flux.

With the wind profiles taken at the different locations of which x is known, $\overline{W}$ at $z = 10$ m is calculated for all 81 runs. To that purpose wind speed averages between the surface and 10 m height were calculated using the measured wind profiles at P0 to P4. This can, of course, only be a crude estimate, but the order of magnitude and the sign should compare. The effect of the sloping terrain is also included in the calculation using a tilt of 0.0033 radians. In Table 3.5 the results are given.

$\overline{W}$ cm s^{-1}:	calc.	EC3	EC2	EC1
mean	1	2	39	38
σ	3	4	6	8
min	-10	-9	26	23
max	10	12	59	56

Table 3.5 Average (of 81 runs) results of the calculated and measured vertical wind velocity component due to the roughness step-change and tilt (or sloping terrain).

It is found that the calculated $\overline{W}$-signal compares favourably with the measured signal at EC3 but not with the $\overline{W}$-signals at EC1 and 2. Furthermore, calculations show that tilt and the roughness step cannot explain the high values of $\overline{W}$ at the EC stations 1 and 2.

The set-up of the eddy-correlation instrumentation at EC0, 1 and 2 was rather bulky causing distortion of the wind field around the sonic-arrays. This can be seen in Fig.3.8 where the mean vertical wind speed is given as a function of the mean horizontal wind speed for EC1 (the results at EC2 and EC0 are comparable to those at EC1). For comparison, the same quantity is given for EC3 which is not bulky. For EC1 there is a clear dependence of $\overline{W}$ on $\overline{U}$, indicating an obstruction of the sensor by other instruments; for EC3 such a dependence is not present.
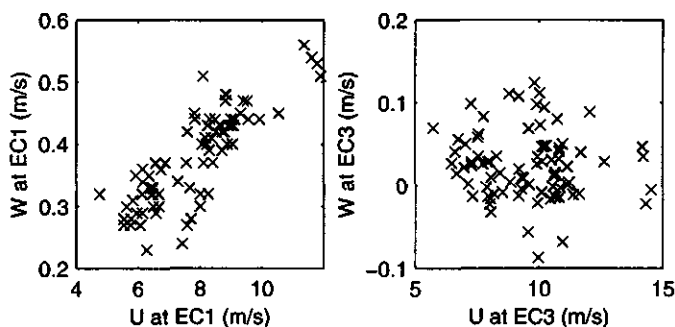
Fig.3.8 The mean vertical wind speed (30 min. average) as a function of mean horizontal wind speed measured at EC1 and EC3 with sonic anemometers (note the difference in $\overline{W}$ scale).

Especially the sonics (EC1 and EC2) mounted on the top of a mast suffered from high values for $\overline{W}$ (up to 0.55 m s^{-1}). The sonic of EC3 gave low (mostly positive) $\overline{W}$ values which were not correlated with $\overline{U}$. It is therefore assumed that the mean vertical wind component is due to the deflection of the streamlines around the instrumental array. Because the length scale of the distorting body (<1 m) is smaller than the integral scale of the flow (approximated as the height above the surface), a simplified version of the theory of Wyngaard (1991) can be used to calculate the corrections for distortion.

The distortion error depends on $\overline{W}_m/\overline{U}$ where $\overline{W}_m$ is the mean measured vertical velocity. We assume that the mean horizontal wind ($\overline{U}$) is not distorted so $\overline{U} = \overline{U}_m$. The following set of equations is used to correct for the distortion

$$\alpha = \arctan\left(\frac{\overline{W}_m}{\overline{U}}\right),$$

$$w = w_m - u_m \sin\alpha,$$

$$u = u_m - w_m \sin\alpha$$

3.19

with which the (co-)variance products can be composed, w represents the real vertical velocity fluctuations. The real momentum flux is then related to the measured momentum flux as

$$\overline{uw} = \overline{uw}_m - \sin\alpha(\overline{u^2 + w^2})_m$$

3.20

The corrected scalar fluxes $(c = \theta, q)$ can be calculated using

$$\overline{wc} = \overline{wc}_m - \sin\alpha(\overline{uc}_m).$$

3.21

To calculate the correction of the scalar fluxes for distortion of the flow around the one-dimensional sonic (EC0, only measuring vertical wind) the mean horizontal wind speed measured at 3 m above the dry terrain was used. The horizontal turbulent heat flux is estimated using Eq.2.14. Then, using an iterating calculation, the vertical scalar fluxes are computed. The procedure demands that the horizontal turbulent scalar flux does not suffer from a large distortion error. This is indeed the case as cross-talk (horizontal fluctuations being registered by the vertical sensor and vice-versa) between the horizontal and vertical velocity components mainly influences the covariances with the vertical velocity.

The correction was especially important at for EC0, 1 and 2 as can be seen in Table 3.6 where the distortion error calculations are summarized. The results for the sensible heat flux show more variation due to the low sensible heat flux above the wet terrain.

	EC0		EC1			EC2			EC3		
	$\overline{w\theta}$	$\overline{wq}$	u_*	$\overline{w\theta}$	$\overline{wq}$	u_*	$\overline{w\theta}$	$\overline{wq}$	u_*	$\overline{w\theta}$	$\overline{wq}$
mean	1.07	1.07	1.31	1.24	1.21	1.29	1.36	1.16	1.00	1.01	1.01
σ	0.01	0.01	0.06	0.63	0.05	0.10	0.61	0.04	0.00	0.03	0.01
max	1.11	1.11	1.45	3.01	1.34	1.66	5.25	1.29	1.00	1.19	1.04
min	1.04	1.04	1.18	-2.10	1.09	1.15	0.87	1.06	1.00	0.96	0.98

Table 3.6 Mean, standard deviation, maximum and minimum distortion error, F/F_m, $F = u_*$, $\overline{w\theta}$ or $\overline{wq}$

Furthermore, the vertical wind variances at EC1 and EC2 were corrected for distortion with factors of, respectively, 1.05 and 1.08.

3.5.1.2 The sonic temperature

No thermocouple was installed at EC3. Therefore, to obtain variances with temperature (turbulent heat flux and other (co-)variances involving temperature) the sonic temperature $\Theta_{son} = \overline{\Theta}_{son} + \theta_{son}$ is used instead. The sonic temperature is calculated from the (measured) speed of sound c, measured along the vertical axis of the sonic, using $T(1 + 0.32e/p) = c^2/403$. In order to obtain the sensible heat flux, a correction is needed for

humidity fluctuations, the travel time of the sound pulse in relation to the speed of sound $\bar{c}$ and the mean wind speed $\overline{U}$. The fluctuating part of the sonic temperature can be approximated as (Schotanus *et al.*, 1983)

$$\theta_{son} = \theta + 0.51q\overline{\Theta} - \frac{2u\overline{U}\ \overline{\Theta}}{\bar{c}^2} \qquad\qquad 3.22$$

which can be used to calculate any covariance product and the temperature variance.

3.5.2 The Lyman-α

This instrument measures the absorption of ultraviolet radiation and consists of a glow discharge source and a detector separated by a distance of about 1 cm. The radiation of the Lyman-α emission line (121.56 nm) is strongly absorbed by atomic hydrogen. Strong enough to permit a path length in the order of 1 to 2 cm where already 50% of the Lyman-α radiation is absorbed at an absolute humidity of 10 gm^{-3} (Kohsiek, 1986). The response of 1 ms together with a small measuring volume makes the instrument ideally suited for measuring fast humidity fluctuations.

There are some disadvantages to the instrument. It has a non-linear response due to the emitted spectrum of lines instead of emitting the Lyman-α line only. Furthermore the instrument is sensitive to O_2 at low humidities. Also, the calibration curve drifts due to detoriation of the emitting source and the windows of the detection and source tubes. A comprehensive overview of Lyman-α technology has been given by Tillman (1991).

The calibration curve of a Lyman-α has a non-linear range and a linear range. In practice it is possible to operate the Lyman-α in its linear range which is determined by calibrating the instruments in a climate chamber as was done for this experiment. The calibration was done by fitting $\rho_v x$, the product of the measured absolute humidity (g m^{-3}) and the distance x between source and detector in cm, against $-a\ln S/S_o + offset$ where S is the normalized signal and a is the slope of the calibration curve. During the experiment, the distance between source and detector was adjusted if necessary to keep the Lyman-α's in their linear range.

3.5.2.1 Co-variances from a log-linear signal

To calculate the (co-)variances, involving the Lyman-α signal, the following procedure was used. The relation between the signal S and the fluctuating absolute humidity can be written as

$$\bar{\rho}_v + \rho'_v = -\frac{a}{x}\ln\left\{\bar{S}\left(1 + \frac{s}{\bar{S}}\right)\right\} + b \approx -\frac{a}{x}\left(\ln\bar{S} + \frac{s}{\bar{S}}\right) + b \qquad 3.23$$

using a first-order Taylor expansion which is allowed for since $s \ll \bar{S}$. It then follows that the standard deviation can be calculated from

$$\sigma_\rho = -\frac{a}{x}\frac{\sigma_S}{\bar{S}} \qquad 3.24$$

and the covariance with some other fluctuating quantity, for example w, as

$$\overline{w\rho_v} = -\frac{a}{x}\frac{\overline{ws}}{\bar{S}} \qquad 3.25$$

3.5.2.2 Spikes

The signal from the Lyman-α's sometimes suffered from spikes. Using the skewness and the kurtosis of the Lyman-α signal as indicators for spikes, bad runs were detected. The spikes are not expected to influence covariances but they lower correlations due to a too high standard deviation. If spikes were detected during a run, the standard deviation of the signal and correlation products with the signal are excluded from the data-set.

3.5.2.3 The Webb Correction

With the Lyman-α absolute humidity fluctuations are measured from which the latent heat flux can be calculated. The method that is used to calculate the latent heat flux from the covariance products $\overline{w\rho_v'}$ and $\overline{w\theta}$ applies the so-called Webb correction (Webb *et al.*, 1981). It is assumed that there is no net vertical transport of dry air,

$$\overline{w\rho'} + \overline{W}\,\bar{\rho} = 0 \qquad 3.26$$

and assuming that $\rho'/\bar{\rho} \approx -\theta/\overline{\Theta}$ there must be a vertical velocity

$$\overline{W} \approx \frac{\overline{w\theta}}{\overline{\Theta}}.$$ 3.27

which is normally of the order of 0.001 ms^{-1}.

The Webb correction accounts for this small vertical velocity and it can be shown that the latent heat flux becomes (Webb *et al.*, 1981)

$$\lambda E = \lambda(1 + \varepsilon_w \sigma)\left\{\overline{w\rho_v'} + \overline{\rho_v}\frac{\overline{w\theta}}{\overline{\Theta}}\right\}$$ 3.28

where $\sigma = \overline{\rho_v}/\overline{\rho_a}$ is the ratio of the mean densities of water vapour and dry air and $\varepsilon_w = M_w/M_a$.

3.5.3 The thermocouple

An extensive description of this specific instrument, home-built at the WAU department of meteorology, is given by Van Asselt *et al.* (1991). A special feature of this thermocouple is its mechanical strength combined with a small time-constant. The response characteristics of a thermocouple are, among other factors, a function of the ratio between the volume and the area of the wire. This ratio is lowered by flattening a circular wire thus improving the response on expense of a somewhat increased radiation error due to a higher interception of global irradiation. The response length of the thermocouple can be estimated from the relation between the Nusselt number for heat exchange and the Reynolds number for the flow around the thermocouple (Appendix A2.1).

In this experiment the instrument is used to measure temperature fluctuations rather than the mean temperature. Winds were strong during the experiment and the standard deviation of the global radiation during half an hour was very low. It is therefore assumed that radiation influences on the fast temperature fluctuations are negligible.

3.5.4 High frequency losses

The thermocouple is relatively slow compared to the sonic and the Lyman-α. The resulting H(igh)F(requency)-loss of temperature variance and the fluxes involving temperature

depend also on along-wind sensor separation d, stability, wind speed and measuring height. The method (Raupach, 1977) to perform the calculations of these losses and some details on the results are given in Appendix A2.

The corrections were computed for each run separately using the mean horizontal wind measured with the sonic anemometers and a fixed separation of 0.5 m at EC3 and 0.25 m for the other EC stations. The corrections did not vary much from run to run, and it was decided to use the average ratio of the real and measured turbulence quantities at each station. The applied corrections are given in Table 3.7.

EC station	$\overline{wt}$	$\overline{wq}$	σ_θ	$\overline{uT}$	$\overline{uq}$
EC0	1.06	1.03	1.04	1.06	1.03
EC1	1.10	1.05	1.04	1.10	1.05
EC2	1.06	1.03	1.03	1.06	1.03
EC3	1.00	1.03	1.00	1.00	1.03

Table 3.7 The average ratios of real and measured turbulence quantities at the four EC stations. These ratios are used to correct the turbulence quantities. It is assumed that sensor separation was 0.5 m at EC3 and 0.25 m at the other three stations.

The measured $\overline{wq}$ only needed a correction for sensor separation. Corrections of the sensible heat flux at EC3 are close to zero because the turbulent heat flux there is calculated using the sonic temperature.

Humidity variance HF-losses were negligible. Temperature variance HF-losses were on average 3%, being somewhat larger for the thermocouple at the lowest level at EC0.

3.6 The weather and selection of runs

The measurements started at June 2, 1987 and lasted to June 25, 1987. Three weather maps (14/6/87, 20/6/87 and 24/6/87 all 1200 UTC) are given in Fig.3.9 to show the development of the weather during the experiment. On June 6 an extensive trough of low pressure, with its centre over England, produced wind from southerly directions all over Europe. Between the 10th and the 17th the weather in La Crau was unsteady with some occasional thunderstorms. The centre of the trough crossed France around the 18th. From then on the weather in La Crau came under the influence of the Azores high. With the axis of the trough over Central Europe and a ridge of high pressure over the Atlantic Ocean, a north-westerly flow pattern developed with the jet stream over France causing Mistral conditions in the south of France. From June 2 to June 19 the wind direction was not within the acceptance angle for a period long enough to get reliable data on advection. After the passage of a weak cold front at the 19th, bringing 5.9 mm of rain, weather conditions became favourable for the purposes of this experiment during the following days.

Mainly because of the steady wind from a suitable direction (Fig.3.4), the period June 20-24, 1987 is selected for the analysis in this thesis. It is decided to concentrate on day-time results of which 81 half hour runs were selected. Runs with a net radiation less than 90 Wm^{-2} are omitted. During these runs, just after sunrise and some time before sunset the flow is in a non-stationary state and fluxes are too small to be measured accurately. Some runs were omitted when the tapes were changed or during maintenance of the equipment.
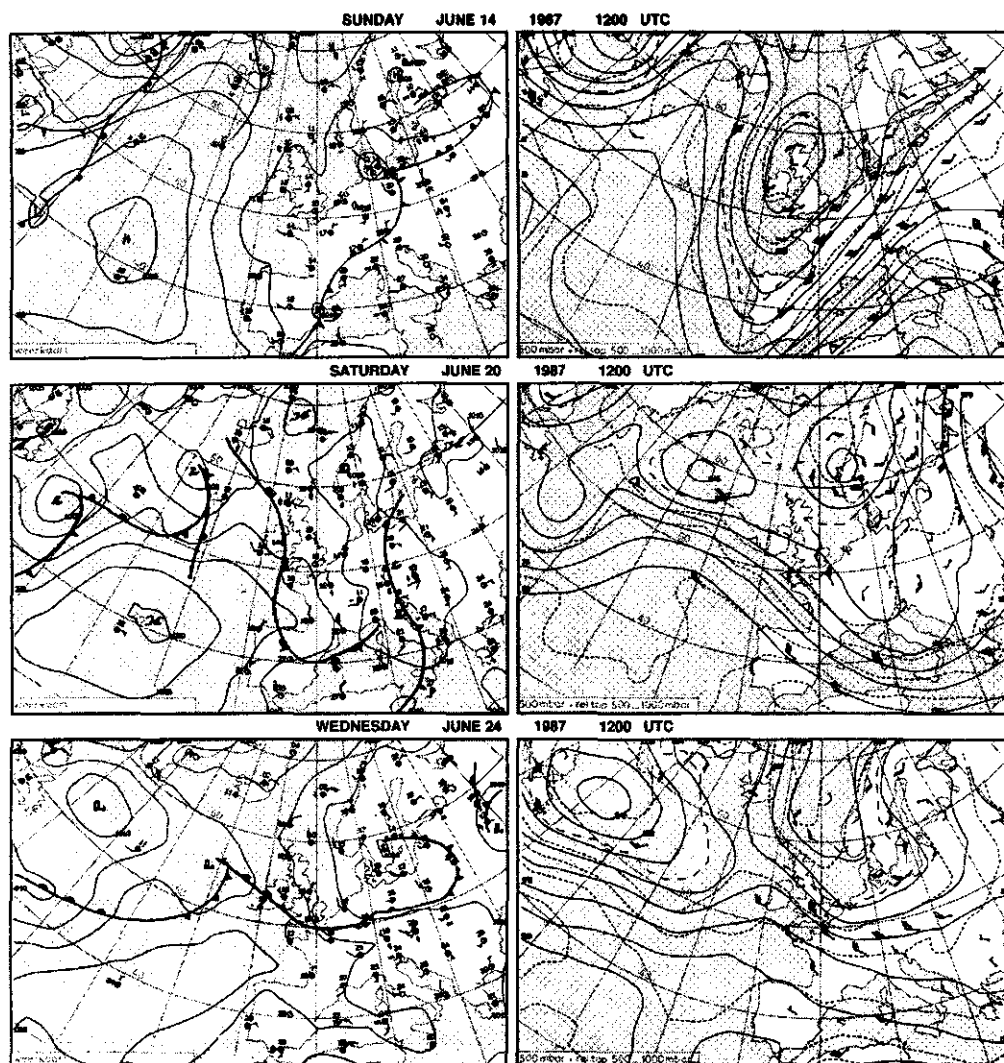
Fig.3.9 Weather maps of June 14, 20 and 24, 1987. The left panels are surface maps. The panels on the right give the flow at 500 hPa (Source: KNMI, 'dagelijks weerbericht').

In Table 3.8 an overview of the runs and the period they cover is given. Missing runs are also indicated.

day	period covered	number of runs	missing runs (starting time is given).
20/6	9:30-16:30	14	14:30
21/6	6:00-17:00	18	7:30 to 8:30, 15:30, 16:30
22/6	7:00-17:00	19	14:00, 14:30
23/6	8:00-17:00	18	15:00
24/6	8:00-13:30	12	none

Table 3.8 Overview of the selected runs for the analysis of local advection.

Air pressure (reduced to sea level) increased continuously during the period from 1010 hPa on June 20 to 1027 hPa on June 24. June 20 is relatively cool with midday temperatures of 23°C in the hut above the dry terrain. The following days are clear, warm days with midday temperatures up to 28°C at the 24th. The Mistral was constantly blowing giving NNW winds of moderate strength (between 7 and 11 ms^{-1} at 10 m height). The 20th was still cloudy with a varying cloud cover between 2/8 and 6/8 and a cloud base between 600 and 1000 m. The following two days were mainly clear days with a cloud cover of less than 3/8 during the day with some Cumulus humulis and Cirrus. June 23 was somewhat cloudier with a continuous cloud cover between 3/8 and 4/8 of mainly Altocumulus and Cirrus fibratus, whereas at the 24th the sky was clear again with a cloud cover of less than 3/8 of Cumulus humulis and Cirrus.

For this thesis and further research a data-set of 163 different quantities per run was compiled. The compilation contains 30 minute averages of:

- Horizontal and vertical turbulent fluxes, standard deviation of vertical wind, horizontal wind, temperature and humidity and the temperature-humidity covariance at 4 locations (EC0 to EC3).

- Wind direction and profiles of wind speed, temperature and humidity up- and downwind (P0 to P4). Downwind distance of the masts from the step-change.

- Incoming shortwave radiation. Reflected shortwave and net radiation, soil heat flux and surface and soil temperatures up- and downwind.

4 THE SURFACE LAYER UPWIND OF THE STEP-CHANGE AND BOUNDARY CONDITIONS

Before the development of the IBL over the downwind terrain can be studied, the conditions over the upwind terrain must be established. The analysis of the upwind experimental results serves two purposes. Firstly, boundary conditions are needed for the initialization of the model (described in 2.5) Secondly, it should be established to what extent the upwind conditions in the field fit in the idealized picture that the model assumes.

In this Chapter the upwind measurement results will be discussed (sections 4.1 and 4.2) and the necessary quantities for the initialization of the model will be compiled (section 4.3). Where applicable, references will be made to Kohsiek *et al.* (1993) and De Bruin *et al.* (1993). They discuss results of an experiment in the dry part of the La Crau region, also performed in June 1987, a few kilometres to the south-west of the location of this experiment. To a large extent, conditions there are comparable with the conditions of the upwind measuring location in this study.

4.1 Characteristics of the upwind surface layer

In this section the upwind wind speed, temperature and humidity measurements together with the fluxes of momentum, sensible heat and latent heat over the upwind terrain are presented.

The MO-similarity relations are applied to calculate the friction velocity u_{*_1} and both the profile and drag method are used to calculate the upwind surface roughness z_{o1}. Using these results, the behaviour of the non-dimensional wind and temperature gradients and the flux-variance relations $\varphi_{\theta,q}$ can be looked into. Furthermore, the method will be tested to calculate the mean temperature and humidity over the upwind terrain at the height of the downwind surface roughness, quantities which are both needed in the model.

A general impression of the upwind conditions is presented in Table 4.1 where horizontal wind speed, temperature, humidity at $z = 3$ m and the Bowen ratio are given. The mean results for the period 9:30 to 14:00 UTC are presented together with the standard deviations of the half-hourly means.

Day	u_1 ms^{-1}	T_1 °C	$\rho_{v,1}$ gm^{-3}	β
20/6	7.5±0.5	20.7±0.4	6.2±0.2	1.7±0.4
21/6	8.9±0.9	22.1±1.1	7.3±0.6	4.6±1.0
22/6	8.1±0.6	23.7±1.1	7.9±0.2	5.5±1.1
23/6	5.7±0.3	26.9±0.9	9.2±0.6	4.7±0.3
24/6	6.3±0.3	26.4±1.0	11.1±0.3	4.4±0.6

Table 4.1 Mean and standard deviation of the upwind mean (for 9:30 to 14:00) of wind direction, wind speed, temperature, absolute humidity at $z = 3$ m and the Bowen ratio from the flux measurements at EC0.

The five-day period can be divided in two periods with near-neutral conditions (June 20-22) and with more convective conditions (June 23, 24) because of a sharp decrease of the average wind speed on June 23 together with the increase of the air temperature. The low Bowen ratio β on June 20 is caused by rainfall (2 mm) on the day before, wetting the upwind terrain only superficially. Apparently, the drying of the upwind surface took one day since the Bowen ratio on June 21 is already much higher compared to June 20.

4.1.1 Friction velocity and surface roughness

As there was only a one-dimensional sonic available for the upwind terrain, no directly measured u_{*1} is available. Therefore, u_{*1} has to be calculated. With the available measurements there are two possible and independent ways to do this. Both techniques are based on MO-similarity.

The first method is the well-known flux-profile method described in section 2.2. The method needs measurements at different levels of temperature and wind speed. It was used here to calculate u_* as well as to obtain an estimate for the surface roughness. There were only measurements at two heights, which is in fact too few to apply the profile method. Still, to get reasonably robust estimates for both z_o and u_* the following procedure was followed. Temperature and wind speed measurements at two heights were used together with an estimate for z_o, assuming zero wind speed there to calculate the fluxes. With these fluxes and Eqs.2.15, 2.16 and 2.17 the wind speed can be calculated. The minimal value for the standard error of estimate,

$$s.e.e = \frac{1}{162}\left\{ \sum_{j=1}^{81} \sum_{i=1}^{2} (U_{ij,obs} - U_{ij,calc})^2 \right\}^{1/2}$$
$$\text{4.1}$$

from 81 runs and 2 measuring levels is used as the criterion to select the appropriate z_o which resulted in a z_o of 0.010 m with a s.e.e of 0.015 ms^{-1} for the wind speed estimates.

The other method is referred to as 'the sigma-w method' (Tillman, 1972). This method applies the relation between u_* and σ_w, φ_w (Eq.2.11), from which an explicit expression for u_* can be derived (also using Eq.2.5),

$$ u_* = \left(\left(\frac{\sigma_w}{1.25} \right)^3 - 3 \frac{kgz}{\Theta} \overline{w\theta} \right)^{1/3}. $$

4.2

Although both methods apply MO-similarity relations, they give independent results because the sigma-w method utilises turbulence measurements whereas the profile method uses mean profile measurements. In Fig.4.1 the results for u_* of both methods are compared.

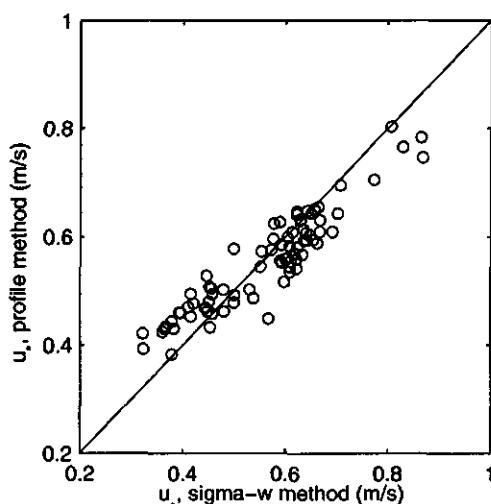*Fig.4.1 The calculated dry terrain friction velocity using the sigma-w and the profile method.*

The profile method gives values of u_* comparable to the sigma-w method with a standard error of estimate (s.e.e) of 0.05 ms^{-1}.

The surface roughness obtained from the profile method (0.010 m) is lower than the 0.013 m found by Kohsiek *et al.* (1993). They used the so-called drag method (Jacobs and Schols,

1986, Wieringa, 1993) to calculate the surface roughness. This method uses the relation between $u_*/U(z)$ (the square root of the 'drag coefficient') and $\ln(z/z_o)$ assuming neutral stability. It can also be used for unstable conditions, since, from Eq.2.15, it follows that

$$z_o = z e^{\frac{-kU(z)}{u_*} - \psi_m(\zeta)} \qquad \qquad 4.3$$

The method can be used here as well. The surface roughness is calculated inserting u_* obtained from the sigma-w method and wind speed measurements at $z = 3$ m in Eq.4.3. An average z_o of 0.018 m is found (15 runs) for near-neutral conditions ($\zeta > -0.02$) when ψ_m can be neglected. The same procedure using $U(0.7)$ and $\zeta > -0.01$ gives $z_o = 0.013$ m (35 runs). These results agree somewhat better with the findings of Kohsiek et al. (1993) compared to the local z_o of 0.010 m. The higher values of the surface roughness found here are probably caused by the trees and the farm situated to the NE of the experiment site.

The error in the surface roughness obtained by the profile method depends mainly on the quality of the wind speed measurements (and of course on the number of levels, which was actually too small over the upwind terrain). An offset of 0.2 ms^{-1} for one of the sensors gives on average, an error of 11% in $\partial U/\partial z$ and an error of 30% in the surface roughness. As this error is mainly caused by the uncertainty in the starting speed of cup anemometers it should not be considered as a random error that can be minimized through repetitive measurements.

The contribution of the absolute errors Δx in each variable x to the relative error of z_o in the drag method can be estimated using

$$\frac{\Delta z_o}{z_o} = \frac{\Delta z}{z} + \frac{k}{u_*}\Delta U + k\frac{U}{u_*^2}\Delta u_* + \frac{U}{u_*}\Delta k. \qquad \qquad 4.4$$

neglecting the error in ψ_m. The main error source is the friction velocity because $\Delta u_*/u_*$ is estimated to be at least 0.1 whereas estimates for the others are $\Delta k = 0.01$, $\Delta U = 0.2$ ms^{-1} and $\Delta z = 0.10$ m.. The probable error in z_o determined using the drag method and $z = 0.7$ m is 15% and for $z = 3$ m it is 24% because of the lower amount of runs. Here the probable error is used since it is the statistical uncertainty of u_* which is important.

Based on this analysis it may be concluded that the 'local' value of the surface roughness, 0.010 ± 0.003 m, is lower than the drag results, 0.013 ± 0.002 at $z = 0.7$ m and 0.018 ± 0.004 at $z = 3$ m. The drag surface roughness also seems to increase with height. This effect can be explained from the upwind presence of terrain heterogeneities (like a farm and trees at a few hundred meters upwind stream) due to which u_* increases with height (Beljaars *et al*, 1983). Additional information may be gained from the observed flux-profile relations to be discussed in the following section.

4.1.2 Wind and temperature flux-profile relations

The non-dimensional mean wind speed and temperature gradients ϕ_m and ϕ_θ are calculated from the data using the profiles measured at P0 and the sensible heat flux from EC0 and the calculated u_* using the sigma-w method. The flux-profile relation for humidity cannot be studied owing to the small, and therefore uncertain, humidity gradient.

It can be shown that to a good precision the gradient from two heights can be calculated from the finite-difference logarithmic approximation,

$$\left(\frac{\partial S}{\partial z}\right)_{z_m} = \frac{S(z_2) - S(z_1)}{z_m \ln(z_2/z_1)} \qquad 4.5$$

where

$$z_m = (z_2 z_1)^{0.5} \qquad 4.6$$

for $z_2/z_1 \approx 4$. Under MO-conditions the expected error in the gradient is less than 2% both for wind and temperature profiles (Arya, 1991).
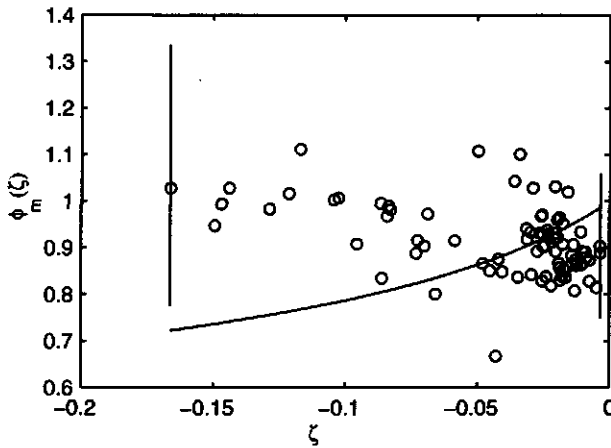
Fig 4.2 The upwind $\phi_m(\zeta)$ relation where the open circles represent the measured values and the drawn line represents the established flux-profile relation given by Eq.2.10. Also indicated are error bars for neutral and unstable conditions based on worst cases of a 0.2 ms^{-1} error in the wind speed difference and a 10% error in the fluxes.

The results for ϕ_m are given in Fig.4.2. The error bars for neutral and unstable conditions are worst case ranges of ϕ_m for an error in the fluxes of 10% and an absolute error in the wind speed difference of 0.2 ms^{-1}.

First it is noted that the selected data-set only covers a small stability range. Within that range ϕ_m behaves rather different from the established flux-profile relation for homogeneous terrain also indicated in the figure. The measured values are too low for the near-neutral conditions, which was also observed by Kohsiek *et al.* (1993). The ϕ_m results for the unstable range are too high. This is probably because the gradient was calculated from measurements at two heights only, which is in fact an incorrect procedure, certainly for unstable conditions. An offset error in the wind speed gradient measurements could explain the difference as the error owing to an offset increases with instability. Decreasing the wind speed difference with 0.3 ms^{-1} would bring the unstable values in accordance with the expected values and hardly influence the results for neutral conditions as can be seen from the error bars.
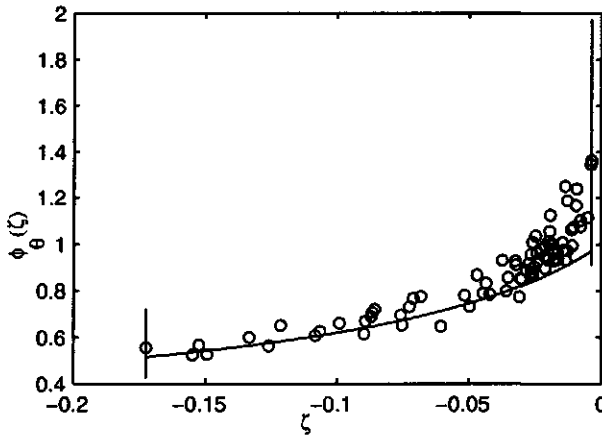
Fig 4.3 The upwind $\phi_\theta(\zeta)$ relation where the open circles are the measured values and the drawn curve is the MO-relation, Eq.2.10. Also indicated are error bars for neutral and unstable conditions based on worst cases of a 0.2 K error in the wind difference and a 10% error in the fluxes.

The upwind non-dimensional temperature gradient (Fig 4.3) agrees well with the MO-relation (Eq.2.10) although the measured ϕ_θ values are somewhat high for the near-neutral range of ζ. Together with the low ϕ_m values in that range, the high values for ϕ_θ again (like in the previous section) reflects the presence of sparsely distributed obstacles upwind of the measuring location (Beljaars *et al.*, 1983) although the drawn error bars also indicate that the ϕ_θ-results for the near-neutral stability are uncertain.

The observed differences between the expected and measured gradient relations do not influence the flux-profile calculations too much because the high values of ϕ_θ in the near-neutral stability range are compensated for by the low values of ϕ_m there (Beljaars, 1982). The deviating behaviour of ϕ_m towards unstable conditions is less important owing to the high sensible heat flux. It is however clear that the upwind conditions are not fully in agreement with the model assumptions. The upwind wind field suffers from terrain heterogeneities as was also concluded from the difference between the 'profile' and 'drag' surface roughness.

4.1.3 Wind, temperature and humidity profiles

Profiles of wind, temperature and humidity can be calculated applying the Monin-Obukhov flux-profile relations given in section 2.2, using the flux measurements obtained with the upwind eddy correlation system EC0 (Fig 3.5) and the measurements of mean wind, temperature and humidity at one height ($z = 3$ m). The measured mean values at the other height (0.75 m) can then be used to check the calculations. The result of the comparison between the measured and calculated wind speed, temperature and humidity is given in Fig.4.4 (81 runs).
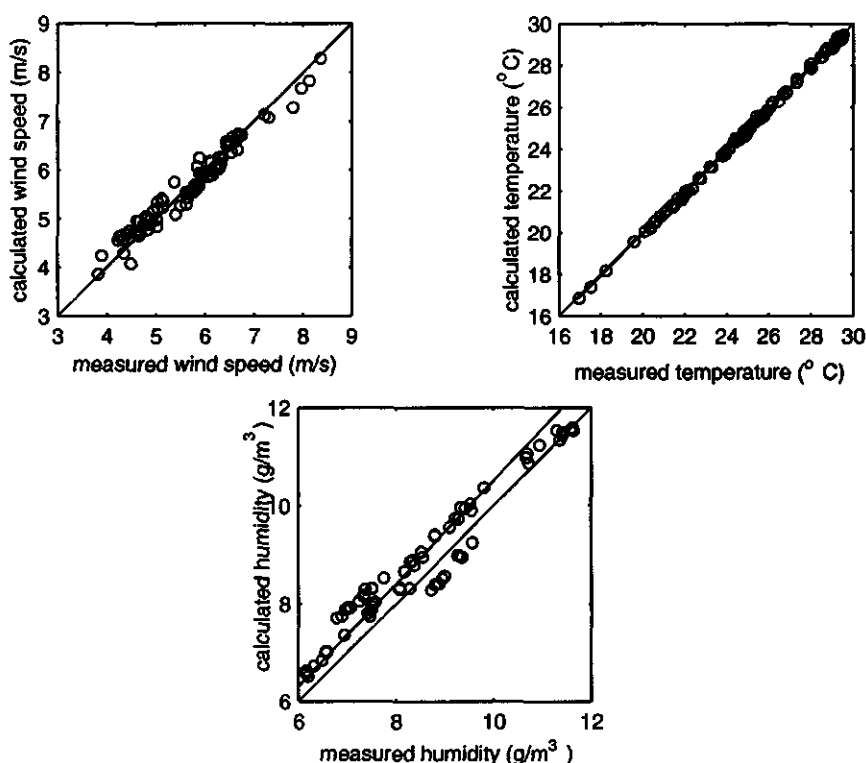

Fig.4.4 Comparison of measured and calculated wind speed, temperature and humidity at z =0.75 m at P0. The
    calculated values are obtained using the MO-flux-profile relations, the measured fluxes from EC0 and the
    measured wind speed, temperature and humidity at z =3 m at P0.

As can be seen a reasonable (wind, humidity) to good (temperature) fit is found for all three quantities. It is thus confirmed that a disturbed wind field owing to roughness heterogeneties does not invalidate flux-profile calculations for sensible heat owing to the contrasting behaviour of u_* and θ_*. The results for humidity mainly reflect the problems of measuring small gradients over dry terrain. It is, however, assumed that the profile method can be used to calculate the upwind temperature at $z = z_{o2}$ since the measured and calculated temperatures agree sufficiently well. This is less so for water vapour but since its vertical gradient is small, the upwind humidity at $z = z_{o2}$ can be also be calculated.

4.1.4 Temperature and humidity flux variance relations

The model uses at its upper and lower boundary equal expressions for the flux-variance relations of temperature and water vapour φ_θ and φ_q (Eq.2.13). Furthermore, the model uses equal modelling constants for the temperature and water vapour field (Eqs.A1.21 to A1.24). This implies that the correlation between vertical wind and temperature fluctuations or transfer efficiency of temperature, $R_{w\theta}$ is assumed to be equal to the transfer efficiency of water vapour, R_{wq} as was discussed in 2.6.

In Fig.4.5 the measured φ_θ is given and compared with relations found in recent literature (De Bruin *et al.*, 1993, Kaimal and Finnigan, 1994). The present result is within the range covered by these two different results and the fitted line (lowest s.e.e.) is given by

$$\varphi_\theta^2 = 5.29(1 - 14.2\zeta)^{-2/3} \qquad\qquad 4.7$$

which will also be used in the model, both for temperature and water vapour.
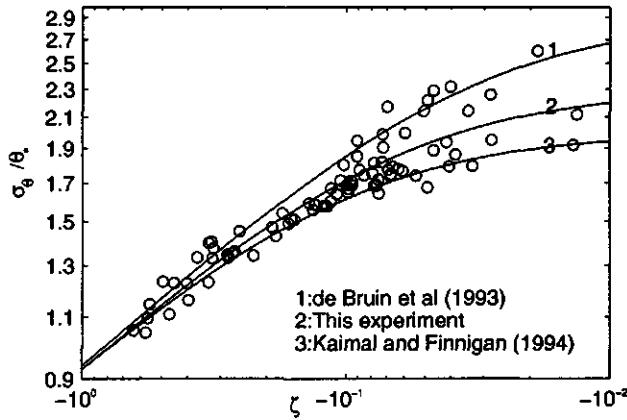
Fig.4.5 The measured temperature flux-variance relation φ_θ compared with the results of De Bruin et al. (1993) and Kaimal and Finnigan (1994).

Observational validation of the non-dimensional relation given in Fig 4.5 must beware of auto-correlation because of the use of the same variables in the left and right hand sides of the equation (Hicks, 1981). Its actual predictive power is better tested by using the relation to calculate the heat flux. Following Tillman (1972) Eq.4.7 can be rewritten (also using Eq.2.5)

$$H_\sigma = \rho c_p \left(\left(\frac{\sigma_\theta}{2.3} \right)^3 \left(\frac{kgz}{\Theta} \right) \left(\frac{1 - 14.2\zeta}{-\zeta} \right) \right)^{1/2} \qquad 4.8$$

The result, for which the sigma-w friction velocity results are used to calculate ζ, is given in Fig.4.6.
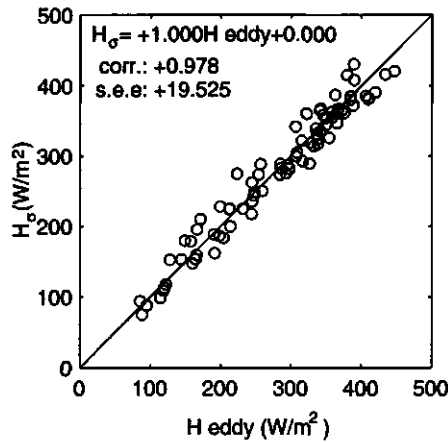
*Fig 4.6. The measured sensible heat flux (H eddy) and the heat flux calculated using Eq.4.8 (H_σ).
The solid line represents the best regression line forced through zero.*

H_σ was calculated in an iterative process first assuming $\zeta \rightarrow -\infty$ which gives a first value for the heat flux. Then ζ could be calculated and a new value for H_σ and so on until the heat flux changes less than 1%. This was usually the case after 4 iterations. It is seen that the results once more confirm the validity of Eq.4.7 for φ_θ.

Next, the behaviour of the water vapour field will be considered. Note that there are only 34 runs which can be used to analyze the upwind results due to the problems with the Lyman-α (section 3.5.2.2). In Fig.4.7, φ_q is given together with the result found earlier for φ_θ.
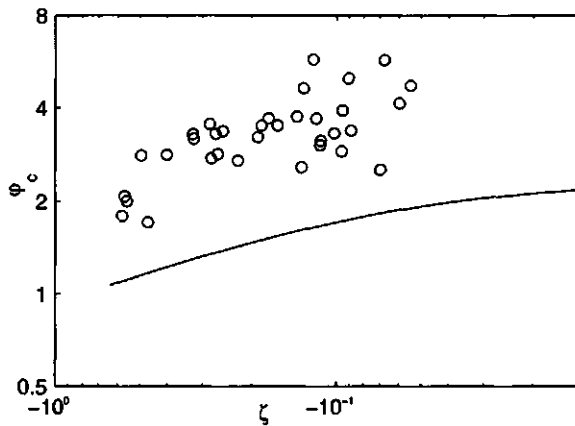
Fig 4.7 The flux-variance function φ_q (open circles) as a function of stability. The drawn line represents φ_θ, Eq.4.7.

It is clear that the upwind water vapour field deviates from MO-similarity. Furthermore it is seen that $\varphi_q > \varphi_\theta$, which was also observed by De Bruin *et al.*, 1993. Furthermore, it is found that $R_{w\theta}$ is 0.46 ± 0.04 whereas R_{wq} is 0.22 ± 0.05. These results also point at a low temperature-humidity correlation as can be seen in Fig.4.8 where $R_{\theta q}$ is given as a function of the surface latent heat flux.
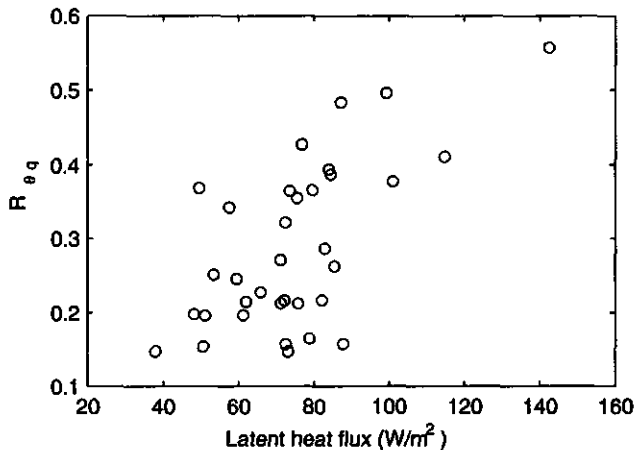
Fig.4.8 Correlation between temperature and humidity fluctuations above the dry terrain as a function of the latent heat flux.

The correlation $R_{\theta q}$ increases with the surface latent heat flux. To understand the behaviour of the correlation between water vapour and temperature in the ASL, its behaviour in the whole PBL needs to be considered. The correlation at the top of the PBL is negative because of entrainment of warm dry air, and positive in the lower part because of warm moist updraughts. A change of sign of $R_{\theta q}$ is normally observed somewhere halfway in the PBL (Wyngaard *et al.*, 1978). Above a dry terrain, during day-time, the updraughts are warm but not necessarily moist, and the effect of the entrainment reduces $R_{\theta q}$ down to a lower level than is normally the case (Mahrt, 1991). Similar reasoning is not valid for wet terrains, since the cooling effect of surface evaporation makes it more probable that moist updraughts are cool. This makes it also plausible that, when the surface latent heat flux increases, $R_{\theta q}$ in the surface layer increases with, this is also consistent with experimental evidence that, over uniform, wet surfaces $R_{\theta q}$ is large (Kohsiek, 1984, Wesely, 1988).

This qualitative picture of the behaviour of $R_{\theta q}$ can be quantified using the so-called 'top-down bottom-up' approach for turbulent scalar transport in the PBL. The top-down bottom up model considers the diffusion of a passive, conservative scalar through the PBL as the superposition of a bottom-up and top-down process (Wyngaard, 1988). The bottom-up process has a surface flux and a zero flux at the top of the mixed layer whereas the top-down process is governed by an entrainment flux at the top of the mixed layer and the surface flux is zero. It can then be shown (Appendix A3) that $R_{\theta q}$ depends on the ratio of the entrainment flux and the surface flux for each scalar, ξ_c, $c = \theta, q$ (Moeng and Wyngaard, 1984).

The relation between ξ_q and $R_{\theta q}$, calculated from Eqs.A3.7-A3.9, is given in Fig.4.9.
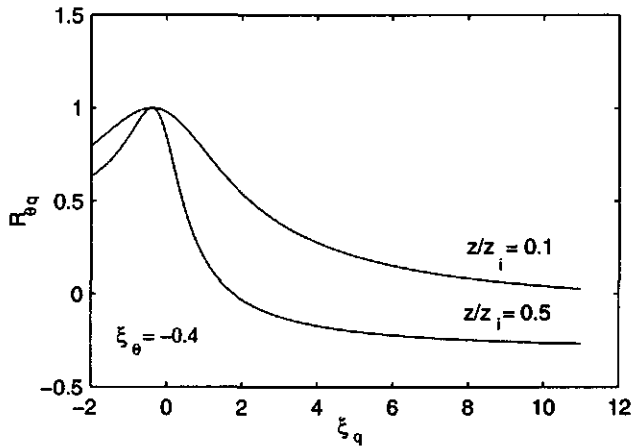
Fig 4.9 The temperature-humidity correlation R_{θ_q} as a function of the ratio of the entrainment and surface flux of latent heat ξ_q at a fixed ratio, $\xi_\theta = -0.4$ for the sensible heat flux for $z/z_i = 0.1$ (the top of the surface layer) and halfway the PBL.

There is a more pronounced influence of ξ_c at higher values of z/z_i as can be seen in Fig.4.9. Furthermore, only when $\xi_\theta = \xi_q$, $R_{\theta_q} = 1$ throughout the PBL.

The top-down bottom-up approach more or less quantifies the often expressed idea that large scale PBL-processes may lower the temperature-humidity correlation in the surface layer. It can thus be concluded here that the observed turbulence structure of the upwind humidity field cannot be reproduced by the model in its present formulation. The model uses $\varphi_\theta = \varphi_q$ whereas each scalar should have its own ϕ-relation depending on ξ_c (Holtslag and Moeng, 1991). To insert the actually measured structure of the upwind surface layer, the model needs to be changed to an extent which is outside the scope of this study.

4.2 Radiation, soil heat flux and the energy balance

The magnitude of the components of available energy A, net radiation R_n and soil heat flux G also depends on soil composition, vegetation cover and water availability. It is expected that the upwind terrain has a different albedo (the ratio of reflected and incoming shortwave radiation) than the downwind terrain due to the different vegetation cover (section 3.3) and soil structure (section 3.2). The effect of a low albedo may compensate for the higher sur-

face temperature of the dry terrain and therefore lead to net radiation values comparable to those of the overgrown surface. However, since the soil heat flux is also expected to be larger over the dry terrain, the upwind A is expected to be smaller. Since all components of A were measured, both up- and downwind, it is feasible to verify this. Before differences in A between the two terrains will be considered , the measurements of the components of A, net radiation and soil heat flux, will be discussed.

4.2.1 Net radiation

Averages and standard deviations of the means of the incoming shortwave or global radiation S_{in}, the up- and downwind reflected radiation S_{out}, the net radiation R_n and surface radiation temperatures T_s measured at the dry (1) and wet (2) terrains are given in Table 4.2 for a five-day period.

Day	S_{in}	$S_{out,1}$	$S_{out,2}$	R_{n1}	R_{n2}	T_{s1}	T_{s2}
	Wm^{-2}	Wm^{-2}	Wm^{-2}	Wm^{-2}	Wm^{-2}	°C	°C
20/6	557±133	90±20	121±25	375±99	399±95	30.6±1.6	19.5±0.9
21/6	872± 40	141± 5	184± 7	590±30	609±31	NA	23.5±0.9
22/6	874± 41	142± 5	184± 7	584±30	613±33	35.4±1.5	24.7±0.8
23/6	855± 41	139± 5	177± 5	565±28	610±33	40.2±1.4	26.5±0.8
24/6	853± 40	140± 5	181± 9	565±29	606±31	39.3±1.4	25.8±0.5

Table 4.2 Means and standard deviation of global, shortwave reflected and net radiation and surface temperature (period 9:30 to 14:00). Dry terrain surface temperatures of 21/6 are not complete. (Index: dry=1,wet=2).

The cloudiness on June 20 is clearly reflected in the relatively low radiation values and the high standard deviation of the mean. The days following June 20 show a very constant behaviour of the radiation regime. A mean global radiation of 870 W m^{-2} is accompanied by a net radiation somewhat below 600 W m^{-2} for the dry terrain and somewhat higher for the wet terrain. The albedo of the dry terrain is 0.16 and the wet terrain has an albedo of 0.21. These values agree well with those found in literature for similar terrain types (Monteith and Unsworth, 1990). Monteith and Unsworth give an albedo of 0.15 for savannas and 0.14 for heather; both are vegetation types which are assumed to be similar in appearance and structure as those in the dry Crau. The surface temperature differs strongly between the two terrains with a maximum of 13.7 K on June 23.

Through the dependence of R_n on specific surface properties different values may be found for each terrain type. In order to check the consistency of the radiation measurements, calculated net radiation, from the separately measured components, can be compared with the measured net radiation using

$$R_n = S_{in} - S_{out} - L_{in} - L_{out}. \qquad\qquad 4.9$$

There are no measurements of incoming longwave radiation. Instead, the difference between the dry and wet terrain can be calculated assuming equal amounts of incoming long- and short-wave radiation. The difference between the net radiation of the dry and wet terrain can then be calculated using

$$dR_{n1,2} = -dS_{out\,1,2} - dL_{out\,1,2} \qquad\qquad 4.10$$

where the outgoing longwave component $dL_{out\,1,2}$ was calculated using Eq.3.8. The comparison for all runs is given in Fig.4.10.
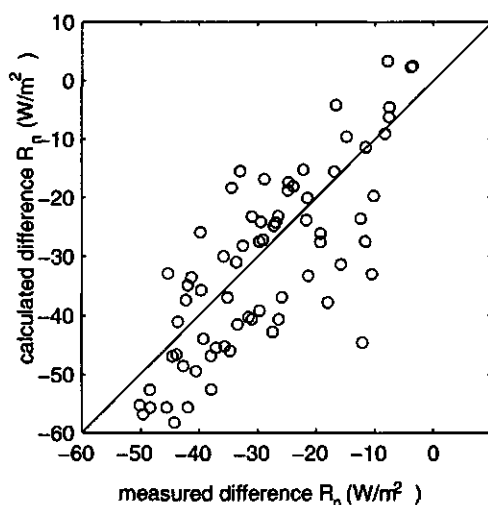

Fig 4.10 Comparison of measured and calculated difference in net radiation between the dry and the wet terrain.

The data for these runs show that the observed and calculated differences in R_n between the dry and wet terrain compare favourably. Some of the scatter may be caused by differences in storage of heat in the canopy and photosynthetic activity. The effect of the lower albedo

of the dry terrain is not such to fully compensate for the effect of differences in the surface temperatures between the terrains. As a result, the net radiation of the dry terrain is lower than that of the wet terrain.

4.2.2 Soil heat flux

Soil heat fluxes are calculated from the transducer measurements combined with results from soil temperature profile measurements as will be pointed out below. The corrections of the transducer measurements are rather uncertain and large (section 3.4.4.2). Two other methods to calculate the soil heat flux are employed here to verify the results of the transducer measurements.

Using the measured soil temperature profiles the soil heat flux can be calculated from the amount of heat that is stored in the soil profile during a certain time interval. This so-called integration method needs the volumetric heat capacity C_s and temperature measurements down to a depth where the temperature is constant during the considered period. The flux is calculated from

$$G = \frac{C_s}{\Delta t} \sum_i \Delta z_i \Delta T_i.$$

4.11

using layers of $\Delta z_{1..4} = 7$, 8, 14 and 31 cm thickness for the dry terrain and 5, 12, 20 and 23 cm for the wet terrain (depth of the temperature sensors can be found in section 3.4.1.3., the properties of the soil in Table 3.4), and a time interval Δt of 30 minutes during which the temperature of layer i changes ΔT_i.

The second method is the gradient method. It uses the vertical temperature gradient and thermal conductivity k to calculate the soil heat flux,

$$G(z) = -k \frac{T(z_1) - T(z_2)}{z_1 - z_2},$$

4.12

For the dry terrain the temperature gradient is obtained from the temperature difference between 0.05 and 0.10 m, for the wet terrain 0.02 and 0.05 m was used. The method also

needs the damping depth D_d (Table 3.4) because the flux at the surface is a factor $e^{z/D}$ larger than the flux at depth z, neglecting the phase shift with depth. Hence, the resulting fluxes are corrected with factors $e^{0.035/0.15} = 1.26$ for the wet terrain and $e^{0.07/0.14} = 1.71$ for the dry terrain.
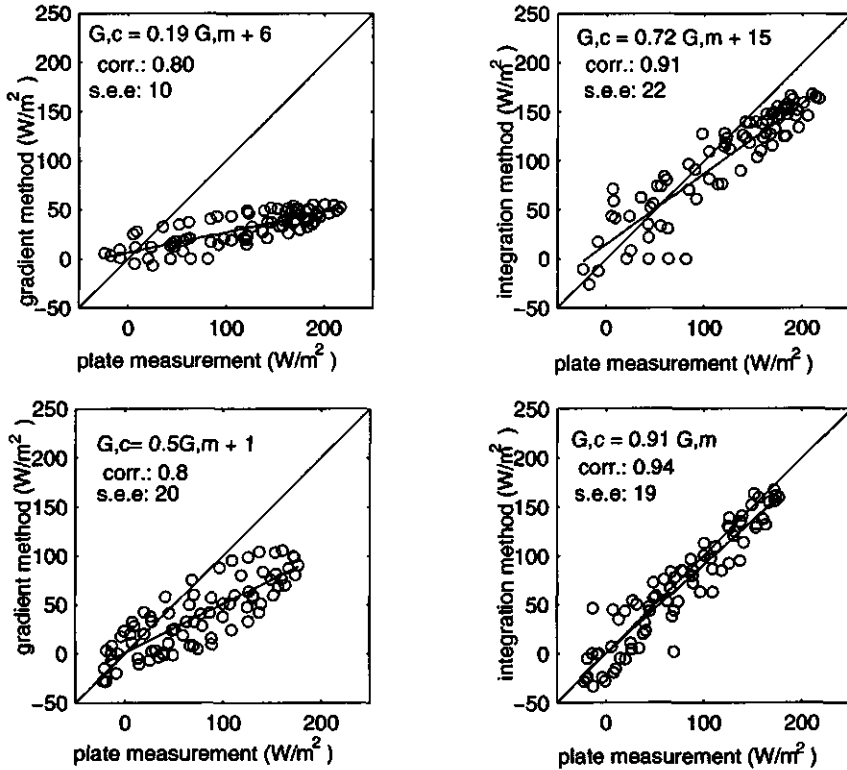
Fig 4.11 Measured and calculated soil heat flux for the dry terrain (top) and the wet terrain (bottom).

The results of the two methods are compared with the corrected transducer measurements in Fig.4.11 for both terrains.

For the dry terrain both calculation methods result in lower fluxes as compared to the corrected transducer measurements for fluxes above approximately 50 W m^{-2}. The comparison between the gradient method and the transducer measurement is influenced by neglecting the phase shift of the temperature wave with depth. A correction for the phase shift is

possible but does not improve the results too much. The measured and calculated soil heat fluxes for the wet terrain compare reasonably well, whereas good agreement was found between the integration method and the transducer measurements.

The soil heat flux into a dry, bare soil is more difficult to determine than that into grass-covered surface with a wetted profile because of the more inhomogeneous soil profile (dry and wet spots) and the complicated coupling of mass and heat transport below the surface in dry bare soils, where heat transport by convection may be important (Menenti, 1984, Ten Berge, 1986).

For the wet terrain both methods are interchangeable as they give comparable results, but for the dry terrain it is not certain which method is to be preferred. The following remarks can be made concerning the different methods.

The pattern of the comparison between the gradient method and the transducer measurements clearly reveals the effect of the neglected phase shift. By shifting the gradient derived fluxes, the correlation between the two methods can be somewhat improved.

The results of the transducer measurements contain in them a large correction because of the difference in the thermal conductivities of the soil and the heat flux transducer. Both the thermal conductivity of the soil and that of the transducer are not known within a factor of, say, 1.5. In addition, an uncertain constant is involved in this correction (Eq.3.12).

The gradient method can be in error as a result of errors in the measured sensor position (and consequently Δz), thermal conductivity and damping depth. Furthermore, it uses the temperature difference obtained from different sensors, thus possibly suffering from offset errors. The integration method, on the other hand, eliminates sensor offset and is less sensitive for errors in sensor position (van Boxel, 1986) and, more important, in k or D (see Table 3.4).

It is concluded that the integration method seems the most robust method to calculate the soil heat flux. It is therefore decided to use the results from the comparison (found in Fig.4.11) between the transducer measurements and integration method to correct the transducer measurements in forthcoming calculations because the transducer measurements are more complete. Errors in the integration method are caused by the discretization of the

integration and the uncertainty in C_s which depends on, inter alia, soil moisture content. With an uncertainty of, say, 10% in C_s, the highest values of the dry terrain soil heat flux of 200 W m^{-2} still have an absolute error of 20 W m^{-2}.

The soil heat fluxes calculated using the above described method at the dry and wet terrains are given in Table 4.3.

Day	G_1	G_2	$(G/R_n)_1$	$(G/R_n)_2$
20/6	64±26	45±24	0.17±0.05	0.11±0.05
21/6	129±13	102±23	0.22±0.01	0.17±0.03
22/6	141±11	122±25	0.24±0.01	0.20±0.03
23/6	157±14	131±27	0.28±0.01	0.21±0.04
24/6	138±14	123±29	0.24±0.02	0.20±0.04

Table 4.3 Period (9:30 to 14:00 UTC) mean and standard deviation of the soil heat fluxes (W/m ^{2}) during that period of the dry (1) and wet (2) terrains and the ratio of soil heat flux and net radiation.

As can be seen, the soil heat flux is an important energy balance component because it consumes 23% of the net radiation for the upwind terrain and 18% for the downwind terrain.

4.2.3 Available energy over the dry and wet terrain

The mean day-time available energy for each terrain is given in Table 4.4.

Day	A_1	A_2
20/6	311±84	353±82
21/6	461±18	507±14
22/6	443±22	491±17
23/6	409±16	478±17
24/6	427±18	483± 9

Table 4.4 The average amount per day of net available energy and standard deviation (Wm $^{-2}$) at the upwind (A_1) and downwind terrain (A_2) (9:30 to 14:00 UTC).

In general the wet, downwind terrain has more energy (A_2) available during day-time than the dry, upwind terrain (A_1). The largest difference is observed on 23/6. The large standard deviation around the mean on 20/6 is caused by the variable cloudiness on that day.

The difference (Fig.4.12) between upwind and downwind available energies $A_2 - A_1$ varies during the day with peak values of 80 Wm^{-2} in the morning around 9:00 UTC and in the afternoon at 15:00 UTC because of the different soil heat fluxes at the two terrains in the morning and the combined effect of R_n and G in the afternoon, respectively.
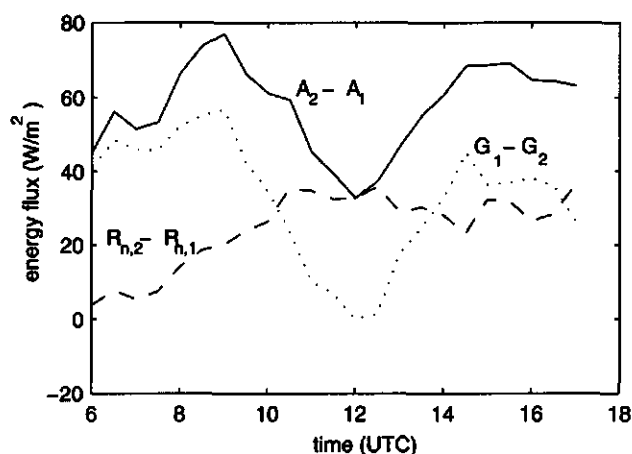
Fig 4.12 The averaged differences (5 days, 9:30-14:00 UTC) in net radiation, soil heat fluxes and available energy between the dry and wet terrain.

Around midday the differences are governed by the difference in net radiation between the two terrains. On average it is found that the wet terrain has 56 Wm^{-2} more energy available to be divided between H and λE, which is 14% of the average A_2.

4.2.4 The energy balance of the dry terrain

The daily course of the half hour means of the energy balance components above the dry terrain during the period June 20 to 24, 1987 is illustrated in Fig.4.13.
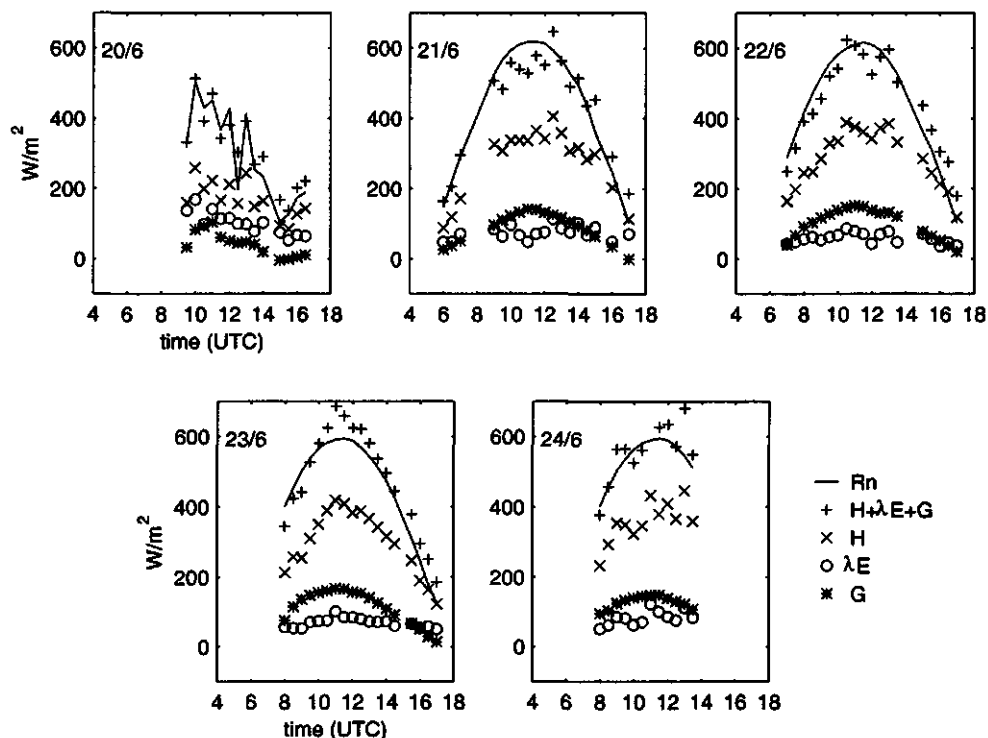
Fig.4.13 The daily course of the surface energy balance components, R_n, G, H and λE at the dry terrain for the days June 20 to 24, 1987. Also indicated is $H + λE + G$.

The mean results of R_n and of $H + λE + G$ are presented in Table 4.5. The probable error is estimated using a relative error of 20% in the half hour means of R_n and $H + λE + G$.

number of runs	Day	R_n	$H + λE + G$
14	20/6	300±17	315±9
18	21/6	452±23	444±13
19	22/6	448±22	445±13
18	23/6	456±23	484±14
12	24/6	538±28	568±18
81		438±10	451±6

Table 4.5 CRAU 1987: The mean results and probable errors of the 81 half hour means of R_n, $H + λE + G$ in W m^{-2}. The mean probable error in R_n and $H + λE + G$ are estimated using a relative error of 20% for $R_n, H, λE$ and G in the half hour means.

During the first three days R_n and $H + \lambda E + G$ balance within a few percent whereas on the last two days the sum of the fluxes is somewhat larger than the net radiation. An explanation for this may be that the moisture front in that part of the soil, where the evaporation takes place, is first above and after June 22 constantly below the soil heat flux transducer. This is known to happen below dry, bare surfaces (Menenti, 1984, Ten Berge, 1986). Heat coming from above and passing through the transducer, adding up to G is subsequently being used to evaporate moisture adding up to λE and the energy is thus accounted for twice.

4.3 Compilation of the initial conditions for the model

In this Chapter the measurements before the step-change over the dry terrain were compared with Monin Obukhov relations for horizontal, homogeneous terrain. Furthermore, the data were used to compile initial and boundary conditions for a second-order closure model. The model assumes horizontal homogeneity upwind of the step-change and uses MO-similarity to calculate its upper boundary conditions. The findings in this Chapter are now summarized together with the decisions which had to be taken in order to compile the set of input data for the model.

The calculation of the upwind friction velocity was performed using the profile method and by using the relation between σ_w and u_*. The results compared favourably. In the model the latter value for u_* will be used because it was compiled from measurements which are more reliable than the profile measurements. The actual upwind surface layer matches with the MO-theory where it concerns temperature but shows deviating behaviour for wind and water vapour. The wind field is disturbed owing to the presence of upwind roughness elements. This is concluded from the difference between a local measure for the surface roughness using profile measurements of up to 3 m and the surface roughness obtained from the drag method which is thought to represent a more regional value. Deviations of the near-neutral non-dimensional gradients of wind speed and temperature can also be explained from terrain heterogeneities. In the model, an upwind surface roughness of 0.01 m will be used.

The transport of water vapour above the dry terrain is found to be much less efficient than that of sensible heat, $\varphi_q > \varphi_\theta$ whereas the model assumes $\varphi_q = \varphi_\theta$. Although the entrainment flux was not measured, the difference between φ_q and φ_θ is attributed to the low ratio of the surface latent heat flux and the entrainment of latent heat. Indirect evidence is the fact that the present measurements show that R_{θ_q} clearly increases with an increasing surface flux of latent heat. Using the so-called top-down bottom-up approach, it was also made plausible that R_{θ_q} decreases drastically with a decreasing surface flux, assuming a constant entrainment flux.

The temperature and humidity at the height of the downwind surface roughness z_{o2} can be calculated from the measured flux and a mean concentration at one height using the flux-profile method. The profile measurements at $z = 3$ m and the measured fluxes at $z = 6.2$ m are used.

All components of the upwind surface energy balance were measured. It is concluded that it is useful to provide the model with different amounts of available energy for the up- and downwind terrain. An increase of available energy after the step-change is found. The difference can be attributed to the high upwind surface temperature while this effect is not fully counterbalanced by the low albedo of the upwind terrain.

It is found that the sum of upwind sensible, latent and soil heat fluxes is equal to upwind net radiation on the first three days of the selected period. On the last two days net radiation equals the sum of the soil and sensible heat flux. The model assumes energy balance at the surface. Hence, the input should consist of two out of the three components sensible heat, latent heat and available energy. Out of the possible combinations, it was decided to provide the model with the measured values of H and λE.

The model also needs the downwind surface resistance and the downwind surface roughness. The calculation of these quantities can only be performed after the measurement results over the downwind terrain are presented.

5 MEAN PROFILES AND FLUXES IN THE INTERNAL BOUND-ARY LAYER

In this Chapter a description of the flow field in the IBL after the step-change will be given. In section 5.1, the results of the mean temperature, humidity and wind speed measurements are presented. Next, the fluxes of sensible and latent heat are presented and the results of the momentum flux measurements are given. Then all ingredients are available to obtain objective estimates for the surface roughness and the surface resistance, which are both needed as lower boundary conditions in the second-order model to be used in this study (Chapter 6).

With the measuring locations at fixed positions after the step-change, fetch over the down-stream terrain varies with the run-to-run variation of the mean wind direction. By comparing measurements from runs with different wind directions it is possible to study the flow structure as a function of the height-to-fetch ratio z/x or z/δ where δ is the IBL-height defined in section 2.4. This can be important for modelling purposes but also serves practical applications like the planning of experiments. In the past, a fetch-dependent description of developing boundary layers has provided useful insight in the adaptation process of disturbed flows (Mulhearn, 1981, Garratt and Ryan, 1989). The presentation of some of the data in sections 5.1 and 5.2 is inspired by this work.

In the first part of this Chapter a value for the downwind surface roughness of 0.05 m will be used. This value for the surface roughness is based on visual inspection of the downwind terrain. A more precise estimate can only be made after a careful study of the downwind development of wind speed and momentum flux. This will be done in section 5.3.

Stomatal control is crucial to the redistribution of available energy between sensible and latent heat after the step-change (Philip, 1987, Kroon and De Bruin, 1993). The controlling function of the stomata, discussed in a qualitative sense in Chapter 1, is quantified by the surface resistance. This quantity was not measured directly, which by the way, is one of the major shortcomings of all experiments on advection until today. The surface resistance, calculated directly from the measurements is compared with a simple parameterization of

the surface resistance in section 5.4. Furthermore, the aerodynamic and climatological resistance to characterize conditions over an evaporating terrain using the 'big leaf' model are also calculated.

5.1 Mean flow characteristics

In Table 5.1 wind direction, wind speed, temperature and humidity at $z = 3$ m are given for the wet, downwind terrain at P4 (subscript 2). The mean results for the day-time period between 9h30 and 14h00 are given together with the standard deviation of the half hour means. During this period there are no missing runs which makes it feasible to compare the different days. Also given are the differences with the upwind quantities (except for wind direction) measured at the same height which were presented before in Table 5.1.

Day	wind direc-tion $^\circ$	$\overline{U}_2$ ms^{-1}	$\overline{U}_2 - \overline{U}_1$ ms^{-1}	$\overline{T}_2$ °C	$\overline{T}_2 - \overline{T}_1$ °C	$\overline{\rho}_{v,2}$ gm^{-3}	$\overline{\rho}_{v,2} - \overline{\rho}_{v,1}$ gm^{-3}
20/6	341±6	6.8±0.6	-0.7±0.5	19.9±0.4	-0.8±0.1	8.0±0.2	1.9±0.1
21/6	342±5	8.4±0.7	-0.6±0.4	21.1±1.1	-1.0±0.1	9.4±0.5	2.1±0.1
22/6	346±6	7.7±0.6	-0.4±0.2	22.7±1.0	-1.1±0.2	9.8±0.2	1.9±0.1
23/6	349±7	5.2±0.2	-0.5±0.2	25.5±0.8	-1.4±0.2	11.2±0.6	2.1±0.1
24/6	336±6	5.5±0.2	-0.8±0.2	24.9±0.8	-1.5±0.2	12.9±0.2	1.8±0.2

Table 5.1 Mean and standard deviation of the mean (for 9:30 to 14:00) wind direction, wind speed, temperature and absolute humidity at $z = 3$ m and $x \approx 300$ m downwind and the difference with the upwind mean quantity measured at the same height. The wet downwind terrain results are from the most distant profile mast P4 (fig.5.1).

The results given in this Table are discussed and used for further calculations in the following subsections.

5.1.1 Wind direction, fetch and IBL-height

The wind direction during all runs is constantly NNW, backing slightly on June 24 with a daily standard deviation of about 6°. From the wind direction and using Eq.3.10, the mean fetch of each measuring location for the each period can be calculated. The results are given in Table 5.2.

Day	P1	P2	P3 EC3	P4	EC1	EC2
	profile	profile	profile turb. $z=13.0$ m	profile	turb. $z=4.1$ m	turb. $z=6.7$ m
20/6	92±16	144±25	210±37	304±53	256±45	180±32
21/6	89±14	139±22	202±33	293±47	247±39	173±28
22/6	80±15	126±23	183±35	265±50	223±42	157±30
23/6	75±14	118±22	172±33	248±47	209±40	147±28
24/6	108±23	170±36	247±52	358±76	302±63	212±45

Table 5.2 Mean and standard deviation of the downwind distance to the step-change of the profile masts P1 to P4 and the eddy correlation stations EC1 to EC3. In the header it is indicated whether profile or/and turbulence measurements took place. The height of the turbulence measurements is also indicated.

Some consideration should be given to the behaviour of fetch x as a function of wind direction in this experiment. Fetch will be used in combination with the measuring height z to study the dependence of flow properties in the IBL as a function of the location after the step-change, given as z/x. Suppose, wind direction variations within a run are normally distributed (for which support is found in the low values of the skewness of the wind direction signal of -0.04±0.4 for 81 runs). Considering the way fetch depends on wind direction it can be understood that its variation will not have a normal distribution. A difference of 1.7° around a wind direction of 330° gives a fetch variation of 8.2% whereas at 360° this is only 0.34%. The proposed procedure in the analysis of fetch dependent processes is therefore as follows. The instances of some quantity $c(z/x)$ from runs with 30 minute mean wind directions within 2° of each other are collected and the median of c for each bin is used. The median fetch value from each bin is used to calculate z/x. In Table 5.3 the wind direction classes and fetch classes (for a perpendicular distance of 100 m) together with the variation within a class are given for the 81 runs of this experiment.

Class	Number of runs	Wind direction Median	Inter-quartile range	Fetch (m) Median	Inter-quartile range
1	3	330	0.7	287	9
2	4	332	0.4	263	5
3	5	334	0.8	249	7
4	6	336	0.7	226	6
5	6	338	0.4	213	3
6	4	340	0.2	198	1
7	11	342	0.4	189	2
8	7	344	0.4	176	2
9	9	346	0.5	169	2
10	6	348	0.4	164	2
11	5	350	0.4	155	1
12	6	352	0.3	150	1
13	5	354	0.5	144	1
14	4	356	1.1	139	2

Table 5.3 The division of 81 runs into classes of wind directions and the resulting classes of fetch for a perpendicular downwind distance of 100 m from the step-change.

Note in Table 5.3, that although the wind direction is increasing with steps of 2°, the fetch increase is uneven because of the non-uniform distribution of wind directions within classes. The segments are chosen in such a way that each class has at least 3 runs in it.

In Fig.5.1 the masts are positioned at their mean (over all 81 runs) downwind distance and profile instrumentation and the eddy correlation systems are indicated. In addition, the run-to-run variation of the fetch for P1 and P4 is given by a horizontal bar. Mean profiles of wind, temperature and humidity at approximately 90, 140, 200 and 290 meters from the leading edge are available. An estimate for the height of the IBL is also drawn in Fig.5.1. It is obtained using Eq.2.27 and a downwind surface roughness of 0.05 m. Doubling the roughness length gives an increase of IBL-height of 19% at a fetch of 10 m and 13% at 100 m.
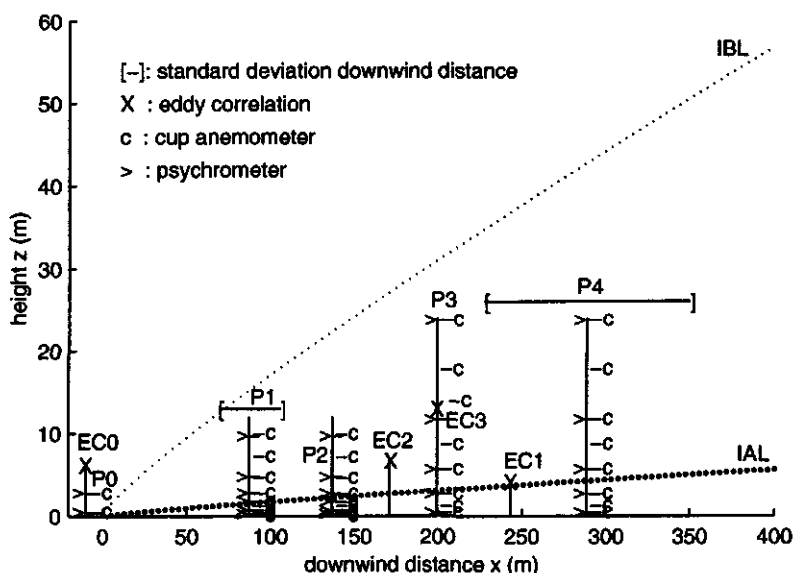
Fig.5.1 A two-dimensional view at the Crau experimental set-up where the distance from the step-change of each downwind mast is calculated using the mean wind direction; IBL-height is obtained from Eq.2.27.

Note that for large x there is an almost linear relation between x and $\delta(x)$ which makes it possible to use z/δ as well as z/x for scaling purposes. It is seen that the first mast, P1, samples the whole depth of the IBL, P2 half of it, the third station P3 reaches the top and P4 comes halfway IBL height. The eddy correlation systems EC1, EC2 and EC3 are all located in the IBL and the lowest system (EC1) is probably most of the time in the IAL. The IAL-height estimate is approximated also using model calculations (Rao *et al.*, 1974) and taken to be 10% of IBL-height. The EC-stations 1, 2 and 3 had mean fetches of 247, 174 and 203 m respectively giving height to fetch ratios of 1:60, 1:26 and 1:16 which differs mainly owing to the different measuring heights (4:6.7:13) and less because of the different fetch (1:0.7:0.9).

5.1.2 Air and surface temperatures

A simplified temperature budget for the two-dimensional case is

$$\overline{U}\frac{\partial\overline{\Theta}}{\partial x} = -\frac{\partial\overline{w\theta}}{\partial z} \qquad\qquad 5.1$$

which is valid at some distance, say 100 m or more, from the step-change. The temperature decrease (Table 5.1) from the dry to the wet terrain going from P0 to P4 with an average fetch of 294 m and at $z = 3$ m is 0.8 to 1.5 K for the day-time runs between 9h30 to 14h00 UTC. This results in a 'bulk' horizontal temperature gradient of, say, $-1.2/300 = -4*10^{-3}$ Km^{-1}. With a mean wind of typically 7.5 ms^{-1} a flux divergence of 40 Wm^{-3} is needed to outweigh the horizontal temperature gradient indicating considerable advection. The mean horizontal temperature gradient between P1 (average fetch 89 m) and P2 (average fetch 139 m) is $-4*10^{-3}$ Km^{-1} while further downstream, between P3 (average fetch 203) and P4, the mean horizontal gradient decreases down to $-1*10^{-3}$ Km^{-1}, leaving a flux divergence of only 8 Wm^{-3}. So, most of the cooling must take place in the first 80 m before P1 to arrive at the bulk average of $-4*10^{-3}$ Km^{-1}.

The largest temperature differences are found at the surface. In Fig.5.2 the daily time-series of the observed up- and downwind surface temperatures (described in section 3.4.2.3, the downwind surface temperature was observed at loc.13, with an average fetch of 140 m) for all 5 days is given together with the temperature difference between the two terrains.
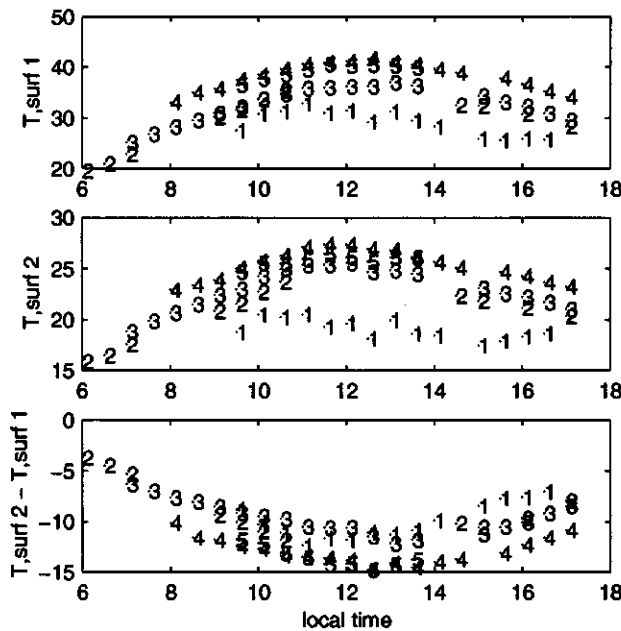

Fig.5.2 The upwind surface temperature (top panel), the downwind surface temperature (middle panel) and the difference between the down- and upwind terrain (bottom panel). The numbers indicate the day (1=20/6).

Because of 2 mm of rain on June 19 causing a relatively high surface evaporation the next day, the surface temperatures on June 20 (number 1 in Fig.5.2) are low. This is the case for both terrains. However, the difference between the two terrains of the surface temperature on this day does not deviate much from what was observed the following days.

Not only the surface temperatures but also the surface temperature difference between the two terrains follows a clear daily cycle. Using the Penman-Monteith approach, as discussed in Chapter 1, the surface temperature T_s can be written as

$$T_s = \frac{\gamma(r_a + r_s)}{\gamma(r_a + r_s) + \Delta r_a}\left(\frac{A\,r_a}{\rho c_p} - \frac{r_a}{r_a + r_s}\frac{dQ}{\gamma}\right) + T_z \qquad 5.2$$

also consistent with the cases discussed in section 1.2. It can be assumed that the air temperature at height z, T_z is constant with a typical downwind decrease of 1 K (Table 5.1), at least relative to the difference of the surface temperatures from the up- and downwind terrain of typically 10 K (Fig.5.2). It can be understood that, since $r_s \gg r_a$, the upwind surface temperature is governed almost solely by the first term within brackets. Over the downwind terrain the first and second term within the brackets are of equal magnitude reflecting the influence of evaporation on surface temperature. This causes a daily cycle of the surface temperature difference with an approximate constant amplitude during the period under consideration since this temperature difference is mainly governed by the upwind conditions. The surface temperature difference between the dry and the wet terrain is somewhat larger on June 23 and June 24 (respectively '4' and '5' in Fig.5.2) compared to the three days before. This is due to the lower wind speed on June 23 and 24 which causes r_a to be larger.

An advective inversion exists when the whole or part of the IBL has a stable stratification while at the same time the upwind temperature stratification is unstable. In Fig.5.3 a division of the 81 runs based on the presence of an inversion in the lowest part of the IBL (0.5 to 2 m) at P1 is given. The '+'-runs in Fig.5.3 thus represent a set of data when there is (at least) a hydrostatically stable stratification in the lower layers at P1, the 'o'-runs are all other runs.

In all cases, the stratification over the upwind terrain is unstable. It is assumed that the set of
'+'-runs represents relatively strong advective conditions (SA) and the 'o'-runs represent
weaker advective influences (WA).
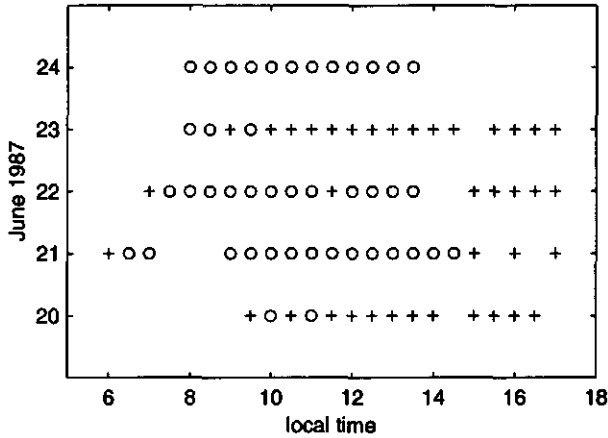
Fig.5.3 A '+' indicates conditions during which the temperature at P1, $z = 0.5$ m is below the temperatures at
$z = 1$ and $z = 2$ m, 'o': all other runs.

On June 20, a cloudy day after a day with light rain, there is sufficient water available to
maintain a high evaporation rate. Because R_n is small and the wind speed is high, r_i will be
large compared to $r_s + r_a$, conditions which are favourable for a negative Bowen ratio after
the step-change (Eq.1.7). Owing to the drying of the surface on June 20 an increase of the
surface resistance can be expected on June 21. Also because R_n is high that day no advective
inversion develops before 14h00. On June 22 the wind speed is somewhat lower and the
veering of the wind causes a lower average fetch than on June 21 (Table 5.1 and 5.2).
However, because of a further decrease of water availability no advective inversion devel-
ops before 14h00 when the net radiation starts to decrease. June 23 is the day with the lowest
fetch and a high difference in up- and downwind surface temperatures. Furthermore an
increase is seen in the air humidity and a decrease of the wind speed that day (Table 5.1).
The surface temperature difference on June 24 is similar but at this day fetches for P1 to P4
are much larger than on June 23 because of backing winds which may explain why June 23
has many strong advective cases compared to June 24.

In Fig.5.4 the mean temperature profiles for each mast are given for the two different advection regimes over the downwind terrain. The temperature profiles in the left panel are the average profiles of all runs during SA ('x' in Fig.5.3). In the right panel the averages of all other profiles are given ('o' in Fig.5.3), during WA-conditions.

The mean temperature profile in P0 was calculated using the flux measurements at EC0 and the temperature at $z = 0.75$ m from P0. The measured upwind temperature measurements are also plotted to show the agreement with the calculated profile.
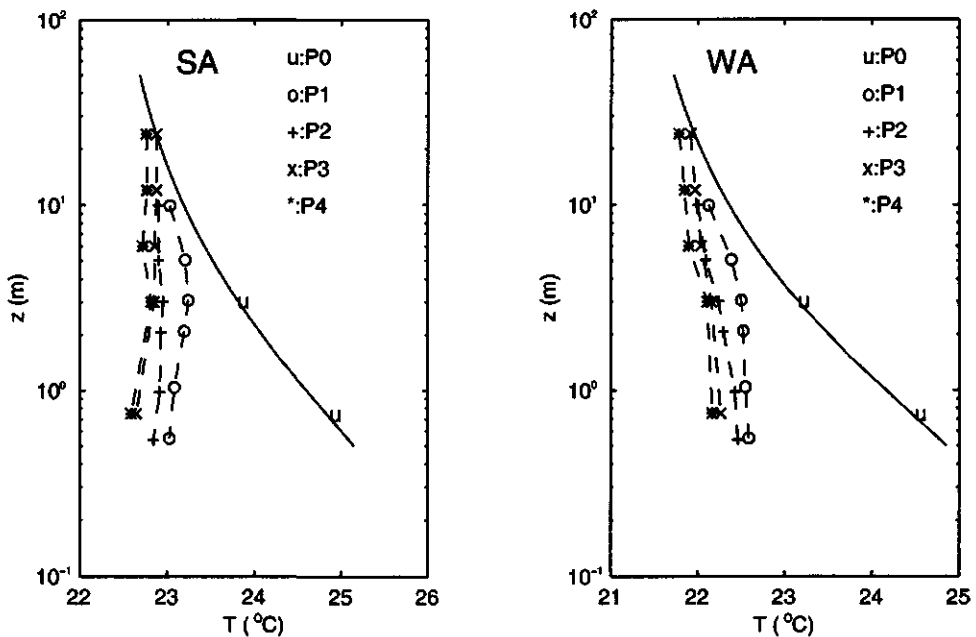
Fig 5.4 Mean temperature profiles P0 to P4. In the left panel average temperature profiles are compiled from runs when there was an advective inversion of at least 3 meter thickness at P1 ('+' in Fig.5.3). In the right panel all other runs are used to obtain the average profiles ('o' in Fig.5.3).

The first SA-temperature profile after the step-change (P1, left panel) exhibits an inversion below approximately 3 m in accordance with the selection criterion whereas the upper part of this profile has a negative lapse rate. The other three profiles have positive lapse rates extending above $z = 3$ m. The strongest advective cooling takes place at $z = 3.5$ m, going from P1 to P2. The cooling between the third and fourth mast is small.

The upwind temperature profile was extended above the highest measuring level in order to obtain an estimate of the IBL-height. The height where the downwind profiles intercepts the upwind profile can be used as a criterion to estimate this height. The P3 and P4 temperature profiles at $z = 25$ m show temperatures close to the upwind temperature indicating average IBL heights of approximately 25 m at P3 and 40 m at P4, which agrees with the estimate based on Eq.2.27 of respectively 30 m for P3, and 42 m for P4. It appears from Fig.5.4 that the IBL is somewhat thicker during WA-conditions.

Using an upwind temperature difference between measuring height and a reference height the temperature profiles after the step-change can be presented in one plot. To this purpose a non-dimensional temperature perturbation is defined

$$\hat{\Theta}(z,x) = \frac{\overline{\Theta}(z,x) - \overline{\Theta}_{s,1}}{\overline{\Theta}(z,0) - \overline{\Theta}_{s,1}} = \frac{\Delta\Theta_2 + \Delta\Theta_s}{\Delta\Theta_1} \qquad 5.3$$

with the upwind vertical temperature difference $\Delta\Theta_1$ between height z and the surface in the denominator and in the numerator the downwind vertical temperature difference $\Delta\Theta_2 = \overline{\Theta}(z,x) - \overline{\Theta}_s(x)$ plus the surface temperature difference $\Delta\Theta_s = \overline{\Theta}_s(x) - \overline{\Theta}_{s,1}$ between the two terrains. For $z/\delta \geq 1$ one would expect $\hat{\Theta} \rightarrow 1$. For small z/δ $\hat{\Theta}$ mainly depends on $\Delta\Theta_s/\Delta\Theta_1$. The upwind temperatures $\overline{\Theta}(z,0)$ are calculated using the flux-profile relations discussed in the previous Chapter. The data reduction through binning in classes of wind directions was applied for each measuring location (see section 5.1.1). So data reduction takes place from 81x22 data-points of the 4 different profiles after the step-change down to 14x22 data points after bin-averaging, finally, the average value of z/δ and $\hat{\Theta}$ for each sensor was calculated which gives 22 data points in the graph below. The result is given in Fig.5.5.
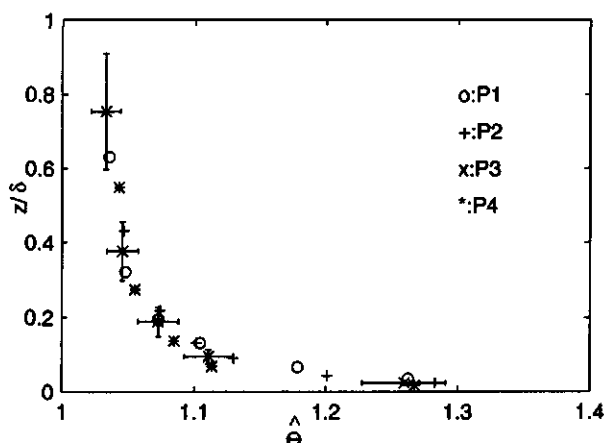
*Fig.5.5 The non-dimensional temperature change as a function of the ratio of measuring height and IBL-height,
z/δ.*

The universal form of the non-dimensional temperature perturbation for this data set can be explained from the compensation of $\Delta\Theta_2/\Delta\Theta_1$ by $\Delta\Theta_3/\Delta\Theta_1$ at each location in the IBL. The two terms are of equal magnitude but have opposite signs. This results in a fairly constant $\hat{\Theta}$ at each location. The results show, generally speaking, the expected behaviour in that $\hat{\Theta}$ approaches, within say 5%, unity for $z/\delta \rightarrow 1$ whereas for small z/δ $\hat{\Theta}$ is larger than unity. However, it was tested that a power law relation, as has been used by others (Garratt, 1992), does not fit the data very well. In this case it is better to consider two layers: $z/\delta < 0.35$ where $\hat{\Theta}$ shows a drastic decrease due to the increasingly large difference between the up- and downwind temperature and the layer with $z/\delta > 0.35$ with a fairly constant temperature decrease and therefore a constant $\hat{\Theta}$.

5.1.3 Humidity

The mean absolute humidity above both terrains increases during the considered period. The relative humidity (calculated from Table 5.1) is 35% above the dry terrain and 50 % at 3 m above the wet terrain during the first 4 days. It increases considerably on day 5 to 45% above the dry terrain and 56% above the wet terrain.

The two-dimensional budget for specific humidity reads

$$\overline{U}\frac{\partial \overline{Q}}{\partial x} = -\frac{\partial \overline{wq}}{\partial z}.$$

<div align="right">5.4</div>

The humidity increase at 3 m height between P0 and P4 is approximately 1.7 g kg^{-1} (Table 5.1) which can be counterbalanced by a flux divergence of -121 Wm^{-3}, 3 times as large as the flux divergence of sensible heat. The flux divergence balancing the horizontal specific humidity gradient would be -98 Wm^{-3} between P1 and P2 and -45 Wm^{-3} between P3 and P4. The observed humidity increase between P2 and P3 is too large. The difference is probably due to differences between the psychrometers of the WAU and the VU. The instruments at P3 and P4 were calibrated separately from the instruments at P1 and P2. Unfortunately, no comparison in the field of these instruments was carried out or possible in a sufficiently objective manner.

The average absolute humidity profiles are given (Fig.5.6) for the two different set of runs, SA and WA (section 5.1.2). The upwind profile is calculated using the mean absolute humidity measured at P0 ($z = 3$ m). The unreliability of the upwind mean humidity measurements is reflected by the difference between the calculated and measured humidity at $z = 0.75$ m. The calculated upwind humidity profile is expected to have the proper shape since the upwind latent heat flux measurements are reliable, as can be concluded from the energy balance results dissused in section 4.2.4.

The downwind profile shapes are identical with approximately equal vertical gradients for SA and WA conditions. The average humidity is somewhat higher during the WA-runs.

Fig.5.6 Mean humidity profiles P0 to P4. In the left panel average humidity profiles are compiled from runs when there was an advective inversion of at least 3 meter thickness at P1 ('+' in Fig.5.3). In the right panel all other runs are used to obtain average humidity profiles ('o' in Fig.5.3).

It could be deduced from these graphs that the IBL for the mean humidity is well above the highest measurement level, also higher than the mean temperature IBL. However, this result is uncertain owing to the error in the measurements of the mean upwind humidity.

5.1.4 Wind speed

The wind speed u_2 given in Table 5.1 is observed in P4 at $z = 3$ m with an average fetch of 294 m. The downwind decrease over this distance of the wind speed of 0.4 to 0.8 ms^{-1} at $z = 3$ m is because of the rougher downwind terrain. The adaptation rate to the new surface roughness depends on the magnitude of the step-change expressed as the ratio of up- and downwind surface roughness. In this case, the downwind-upwind ratio of surface roughness is below 10 whereas most studies on smooth-to-rough changes deal with ratios around 100.

E.g, a well-known experiment around a roughness step-change was performed by Bradley (1968). He measured the downwind development of velocity profiles around a step-change with $z_{o2}/z_{o1} = 125$.

In Fig.5.7 the mean wind profiles of the 81 day-time runs are given. The downwind profiles show a clear decrease of the wind speed compared to the upwind wind speed.

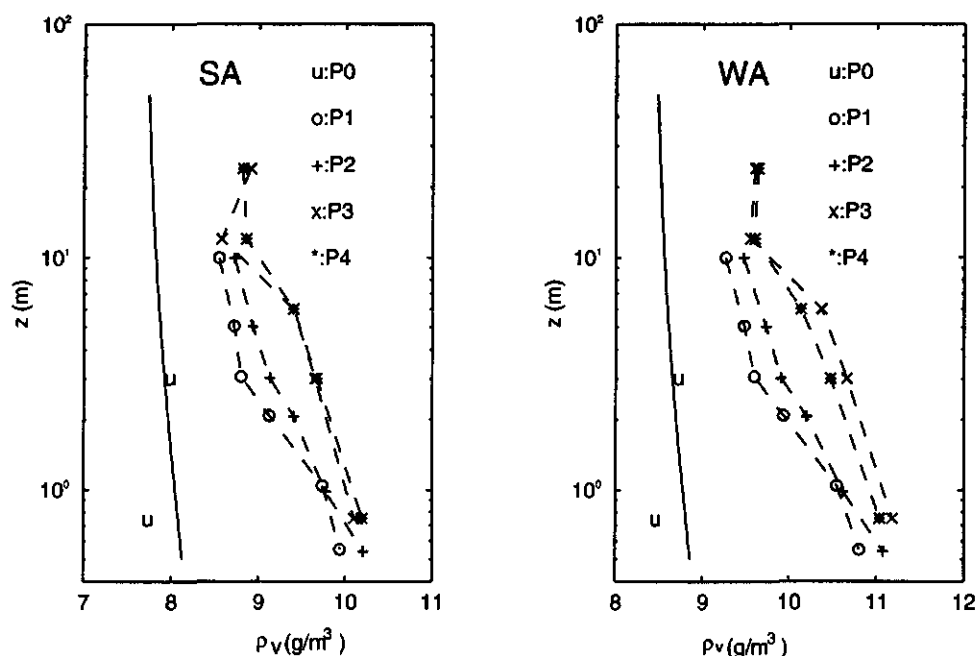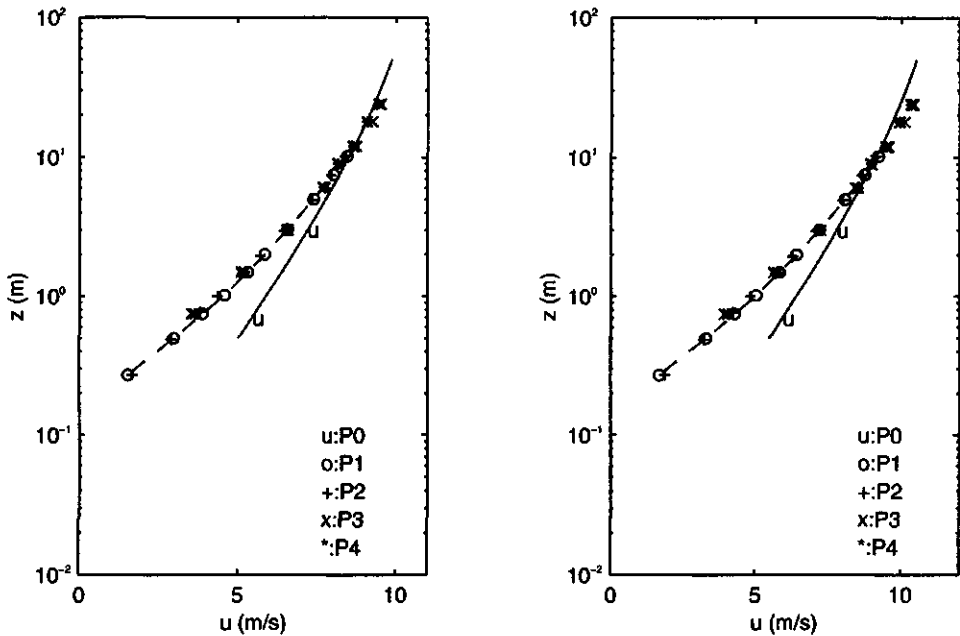*Fig 5.7 Mean wind profiles P0 to P4. In the left panel average wind profiles are compiled from runs when there was an advective inversion of at least 3 meter thickness at P1 (WA conditions, '+' in Fig.5.3). In the right panel all other runs are used to obtain the average profiles (SA conditions, 'o' in Fig.5.3).*

With a fetch of 100 m or more, the gradient in the x –direction apparently is already small. A 'on the back of a matchbox' estimate of the horizontal gradient of $\overline{U}$ can be made using the observed momentum flux divergence. The estimate is based on the equation of U for the steady state two-dimensional case and retaining the leading terms,

$$\overline{U}\frac{\partial \overline{U}}{\partial x} \approx -\frac{\partial}{\partial z}\overline{uw}. \qquad 5.5$$

Using the measured momentum fluxes at EC1 and EC3, the right hand side of Eq.5.5 is found to be -0.002 ms^{-2} on average (for 81 runs) with a (large) standard deviation of 0.009 s^{-1}. So, at about 200 m from the step-change and at $z \approx 7$ m (the geometric mean of the flux observation levels from EC1 and EC3) the horizontal gradient of the mean wind speed is approximately -2×10^{-4} s^{-1}. So, going from P1 to P4 (200 m distance, mean wind speed 8 ms^{-1}), the decrease of the wind speed must be of the order of 0.1 ms^{-1}, a small difference which is difficult to resolve.

The best fit through the upwind measurements, which was extended above the highest downwind measuring level using MO-theory, is also drawn. This profile is calculated using Eqs.2.15-2.17, the upwind u_* at EC0 and the wind speed at P0, $z = 0.7$ m together with the upwind sensible heat flux. Note that a similar result is obtained when the wind speed at P0, $z = 3$ m is used or zero wind speed at $z_o = 0.01$ m indicating the consistency of the measurements. It is found that the calculated upwind wind speed above $z = 10$ m is below the measured downwind value at these levels for both weak and strong advection although the effect is smaller for the SA-runs. A possible explanation could be that the decrease in the lower layers after the roughness step is accompanied by an acceleration higher up in the IBL because of the somewhat elevated road between the up- and downwind terrain. Another possibility is that the flow is upslope towards the mast, similar to the situation described by Peterson *et al.* (1980). However, the terrain slopes in the other direction. A third reason could be that the upwind wind speed above the measuring levels there is underestimated when extrapolated from the lower measurements because of non-uniform fetch conditions (section 4.1.3).

5.2 The sensible and latent heat flux

In the Table 5.4 the average Bowen ratio β per day at the different locations is given.

day	EC0 $z = 6.1$ m	EC3 $z = 13$ m	EC2 $z = 6.7$ m	EC1 $z = 4.1$ m
20/6	1.67	0.69	0.19	0.07
21/6	4.38	NA	0.52	0.25
22/6	5.25	1.76	0.44	0.19
23/6	4.70	1.44	0.33	0.12
24/6	4.29	1.15	0.27	0.16

Table 5.4 The mean Bowen ratio (from 9:30 - 14:00 UTC) before and after the step-change.

The Bowen ratios on the 20th, up- and downwind, are low compared to those for the following days due to rain on June 19 and cloudy weather. The upwind Bowen ratio β_1 increases until the 22nd to decrease somewhat the following days and it is on average three times as large as the Bowen ratio at EC3; β_1 is 9 (June 20) to 16 times (June 24) the Bowen ratio at EC2 and 23 to 40 times the Bowen ratio at EC1. The day-time mean (9:30-14:00) Bowen ratios are always positive.

In Fig.5.8 the time series of the turbulent fluxes of sensible and latent heat after the step-change for the period June 20 to 24, 1987 are plotted.
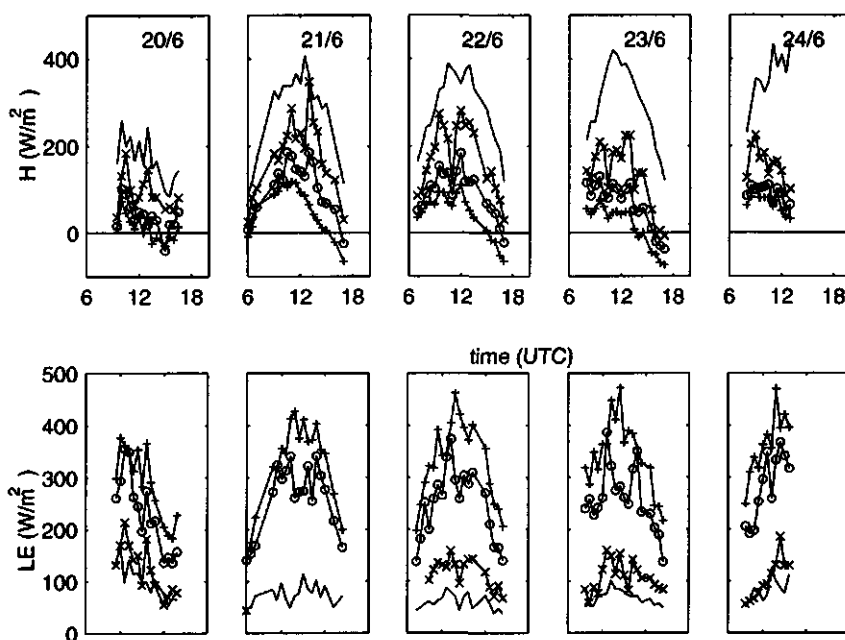
Fig.5.8 The sensible heat flux (top 5 plots) and latent heat flux (lower 5 plots) on the 5 different days (only drawn line: EC0, line with +: EC1, with o: EC2 and with x: EC3). On 21/6 and 22/6 some runs of the latent heat flux data are missing.

Both the sensible and latent heat flux show the expected difference for the dry-to-wet transition. The sensible heat flux decreases going from EC3 to EC1 i.e. with decreasing z/x whereas the latent heat flux increases considerably. The average flux divergences can be calculated directly from the flux measurements at EC1 to EC3. The latent heat flux divergence is on average (45 day-time runs) -31 Wm^{-3} and the sensible heat flux divergence is found to be 15 Wm^{-3}. These figures are consistent with the results derived earlier from the mean profile measurements given in sections 5.1.2 and 5.1.3.

The sensible heat flux is found to be negative (directed towards the surface) on June 20 after 12h30 UTC at EC1 and after 15h00 at EC2. On June 21 the sensible heat flux changes sign at 16h00 at EC1 and one hour later at EC2 which is also the case on June 22. Only on June

23 negative fluxes were observed at all three downwind EC-stations while the upwind heat flux still was positive. This was the case starting at 16h00 when EC3 and EC2 gave negative fluxes, two hours after the sensible heat flux at EC1 changed sign.

In Fig.5.8 it is seen that on some occasions the fluxes at EC3 are close to the upwind fluxes while on other instances this is not the case. It also seen that this pattern is not equal for the sensible and latent heat flux. This points at a variation of IBL-height in time and a difference between the flux-height relation of latent and sensible heat. In Fig.5.9 the downwind flux normalized with the upwind flux (which in theory should be the flux at the top of the IBL),

$$\hat{F}_s = \frac{\overline{ws}(z,x)}{\overline{ws}_o} \qquad\qquad 5.6$$

is given as a function of z/δ where δ was calculated using Eq.2.27 and Eq.3.10.

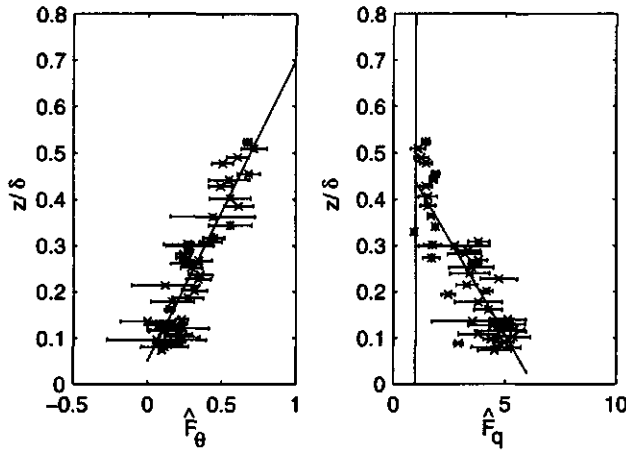Fig.5.9 Normalized fluxes of sensible and latent heat as a function of z/δ. The error bars indicate the interquartile range for each bin.

Again bin-averaging based on wind direction is applied before plotting. The result can be used to approximate the downwind surface fluxes. The so-called 'constant flux layer' in the homogeneous ASL is not more than a concept. It actually is the layer where the variation of

the fluxes with height can be neglected, i.e are within 10% of the surface flux which is also approximately the lowest 10% of the PBL. In an analogous fashion, the IAL-depth or inner layer (Garratt, 1992) for some flux can be defined here simply as

$$h_{ial} = 0.1*h_{ibl}. \qquad\qquad 5.7$$

where h_{ibl}, the height where $\hat{F}_\theta = 1$, may differ from δ, given by Eq.2.27, depending on the transported property and stability. Assuming a linear relation between $\hat{F}$ and z/δ it is found that $h_{ibl,\theta} = 0.70\delta$ and $h_{ibl,q} = 0.45\delta$. It is then found that for a fetch of 200 m (where, on average, the flux measurements were taken) $h_{ibl,\theta}/x \approx 1.2*10^{-1}$ and $h_{ibl,q}/x \approx 8.0*10^{-2}$ which gives $h_{ial} = 0.008*x$ using the lower of the two IBL-heights. There are few comparable data from experiments available in literature because this type of study has been performed mainly for changes of the surface roughness under near-neutral conditions or turbulence measurements at different heights were not yet feasible (Dyer and Crawford, 1965). For the smooth-to-rough case it is found that height-to-fetch ratios of 1 to 100 are needed to be in the constant flux layer or IAL (Garratt, 1992). Here, a different thickness of the IAL for latent heat and sensible heat is found, but both are close to this figure. Note also that the results for the sensible heat flux are more robust because of the scaling with the upwind flux which is large for sensible heat but small for latent heat.

It was shown here that the fluxes vary approximately linearly with height within the measuring range covered by the data. The following procedure is therefore used to obtain estimates of the surface fluxes of sensible and latent heat. For each run the measured flux-height variation is used to calculate the flux at $h_{ial} = 0.008x$ of which it is assumed to represent the surface fluxes. The data of Dyer and Crawford (1965) but also calculations with models show that the horizontal gradient of fluxes is small throughout the IBL compared to the vertical divergence except for the first few meters. Therefore it is also assumed that the data from EC1 to EC3 can be used to perform these calculations.

The results for the surface fluxes obtained using this procedure can be compared with the fluxes measured at EC1 ($z = 4$ m). The average surface latent heat flux near EC1 (81 runs) is found to be 396 Wm^{-2} compared to 329 Wm^{-2} at $z = 4$ m. The surface sensible heat flux is 31 Wm^{-2} below the flux at 4 m height with a flux at the surface of 7 Wm^{-2} and 38 Wm^{-2} at 4

m height. The mean sum of the surface fluxes (81 runs) is 403 Wm^{-2} while it is 367 Wm^{-2} at $z = 4$ m. The mean available energy is on average 399 Wm^{-2} which is very close to the mean sum of the surface fluxes. The imbalance between downwind available energy and the sum of the fluxes at $z = 4$ m is consistent with the earlier finding that the available energy over the downwind terrain is larger than upwind. A run-to-run comparison of available energy and the sum of the calculated surface fluxes is given in Fig.5.10.
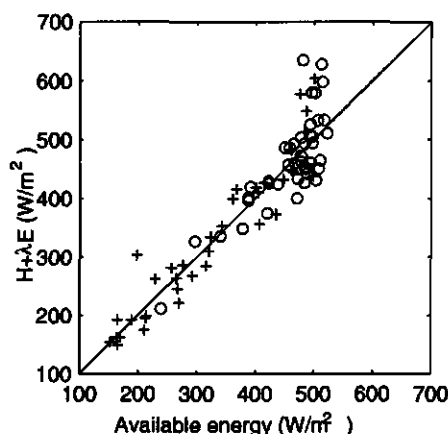
Fig.5.10 The relation between available energy at the surface and the calculated surface fluxes 'o' denote WA runs and 'x' denote SA runs.

It is seen that there is good agreement, apart for 7 mid-day runs where the sum of the latent and sensible heat flux is larger than the available energy $R_n - G$. A larger value for the IAL height in the procedure used to calculate the surface fluxes is needed to get better agreement for these runs which is an indication that the IAL is thicker around midday.

The subdivision of runs with weak advection and strong advection (section 5.1.2) is used in Table 5.5 and separate averages of the latent heat and sensible heat fluxes during WA- and SA- conditions are calculated. Also given is the downwind available energy, A_2, calculated from the measured net radiation and soil heat flux (Fig.3.4, loc.13).

	WA (weak advection)	SA (strong advection)
runs	43	38
λE_2	425	362 Wm^{-2}
H_2	37	-27 Wm^{-2}
A_2	459	331 Wm^{-2}

Table 5.5 Average fluxes and available energy during weak and strong advective conditions.

For the WA-case 93% of the available energy is consumed by evaporation and 7% is used for sensible heat. For the SA-case sensible heat contributes some 8% to evaporation. As before good agreement is found between the sum of the fluxes and the available energy in both cases.

5.3 The momentum flux and the surface roughness

The overall means (81 runs) of u_* observed at the three different locations after the step-change are 0.66, 0.67 and 0.64 ms^{-1} at respectively EC1, EC2 and EC3 while the upwind average was 0.56 ms^{-1}. So, u_* is clearly higher after the transition but it does not reveal a clear trend with height.

The mean day-time average (9:30 to 14:00 UTC) u_* is given in Table 5.6 to compare the results for the different days.

day	u_* EC1 ms^{-1}	ratio to upwind u_*	u_* EC2 ms^{-1}	ratio to upwind u_*	u_* EC3 ms^{-1}	ratio to upwind u_*
20/6	0.66±0.05	1.11±0.06	0.67±0.05	1.13±0.07	0.66±0.08	1.12±0.10
21/6	0.78±0.07	1.14±0.07	0.83±0.10	1.21±0.08	0.78±0.06	1.15±0.09
22/6	0.71±0.06	1.16±0.06	0.73±0.06	1.20±0.08	0.72±0.08	1.17±0.11
23/6	0.51±0.06	1.32±0.10	0.51±0.02	1.33±0.13	0.46±0.08	1.17±0.13
24/6	0.56±0.03	1.26±0.16	0.55±0.05	1.25±0.20	0.51±0.04	1.16±0.18

Table 5.6 The day-time average (9:30 to 14:00 UTC) friction velocity at the different eddy correlation stations and the ratio with the upwind value.

Relatively high values for u_* are found on the first three days whereas much lower values are observed on June 23 and 24 as was already discussed in the previous Chapter. The

downwind-upwind ratio of the friction velocity increases somewhat from June 20 to 22 and increases considerably on June 23 at EC1 and EC2 but remains constant at EC3. Because the flux does not change much going from EC1 to EC2, it is assumed that the momentum flux observed at EC1 is representative for the downstream surface momentum flux.

Since u_* is already constant with height below, say, 7 m, the surface roughness $z_{o,2}$ can be calculated with the drag method (Eq.4.3) using the wind speed measured at P4, ($z = 0.75$ m) and the momentum flux measured at EC1 at a height of 4.1 m. Using all runs, a surface roughness of 0.067 m is found. Only using those runs with wind speeds above 4 ms^{-1} gives $z_{o,2} = 0.062$ m. The stability correction can be neglected (it results in a $\approx 1\%$ change of z_o for wind speeds above 4 ms^{-1} and 4% for the other runs) owing to the low measuring height. A similar procedure for $z = 1.5m$, gives a z_o of 0.08 m for wind speeds above 5 ms^{-1}. A larger surface roughness would be found using the profile method (taking the levels from 0.5 m to 2 m) as can be deduced from Fig.5.7. So the downwind terrain is relatively rough compared to the region in which it is embedded whereas the upwind terrain was found to be relatively smooth (section 4.1).

5.4 The surface, aerodynamic and isothermal resistances

As was demonstrated in the introduction (section 1.2) and in section 5.1.2 the resistances r_i, r_a and r_s are crucial to the distribution of the available energy between H and λE. Here estimates for the surface resistance r_s, the climatological resistance r_i and the aerodynamic resistance r_a will be calculated. Estimates for the surface resistance will be obtained in two ways.

Firstly, r_s can be calculated directly from the surface latent heat flux and the saturation deficit between the surface and some reference height z_r,

$$r_s = \frac{Q_s(\Theta_{o,2}) - Q(z_r)}{\overline{wq}_{o,2}} - r_a \qquad\qquad 5.8$$

in which $Q_s(\overline{\Theta}_{o,2})$ is the saturation specific humidity at the surface temperature $\overline{\Theta}_{o,2}$ and $r_a = \overline{U}(z)/u_{*,2}^2$ assumed to be equal for temperature, humidity and momentum.

Secondly, a parameterization of Noilhan and Planton (1989) to calculate the surface resis-
tance is applied in order to compare it with the more direct method. Kroon and De Bruin
(KdB, 1993) extended the model as used here with this parameterization to study the
feedback between the downwind surface resistance and the downwind surface temperature
and water vapour deficit. The parameterization is fully empirical and based on plant-phy-
siological characteristics of a short crop. It is postulated that the canopy has a minimum
surface resistance $r_{s,\min}$ and r_s increases depending on temperature, the saturation deficit, the
amount of photosynthetically active radiation and soil water status. The relation is expressed
as

$$r_s = \frac{r_{s,\min}}{LAI} \frac{F_1}{F_2 F_3 F_4}.$$

5.9

KdB assumed that the influence of photosynthetically active radiation, soil water status and
the leaf area index (resp. F_1, F_2 and LAI) are constant for all $x > 0$, and used

$$F_3 = 1 - 40D$$

5.10

to describe the influence of the saturation deficit D which shows that r_s increases with water
vapour deficit. The temperature influence can be described using

$$F_4 = 1 - 0.0016*(25 - \overline{\Theta}(z))^2.$$

5.11

which assumes a minimum resistance at a temperature of 25°C and r_s is infinite for tem-
peratures close to 0 or 50°C.

First, r_s, calculated using Eq.5.8, is given in Fig.5.11 together with the climatological resis-
tance r_i (Eq.1.8) and the aerodynamic resistance r_a where the mean wind speed at $z = 3$ m
from P4 was used for $\overline{U}$ and u_* was taken from EC1. The given run numbers along the x-axis
indicate the runs that started at 12:00 UTC.
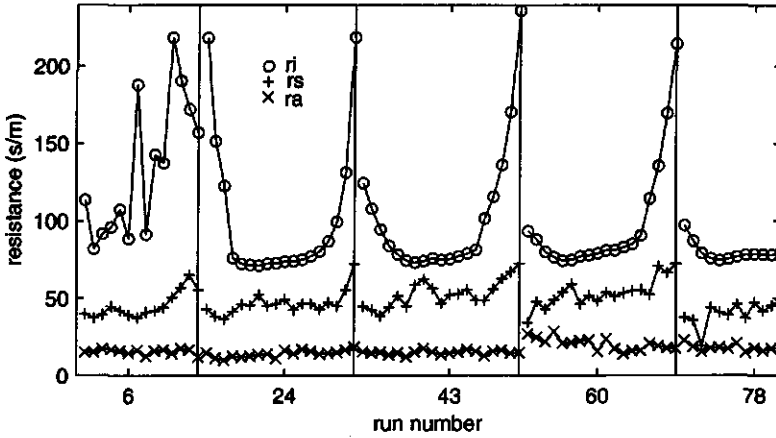
Fig.5.11 Surface, aerodynamic and climatological resistances of the 81 runs. Surface resistance was calculated using Eq.5.8. The labels on the x-axis indicate the number of the runs that start at 12:00.

The aerodynamic resistance is relatively small compared to r_s and r_i, certainly during the first three days. The surface resistance is always below r_i but around mid-day the difference is small. Towards the evening hours r_i increases rapidly with the rapid decrease of net radiation compared to the saturation deficit at reference height as can be deduced from Eq.1.8. At the same time r_s increases whereas r_a shows no daily cycle. So, the increase of r_s must be because of a relative decrease of $\overline{wq}$ compared to the saturation deficit between the surface and reference height. The increase of r_i is relatively larger and at some point an inversion forms when $r_i > r_s + r_a$ (Eq.1.9). On June 20 r_i indeed is relatively high but on June 23, the other day with relative strong advection, this is not the case.

For the parameterization given in Eq.5.9 a value for $r_{s,min}$ is needed. A rather arbitrary value of 30 sm^{-1} is used. The lowest value of r_s in Fig.5.11 is 19 sm^{-1} (on June 24) but it is suspect because of a spike in the surface temperature at that time; the next lowest value is 34 sm^{-1} observed on June 23. Using the temperature and saturation deficit at P4, r_s can be calculated using Eq.5.9. It is then found (Fig.5.12, upper panel) that at least the magnitude and the daily pattern is reproduced for a large part by this very simple parameterization.
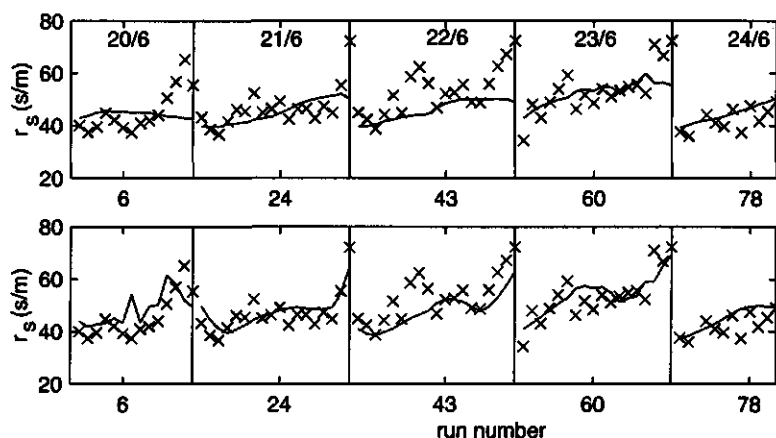
Fig.5.12 The Noilhan-Planton parameterization (Eq.5.9) for surface resistance (drawn line) compared with the 'measured' surface resistance (x). Upper panel: without radiation correction. Lower panel: including the radiation correction given by Eq.5.12.

However, the increase of r_s at the end of each day is not predicted well. This could be because the influence of the photosynthetically radiation was not included in the calculation of r_s. The influence of the depletion of soil water obviously is small for the considered period because the model still works satisfactorily on June 24. In Fig.5.13, the factor F1, by comparing results from Eq.5.8 and Eq.5.9, and also assuming that $F_2 = 1$ is given as a function of incoming shortwave radiation.
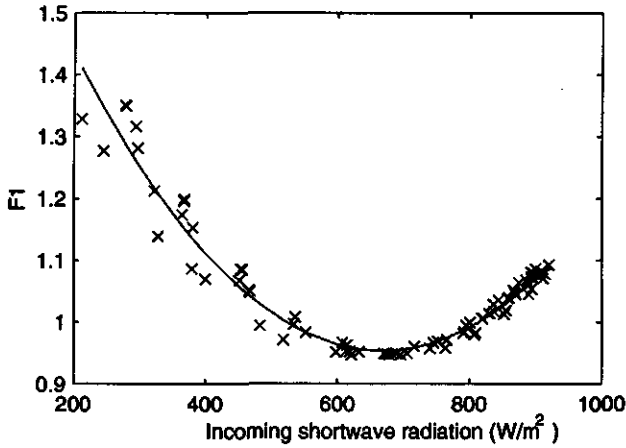
Fig.5.13 The factor F1 (Eq.5.15) as a function of global radiation.

A minimum F1 around S_e of 640 Wm^{-2} (which is 70% of the maximum S_e observed in the period 20 to 24 June) is found, and a quadratic fit gives

$$FI = 0.90 \left(\frac{S_{in}}{640} \right)^2 - 1.88 \frac{S_{in}}{640} + 1.93.$$

5.12

The correlation between the calculated and measured *F1* would increase from 0.97 to 0.98 if net shortwave radiation instead of incoming shortwave radiation would have been used. However, the good relation with the incoming radiation is thought to be of more general use. The factor F1 is then used to calculate r_s in Fig.5.12, lower panel, given by the drawn line. Note that global radiation is not the same as photosynthetically active radiation but the magnitude of both quantities is probably sufficiently correlated. Considering the simplicity of the model, the result may be of some use although the factors *F1* to *F4* also depend on crop type.

6 TRANSFER MECHANISMS OF HEAT AND WATER VAPOUR IN THE IBL

In Chapters 4 and 5 the data-set was described up to the point where it can be used to initialize and test the model. In order to gain the best insight in the turbulence structure of the IBL it would be useful to combine modelling efforts and measurements. In this Chapter results from the experiment and modelling results are combined to describe the transfer mechanisms of temperature and water vapour in the IBL.

Before the model can be used to complement the measured data, its performance needs to be studied to recognize the limitations of the model. As was described in section 2.5 the model operates in two parts. The first part is the 1-dimensional form (i.e. neglecting advection) of the model in which the equilibrium conditions over the upwind terrain are calculated. The results from this part of the model should therefore comply with MO-theory. A comparison between MO-surface layer characteristics and the modelling results is given in section 6.1. Profiles and fluxes after the step-change were already given in Chapter 5, these results will be compared with the model calculations, also in section 6.1.

The turbulence structure of the wind field undergoes a change due to a step-change of surface roughness and also because the temperature stratification changes, its characteristics are given in section 6.2.

The observed properties of the turbulent temperature and water vapour field after the step-change will be presented to gain insight in the process of adaptation to the new downwind conditions. To this purpose temperature and water vapour flux-variance and flux-profile relations are given in sections 6.3 and 6.4 using the data from EC1, EC2 and EC3 (Fig.5.1). Where relevant, model calculations are included to complement the measurements.

It is expected that flow properties in the IBL depend both on flow stratification and the position in the flow field. The flow stratification is expressed using a stability parameter ζ_l which differs from the stability parameter ζ in that the surface fluxes appearing in ζ are replaced by their in-situ measured values. Note that this so-called local stability parameter (Shao and Hacker, 1989) is closely related to the Richardson flux number,

$$\zeta_t = Ri_f \phi_m = \frac{g}{\Theta} \frac{\overline{w\theta}}{\overline{uw}\partial \overline{U}/\partial z} \phi_m. \qquad\qquad 6.1$$

The position in the flow field is given by z/x or z/δ and where appropriate, results are presented as a function of z/x or z/δ using the procedure discussed in section 5.1.1.

6.1 Model performance

The second-order closure model to be validated has been developed and first used for meteorological purposes by a group from NCAR, USA (Wyngaard *et al.*, 1974a). It was shown that realistic results could be obtained for the convective and the stable PBL (Wyngaard *et al*, 1974; Wyngaard, 1975 respectively). Furthermore, the model also appeared very useful for studying the two-dimensional flow over a surface roughness step-change under neutral conditions in the ASL (Rao *et al.*, 1974a). It gave realistic results for the mean flow properties (temperature and humidity) after an abrupt and combined change of surface roughness, temperature and humidity (Rao *et al.*, 1974b). However, as Wyngaard (1982) explains in his well-known review on boundary layer modelling, second-order closure should be used with caution in geophysical flows. An important bottle-neck to the universal applicability of the model is the sensitivity of the closure assumptions and modelling 'constants' to the convective state of the flow as was also shown by Kroon (1985).

6.1.1 Initialization: Homogeneous conditions

To test the ability of the model to reproduce the unstable and homogeneous ASL, a representative run (run 42, June 22 11h30) was chosen from all runs which were used to test the model (Table A4.1). For all runs with the model, $z_{o,1} = 0.01$ m and $z_{o,2} = 0.07$ m (see sections 4.1.1 and 5.3). Other relevant input quantities for run 42 are repeated in Table 6.1.

Run	Time (decimal)	H Wm^{-2}	λE Wm^{-2}	u_* ms^{-1}	$T(z_{o,2})$ °C	$\rho_v(z_{o,2})$ gm^{-3}	r_t, down-wind sm^{-1}	dd °	L m
42	11.50	362	72	0.63	28.1	8.2	46.9	346	-61

Table 6.1. Initialization parameters for the second-order model (run 42). From left to right: run number, decimal time, the upwind surface sensible and latent heat flux, the upwind friction velocity and upwind the temperature and absolute humidity at z_{o2}, the downwind surface resistance, wind direction and the Obukhov length.

The model calculates the ASL up to $z = 50$ m with a logarithmic grid consisting of 41 levels.

The flux-profile relations as produced by the model are compared with the MO-relations (Eq.2.10) in Fig.6.1.
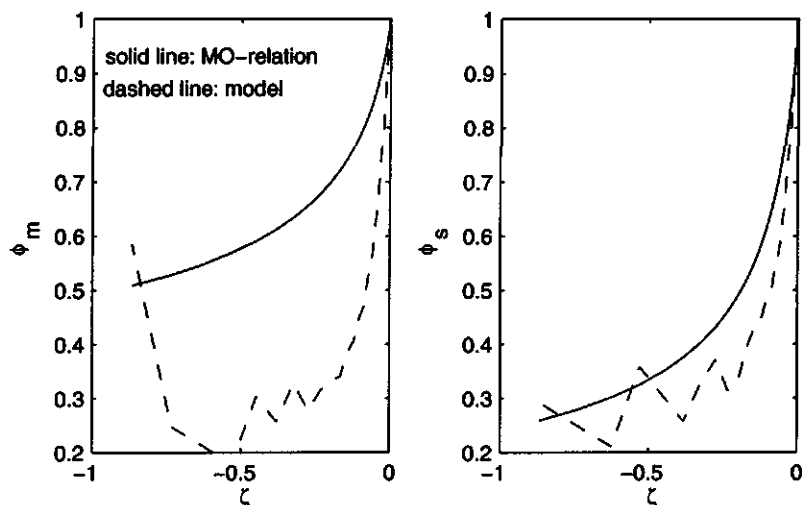
Fig.6.1 Comparison of the model and MO-theory: The non-dimensional vertical gradients of wind speed (left panel) and temperature or water vapour (right panel). Dashed line: modelling result, drawn line: MO-relation.

As was already shown by Kroon (1985), it is mainly ϕ_m which deviates from the expected curve. Several reasons have been put forward which may be responsible for this problem (Kroon, 1985, Wyngaard, 1982) and some tests were performed for this study to verify these ideas.

As is shown in Appendix A1, the values for the constants C_{13} (Eq.A1.21) and d_1 (Eq.A1.22) are calculated inserting $\zeta = 0$ in the MO-relations which are used at the boundaries of the model. We have tested the sensitivity of the model for different constants in the MO-relations for which many alternatives are available (Yaglom, 1977). The value of 16 in Eq.2.10 was replaced by 22 for ϕ_m and 13 (Wieringa, 1980) for $\phi_{\theta,q}$. This appeared to have very little effect on the results and did not improve the modelled ϕ_m.

The model uses a governing turbulence relaxation time scale $\tau_\varepsilon = 2TKE/\varepsilon$. It is then assumed that time scales for relaxation processes, like the dissipation of temperature fluctuations or pressure destruction of the heat flux, are proportional to τ_ε. For the model, the proportionality factors are determined by solving the governing equations at $\zeta = 0$. However, many of these factors are functions of ζ as can be deduced from field experiments (Bradley *et al.*, 1982, Lang *et al.*, 1983, Lang and Bradley, 1983), as can also be deduced from the analysis of Kroon (1985), and as is shown in Appendix A1. Other studies revealed the inadequacy of the parameterization of the pressure-covariance term in the $\overline{u\theta}$-equation (Eq.A1.10, $i = 1$), and it was suggested that (co-)variances which contain horizontal wind speed fluctuations need a different time scale (Raupach, 1983, Raupach and Legg, 1983).

It is possible to calculate some of the relations between the proportionality factors and stability exactly (Appendix A1, Eqs.A1.18-A1.24). The largest variation with stability is then found for $C_{33}(\zeta)$, the factor in the parameterization of the pressure term in the w^2-equation (Eq.A1.20), which is also discontinuous close to $\zeta = -0.4$. Large variations are also found for d_1, appearing in the $\overline{us}$-equation (Eq.A1.22), and C_{22} in the $\overline{v^2}$-equation (Eq.A1.19). The replacement of the constant proportionality factors, used in the model, by the functions A1.18 to A1.24 is not feasible because $C_{33}(\zeta)$ is a discontinuous function.

The model assumes gradient-diffusion behaviour of turbulent transport whereas it is known that this assumption no longer holds for the transport of TKE under unstable conditions (Wyngaard, 1982). However, the deviation of ϕ_m already appears for near-neutral conditions for which it is known that the transport terms are unimportant.

It must be concluded that we still have no good solution for this problem. However, although ϕ_m, as produced by the model, deviates considerably from the observed ϕ_m, it does not prevent the model from reproducing the flux-profile relations of the temperature and water vapour field reasonably well. The scalar flux-profile relation ϕ_s shows good agreement with the MO flux-profile relation although it decreases a little too fast with increasing instability as can be seen in Fig.6.1 (right panel).

It was shown that the shear production of TKE, ϕ_m, is not reproduced properly by the model. Next, the flux-variance relations $\varphi^2_{u,v,w}$ are considered separately and $\varphi^2_u + \varphi^2_v + \varphi^2_w$, which is twice the amount of TKE. The modelling result of these relations is compared to the empirical relations (Eq.2.11) in Fig.6.2 where the sum

$$\frac{\overline{u^2} + \overline{v^2} + \overline{w^2}}{u_*^2} = \frac{2TKE}{u_*^2} = \varphi^2_u + \varphi^2_v + \varphi^2_w$$

is given also.
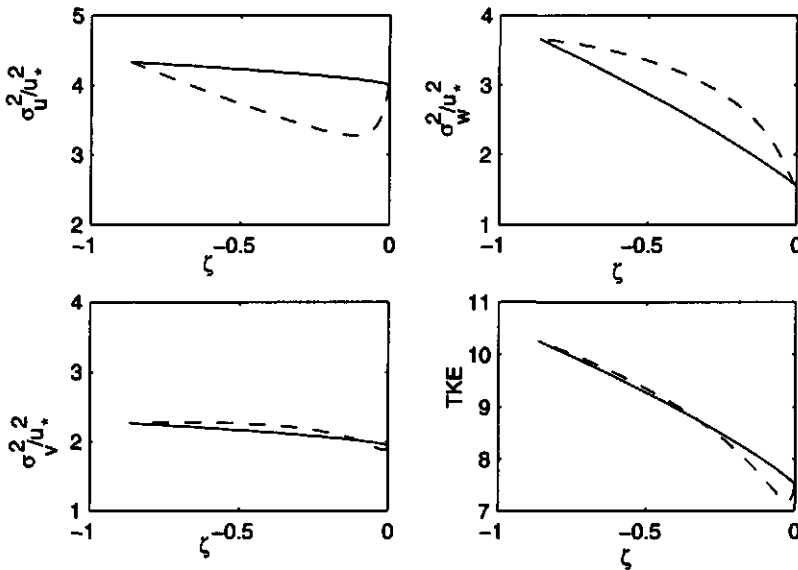
Fig.6.2 *Comparison of the model and MO-theory: the flux-variance functions for the wind components produced by the second-order model and the Monin-Obukhov flux-variance functions. The sum of these components, representing twice the turbulent kinetic energy (TKE), is given in the lower right panel. Dashed line: modelling result, drawn line: MO-relation.*

The model produces a too large φ_w, φ_u is too small but φ_v compares favourably. Since φ_w and φ_u compensate, the model calculates the sum (Fig.6.2, lower right panel) rather well. It must be concluded that the model is not capable to reproduce the turbulence structure of the wind field but it provides the atmosphere with the proper amount of TKE.

The turbulence structure of scalars is more important for this study. The calculated non-dimensional variance for scalars (humidity and temperature) is compared with the semi-empirical MO-relation (Eq.4.7) in Fig.6.3 (left panel) and it is seen that the modelling results compare favourably with MO-theory.
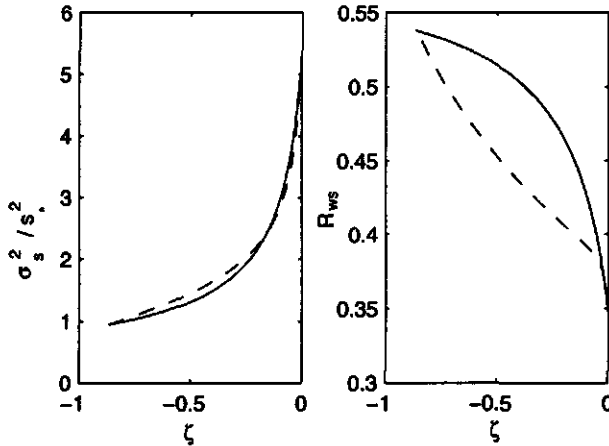
Fig.6.3 Comparison of the model and MO-theory: the flux-variance relation φ_s (left panel) and the transfer efficiency R_{ws} (right panel). Dashed line: modelling result, drawn line: MO-relation.

Note that during the initialization phase the model assumes (implicitly) perfect correlation between water vapour and temperature fluctuations so $\varphi_q = \varphi_\theta$. In section 4.1.4 it was already shown that this is in fact not a valid assumption.

Because φ_w increases too fast, it follows that the transfer efficiency R_{ws} increases too slow towards unstable conditions as can be seen in Fig.6.3 (right panel).

It was verified that the results discussed in this section do not change when runs with larger or smaller Obukhov lengths are used. Deviating behaviour always increases with height until the upper 7 grid points. However, once the Obukhov length becomes too small, the absolute difference with the MO-relations is almost unrecoverable at that point. By trial and error it is concluded that only runs with an Obukhov length larger (absolute value) than the height of the grid, 50 m, can be used to run the model. This requirement excludes the runs from June 23 and 24 when the Obukhov length was always below 30 m. In the following

sections the results from 27 runs with the model, based on the measurements from 9h30 to 14h00 UTC of June 20 to June 22, will be used and compared with the measurements. Measuring results as such are given for the whole set of 81 runs.

6.1.2 Mean profiles after the step-change

Part 2 of the model calculates the downwind IBL properties up to the last profile mast P4. There are three downwind surface parameters which are needed as lower boundary conditions for this part of the model: surface resistance, surface roughness and available energy (see section 2.5) which are all three assumed to be constant downstream. To illustrate the ability of the model to produce the measured profiles and to study the sensitivity of the results to the lower boundary conditions, the data from the run 42 (June 22, 11:30- 12:00 UTC) were used (Table 6.1).

The measured and calculated temperature profiles before and after the step-change are given in Fig.6.4a and the measured and calculated humidity profiles in Fig.6.4b.
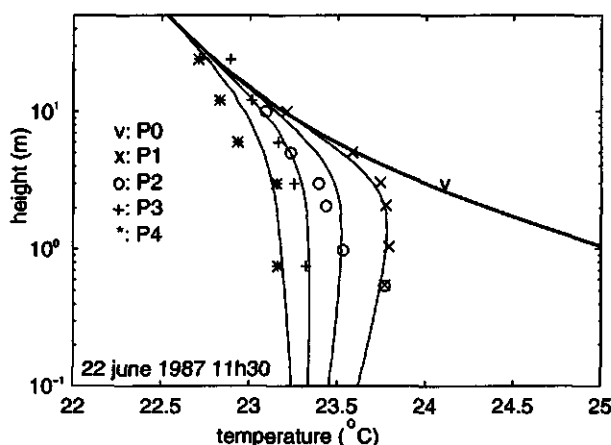
Fig.6.4a Calculated (lines) and measured (symbols) temperature profiles. June 22, 11h30. The drawn profiles are from right to left for P0 to P4.
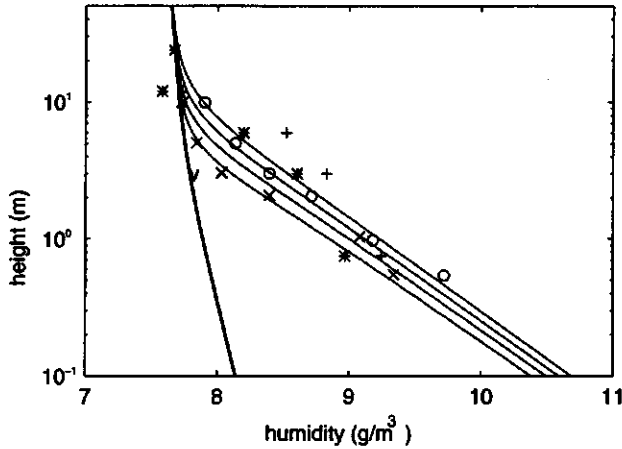
Fig.6.4b Calculated and measured water vapour profiles. June 22, 11h30. See for legend Fig.6.4a. The drawn profiles are from left to right for P0 to P4.

The temperature field shows the proper amount of cooling between P1 and P4. The height of the advective inversion at P1 is also calculated rather well with the model. Going from P1 to P2 the cooling calculated by the model is smaller than was observed. This is consistent with the fact that the calculated increase of the humidity from P1 and P2 is somewhat smaller than the measured amount.

As for all runs which were compared with the model, it was found necessary to correct for offset errors in the measured profiles. For this run, the offset was approximately 0.3 K for the temperature profiles and 0.7 gm^{-3} for the water vapour profiles to get the best fit for the profiles at P1 and P2 and 1.2 gm^{-3} for the profiles at P3 and P4. The need for this correction points at the earlier mentioned difficulties with the psychrometer measurements in section 5.1.3. After the correction, the downwind measured and calculated profiles at P1 and P2 compare very well for this run whereas the water vapour measurements from P3 and P4 show more scatter. It is, however, important to note that the measured and modelled vertical water vapour gradients for P3 and P4 compare rather well. This is illustrated for run 42 and location P4 in Fig.6.5.
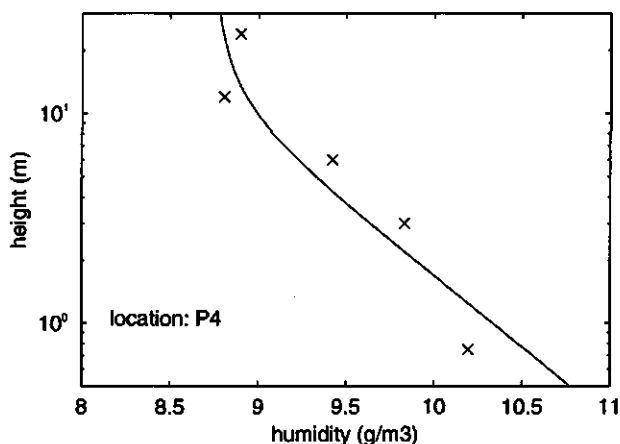
Fig.6.5 The calculated and measured humidity profile at location P4 for run 42, June 22, 11h30.

From the overall reasonable agreement for this one run it could be concluded that the method to calculate r_s, as discussed in section 5.4, seems to work reasonably well. There are, however, also examples where this was not the case. An example is given in Fig.6.6 (run: June 20, 12h30) which also serves to demonstrate the sensitivity of the calculations to the surface resistance and the downwind available energy.
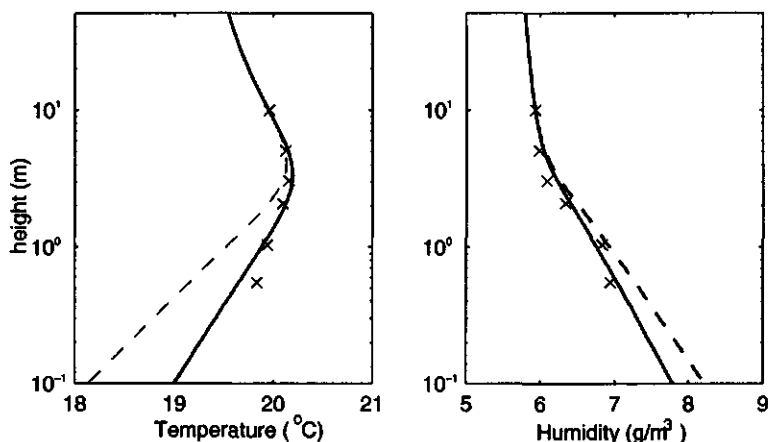
Fig.6.6 Calculated and measured temperature and water vapour profiles at P0 and P1, June 20, 12h30. The drawn lines represent the model calculations using $r_s = 56\ sm^{-1}$, the dashed lines are for $r_s = 37\ sm^{-1}$.

In this case, the estimated r_s of 37 sm^{-1} appears to be too small, and this was so for almost all runs of June 20. A better fit with the measured data is found when r_s is increased to approximately 56 sm^{-1}. The agreement between the modelled and measured humidity at P1 also improves with this higher r_s (Fig.6.6, right panel).

To illustrate up to what extent the model is able to reproduce the measured wind profiles, the modelled and measured results from the run taken at June 22, 11h30 are compared in Fig.6.7.
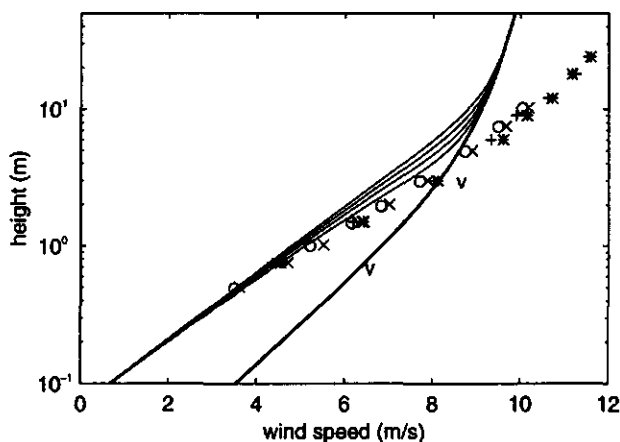
Fig.6.7 Measured and modelled wind speed profiles (Legend: see Fig.6.4a).

The measured and calculated profiles up to, say, 5 m (i.e $\zeta \approx -0.1$) compare reasonably well. Above that height, the wind speed gradient is underestimated by the model as could be expected from the problems concerning the initialization of ϕ_m discussed in section 6.1.1.

6.1.3 Fluxes after the step-change

The calculated fluxes, using the model, are compared with the measured values for 27 runs. For each run and for each of the three EC-stations, the results from the proper grid point in the model were selected based on the wind direction and the measuring height. The results for the friction velocity, the sensible heat flux and the latent heat flux are given in Fig.6.8.
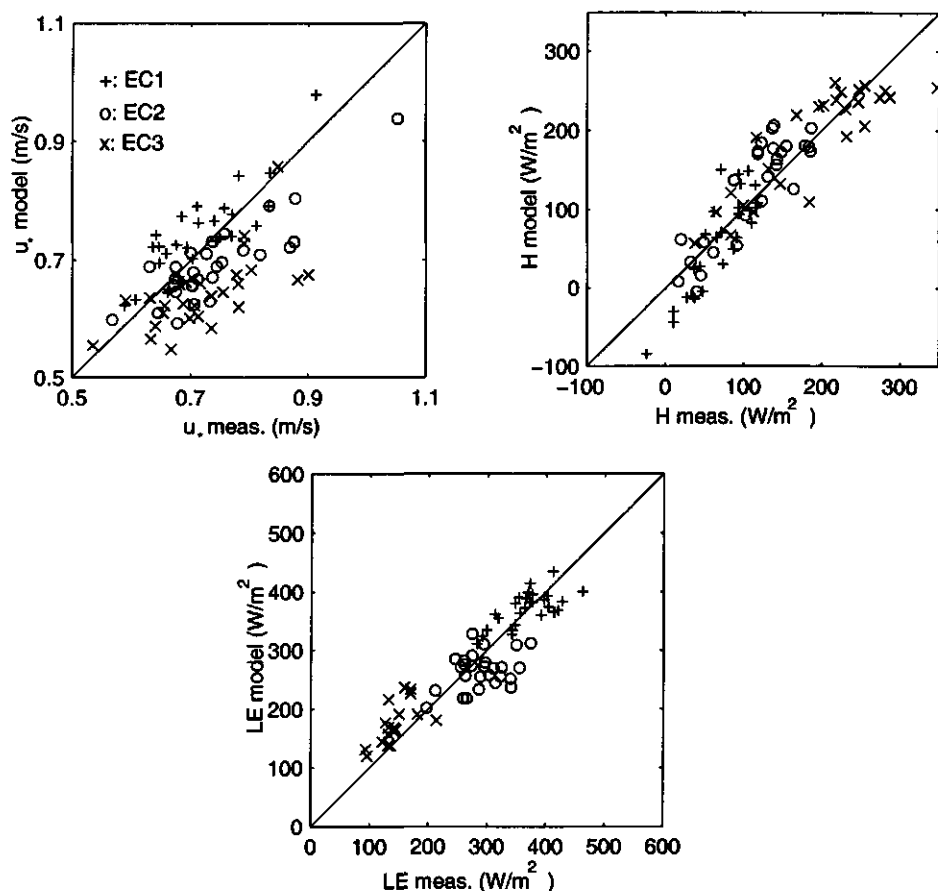
Fig.6.8 The comparison of the modelled and measured fluxes of momentum (given as the friction velocity), sensible heat and latent heat ('+': EC1, 'o': EC2, 'x':EC3).

The comparison for the friction velocity shows considerable scatter which is reflected in the low correlation (0.54, s.e.e of 0.07 ms^{-1}) between the model and measured results. It is seen that the results differ for each EC-station. The model predicts a larger decrease with height than was observed. On average, u_* is overestimated by the model at EC1 by 4%; at EC2, u_* calculated by the model is 5% too low and 10% too low at EC3. The too high u_* at EC1 indicates that, although the calculated wind profile seems to suggest the need for a higher $z_{o,2}$ (Fig.6.7), the momentum flux is already too large. This apparent contradiction may be

due to the problems with the model to simulate the wind field properly. Furthermore, the model only represents an idealized picture of the actual conditions, as it simulates a single surface roughness step-change. However, the air arriving at the smooth to rough step-change around which the experiment was set up has experienced a large range of roughness variations of which the effect has not yet ceased (sections 4.1.2, 4.1.3 and 5.1.4).

The modelled and measured sensible heat flux compare favourably, except that, for some runs, the model predicts negative sensible heat fluxes at EC1 whereas positive fluxes were observed. The result at EC3 (average of 27 runs) is that the modelled flux is on average 1.06 ± 0.26 times the measured flux, at EC2 this factor is 1.11 ± 0.55 and at EC1 this factor is no longer meaningful because of the low fluxes. The latent heat flux, calculated with the model, shows good agreement with the measured flux. At EC1 the ratio of the modelled and the measured latent heat flux is 1.02 ± 0.08, at EC2 it is 0.93 ± 0.14 and at EC3 the factor is 1.23 ± 0.19 (but the latent heat flux is small at EC3). The results are encouraging since it thus appears that they are not very sensitive to the problems with the modelling of the wind field and the observed errors in the upwind profile measurements. The objective procedure which was used in Chapter 5 to calculate the up- and downwind input parameters, like the surface resistance, also proves to be adequate except for June 20 when the surface flux of latent heat is overestimated.

Rao *et al.* (1974b) have shown that their second-order model used in this study is capable to simulate the mean flow field after a dry, hot to a cool, wet surface step-change. The above results supplement their findings as it is shown that the model is also capable to simulate the fluxes of latent and sensible heat after the step-change and to a lesser extent, of momentum. The Penman-Monteith approach used at the lower boundary which replaced the constant relative humidity as was used by Rao *et al.* (1974b), appears to be very helpful to arrive at these realistic results. It is now possible to proceed with the combined results from the experiment and the model, to study the flux-variance and flux-profile relations in the IBL.

6.2 Flux-variance relations of wind

The intensity of turbulence fluctuations and their ability to carry along atmospheric con-
stituents is important for the transport of heat and water vapour. The mean of 81 runs of the
standard deviations of the vertical wind component W and the horizontal wind U (total wind
vector) observed at the different downwind locations are given in Table 6.2.

	EC1	EC2	EC3
σ_u (ms^{-1})	1.73±0.31	1.74±0.34	1.69±0.33
σ_w (ms^{-1})	0.83±0.14	0.87±0.16	0.94±0.16
$\sigma_{w,2}/\sigma_{w,1}$	1.10±0.05	1.10±0.06	1.10±0.08

*Table 6.2 The mean standard deviations (81 runs) of vertical and horizontal wind at the three Eddy Correlation
stations after the step-change and the ratio of the downwind $\sigma_{w,2}$ with the calculated upwind $\sigma_{w,1}$.*

It is found that on average σ_w increases with height and σ_u is fairly constant in the IBL. In
the homogeneous surface layer σ_u/σ_w is below 2 most of the time and relatively constant
compared to either φ_w or φ_u under unstable conditions (e.g. De Bruin *et al.*, 1993). At EC3
σ_u/σ_w is small compared to the other two locations (1.8 compared to 2.0) because of the
relatively high σ_w at EC3. This could be because of a quicker adaptation of σ_w compared to
σ_u in the lower layers of the IBL (Beljaars, 1987).

Next, it is seen whether the flux-variance relations, φ_w and φ_u answer to local scaling. The
comparison for $\varphi_w = \sigma_w/u_*$ is given in Fig.6.9.
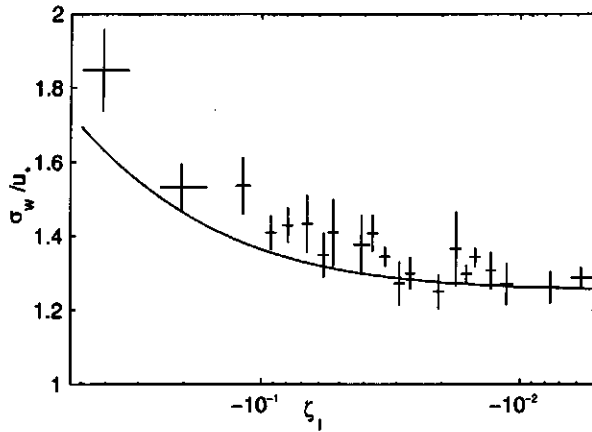
Fig.6.9 The flux-variance relation φ_w as a function of the local stability. The vertical and horizontal bars indicate the variation (given as the interquartile range) of resp. φ_w and ζ_l in each bin. The drawn line is φ_w given by Eq.2.11.

The results of all three eddy correlation stations were grouped into 24 classes of stability and each point in the graph represents the median value of 7 to 13 runs, 22 classes in the unstable range and 2 classes (not plotted) represented near-neutral to stable conditions. In the unstable range, φ_w increases with instability at a somewhat higher rate compared to the homogeneous case (drawn line). For near-neutral conditions ($\zeta_l = -0.0034 \pm 0.0005$) $\varphi_w = 1.26 \pm 0.06$ (not shown in Fig.6.9) which agrees very well with the neutral value of 1.25. For stable conditions up to $\zeta_l = 0.02$ a φ_w of 1.32 ± 0.07 was found (also not shown in Fig.6.9), which is below the (constant) value of 1.5 for φ_w under stable conditions, in the homogeneous surface layer (De Bruin *et al.*, 1993).

Due to the use of u_* in both φ_w and ζ_l the result in Fig.6.9 may be artificial (Hicks, 1978). However, this can be checked using a rewritten form of Eq.2.11,

$$\sigma_w = 1.25\left(u_*^3 + 3\frac{kgz}{\Theta}\overline{w\theta_v} \right)^{1/3}. \qquad\qquad 6.2$$

The result given in Fig.6.10 shows that σ_w is underestimated at EC3 and EC2 (respectively by 7% and 4 % based on the best fit through the origin) whereas at the lowest location in the IBL σ_w is estimated correctly within 1%.
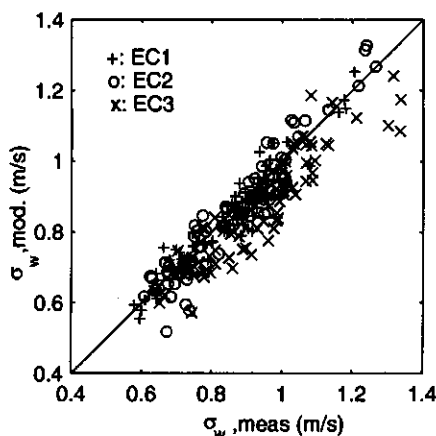
Fig.6.10 Comparison of the measured and calculated downwind σ_w.

From Eq.6.2, σ_w can be considered as the sum of two velocity scales for the ASL: the friction velocity, representing shear produced turbulence and a velocity scale for local free convection, when surface layer behaviour is like that in free convection (Tennekes, 1970). The convective scale represents larger eddies whereas the friction velocity represents the smaller eddies. Going downwind the friction velocity is increasing due to the surface roughness change whereas the convective part decays because of the decaying sensible heat flux. However, the adaptation of large eddies to the new terrain conditions is probably relatively slow and it may therefore be that local scaling fails for the convective term whereas it is valid for the dynamical part, also since u_* adapts relatively fast (see section 5.3) to new terrain conditions. This hypothesis is supported by the increasing difference between the calculated and measured σ_w going from EC1 to EC3 and the better local scaling for neutral conditions.

The non-dimensional standard deviation φ_u of the horizontal wind speed is given in Fig.6.11 as a function of ζ_l. In advance, it should be noted that σ_u is not expected to follow MO-similarity (Kaimal and Finnigan, 1994) and depends on the height of the PBL, a quantity which was not measured. However, in order to compare the data with results from other sources, local MO-scaling is applied.
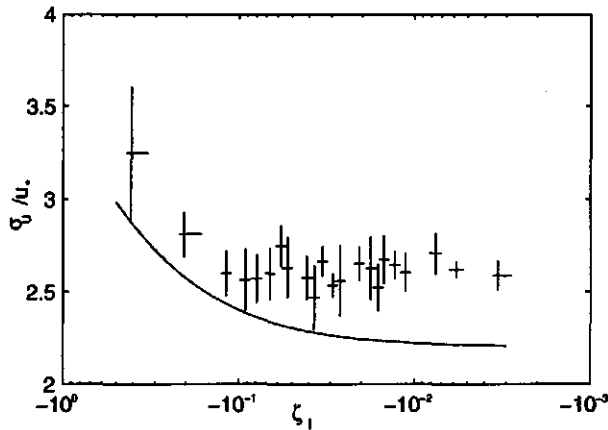
Fig.6.11 As Fig.6.10 but for φ_u

Also indicated in the figure the flux-variance relation

$$\varphi_u = 2.2(1 - 3\zeta_l)^{1/3} \qquad\qquad 6.3$$

(De Bruin *et al.*, 1993). For this experiment and for near-neutral conditions it was found here that $\varphi_u = 2.6 \pm 0.08$ and for stable conditions $\varphi_u = 2.7 \pm 0.08$ which is also somewhat higher than the (constant) value for φ_u under stable conditions of 2.5 given by De Bruin *et al.* (1993). The (small) difference can possibly be explained from the fact that De Bruin *et al.* used σ_u from a cup anemometer which is prone to frequency losses whereas here data from a sonic anemometer were used, both for σ_u and u_*.

Finally, some of the experimental results are compared with the model results. It was already shown in section 6.1.1 that the model is not able to reproduce the vertical structure of σ_u and σ_w properly under homogeneous conditions. The modelling results for these quantities after the step-change are compared to the measured values for the 27 runs (June 20, 21 and 22, 9h30 to 14h00 lt) in Fig.6.12.
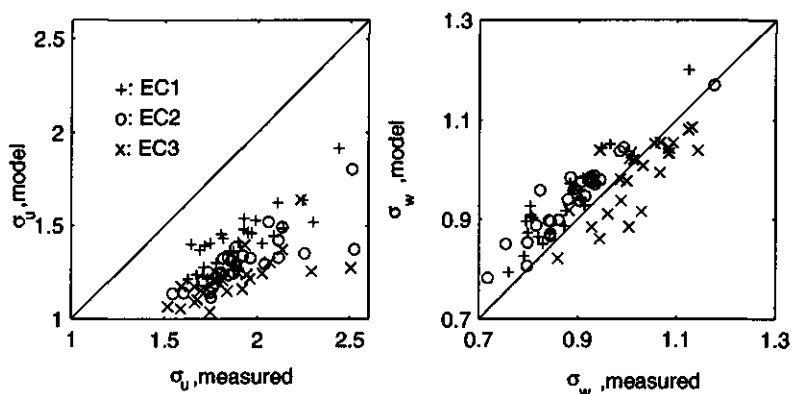
Fig.6.12 A comparison of modelled and measured standard deviations of horizontal wind (left panel) and vertical wind (right panel)

For σ_u the model gives values which are much too low at all three EC-stations. This is as expected since the model underestimates σ_u/u_* over homogeneous terrain (Fig.6.2), and, on top of this, underestimates the downwind momentum flux (section 6.1.3). The calculated standard deviation of the vertical wind compares reasonably well with the measured σ_w on average but the model gives a relatively low σ_w at EC3 and overestimates σ_w at EC2 and EC1. Finally, the calculations were repeated, using a 30% increased downwind surface roughness. This hardly influenced the results, as the wind standard deviations only increased 3%.

6.3 Flux-variance relations of temperature and water vapour

The average values for all 81 runs of the downwind σ_θ (left panel) and σ_q (right panel) are given in Fig.6.13 for the locations EC1 to EC3 together with the standard deviations around the mean indicated as horizontal bars. Also given are the upwind σ_θ and σ_q at the heights of EC1 to EC3. These were calculated using Eq.4.7 in which for σ_q the value of 2.3 was replaced by 5, based on Fig.4.7.
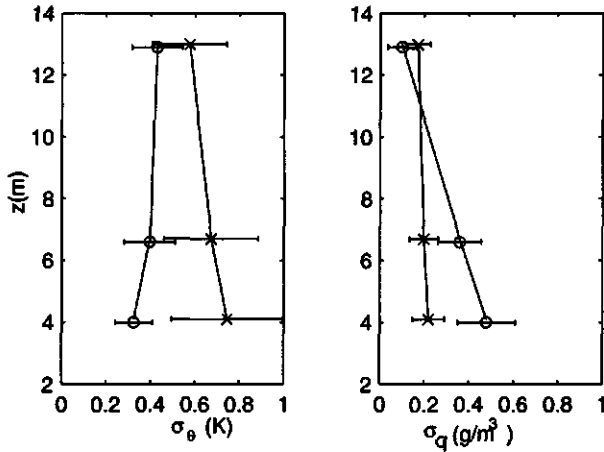
Fig.6.13 The averages and standard deviations (indicated with a bar) of 81 half hour σ_θ (left panel) and σ_q (right panel) over the downwind terrain ('o') at EC3 to EC1 and at the heights of EC1 to EC3 over the upwind terrain ('x').

After the step-change studied here, σ_q increases, and σ_θ decreases in the downwind direction. The largest downwind decrease of σ_θ and increase of σ_q was observed at the height of EC1. On average, σ_θ increases with height in the IBL whereas σ_q decreases with height. It is seen that, at or around 13 m, σ_q is below or at its upwind level whereas this is not the case for σ_θ.

In the homogeneous and unstable day-time surface layer, both the temperature variance and the humidity variance decrease with height and increase with increasing instability (Eq.2.13). In the IBL, local similarity can be expected if the relation between fluxes and standard deviations depends on the local terms in the scalar-variance budget, production and dissipation of scalar variance. This is the case when advection and transport of variance can be neglected, or if these non-local processes cancel out (section 2.6). The experimental results of local scaling for φ_s with $s = \theta, q$ are given in Fig.6.14a,b and are compared with the MO-relation for the homogeneous surface layer where again ζ_l replaces ζ.
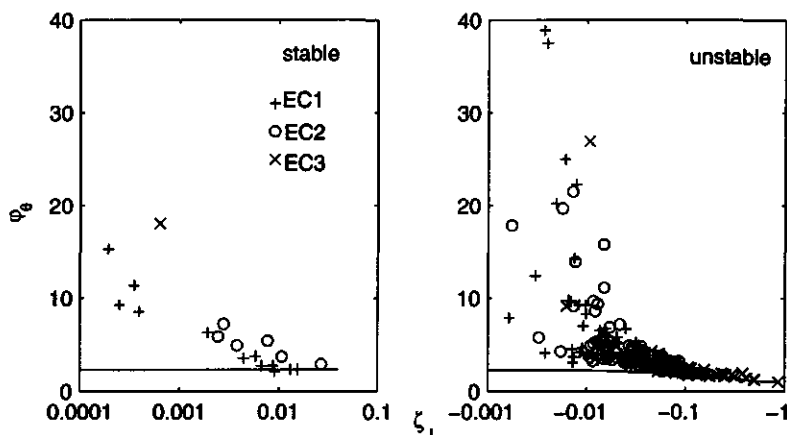
Fig.6.14a *The non-dimensional standard deviation of temperature,* φ_θ, *as a function of the local stability parameter.*
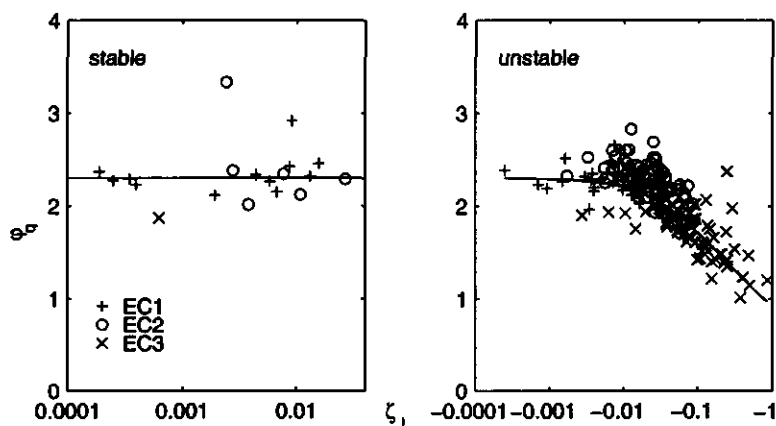
Fig.6.14b *The non-dimensional standard deviation of water vapour,* φ_q, *as a function of the local stability parameter.*

The water vapour fluctuations follow local scaling reasonably well, both for stable and unstable conditions. The local value of φ_θ is much too large for near neutral conditions as was also found by Motha *et al.* (1979b) which points at a relatively weak association between temperature fluctuations and the net transport of heat. Only when the heat flux is

large, a return to local scaling behaviour was observed (for approximately $\zeta > 0.01$ under stable conditions and for $\zeta < -0.1$ under unstable conditions). To see where local scaling for temperature fails, the next step is to consider the relation between $\varphi_\theta/\varphi_{MO}$ and z/δ, φ_{MO} was calculated using Eq.4.7 and ζ_l was used with the virtual heat flux. A constant value of 2.3 was used for φ_{MO} when $\zeta_l < 0$. The profile given in Fig.6.15 was calculated using all 81 runs and the procedure described in 5.1.1.
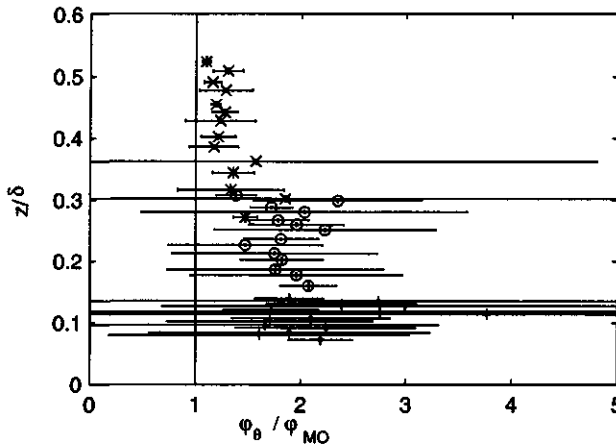
Fig.6.15 The flux-variance relation φ_θ, normalized with φ, calculated using Eq.4.7, as a function of position in the IBL. The horizontal error bars indicate the interquartile range for the flux-variance relation and the vertical bars give the interquartile range for z/δ (symbols in the middle of the error bars: '+':EC1, 'o':- EC2, 'x':EC3).

It is seen in Fig.6.15 that the deviations from local scaling are large for low values of z/δ. It cannot be decided whether there is a maximum around $z/\delta = 0.15$ or below that level since no data are available below $z/\delta = 0.15$. It can however be concluded that the flux-variance relation for temperature in the IBL is also a function of z/δ. The large scatter in the lower region of the IBL is because φ_θ becomes very large when $\overline{w\theta}$ is small. A similar analysis for water vapour revealed no trend with height and little scatter around unity, thus confirming the result given in Fig.6.14.

The deviations from local scaling for temperature could be explained if all terms in the budget for temperature variance (Eq.A1.5) would be available. For instance, Raupach and Legg (1983) measured the dispersion of a passive tracer from an elevated line source. They found that close to the source dissipation and advection were the dominant terms, whereas

at a larger distance production became significant. For their analysis, very detailed measurements in a wind tunnel were performed. From the data of this experiment, the production of $\overline{\theta^2}$,

$$P_{\theta,z} = -\overline{w\theta}\partial\Theta/\partial z$$

can be calculated. The vertical temperature gradient occurring in $P_{\theta,z}$ is calculated using a second-order polynomial fit through the lowest 4 levels of the temperature measurements at P3 for EC1 and EC2, for the vertical temperature gradient at EC3 m a linear fit through the 3 highest measuring levels was used to calculate the gradient. It is assumed, as before, that the change in the x-direction of the fluxes is small compared to the vertical flux differences.
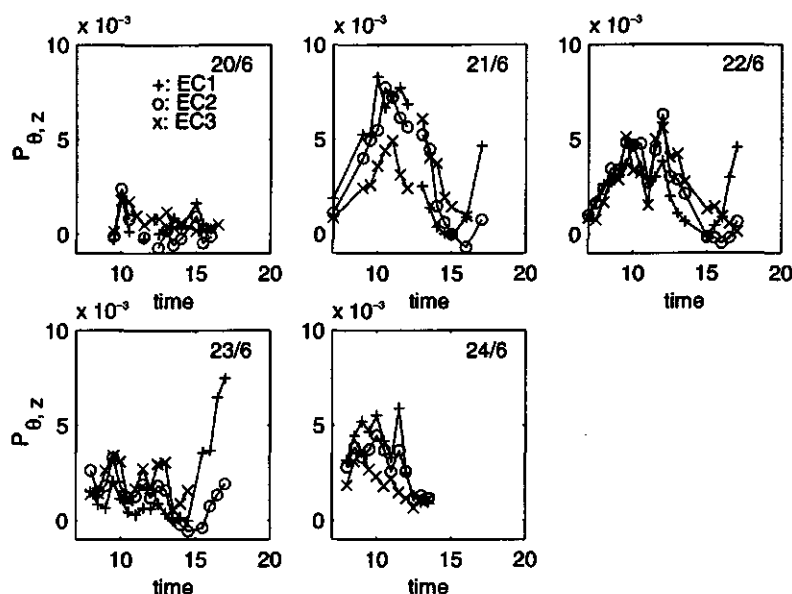
Fig.6.16 $P_{z,\theta} = -\overline{w\theta}\partial\Theta/\partial z$ at three heights (4.1, 6.7 and 13.0 m) for location P3.

On June 20, $P_{\theta,z}$ (Fig.6.16), is low compared to the other days. On June 21 and 22, $P_{\theta,z}$ decreases with height until, say, 13h00 to increase with height after that time. Once the layer up to 4 meters becomes stable the 'homogeneous' situation is restored. On June 23, the day with the shortest fetch, a different pattern is found. During the whole day, until 15h00, $P_{\theta,z}$

is low in the lower part of the IBL. As on the other days, the negative trend with height returns once the IBL becomes fully stable. On June 24, runs are available up to the point when the advective inversion was forming. Before that time $P_{\theta,z}$ decreased with height.

An estimate for the advection term in the budget of σ_θ^2 is obtained using the difference between the observed downwind temperature variance and the calculated upwind temperature variance (using Eq.4.7) at the height of the downwind measuring level,

$$A_{\theta,x} = -\overline{U}(z)\frac{\partial(\overline{\theta^2}/2)}{\partial x} \approx -f(x,z)\overline{U}(z)\frac{\overline{\theta^2}_2 - \overline{\theta^2}_1}{2x} \qquad 6.4$$

where the horizontal wind speed U was measured with the sonic anemometers at EC1 to EC3. Close to the step-change the advection term will be relatively large and it decreases with the downwind distance as the temperature field adapts to the underlying surface. Tacitly assuming the validity of the model, it was used here to calculate a factor $f(z,x)$ for each location in the IBL by which the local value for the advection is smaller compared to the 'bulk' value in Eq.6.4. This factor (0.2, 0.3 and 0.8 for EC1, EC2 and EC3 respectively) is then used to correct the bulk value to a local value. This way at least an order of magnitude estimate is obtained for the advection of σ_θ^2. The results, consisting of data from EC1, EC2 and EC3 and the runs from June 21 and 23 are given in Fig.6.17 together with $P_{\theta,z}$. The upper panels give, from left to right, the results for EC1 to EC3 on June 21, the lower panels for June 23.
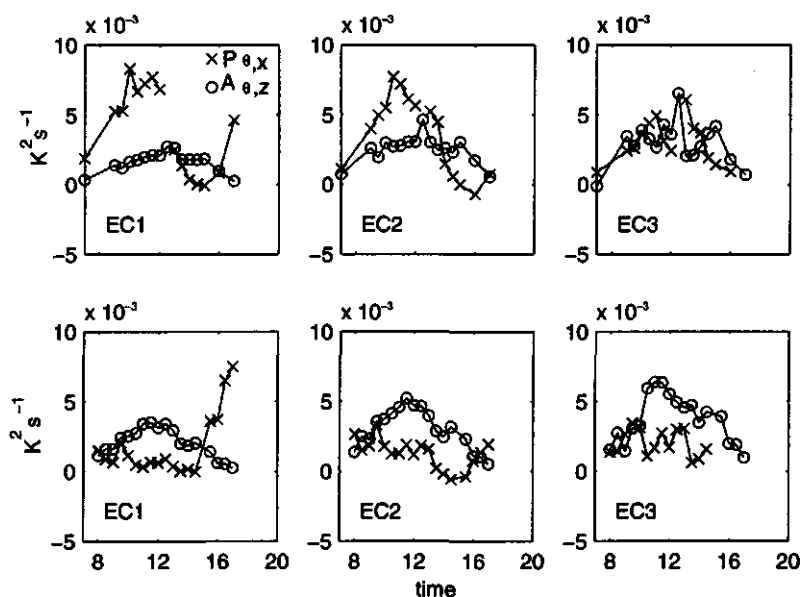
*Fig.6.17 Advection ('o') and production ('x') of temperature variance on 2 days at three different levels at P3
(4.1, 6.7 and 13 m on June 21: upper three panels, 4.1, 6.7 and 13.0 on June 23: lower three panels).*

On June 21, $A_{\theta,x}$ is fairly constant both in time and place. In the morning, $A_{\theta,x}$ is relatively small compared to $P_{\theta,z}$ at EC1 and EC2, but large in the afternoon due to the decrease of $P_{\theta,z}$ while at EC3 $A_{\theta,x} \approx P_{\theta,z}$. Finally, towards the end of the day when the IBL below 4 m becomes stable, $A_{\theta,x}$ is no longer important at EC1 (below the temperature inversion) whereas at EC2 and EC3 both $A_{\theta,x}$ and $P_{\theta,z}$ seem to disappear. This is also in agreement with the change from SA-conditions to WA-conditions as defined in Fig.5.3.

The height of the advective inversion is close to the height of EC1 on June 23, which explains the low $P_{\theta,z}$. Around 13h00 the inversion height increases which can be deduced from the decrease of $P_{\theta,z}$ at EC2. During a few runs around 15h00 $P_{\theta,z}$ becomes negative due to a counter-gradient sensible heat flux. At EC3, $P_{\theta,z}$ is small compared to $A_{\theta,x}$ until 16h00.

Although this gives an incomplete picture of the temperature variance budget, since it is not attempted to estimate $T_{\theta,z}$ and N_θ, it at least shows how variable the conditions in the IBL can be. The magnitude of $A_{\theta,x}$ and $P_{\theta,z}$ depends on the terrain conditions, the time of day and the

location in the IBL. The contribution of $A_{\theta,x}$ is often at least as large as $P_{\theta,z}$, certainly close to the advective inversion, which may explain why local scaling does not work for temperature variance most of the time. The advected and entrained portion of temperature variance is probably responsible for the relatively large value of φ_θ (Fig.6.14b).

The local scaling hypothesis can also be tested using the model. The flux-variance parameters φ_θ and φ_q, as calculated by the model, are given as functions of ζ_l, also calculated from the model, in Fig.6.18.
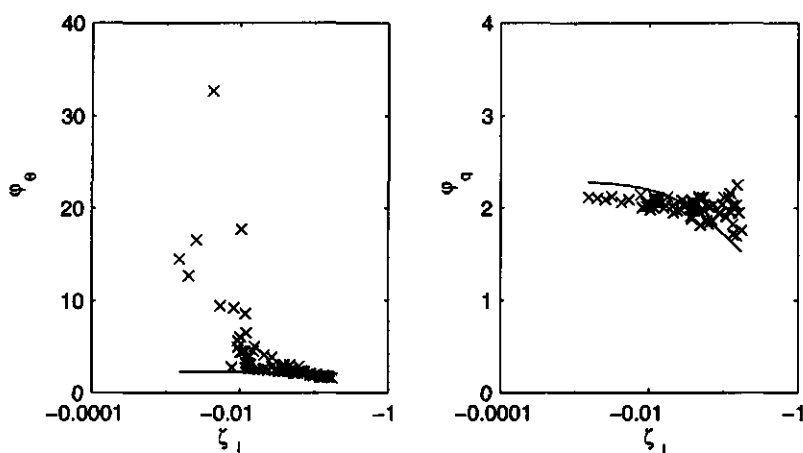
Fig.6.18 Local similarity tested with the second-order model. Left panel: φ_θ, right panel: φ_q. The symbols are the modelling results for the locations EC1, EC2 and EC3 (27 runs). The drawn line is the MO-relation Eq.4.7.

The results of the model agree reasonably with the measurements, as can be seen by comparing Fig.6.14 and Fig.6.18. The model also indicates that local scaling seems to work reasonably well for water vapour but φ_θ is much too high for values of ζ_l close to zero. The behaviour in the local free convective limit for cannot be reproduced with the model in its present form as was already explained in section 6.1.1. Nonetheless, the model results at $\zeta = -0.2$ also seem to agree with the measurements in that less scatter is found for φ_θ than for φ_q.

The observed and calculated differences between φ_θ and φ_q must be accompanied by low values of $R_{\theta q}$. After the step-change it can be expected that $R_{\theta q}$ is a function of the location in the IBL. The measured and modelled $R_{\theta q}$ are compared in Fig.6.19.
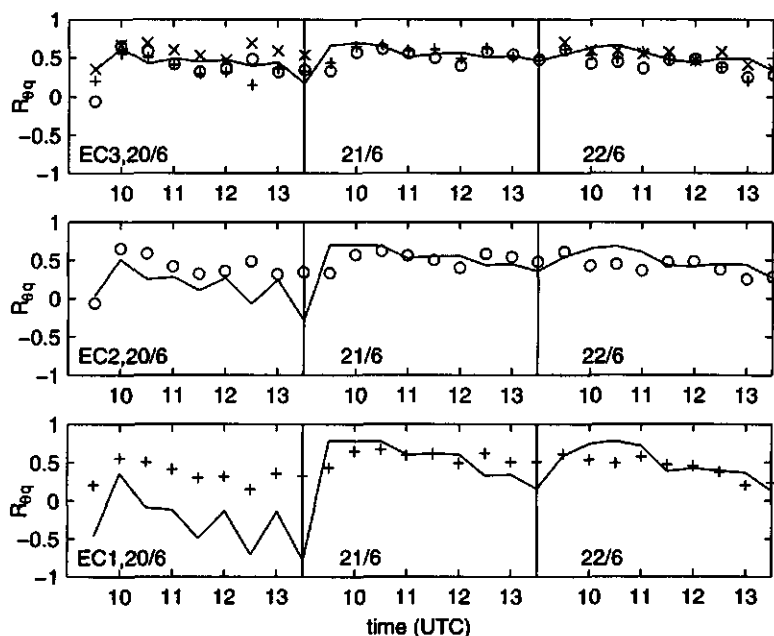
Fig.6.19 The correlation between temperature and humidity fluctuations at EC3 ('x'), EC2 ('o') and EC1 ('+')
(top to bottom). In the upper panel the measured values of all three stations are plotted for reference
(note that the measured R_{θ_q} at EC3 is not available on June 21). The drawn line is for the model results.

The upper panel gives the modelling results for EC3 and the measured R_{θ_q} at EC1 to EC3.

The lower two panels give the calculated and the measured results for EC2 and EC1. The course of R_{θ_q} with height clearly depends on the 'advective state' of the IBL. On June 20 the model predicts a large increase with height of R_{θ_q} because it changes sign that day between EC1 and EC2. The measurements do not show the change of sign but an increase with height was observed. The modelling results and the measurements differ on June 20 because the surface resistances, used in the model, were underestimated for these runs for that day (see also section 6.1.2).

The model predicts that R_{θ_q} decreases with height until 12h00 on June 21 and June 22. The observed magnitude of R_{θ_q} is in agreement with the model for these days but the height dependence is not confirmed convincingly mainly because the differences are too small to be resolved by the measurements.

The low $R_{\theta q}$ also implies that the transfer efficiencies of temperature and water vapour are not equal. The ratio $R_{w\theta}/R_{wq}$, is given in Fig.6.20 using the same format as for Fig.6.19.
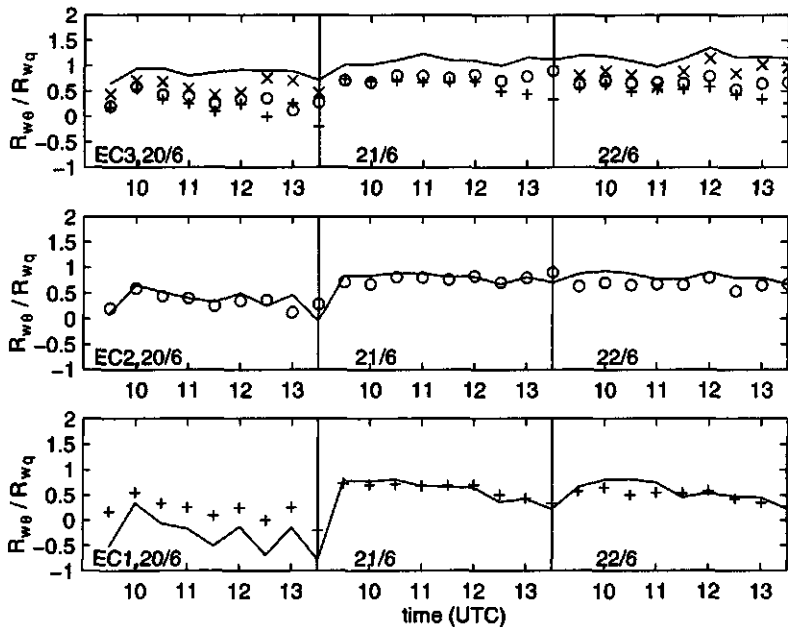
Fig.6.20 The observed ratio of the transfer efficiencies for EC1 ('+'), EC2 ('o'), and EC3 ('x') on June 20 to June 22 compared with the model (drawn line).

In this case there is a rather good agreement between model and experiment, except for the results at EC3 where the model gives ratios higher than unity whereas from the measurements value below unity are found (except for 2 runs on June 22). The results for EC1 on June 20 are not so good, for reasons given earlier when the results for $R_{\theta q}$ were discussed. Finally, it is noted that the results are consistent with the results in Fig.6.14 since $R_{w\theta}/R_{wq} = \varphi_q/\varphi_\theta$.

It is found from the measurements that R_{wq} is larger than $R_{w\theta}$ in the IBL up to EC3 for this experiment. At EC1 and EC2, $R_{w\theta}/R_{wq}$ is always below unity, both for the model results and the measurements. The model gives higher values than measured at EC3 and also higher than unity on some occasions. As already said, the model assumes equal transfer efficiencies at the upper and lower boundary. These findings (both modelling and measurements),

together with the upwind measuring results, seem to indicate that this is certainly wrong for the upper boundary. Based on the data from this experiment, such a firm conclusion cannot be drawn for the lower boundary.

6.4 Flux-profile relations of wind, temperature and water vapour

In this section the flux-profile relations of wind, temperature and water vapour are studied in terms of ϕ-relations (Eq.2.9) and eddy diffusivities (Eq.2.31). The profile data of P3 and the turbulence measurements of EC1, EC2 and EC3 were used for the calculations in this section.

The behaviour of ϕ_m over the downwind terrain as a function of ζ_l and z/δ is presented in section 6.4.1, where the turbulent Prandtl number K_m/K_θ and the turbulent Schmidt number K_m/K_q are also given. These ratios are expected to be a measure of the relative height of the IBL for water vapour, δ_q, and temperature, δ_θ, compared to the IBL for momentum, δ (Kaimal and Finnigan, 1994),

$$\frac{\delta}{\delta_c} = \left(\frac{K_m}{K_c} \right)^{0.8} \qquad 6.5$$

assuming that δ and δ_c are smaller than the height of the ASL.

The behaviour of K_θ and K_q after the step-change is given in section 6.4.2. The magnitude and behaviour of

$$\frac{K_\theta}{K_q} = \frac{\phi_q}{\phi_\theta} \qquad 6.6$$

is important for the applicability of the Bowen ratio method (Dugas *et al.*, 1991) as was also explained in section 2.6.

6.4.1 Non-dimensional wind speed and the turbulent Prandtl and Schmidt numbers

The turbulent Prandtl number is

$$\Pr_t = \frac{K_m}{K_\theta} \qquad\qquad\qquad 6.7$$

and the turbulent Schmidt number is defined as

$$Sc_t = \frac{K_m}{K_q} \qquad\qquad\qquad 6.8$$

where K_m is the eddy diffusivity for momentum.

The eddy diffusivities were calculated from the measurements at the three locations of EC1 to EC3. It appeared that consistent results for K_θ and K_q could only be obtained for runs with a temperature difference between two levels larger than 0.1 K and for water vapour differences above 0.3 gm^{-3}. Furthermore a minimum absolute value of the sensible heat flux of 10 Wm^{-2} was required. With these constraints, 32 out of the 81 runs could be used in the analysis. The gradients at EC1, EC2 and EC3 are calculated using the logarithmic finite difference form used before (Eq.4.5) from the measurements at two heights with geometric heights of 4.3, 6 and 12 m which are sufficiently close to the measuring heights of the fluxes. These calculations were then repeated, to check the results, using a quadratic fit through all profile measurements. The derivative of this quadratic function was then used to calculate the gradient at each height. This gave results very similar to those obtained using the finite difference approach.

The behaviour of ϕ_m is considered first. After a simple smooth-to-rough step-change under near neutral conditions it is expected that ϕ_m is large compared to its homogeneous value (Wyngaard, 1982). And indeed, model calculations for neutral conditions (Rao et al., 1974a) showed the largest deviation of ϕ_m from its homogeneous value around $z/\delta = 0.25$. The non-dimensional height of this maximum decreases with the strength of the step-change. Here, $\phi_m/\phi_{m,MO}$ is given (Fig.6.21) where $\phi_{m,MO}$ is calculated using Eq.2.10 and the observed ζ_i.
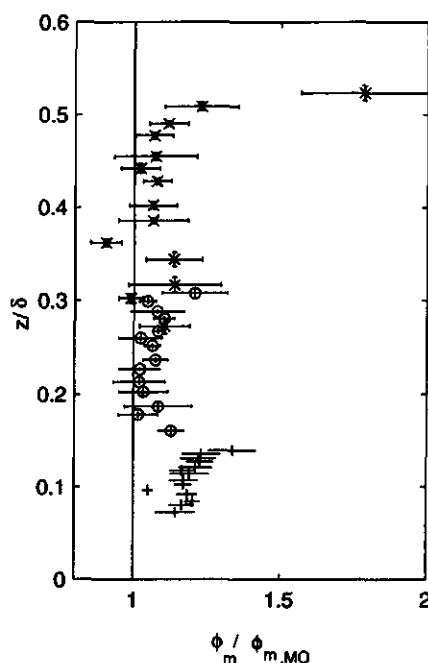
Fig.6.21 The normalized ϕ_m after the step-change, $\phi_m/\phi_{m,MO}$, as a function of z/δ. The horizontal error bars indicate the interquartile range for ϕ_m and the vertical bars give the interquartile range for z/δ (symbols in the middle of the error bars: '+':EC1, 'o':EC2, 'x':EC3).

The non-dimensional wind speed after the step-change shows a peak around 0.15 which is consistent with the fact that the roughness step-change is weak compared to the roughness step-change studied in Rao *et al.* (1974a). It is also found that ϕ_m is somewhat too high in the whole IBL. The deviation from local scaling towards the top of the IBL is in conformity with the findings over the upwind terrain where deviating behaviour was also found for large values of ζ. One could conclude that local scaling does not work for $z/\delta < 0.2$ down to at least $z/\delta = 0.05$, i.e. when $z/x \approx 0.009$.

Next, Sc_t and Pr_t are given in Fig.6.22.
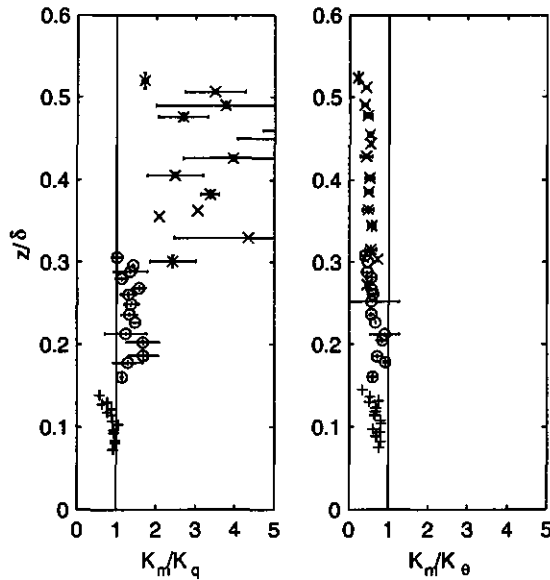
Fig.6.22 The turbulent Schmidt number (left panel) and the turbulent Prandtl number in the IBL ('x':$z = 13$ m, 'o': $z=6.7$ m, '+':$z = 4.1$ m at P3).

For all z/δ Pr_t is below unity (≈ 0.6) and decreases with z/δ for $z/\delta > 0.2$. The turbulent Schmidt number is below unity around $z/\delta = 0.1$, it increases rather drastically with z/δ for $z/\delta > 0.15$, and it is always larger than Pr_t.

Because of the large variation of the ratios given in Fig.6.22, it is not possible to apply Eq.6.5 in an objective way to estimate IBL heights. Nonetheless, it seems that $\delta_q < \delta$ because $Sc_t > 1$ in the largest part of the IBL whereas the opposite can be concluded for temperature which is also consistent with the result presented in Fig.6.13.

Only the results from the measurements were used in this section because the wind profiles and the friction velocities, calculated using the model, did not agree favourably with the measured profiles and friction velocities (sections 6.1.2 and 6.1.3).

6.4.2 The ratio of the eddy diffusivities for heat and water vapour

Here, the dependence of K_θ/K_q on the location in the IBL is considered. It is assumed that both modelling results and experimental data can be used since it was shown that temperature and humidity profiles and the fluxes of latent and sensible heat compared favourably. The ratio K_θ/K_q and

$$\frac{K_s}{K_{s,MO}} = \frac{\phi_{s,MO}}{\phi_s} \qquad\qquad 6.9$$

for $s = \theta, q$, where the subscript 'MO' indicates (local) scaling behaviour according the modified MO-theory, are given as a function of z/δ in Fig.6.23.
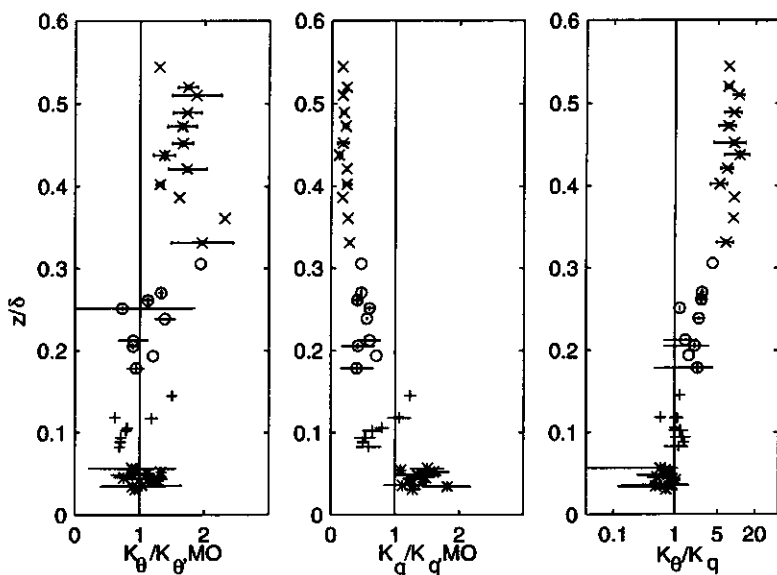
Fig.6.23 *Measuring results of the eddy diffusivities of temperature and water vapour as a function of* z/δ. *('*': using the calculated surface flux and the measured gradient at* $z=1.5$ m; '+': $z=4.1$ m; 'o': $z=6.7$ m; 'x': $z=13$ m at P3).

Again, $\phi_{s,MO}$ was calculated using ζ_l and Eq.2.10. Using the calculated surface fluxes and the measured gradient at $z = 1.5$ m (approximately in agreement with $z/x = 0.008$, the estimated height of the IAL at P3, see section 5.2), the eddy diffusivities close to the surface were also calculated.

Although a little more detail would have been desirable, the result is interesting. The deviation from local scaling seems to increase with z/δ and in opposite directions for temperature and water vapour due to which K_θ/K_q increases with z/δ. Below $z/\delta = 0.2$, it is uncertain what exactly happens with temperature and humidity separately, however, the ratio K_θ/K_q seems to be below unity for $z/\delta < 0.1$. So, the ratio K_θ/K_q is very sensitive to the location in the IBL (note the logarithmic x-axis in most left panel). According to the measurements, the ratio can be below unity whereas higher in the IBL it is above unity. The result is furthermore consistent with the increase with height of the ratio of the transfer efficiencies as discussed in 6.3.

With the model it is possible to study K_θ/K_q for different individual cases. The calculated ratio of the eddy diffusivities for a run where the temperature profiles showed a strong advective inversion (June 20, 11h00) and for a run (June 22, 11h00) where this was not the case are given in Fig.6.24.
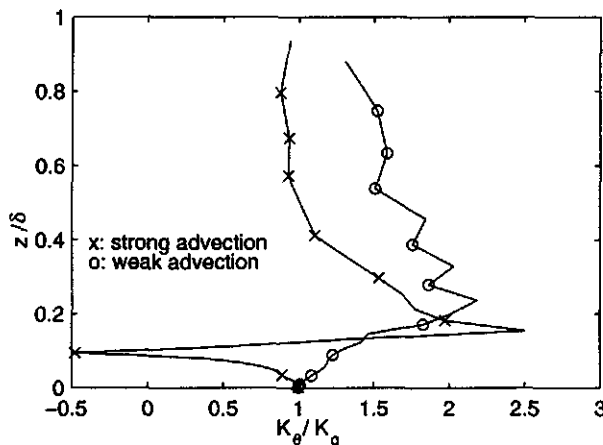
Fig.6.24 Modelled ratio of the eddy diffusivities of temperature and water vapour for a run with strong advection and a run with weak advection.

For the stronger advective case, K_θ/K_q is found to be below unity below the inversion, and above unity above the inversion. The return to unity may be an artefact of the model. There are strong indications that K_θ is larger than K_q over the upwind terrain. In fact, a typical value for K_θ/K_q over the upwind terrain can be estimated by inserting Eq.4.7 in Eq.2.41 and, as before, replacing the value of 2.3 in Eq.4.7 with 5 for φ_q based on the results presented in Fig.4.7. This gives a value of 4.7 for K_θ/K_q, which is close to the value found in the mid-IBL after the step-change. For the case when there is weak advection, the model predicts that $K_\theta > K_q$ for the whole IBL.

The results discussed here, only serve to demonstrate that K_θ/K_q is a function of z/δ and the magnitude and sign of the sensible heat flux. What that function looks like and whether some universal function can be found remains to be seen and is outside the scope of this study. The results also indicate that the ratio K_θ/K_q changes drastically close to the surface where the Bowen ratio measurements usually are carried out.

7 THE APPLICABILITY OF BOWEN RATIO METHODS ABOVE INHOMOGENEOUS TERRAIN

The use of micro-meteorological methods to determine the surface fluxes in the IBL may lead to erroneous results. Kroon (1985) found small differences between the fluxes in the constant flux layer as calculated with the model and the fluxes obtained using the BREB method (section 1.1) on profiles generated by the model. However, several questions remained to be answered because the analysis was performed for one run only and the model gave extremely high surface fluxes. The version of the model which was used to test the flux-profile methods above inhomogeneous terrain assumed a 100% relative humidity at the lower boundary. With the present version of the model, the surface fluxes are calculated using the Penman-Monteith approach at a fixed surface resistance (section 2.5, also: Kroon, 1985, Kroon and De Bruin, 1993).

The present model will be used to calculate the difference between the flux densities derived from three micro-meteorological methods and the surface flux densities $\lambda E_s = \lambda E(0,x)$ and $H_s = H(0,x)$ under conditions of local advection. The model will be used to calculate the surface fluxes directly. These results are then compared with the surfaces fluxes obtained from the application of the mean gradient Bowen ratio and the standard deviation Bowen ratio on temperature and humidity profiles generated with the model. To perform the various calculations for the analysis presented here, it is assumed that the surface fluxes calculated by the model are the actual surface fluxes. It cannot be established whether this is a correct assumption because the surface fluxes were not measured. The only justification is, that the surface latent heat fluxes derived from the measurements with the method given in section 5.2 are almost equal to those calculated by the model: the surface latent heat flux derived from the measurements was, on average, 0.96 ± 0.09 times the surface latent heat flux as calculated with the model.

The three methods to determine the surface latent heat flux to be evaluated are:

- The eddy correlation method. With this method, $\overline{w\theta}$ and $\overline{wq}$ are obtained directly from the measurements at the height of the measurement from which the energy fluxes can be calculated using Eqs.2.2 and 2.3. This method also gives a direct measure of the Bowen ratio $\beta(z,x)$.

- The BREB method using β_g (Eq.2.32) and referred to as the gradient method. The gradient of temperature and humidity is measured using two levels. It is assumed that $K_\theta = K_q$ (section 2.6). Using Eqs.1.1, 1.2 and 2.29, and the available energy A, the latent heat flux λE_g can be obtained from

$$\lambda E_g = \frac{A}{1 + \beta_g} \qquad\qquad 7.1$$

- The BREB method using β_σ (Eq.2.34), referred to as the standard deviation method. Both σ_θ and σ_q need to be measured and it is assumed that $R_{w\theta} = R_{wq}$ (section 2.6). Analogous to Eq.7.1 it follows that

$$\lambda E_\sigma = \frac{A}{1 + \beta_\sigma} \qquad\qquad 7.2$$

In section 7.1 the eddy correlation method will be treated and the IAL height is determined. The gradient method is considered in section 7.2, and the confusion concerning the findings in the experiments mentioned in section 1.3, is also discussed here. Finally, in section 7.3, the standard deviation method is evaluated.

The first 27 runs (the day-time runs from June 20, 21 and 22) given in A4.1 are used as input for the evaluation. For each model run, the relevant quantities are available at 6 different distances from the step-change and at 41 different model levels thus providing a large range for z/x. Selections can be made depending on the method to be tested.

The difference between the latent heat flux that is obtained using the Bowen ratio method and the surface latent heat flux

$$\lambda E_s = \frac{A}{1 + \beta_s} \qquad\qquad 7.3$$

is defined as the fractional difference,

$$\frac{\lambda E}{\lambda E_s} = \frac{1 + \beta_s}{1 + \beta} \qquad\qquad 7.4$$

There are two error sources due to local advection when measuring at height z: the latent heat flux at some height above the surface is different from the surface latent heat flux (and for the cases studied here), and when the indirect methods are used to determine the Bowen ratio, like the gradient method or the standard deviation method a further error may be due to the inequality of the eddy diffusivities and transfer efficiencies for heat and water vapour.

The fractional difference for the latent heat flux using the eddy correlation method simply reads

$$\frac{\lambda E(z,x)}{\lambda E_s} = \frac{1+\beta_s}{1+\beta(z,x)}. \qquad 7.5$$

For the BREB method, when β_g is used, Eq.7.4 can be rewritten as

$$\frac{\lambda E_g}{\lambda E_s} = \frac{1+\beta_s}{1+\beta(z,x)/I_K} \qquad 7.6$$

in which

$$I_K = \frac{\beta(z,x)}{\beta_g} = \frac{\overline{w\theta}}{\overline{wq}}\frac{\partial \overline{Q}/\partial z}{\partial \Theta/\partial z} = \frac{K_\theta}{K_q} \qquad 7.7$$

following from Eqs.1.2, 2.31 and 2.32. Hence, a part of the error is because $\beta(z,x) \neq \beta_s$ and the other part is due to the inequality $\beta(z,x) \neq \beta_g$.

For the case when β_σ is used, Eq.7.4 can be rewritten as

$$\frac{\lambda E_\sigma}{\lambda E_s} = \frac{1+\beta_s}{1+\beta(x,z)/I_R} \qquad 7.8$$

where

$$I_R = \frac{\beta(z,x)}{\beta_\sigma} = \left|\frac{R_{w\theta}}{R_{wq}}\right| \qquad 7.9$$

which follows from Eqs.1.2, 2.33 and 2.34. Similar to Eqs.7.6 and 7.7, part of the error is caused by the fact that $\beta(z,x) \neq \beta_s$, and the other part stems from the inequality $\beta(z,x) \neq \beta_\sigma$ or $|R_{w\theta}| \neq |R_{wq}|$.

7.1 The error in λE_s due to the difference between $\beta(z,x)$ and β_s

The actual fluxes at height z can be observed using eddy correlation measurements. The flux divergence (due to which the Bowen ratio also varies with height even if $H + \lambda E$ is constant with height) is the only error source when the eddy correlation method is applied.

For the dry/warm to wet/cool step-change and when the surface sensible heat flux is positive $|\beta_{(z,x)}| > |\beta_s|$ because $0 < H(0,x) < H(z,x)$ and $\lambda E(0,x) > \lambda E(z,x) > 0$. For a sensible heat flux directed towards the surface $|\beta_{(z,x)}| < |\beta_s|$ because $H(0,x) < H(z,x) < 0$ and $\lambda E(0,x) > \lambda E(z,x) > 0$. It is then assumed in both cases that $\beta(z,x)$ and β_s are both positive or both negative. The height-to-fetch ratio where the fluxes of sensible heat and latent heat are within 10 % of the surface fluxes defines the IAL height in accordance with the definition given in section 1.1. This height, h_{ial}, is given in Fig.7.1 both for latent heat and sensible heat.
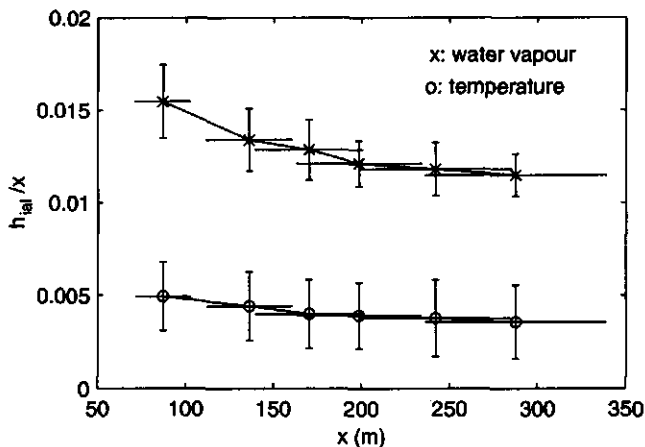
Fig.7.1 *The height where the fluxes after a dry-to-wet step-change are within 10% of the surface fluxes as a function of z/x. The median value for 6 locations over 27 runs after the step-change is given together with the interquartile ranges of z/x and h_{ial}/x.*

The IAL for the latent heat flux is thicker than for sensible heat because $d\lambda E/dz \approx -dH/dz$ and $\lambda E_s > |H_s|$ for the cases studied here (with a range of downwind surface Bowen ratios between -0.6 and 0.3). In order to be in the IAL, as defined above, and for both fluxes, z/x must be below 0.005. This is a rather low value compared to the commonly used value of

0.01, and for most applications for which the latent heat flux is needed, this may be a somewhat too rigid demand. A definition for IAL height based on the fractional difference should therefore specifically mention which quantity is considered and to what extent it is allowed to differ from unity. A further restriction used here is that the IAL should not be thicker than the height of the advective inversion (if present) since it was assumed that $0 < H(0,x) < H(z,x)$ or $H(0,x) < H(z,x) < 0$.

7.2 The error in λE_s due to the difference between β_g and β_s

The BREB-gradient method is applied to calculate the surface flux. The gradients of temperature and water vapour were calculated as the finite differences from the temperatures and humidities calculated by the model at $z = 1$ and 2 m to simulate a 'normal' field experiment at 6 locations and 27 runs thus providing a sufficiently large range for z/x. The ratio $\lambda E_g/\lambda E_s$, as a function of z/x, is given in Fig.7.2 where 20 out of 27 runs were used: 10 runs for which both β_g and β_s are positive and 10 runs for which these Bowen ratios are negative. Runs for which β_g and β_s had different signs were excluded (7 runs).
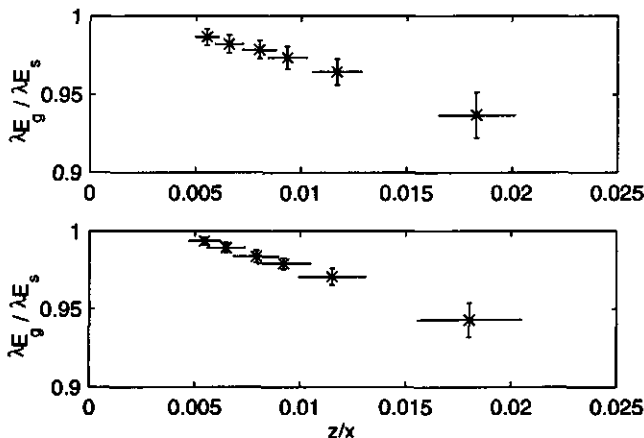
Fig.7.2 The ratio of λE_g and λE_s (Eq.7.5). The bars indicate the interquartile ranges with the median in between. The upper panel gives the result for all runs where both β_s and β_g were negative (10 runs), the lower panel is for positive β_s and β_g (10 runs).

From Fig.7.2 it appears that λE_g does not differ much from λE_s and the difference is about equal for positive and negative Bowen ratios. In both cases the surface latent heat flux is underestimated. This is, at first sight, a remarkable result, since K_θ/K_q may deviate considerably from unity as is shown in Fig.7.3 where $K_\theta/K_q = \beta(z,x)/\beta_g$, calculated using Eq.7.7, is plotted ('x' symbols). The behaviour of β_s/β_g is also plotted (Fig.7.3, 'o' symbols). Two different plots are given for the cases when both β_g and β_s are negative (upper panel) and when they are positive (lower panel)

Fig.7.3 β_{ref}/β_g as a function of z/x where $\beta_{ref} = \beta_s$ for the 'o'-symbols and $\beta_{ref} = \beta(z,x)$ for the 'x'-symbols which then represent I_K. For further information see Fig.7.2.

Now, the reason why $\lambda E_g/\lambda E_s \approx 1$ can be understood from Eq.7.5 which shows that this is the case because $I_K > 1$ when $|\beta_s| < |\beta(z,x)|$ and $I_K < 1$ when $|\beta_s| > |\beta(z,x)|$ thus partly compensating for the difference between β_s and $\beta(z,x)$.

Note that for this case, when $\beta_s/\beta_g > 1$, $K_\theta/K_q < 1$ and when $\beta_s/\beta_g < 1$, $K_\theta/K_q > 1$. This could be considered as a rather trivial result, if it had not caused some confusion about the behaviour of K_θ/K_q after two earlier experiments (section 1.3). Measurements over an irrigated rice crop near Griffith, Australia (Lang et al., 1983a) of β_g and $\beta(z,x)$, the latter measured with eddy correlation apparatus, were performed after a dry to wet step-change at $z/x \approx 0.005$ with an upwind Bowen ratio of typically 17 and a negative Bowen ratio down-

wind. It was found that $K_\theta < K_q$. On the other hand, from an earlier experiment over well-watered alfalfa near Nebraska, USA, it was concluded that $K_\theta > K_q$ (Verma *et al.*, 1978), also in a stable IBL at $z/x \approx 0.008$. However, Verma *et al.* used lysimeters to measure λE_s and they calculated H_s using $A - \lambda E_s$. Next, they presented the ratio β_s/β_g as K_θ/K_q. This may explain the difference between the experimental results of Lang *et al.*, (1983a) and Verma *et al.* (1978). Although this difference was not noticed until now, Lang *et al.* analyzed K_θ/K_q whereas Verma *et al.* analyzed β_s/β_g. Further proof for this hypothesis can also be found in Verma *et al.* (1978) as they observed that $\lambda E_g < \lambda E_s$ which is consistent with Fig.7.2. The observed fractional difference was typically 80% which is worse than predicted here by the model for the Crau experiment but this depends probably on the different conditions in Nebraska where temperature profiles showed inversions up to at least 10 m.

7.3 The error in λE_s due to the difference between β_σ and β_s

The latent heat flux can also be calculated using the Bowen ratio from the standard deviations of temperature and water vapour, β_σ. The difference between $\beta(z,x)$ and β_s is caused by the flux divergence in the IBL and because $R_{w\theta} \neq R_{wq}$. The ratio $\lambda E_\sigma/\lambda E_s$ is given in Fig.7.4 as a function of z/x where again separate plots are given for negative and positive Bowen ratios.
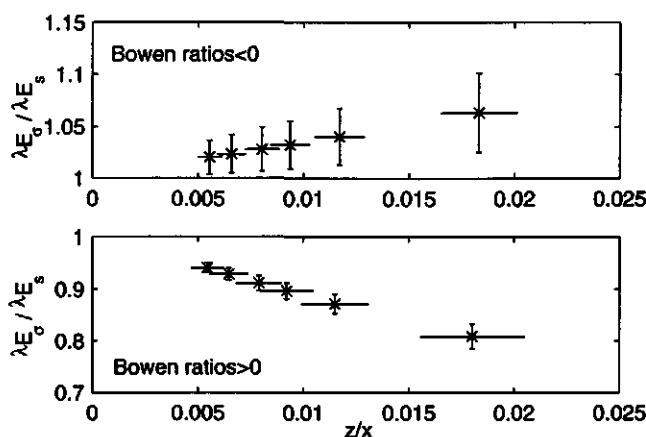
Fig.7.4 The ratio of λE_σ and λE_s (Eq.7.8). (for further information see Fig.7.2).

For negative Bowen ratios in the IAL (upper panel, Fig.7.4), this method performs as good as the gradient method although $\lambda E_\sigma > \lambda E_s$ whereas with the gradient method λE_s was underestimated for this case.

For positive Bowen ratios, the difference between λE_σ and λE_s is much larger than was found for the similar case with β_g. The error for this case (lower panel, Fig.7.4) increases faster with z/x than for the negative Bowen ratios because $I_R = \beta(z,x)/\beta_\sigma$ is always less than unity (Fig.7.5, 'x' symbols) thus amplifying the error when $\beta(z,x) > \beta_s > 0$. Moreover, I_R is smaller when the Bowen ratios are positive as can also be seen in Fig.7.5.
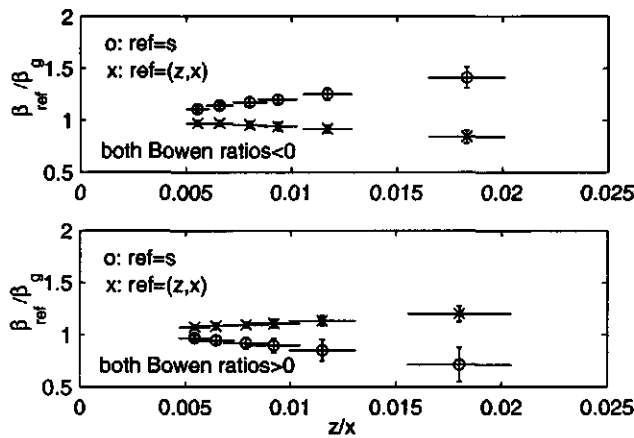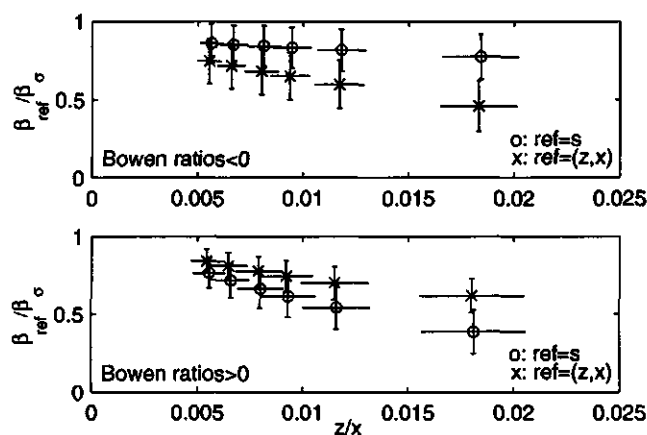

Fig.7.5 β_{ref}/β_σ as a function of z/x where $\beta_{ref} = \beta_s$ for the 'o'-symbols and $\beta_{ref} = \beta_{(z,x)}$ for the 'x'-symbols (I_R) (for further information see also Fig.7.2).

7.4 Concluding remarks

With the eddy correlation method λE_s can be estimated to within 10% for $z/x < 0.01$. A similar accuracy for the sensible heat flux requires measurements at $z/x \leq 0.005$. The requirement of low measuring levels for the eddy correlation equipment is conflicting with the demand that the instruments should be installed sufficiently high above the surface in order to prevent high frequency losses (section 3.5.4, appendix A2).

The results in Fig.7.2 show that the BREB-gradient method can be used for $z/x \leq 0.03$ if an error of 10% in the surface latent heat flux is acceptable. An explanation for this remarkable result is that the difference between the Bowen ratio at the surface and at some level above the surface is compensated for by the difference of the eddy diffusivities at the height where the gradient is measured. For the BREB-standard deviation method this is also the case for the stable IAL (Fig.7.4). For the unstable IAL z/x should be below 0.008 to achieve the same accuracy because the ratio of the transfer efficiencies amplifies the effect of the difference between β_s and $\beta(z,x)$ under these conditions.

The evaluation of the eddy correlation method and the two different Bowen ratio methods was performed using a model which still has a number of shortcomings. A first step would be to repeat the calculations using the newest version of the model where the downwind surface resistance is calculated at the lower boundary instead of using a fixed value.

These results are based on a limited number of cases where the upwind Bowen ratio varied between 1 and 7 and the downwind Bowen ratio between -0.2 and 0.5 (according to the model). Furthermore, conditions were such that the upwind available energy was below the downwind energy which is not always the case (Lang *et al.*, 1983a). It should therefore be strongly emphasized that many more cases should be studied and that general conclusions can not be drawn. For the cases studied here, a number of factors may have cooperated in a favourable manner due to which the error sources cancel out. However, it is significant to note that the model can be used to forecast which conditions are favourable and which are not for the application of micro-meteorological methods to determine the surface fluxes under conditions of local advection.

The analysis in this Chapter also helped to understand the apparently conflicting results of Lang *et al.* (1983a) and Verma *et al.* (1978) concerning the ratio $K_\theta/K_q = \beta(z,x)/\beta_g$. It is postulated here that in both experiments $K_\theta/K_q < 1$ were it not that Verma *et al.* did not measure this ratio. They measured β_s/β_g which can be greater than one already close to the surface in the stable 'IAL' in which $K_\theta/K_q < 1$.

8 SUMMARY AND CONCLUSIONS

The horizontal transport or advection of air from one surface type to another influences the turbulence structure of the Atmosferic Surface Layer (ASL), the lowest 10% of the Planetary Boundary Layer (PBL). Close to the leading edge of a terrain change, the air is not adapted to the underlying surface and simple methods to determine the surface fluxes are no longer valid. This study dealt specifically with a step-change from a dry and almost bare surface to irrigated grass. We concentrated on the transfer mechanisms of heat and water vapour. The layer in which the influence of the new terrain properties is already felt is referred to as the Internal Boundary Layer (IBL), part of which is adapted to the new surface, the Internal Adapted Layer (IAL). In this study **local** advection was considered, i.e. when IBL height is less than ASL height which is approximately the case for fetches less than 1 km.

8.1 Objectives

It was pointed out in Chapter 1 that, because of seemingly contradicting conclusions in earlier studies and because of shortcomings of the models used to simulate the flow in the IBL, further research was needed. A second-order closure model to study local advection was available but there were not enough reliable data to verify the model. In Chapter 1 the goals of this study were formulated:

- to collect a data-set from a micro-meteorological experiment to verify the model
- to improve our understanding of the transfer mechanisms of heat and water vapour under conditions of local advection in order to be able to predict how these transfer mechanisms differ from the homogeneous situation.

Also in Chapter 1, the resistance approach (the Penman-Monteith model) to air-surface exchange of heat and water vapour was used to describe the conditions during which local advection is important. The sign of the Bowen ratio in the IAL uniquely depends on $r_a + r_s - r_i$, respectively the aerodynamic resistance, the surface resistance and the isothermal resistance. Advection becomes more important as r_i becomes larger than $r_a + r_s$. It was also indicated that several feedback processes can be important, but they were not specifically dealt with in this study.

8.2 Theory

In Chapter 2 the theoretical background was given. The formulation for the height of the neutral IBL was discussed. This height δ depends on fetch and the downwind surface roughness. Next, the model to be tested was introduced. It uses second-order closure to solve the flow equations. It first (the one-dimensional module) is used to calculate the equilibrium conditions over the upwind terrain assuming Monin-Obukhov (MO) conditions at the boundaries. The MO relations represent the structure of the flow in the Atmosferic Surface Layer (ASL) as a function of thermal stability. Next, the model calculates the flow after the step-change. An important feature of this model is that it uses the Penman-Monteith equation at the lower surface with a constant surface resistance to calculate the latent heat flux.

The transfer mechanisms of heat and water vapour were described using the flux-profile relations and the flux-variance relations. It was shown that, for homogeneous conditions, these relations are closely connected and an explicit relation was derived between the dimensionless standard deviations of wind, concentration (temperature or humidity) and the dimensionless vertical gradient of the mean concentration. The result agreed well with the measured MO relations. This result could be obtained because the standard deviation of vertical wind was used as the velocity scale for the ASL instead of the friction velocity.

8.3 The Crau experiment

In Chapter 3 the experiment that was carrried out in June 1987 in La Crau, France was described. Around an abrupt change from a dry and almost bare terrain to irrigated grass mean vertical profiles and eddy correlation measurements as well as many other measurements were collected. From the data set 81 day-time runs were selected, all from the period June 20 to June 24 when local advective conditions prevailed.

The wind speed was typically 7 ms^{-1} at $z = 3$ m from directions between 330° and 360°, i.e at angle between 20° and 50° with the leading edge. For the analysis, the flow was considered to be two-dimensional and fetch was calculated as a function of wind direction. The Obukhov length over the upwind terrain varied between -9 (very unstable temperature stratification) and -470 m (neutral stratification). The upwind temperature at $z = 3$ m was

typically 1 K above the temperature at the same height, 300 m downwind of the step-change. The downwind surface temperature was 10 K below the upwind surface temperature. The upwind surface Bowen ratio was between 1 (June 20, one day after rain) and 8 (two days later). Over the downwind terrain the Bowen ratio varied strongly with the height to fetch ratio z/x but it was typically between 1.2 at $z/x = 0.06$ and 0.1 at $z/x = 0.01$. We found that the wet terrain had 56 Wm^{-2} more available energy from radiation which is 14% of the average downwind available energy. Net radiation and soil heat flux each contributed 50% to this difference. The difference in available energy had a daily course with two maxima because of two maxima, one in the morning and in the afternoon, for the difference between the up- and downwind soil heat fluxes.

8.4 The upwind flux-profile and flux-variance relations

In Chapter 4, the observed flux-profile and flux-variance relations over the dry terrain were compared with the Monin Obukhov (MO) relations. Furthermore, the data were used to compile initial and boundary conditions for the second-order closure model.

Temperature appeared to behave in accordance with the MO-theory, but deviations were found for wind and water vapour. The wind field was disturbed, probably because the upwind terrain was relatively smooth compared to the regional average. This could be concluded because a local measure for the surface roughness was smaller than a more regional value.

The transport of water vapour above the dry terrain was less efficient than the transport of sensible heat. Although the entrainment flux at the top of the PBL was not measured, the different efficiencies were attributed to the low ratio of the surface latent heat flux and the entrainment of latent heat at the top of the Planetary Boundary Layer (PBL). Indirect evidence for this was that the temperature-humidity correlation clearly increased with the surface flux of latent heat. This evidence was also supported by the so-called top-down bottom-up theory, used here to calculate temperature-humidity correlation.

8.5 The analysis of fetch dependent processes

In Chapter 5 it was pointed out that fetch variation depending on wind direction does not have a normal distribution whereas wind direction has. A special procedure for the analysis

of fetch dependent processes was proposed. Furthermore a vertical length scale δ, representing the height of the IBL under neutral conditions, proved useful to present fetch dependent data.

Using a simple criterium, runs with weak advection and strong advection were separated. The subdivision could be related, in a qualitative sense, with the behaviour of $r_a + r_s - r_i$ but not for all runs, probably because fetch varied to much.

8.5.1 The downwind surface fluxes of latent and sensible heat

It was shown that the sensible and latent heat fluxes in the IBL normalized with the upwind surface flux vary approximately linearly with z/δ within the measuring range covered by the data. The ratio of the down- and upwind sensible heat flux approaches unity at 0.7δ, the same ratio for the latent heat flux heat was found at 0.5δ. Based on this result it was decided to use a simple procedure to obtain an estimate for the downwind fluxes at the surface, approximately 200 m from the step-change. For each run the measured flux-height variation was used to calculate the flux at the top of the IAL, $h_{ial} = 0.008x$. The fluxes calculated this way were shown to compare favourably, at least for most runs, with the available energy at the surface both for weak and strong advective conditions.

8.5.2 The downwind friction velocity and surface roughness

The downwind friction velocity u_* was almost constant with height and was about 1.17 times the upwind u_{*}. The drag method was used to calculate the downwind surface roughness giving $z_o = 0.07$ m. A larger surface roughness would be found using the profile method. This means that the downwind terrain is relatively rough compared to the region in which it is embedded whereas the upwind terrain was found to be relatively smooth.

8.5.3 The downwind resistances r_s, r_i and r_a

The aerodynamic resistance r_a over the downwind terrain was always small compared to r_i and r_s. The isothermal resistance r_i was relatively high in the morning and the evening (200 sm^{-1}) and smaller (around 80 sm^{-1}) around midday. The surface resistance r_s was approximately 40 sm^{-1} in the morning and 70 sm^{-1} towards the evening. The surface

resistance was calculated from the surface latent heat flux and the saturation deficit between the surface and some reference height. It was also calculated using a simple parameterization based on plant-physiological characteristics of a short crop. It appeared that, after a correction depending on incoming short wave radiation, the simple parameterization performed satisfactorily.

8.6 Transfer mechanisms of heat and water vapour

In Chapter 6 the model was tested and also used, in combination with the measurements, to study the structure of the IBL.

8.6.1 Verification of the model

It was shown that the one-dimensional module of the model can only partly reproduce the Monin-Obukhov characteristics of the homogeneous surface layer. Good results are obtained for the flux-variance and the flux-profile relations of temperature and moisture. The MO flux-variance relations for the vertical and the longitudinal wind speed components could not be reproduced by the model, only for the lateral wind speed component reasonable agreement was found. However, the amount of TKE (Turbulent Kinetic Energy) is predicted well because vertical wind speed fluctuations are overestimated and longitudinal wind speed fluctuations are underestimated. The transfer efficiencies for water vapour and temperature are underestimated because vertical wind speed fluctuations are overestimated. The flux-profile relations calculated by the model are about equal for wind, temperature and water vapour. This means that the dimensionless vertical wind gradient decreases too fast with increasing thermal instability.

The comparison between the downwind measurements and the model started with the comparison of the measured and calculated mean vertical profiles. Because the above described problems grow worse with increasing instability only those runs could be used for which the upwind Obukhov length was below approximately -50 m. The measured profiles of temperature and humidity were reproduced by the model with good accuracy but the results depend on the choice of r_s. Although other input quantities may also be important, a different r_s has the largest effect on the redistribution of available energy between the latent heat and sensible heat flux. The calculated wind profiles did not compare too well with the

measured profiles. This could be expected since the model is not able to reproduce a proper flux-profile relation for wind under homogeneous conditions. The model also underestimates the horizontal wind speed fluctuations severely but gave reasonable results for the vertical wind speed fluctuations. The calculated and measured downwind fluxes compared satisfactorily. For the momentum flux after the step-change the model predicted a too large decrease with height. Finally, it was found that the measured statistics of the temperature and water vapour field could be reproduced by the model. The model compared well with the measurements although several feedback mechanisms were not incorporated in the model. For example, net radiation, surface resistance and soil heat flux should be calculated by the model because they might vary with fetch.

8.6.2 The structure of the IBL

The model and the measurements were used to unravel the structure of the IBL, mainly concentrating on the transfer mechanisms of heat and water vapour. It was expected that flow properties in the IBL depend both on thermal stratification and the position in the flow field. The relation with thermal stratification was studied using local Monin-Obukhov scaling. The difference with usual MO-scaling is that locally measured parameters are used instead of surface parameters.

The measured local scaling relation for the vertical wind speed fluctuations agreed with the MO-relation for the near neutral thermal stratification but increased too fast towards unstable conditions. It was postulated that the forced convective contribution to vertical wind speed fluctuations adapts quicker to the new conditions than the free convective contribution.

The measurements indicated that local scaling can be used for water vapour but not for temperature. Water vapour is transferred more efficiently than heat in the IBL after a dry to wet step-change. It was also found that the production of temperature fluctuations is at times small compared to horizontal advection of these fluctuations which makes it plausible that local scaling failed for temperature.

As expected for a smooth-to-rough step-change, it was found that the non-dimensional vertical gradient of mean wind speed was large compared to its homogeneous counterpart. The maximum deviation was found around $z/\delta = 0.15$.

The flux-gradient ratios or eddy diffusivities were estimated using the calculated surface fluxes and the gradients from the profile measurements. It was found that the flux-gradient ratio for heat was smaller than that for water vapour in the lower part of the IBL in agreement with the ratio of the transfer efficiencies. Higher up in the IBL and for less strong advective conditions it was found that the flux-gradient ratio for heat was larger than that for water vapour. The model was used to illustrate that the behaviour in the IBL of the ratio of the eddy diffusivities for heat and water vapour also depends on the importance of advection.

The experimental results could not be used to determine the IBL height directly because the measurements were too close to the surface or too far from the step-change. However, the relative magnitude of the eddy diffusivities of heat, water vapour and momentum can be used as indicators for the thickness of their IBL's. A measure for the relative magnitude of the eddy diffusivity for water vapour is the turbulent Schmidt number, and the turbulent Prandtl number for temperature. The turbulent Schmidt number was observed to be larger than 1 higher up in the IBL, and smaller than 1 in the lower part. The turbulent Prandtl number decreased from the surface to the top of the IBL and was always below one. In the lower part of the IBL it was larger than the turbulent Schmidt number. These results indicated that the IBL for heat is relatively thick, thicker than that of momentum, which on its turn is thicker than that of water vapour.

8.7 The Bowen ratio method applied in the IBL

In Chapter 7, the model was used to calculate the height of the IAL, defined as the height where the flux differs 10 % from its surface value. A thicker IAL was found for water vapour with a typical height-to-fetch ratio of 0.01 whereas for temperature the height of the IAL was found to be approximately 0.005 times x. So 'the IAL' does not exist and a clear definition must always be given since each quantity seems to have its own IAL.

The applicability of the Bowen ratio method to measure the surface fluxes in the IBL was also studied in Chapter 7, both for the unstable and stable IAL. The model was used to calculate both the surface flux directly and from the application of the mean gradient Bowen ratio and the standard deviation Bowen ratio on temperature and humidity profiles generated with the model.

The gradient Bowen ratio can be used at fetch-to-height ratios up to $z/x = 0.02$, both for the unstable and stable IAL if an error of 10% in the surface latent heat flux is acceptable. The explanation given for this high fetch-to-height ratio was that the difference between the Bowen ratio at the surface and at some level above the surface is compensated for by the ratio of the eddy diffusivities at the height where the gradient is measured. For the Bowen ratio from standard deviations the error in the stable IAL was found to be below 10%, up to $z/x = 0.02$ because the ratio of the transfer efficiencies is below unity which weakens the error due to the flux divergence. For the unstable IAL z/x must be below 0.008 to achieve the same accuracy because now the ratio of the transfer efficiencies amplifies the error. For the cases studied here, a number of factors may have cooperated in a favourable manner due to which the error sources cancel out. However, it is significant to note that the model can be used to forecast which conditions are favourable and which are not for the application of micro-meteorological methods to determine the surface fluxes under conditions of local advection.

It was also shown in Chapter 7 that, in order to determine the ratio of the eddy diffusivities of water vapour and heat, the fluxes must be measured at a height between the levels from which the vertical gradients are calculated. This requirement was not always fulfilled in earlier experiments which has caused considerable confusion.

9 SAMENVATTING

De energie afkomstig van de zon warmt onder meer het aardoppervlak op en vandaar uit ook de lucht via de zogenaamde voelbare warmteflux. Verder wordt een deel van de zonne-energie gebruikt voor de verdamping van eventueel aanwezig water. Het hangt van veel factoren af hoe de beschikbare energie verdeeld wordt tussen de voelbare warmteflux en de verdamping of latente warmteflux. De verhouding tussen deze fluxen is de Bowen-verhouding. Er zijn diverse methoden beschikbaar waarmee de Bowen-verhouding en de fluxen bepaald kunnen worden uit metingen van temperatuur, vochtgehalte en windsnelheid boven het aardoppervlak. Deze methoden berusten op de aanname dat er alleen verticale uitwisseling is van warmte omdat het aardoppervlak over grote afstand horizontaal en homogeen is. En dat is natuurlijk niet zo. In deze studie werd gekeken naar een ogenschijnlijk eenvoudige complicering: de uitwisseling van voelbare warmte en waterdamp tussen geïrrigeerd gras (het natte terrein) en de atmosfeer, in de nabijheid van kaal en droog terrein (het droge terrein).

Boven het droge terrein zal de lucht sterker opwarmen dan boven het natte terrein. We beschouwden alleen het geval waarbij de wind deze relatief warme lucht transporteert naar het natte terrein. Dit horizontale transport wordt advectie genoemd. Gezien het feit dat we alleen de processen bestuderen nabij de terreinovergang en omdat het natte terrein klein is ten opzichte van het droge terrein spreken we van lokale advectie. De gevolgen van deze vorm van advectie zijn alleen merkbaar in ongeveer de onderste 100 meter van onze atmosfeer, de Atmosferische Oppervlakte Laag (AOL). Van onderaf past de lucht zich aan aan het nieuwe oppervlak. De aangepaste laag na de overgang wordt de Intern Aangepaste Laag (IAL) genoemd. De laag daarboven, die ook nog eigenschappen van voor de terreinovergang vertoont, is de Interne GrensLaag (IGL). In het hier bestudeerde geval kan de aldus aangevoerde voelbare warmte gebruikt worden voor verdamping als de omstandigheden een neerwaartse warmtestroom toelaten. Het kan ook zo zijn dat de zijdelings aangevoerde voelbare warmte alleen de opwaartse warmtestroom vanaf het gras verhindert en aldus de verdamping indirect verhoogt.

Doel van dit onderzoek

In Hoofdstuk 1 werd uiteengezet dat een experiment nodig was vanwege eerdere tegenstrijdige resultaten ten aanzien van de turbulente structuur van de IGL. Verder ook nog omdat het beschikbare model waarmee de stroming in de IGL gesimuleerd kan worden tekortkomingen vertoonde en nog nooit vergeleken was met metingen. In Hoofdstuk 1 werden dan ook de volgende doelstellingen geformuleerd:

- Er moet een dataset komen om het bovengenoemde model te testen.

- Het verbeteren van het inzicht in de transportmechanismen van voelbare warmte en waterdamp tijdens lokale advectie.

Ook nog in Hoofdstuk 1 werd het Penman-Monteith-model gebruikt om te bepalen wanneer lokale advectie belangrijk is. In dit model worden de belangrijkste factoren die de voelbare en latente warmteflux bepalen vervat in een aantal weerstanden. Gedemonstreerd werd dat het teken van de Bowen-verhouding afhangt van het teken van $r_a + r_s - r_i$, respectievelijk de aerodynamische weerstand, de oppervlakteweerstand en de isotherme weerstand. Lokale advectie wordt belangrijker naarmate r_i groter is dan $r_a + r_s$. Dat is het geval tijdens winderig en bewolkt weer als droge en warme lucht over een oppervlak stroomt waar voldoende vocht beschikbaar is voor verdamping.

Theorie

In Hoofdstuk 2 werd de theoretische achtergrond van dit onderzoek besproken. Een formulering voor de hoogte van de IGL (δ) tijdens neutrale condities werd gegeven. Deze hangt af van de afstand tot de overgang en de ruwheid van het terrein. Vervolgens werd het model kort geïntroduceerd. Het betreft een model dat tweede-ordesluiting toepast om de stromingsvergelijkingen op te lossen. Het model berekent eerst een evenwicht voor de overgang (de eendimensionale module) met als randvoorwaarden de Monin-Obukhov-relaties. Deze MO-relaties beschrijven de structuur van de AOL boven homogeen terrein als functie van de thermische gelaagdheid van de AOL. Vervolgens wordt de stroming na de overgang berekend. Belangrijk is hier dat het model de Penman-Monteith-vergelijking gebruikt met een constante oppervlakteweerstand r_s om de verdamping bij het oppervlak te berekenen.

De transportmechanismen van voelbare warmte en waterdamp werden beschreven middels de flux-profiel- en flux-variantierelaties. Er werd een verband afgeleid tussen de dimensieloze standaarddeviatie van verticale wind, van concentratie (temperatuur of vocht) en de dimensieloze verticale gradiënt van de gemiddelde concentratie voor homogene omstandigheden. De aldus verkregen functie bleek zich geheel conform de Monin-Obukhov-theorie te gedragen. Dit resultaat werd verkregen omdat, in plaats van de wrijvingssnelheid, de standaarddeviatie van verticale wind als snelheidsschaal in de AOL gebruikt werd.

Het experiment

In Hoofdstuk 3 werd het experiment beschreven dat in juni 1987 werd uitgevoerd in La Crau, Frankrijk. Aan weerszijden van een abrupte overgang van een droog, bijna kaal terrein naar geïrrigeerd gras werden onder meer verticale profielen van wind, temperatuur en vocht en de turbulente karakteristieken van de AOL gemeten. Uit de totale dataset werden 81 runs geselecteerd, alle verzameld in de periode van 20 juni tot 24 juni tijdens gunstige weersomstandigheden voor lokale advectie.

De windsnelheid was zo'n 7 ms^{-1} op 3 meter boven het oppervlak ($z = 3$ m) uit richtingen tussen 330° en 360°, dat wil zeggen dat de overgang aangestroomd werd onder een hoek tussen de 20° en 50°. Verondersteld werd dat de stroming tweedimensionaal was. De afstand tot de overgang vanaf een stroomafwaartse locatie, de 'fetch' x, werd berekend uit de windrichting en de loodrechte afstand tot de overgang. De omstandigheden boven het droge terrein variëerden van zeer onstabiel tot neutraal met Obukhov- lengtes tussen de -9 m en -470 m. De temperatuur op 3 m boven het droge terrein was 1 K boven de temperatuur op dezelfde hoogte boven het gras, 300 m van de overgang. De oppervlaktetemperatuur van het droge terrein was 10 K hoger dan de oppervlaktetemperatuur van het gras. De Bowen-verhouding boven het droge terrein lag tussen de 1 (20/6/87, een dag na regen) en 8 (2 dagen later). Boven het gras hing de Bowen-verhouding sterk af van de hoogte-fetchverhouding (z/x) en was typisch 1.2 voor $z/x = 0.06$ en 0.1 voor $z/x = 0.01$. Het gras had 56 Wm^{-2} meer stralingsenergie beschikbaar om te verdelen tussen H en λE. Dit was 14% van de beschikbare stralingsenergie boven het gras. De nettostraling en de bodemwarmteflux droegen ieder ongeveer de helft bij aan dit verschil. Het verschil in

beschikbare energie tussen de twee terreinen vertoonde een dagelijkse gang met twee maxima ten gevolge van pieken in de ochtend en de middag in het verschil tussen de bodemwarmtefluxen van de twee terreinen.

De flux-profiel- en flux-variantierelaties boven het droge terrein.

In Hoofdstuk 4 werden de waargenomen flux-profiel- en de flux-variantierelaties vergeleken met de MO-relaties. Verder werden de data gebruikt om de rand- en beginvoorwaarden op te stellen voor het model.

Temperatuur gedroeg zich in overeenstemming met de MO theorie maar vocht en wind vertoonden afwijkend gedrag. Het windveld was waarschijnlijk verstoord omdat het droge terrein relatief glad was ten opzichte van het regionale gemiddelde.

Het vochttransport boven het droge terrein was minder efficiënt dan het transport van voelbare warmte. Hoewel de flux aan de top van de Planetaire GrensLaag (PGL, overdag ongeveer 1 km dik) niet bekend was, werd de lage efficiëntie van het vochttransport geweten aan de lage oppervlakteflux van vocht in verhouding tot de flux aan de top van de PGL. Indirect bewijs was dat de correlatie tussen temperatuur en vochtfluctuaties duidelijk toenam als de vochtflux hoger was. Dit bewijs werd ondersteund door een theorie die de invloed van de verhouding tussen de oppervlaktefluxen en de fluxen aan de top van de PGL in rekening brengt om de correlatie tussen temperatuur en vochtfluctuaties te berekenen.

Het analyseren van Fetch-afhankelijke processen

In Hoofdstuk 5 werd uitgelegd dat de variatie van fetch met de windrichting niet normaal verdeeld is terwijl de windrichtingvariaties dit wel zijn. Een speciale procedure voor de analyse van fetch-afhankelijke processen werd beschreven.

De latente en sensibele warmtefluxen boven het gras

We lieten zien dat de fluxen in de IGL, genormaliseerd met de oppervlaktefluxen van het droge terrein, evenredig waren met z/δ voorzover de metingen reikten. De genormaliseerde voelbare warmteflux naderde 1 op 0.7δ en de genormaliseerde latente warmteflux op 0.5δ. Op grond van dit resultaat werd besloten om de oppervlaktefluxen van het gras te berekenen

middels een lineaire extrapolatie van de gemeten fluxen tot de veronderstelde hoogte van de constante-fluxlaag ($z = 0.008x$). De som van de aldus berekende fluxen was, voor de meeste runs, gelijk aan de beschikbare stralingsenergie.

De wrijvingssnelheid en de ruwheidslengte na de overgang

De benedenwindse u_* was bijna constant met de hoogte en was 1.17 keer de u_*. De 'drag-methode' werd gebruikt om de ruwheidslengte te berekenen; dit resulteerde in $z_o = 0.07$ m. Een schatting uit de windprofielen leverde een grotere z_o op. Dit duidt erop dat het grasterrein relatief ruw was ten opzichte van de omgeving als geheel.

De weerstanden r_s, r_i and r_a boven het gras

De aerodynamische weerstand r_a boven het benedenwindse terrein was altijd klein (≈ 16 sm^{-1}) vergeleken met r_i en r_s. De isotherme weerstand r_i was 's morgens en 's avonds relatief hoog (200 sm^{-1}) en lager rond de middag (80 sm^{-1}). De oppervlakteweerstand r_s steeg meestal gedurende de dag van zo'n 40 sm^{-1} tot 70 sm^{-1} aan het einde van de dag. De oppervlakteweerstand werd bepaald uit de verdamping en het verzadigingsdeficiet tussen het oppervlak en een referentiehoogte. Daarnaast werd een simpele parameterisatie gebruikt, gebaseerd op de fysiologische eigenschappen van een kort gewas. Deze twee methoden om r_s te berekenen kwamen goed overeen, vooral na een correctie voor globale straling.

Modelverificatie

In Hoofdstuk 6 werd eerst de eendimensionale module van het model getest. Het bleek dat deze module slechts gedeeltelijk de MO-karakteristieken van de homogene AOL kon reproduceren. Goede resultaten werden verkregen voor de flux-profielrelaties en de flux-variantierelaties voor temperatuur en vocht. De MO flux-variantierelaties voor verticale windsnelheidfluctuaties en voor de longitudinale windsnelheidfluctuaties konden niet worden gereproduceerd door het model; alleen voor de fluctuaties loodrecht op de gemiddelde windrichting werden goede resultaten gevonden. De transportefficiënties voor warmte en waterdamp werden onderschat omdat de verticale windsnelheidsfluctuaties te

hoog uitkwamen. De door het model berekende flux-profielrelaties bleken ongeveer gelijk voor wind, temperatuur en vocht en dat betekent dat de flux-profielrelatie voor wind veel te snel afneemt met toenemende thermische onstabiliteit.

De vergelijking tussen de benedenwindse metingen en de modelberekeningen betrof eerst de verticale profielen van de gemiddelde windsnelheid, de temperatuur en de vochtigheid. Omdat de bovenstaande problemen van het model groter waren voor de thermisch onstabielere AOL, werden alleen die runs gebruikt met Obukhov-lengtes kleiner dan -50 m. De profielen met het model berekend kwamen goed overeen voor temperatuur en gedeeltelijk voor vocht. De resultaten hingen sterk af van r_s. Hoewel andere invoergrootheden een rol zouden kunnen spelen bleken de resultaten zeer gevoelig voor deze grootheid omdat r_s de herverdeling van beschikbare energie aan het oppervlak tussen de voelbare warmteflux en de latente warmteflux bepaalt. De berekende windprofielen kwamen slecht overeen met de gemeten profielen. Dit was verwacht omdat het model ook al niet in staat was om de flux-profielrelaties onder homogene omstandigheden te reproduceren. Met het model werden de horizontale windsnelheidfluctuaties na de overgang sterk onderschat maar de resultaten voor de verticale windsnelheidfluctuaties kwamen aardig overeen. De berekende en gemeten fluxen boven gras stemden goed overeen. Behalve de impulsflux, die minder afnam met de hoogte dan het model berekende. Tenslotte werd gevonden dat het model enkele van de gemeten turbulentiekarakteristieken van temperatuur en vocht $(R_{\theta q}, R_{w\theta}/R_{wq}, \varphi_\theta, \varphi_q)$ goed genoeg kon reproduceren. In zijn algemeenheid stemden de modelresultaten dus behoorlijk goed overeen met de metingen terwijl er nogal wat feed-backmechanismen ontbreken in het model. Zo moeten eigenlijk de nettostraling, de bodemwarmteflux en de oppervlakteweerstand als functie van de overgang berekend worden omdat ze vermoedelijk een functie van fetch zijn.

De structuur van de Interne Grenslaag

De modelberekeningen en de meetresultaten werden gebruikt om de structuur van de IGL te bestuderen. Daarbij werd de meeste aandacht besteed aan de transportmechanismen van waterdamp en voelbare warmte. Verwacht werd dat de stromingseigenschappen in de IGL zowel van de thermische stabiliteit als van de positie na de overgang afhingen. De relatie

met de thermische stratificatie werd bestudeerd met gebruikmaking van locale Monin-Obukhov-schaling. Het verschil met de gebruikelijke MO-schaling is dat lokaal gemeten parameters gebruikt worden in plaats van de oppervlakteparameters.

De gemeten locale schalingsrelatie voor de variaties van de verticale windsnelheid kwam goed overeen met de locale MO-functie voor neutrale condities maar nam te snel toe met toenemende thermische onstabiliteit. Ter verklaring hiervan werd verondersteld dat de gedwongen-convectiebijdrage aan de verticale windsnelheidfluctuaties zich sneller aan de nieuwe omstandigheden aanpast dan de vrije-convectiebijdrage.

De metingen lieten zien dat vocht zich conform de locale MO-theorie gedroeg terwijl dit niet het geval was voor temperatuur. In de IGL na een droog-nat-overgang wordt vocht efficiënter getransporteerd dan warmte. Ook werd gevonden dat de produktie van temperatuurfluctuaties gedurende sommige runs klein is ten opzichte van de advectie van deze fluctuaties. Dit maakt het aannemelijk dat locale schaling voor temperatuur niet werkt.

De dimensieloze verticale gradient van de gemiddelde windsnelheid in de IGL was groter dan in het homogene geval. Dit stemt overeen met wat verwacht wordt. De grootste afwijking werd gevonden rond $z/\delta = 0.15$.

De flux-gradiëntverhoudingen, ofwel de turbulente diffusiecoëfficiënten, voor vocht en warmte werden bepaald uit de metingen. Het resultaat was dat de flux-gradiënt verhouding voor temperatuur kleiner was dan die voor vocht onderin de IGL. Dit stemde redelijk overeen met de waargenomen verhouding van de transportefficiënties. Met het model werd geïllustreerd dat het gedrag van de verhouding van deze diffusiecoëfficiënten in de IGL onder meer afhangt van de mate van locale advectie.

De experimentele resultaten konden niet gebruikt worden om de IGL-dikte goed te bepalen omdat te dicht bij het oppervlak gemeten werd. Echter, de grootte van de flux-gradiënt verhoudingen voor warmte, waterdamp en impuls kan dienen als indicatie voor de dikte van de bijbehorende grenslagen. Een maat hiervoor is het turbulente Schmidt-getal voor vocht en het turbulente Prandtl-getal voor temperatuur. Het turbulente Schmidt-getal was groter dan 1 hogerop in de IGL, en kleiner dan 1 lager in de IGL. Het turbulente Prandtl-getal was lager hogerop in de IGL en was overal kleiner dan 1. In het onderste deel van de IGL was

het turbulente Prandtl-getal echter wel groter dan het turbulente Schmidt-getal. Deze resultaten geven aan dat de IGL voor vocht het dunst moest zijn, dunner dan die voor impuls en van voelbare warmte.

Het gebruik van de Bowen-verhoudingmethode in de Interne Grenslaag

In Hoofdstuk 7 werd het model eerst gebruikt om de hoogte van de IAL uit te rekenen, gedefiniëerd als de hoogte waar de flux 10% afwijkt van de oppervlakteflux. De IAL voor waterdamp was in dit geval dikker ($z/x \approx 0.01$) dan voor temperatuur ($z/x \approx 0.005$).

Vervolgens werden de gevolgen doorgerekend voor het gebruik van de Bowen-verhouding methode in de stabiele en onstabiele IAL om de oppervlaktefluxen te bepalen. Het model werd gebruikt om de oppervlaktefluxen direct te berekenen. Deze resultaten werden vergeleken met de fluxen die verkregen werden door de zogenaamde gradiënt-Bowen-verhoudingmethode en de standaarddeviatie-Bowen-verhoudingmethode toe te passen op de door het model berekende temperatuur- en vochtprofielen en de standaarddeviaties van temperatuur en vocht.

De gradiënt-Bowen-verhouding bleek nog tot $z/x = 0.02$ gebruikt te kunnen zowel in de stabiele IAL als de onstabiele IAL. De verklaring voor deze hoge z/x was dat het verschil tussen de Bowen-verhouding aan het oppervlak en op enige hoogte gecompenseerd werd door de grootte van de verhouding van de turbulente diffusiecoëfficiënten voor warmte en waterdamp ter hoogte van de gradiëntmeting. De standaarddeviatie-Bowen-verhouding methode kon tot $z/x = 0.02$ gebruikt worden in de stabiele IAL omdat de verhouding van de transportefficiënties van voelbare warmte en waterdamp kleiner dan 1 is en aldus voor de fluxdivergentie compenseerde. In de onstabiele IGL moet z/x kleiner dan 0.008 zijn om dezelfde nauwkeurigheid te verkijgen omdat nu de verhouding van de transportefficiënties van voelbare warmte en waterdamp de fout ten gevolge van de fluxdivergentie versterkt. Deze resultaten zijn alleen geldig voor de hier bestudeerde gevallen. Een aantal factoren kunnen elkaar gunstig beïnvloed hebben zodat de fouten klein bleven. Het is echter

belangrijk om te constateren dat met het model voorspeld kan worden welke omstandigheden gunstig zijn voor de toepassing van micro-meteorologische methoden om de fluxen te bepalen in de IGL.

Verder werd in Hoofdstuk 7 nog aangetoond dat, om de verhouding van de turbulente diffusiecoëfficiënten van warmte en waterdamp te bepalen, de fluxen gemeten moeten worden op de hoogte waarvoor de gradiënten bepaald worden. Aan deze voorwaarde werd niet altijd voldaan in vroegere experimenten hetgeen nogal wat verwarring veroorzaakt heeft.

REFERENCES

Antonia, R.A. and Luxton, R.E., 1971: The response of a turbulent boundary layer to a step change in surface roughness Part 1. Smooth to rough. J.Fluid.Mech. 48, 721-761.

Antonia, R.A. and Luxton, R.E., 1972: The response of a turbulent boundary layer to a step change in surface roughness Part 2. Rough to smooth. J.Fluid.Mech. 53, 737-757.

Arya, S.P.S., 1991: Finite-difference errors in estimation of gradients in the atmospheric surface layer. J.App.Meteor. 30, 251- 253.

Aubert, G., 1968: Classification des sols utilisee par les pedologues Francais. In: Soil map of the world, Joint FAO/UNESCO Project, Approaches to soil classification. FAO/U-NESCO, Rome, 78-94.

Beljaars, A.C.M., 1982: The derivation of fluxes from profiles in perturbed areas. Bound.Layer Meteor. 24, 35-55.

Beljaars, A.C.M., 1987: On the memory of wind standard deviation for upstream roughness. Bound.Layer Meteor. 38, 95-101.

Beljaars, A.C.M., Schotanus, P. and Nieuwstadt, F.T.M., 1983: Surface layer similarity under non-uniform fetch conditions. J.Clim.App.Meteor. 22, 1800-1810.

Bendat, J.S. and Piersol, A.G., 1971: Random data: analysis and measurement procedures. Wiley Interscience New York, 407 pp.

Berge, H.F.M. ten, 1986: Heat and water transfer at the bare soil surface. Ph.D.Thesis Wageningen Agricultural University, 214 pp.

Bink, N.J. and Kroon, L.J.M., 1990: The behaviour of the transfer efficiencies of sensible heat and water vapour under conditions of local advection. In: Preprint of the Ninth symposium on Turbulence and Diffusion, April 30-May 3, Riso, Roskilde, Denmark, Am.Meteor.Soc., 232-234.

Bottemanne, F.A., 1982: Nauwkeurigheid bij temperatuurmetingen met platina weerstandsthermometers [In Dutch]. intern rapport, Lab. voor Natuur- en Weerkunde Wageningen Agricultural University, 13 pp.

Bradley, E.F., 1968: A micrometeorological study of velocity profiles and surface drag in the region modified by a change in surface roughness. Q.J.R.Meteorol.Soc. vol.94,no.401, 361-379.

Bradley, E.F., Antonia, R.A. and Chambers, A.J., 1981a: Temperature structure in the atmospheric surface layer I. The budget of temperature variance. Bound.Layer Meteor. 20, 275-292.

Bradley, E.F., Antonia, R.A. and Chambers, A.J., 1981b: Turbulence Reynolds number and the turbulent kinetic energy balance in the atmospheric surface layer. Bound.Layer Meteor. 21, 183-197.

Bradley, E.F., Antonia, R.A. and Chambers, A.J., 1982: Streamwise heat flux budget in the atmospheric surface layer. Bound.Layer Meteor. 23, 3-15.

Brakke, T.W., Verma, S.B. and Rosenberg, N.J., 1978: Local and regional components of sensible heat advection. J.Appl.Meteor. 17, 955-963.

Brost, R.A., 1979: Some comments on the "Turbulent exchange coefficients for sensible heat and water vapor under advective conditions". J.Appl.Meteor. 18, 378-380.

Brutsaert, W.H., 1982: Evaporation into the atmosphere. Environmental Fluid Mechanics. D. Reidel Publ. Co. Dordrecht, Holland, 299 pp.

Buringh, P., 1970: Introduction to the study of soils in tropical and sub-tropical regions 2nd ed. Pudoc Wageningen, 99 pp.

Busch, N.E. and Kristensen, L., 1976: Cup anemometer overspeeding. J.Appl.Meteor. 15, 1328-1332.

Businger, J.A., 1982: Equations and concepts. In: Nieuwstadt, F.T.M and van Dop, H., Atmospheric turbulence and air pollution modelling. Reidel Publishing, Dordrecht, The Netherlands, 1-36.

De Bruin, H.A.R, Bink, N.J. and Kroon, L.J.M., 1991: Fluxes in the surface layer under advective conditions. In: Schmugge, T.J. and André, J.C., Land surface evaporation. Springer-Verlag, New York, 157-169.

De Bruin, H.A.R., Kohsiek, W. and Van den Hurk, 1993: A verification of some methods to determine the fluxes of momentum, sensible heat and water vapour standard deviation and structure parameter of meteorological quantities. Bound.Layer.Meteor. 63, 231-257.

De Bruin, H.A.R. and Bink, N.J., 1994: The use of σ_θ as a temperature scale for the Atmospheric Surface Layer. Bound.Layer Meteor. 70, 79-93.

Doorenbos, J. and Pruitt, W.O., 1975: Crop water requirements. FAO Irrigation and Drainage Paper 24, FAO, Rome.

Dugas, W.A., Fritschen, L.J., Gay, L.W., Held, A.A., Matthias, A.D. Reicosky, D.C., Steduto, P. and Steiner, J.L., 1991: Bowen ratio, eddy correlation, and portable chamber measurements of sensible and latent heat flux over irrigated spring wheat. Agric.Forest Meteor. 56, 1-20.

Dyer, A.J. and Crawford, T.V., 1965: Observations of the modification of the microclimate at a leading edge. Q.J.R.Meteorol.Soc. 91, 345-348.

Dyer, A.J. and Hicks, B.B., 1970: Flux-gradient relationships in the constant flux layer. Q.J.R.Meteorol.Soc. 96, 715-721.

Elliott, W.P., 1958: The growth of the atmospheric internal boundary layer. Trans-.Am.Geo.Un. 39, No.6, 1048-1054.

Evans, G.N., 1971: Evaporation from rice at Griffith, N.S.W. Agric.Meteor. 8, 117-127.

Garrat, J.R., 1990: The internal boundary layer - a review. Bound.Layer Meteor. 50, 171-303.

Garrat, J.R. and Ryan, B.F., 1989: The structure of the stably stratified internal boundary layer in off-shore flow over the sea. Bound.Layer Meteor. 47, 17-40.

Garrat, J.R. and Hicks, B.B., 1990: Micrometeorological and PBL experiments in Australia. Bound.Layer Meteor. 50, 11-30.

Gay, L.W. and Bernhofer, Ch., 1991: Enhancement of evapotranspiration by advection in arid regions. In: Hydrological interactions between atmosphere, soil and vegetation (Proceedings of the Vienna symposium 1991) IAHS Publ.no.204, 147-156.

Geze, B., Horemans, P., Moinerau, J. And Medintzeff, A., 1966: Carte pédologique de la France.

Halldin, S. and Lindroth, A., 1992: Errors in net radiometry: Comparison and evaluation of six radiometers designs. J.Atm.Oc.Tech. 9, No.6, 762-783.

Hicks, B.B., 1981: An examination of turbulence statistics in the surface boundary layer. Bound.Layer Meteor. 21, 389-402.

Hill, R.J., 1989: Implications of Monin-Obukhov similarity theory for scalar quantities. J.Atmos.Sci 46, no.14, 2236-2244.

Holtslag, A.A.M. and Moeng, C.H., 1991: Eddy diffusivity and counter-gradient transport in the convective atmospheric boundary layer. J.Atmos.Sci 48, no.14, 1690-1698.

Jacobs, A.F.G. and Schols, E., 1986: Surface roughness parameter estimated with a drag technique. J.Clim.Appl.Meteor. 25, 1577-1582.

Kaimal, J.C., Wyngaard, J.C., Izumi, Y. and Cote, O.R., 1972: Spectral characteristics of surface-layer turbulence. Q.J.R.Meteorol.Soc. 98, 563-589.

Kaimal, J.C. and Wyngaard, J.C., 1990: The Kansas and Minnesota experiments. Bound.Layer Meteor. 50, 31-47.

Kaimal, J.C. and Finnigan, J.J., 1994: Atmospheric boundary layer flows, their structure and measurement. Oxford University Press, New York, 289 pp.

Kohsiek, W., 1984: Inertial subrange correlation between temperature and humidity fluctuations in the unstable surface layer above vegetated terrains. Bound.Layer Meteor. 29, 211-224.

Kohsiek, W., 1986: The KNMI Lyman-alpha hygrometer. KNMI Technical Report TR-87, 12 pp.

Kohsiek, W., van der Vliet, J.G. and Monna, W.A., 1987: Crau 1987, the KNMI contribution. KNMI Technical Report TR-110, 41 pp.

Kohsiek, W. De Bruin, H.A.R. and Van den Hurk, B., 1993: Estimation of the sensible heat flux of a semi-arid area using surface radiative temperature measurements. Bound.Layer Meteor. 63, 213-230.

Kroon, L.J.M., 1985: Profile derived fluxes above inhomogeneous terrain: a numerical approach. Ph.D.Thesis Wageningen Agricultural University, 159 pp.

Kroon, L.J.M. and De Bruin, H.A.R, 1993: Atmosphere-vegetation interaction in local advection conditions: effect of lower boundary conditions. Agric.Forest Meteor. 64, 1-28.

Lemon, E.R., Glaser, A.H. and L.E. Satterwhite, 1957: Some aspects of the relationship of soil, plant and meteorological factors to evapotranspiration. Proc.Soil Sci. Amer. 21, 464-468.

Lang, A.R.G., Evans, G.N. and Ho, P.Y., 1974: The influence of local advection on evapotranspiration from irrigated rice in a semi-arid region. Agric.Meteor. 13, 5-13.

Lang, A.R.G., McNaughton, K.G., Fazu, C., Bradley, E.F. and Othaki, E., 1983a: Inequality of eddy transfer coefficients for vertical transports of sensible heat and latent heat under advective inversions. Bound.Layer Meteor. 25, 25-41.

Lang, A.R.G., McNaughton, K.G., Fazu, C., Bradley, E.F. and Othaki, E., 1983b: An experimental appraisal of the terms in the heat and moisture flux equations for local advection. Bound.Layer Meteor. 25, 89-102.

Lang, A.R.G and Bradley, E.F., 1983: Pressure covariance terms in the heat and moisture flux equations for local advection. Proc.Eighth.Aus.Fluid Mech. Conf., Newcastle, N.S.W. 28 Nov - 2 Dec 1983, 1A.1-1A.4.

Lenschow, D.H., 1986: Probing the atmospheric boundary layer. American Meteor.Soc. Boston, 269 pp.

Mahrt, L., 1991: Boundary-Layer moisture regimes. Q.J.R.Meteorol.Soc. 117, 151-176.

McBean, G.A., 1973: Comparison of the turbulent transfer processes near the surface. Bound.Layer Meteor. 4, 265-274.

McBean, G.A. and Miyake, M., 1972: Turbulent transfer mechanisms in the atmospheric surface layer. Q.J.R.Meteorol.Soc. 98, 383-398.

McNaughton, K.G., 1976a: Evaporation and advection I: evaporation from extensive homogeneous surfaces. Q.J.R.Meteorol.Soc. 102, 181-191.

Menenti, M., 1984: Physical aspects and determination of evaporation in deserts applying remote sensing techniques. Ph.D.Thesis Wageningen Agricultural University, 202 pp.

Millar, B.D., 1964: Effect of local advection on evaporation rate and plant water status. Aust.J.Agric.Res. 15, 85-90.

Miyake, M., 1965: Transformation of the atmospheric boundary layer over inhomogeneous surfaces. Sci.Rep. 5R-6 Univ.of Washington, Seatlle, USA.

Moeng, C.H. and Wyngaard, J.C., 1984: Statistics of conservative scalars in the convective boundary layer. J.Atmos.Sci. 41, no.21, 3161-3169.

Monin, A.S. and Yaglom, A.M., 1971: Statistical fluid mechanics: mechanics of turbulence. (Ed. J.L.Lumley) Volume 1, MIT Press, London, 769 pp.

Monteith, J.L., 1965: Evaporation and environment. Symp.Soc.Exp.Biol. 19, 205-234.

Monteith, J.L., 1981: Evaporation and surface temperature. Q.J.R.Meteorol.Soc. 107, 1-27.

Monteith, J.L. and Unsworth, M.H., 1990: Principles of environmental physics, 2nd edition. Edward Arnold London, 291 pp.

Motha, R.P., Verma, S.B. and Rosenberg, N.J., 1979a: Exchange coefficients under sensible heat advection determined by eddy correlation. Agric.Forest Meteor. 20, 273-280.

Motha, R.P., Verma, S.B. and Rosenberg, N.J., 1979b: Turbulence under conditions of sensible heat advection. J.App.Meteor. 18, 467-473.

Mulhearn, P.J., 1981: On the formation of a stably stratified internal boundary-layer by advection of warm air over a cooler sea. Bound.Layer Meteor. 21, 247-254.

Muller, S.H., The, H., Kohsiek, W. and Monna, W.A.A., 1990: Description of the Crau data set: Meteosat data, radiosonde data, Sea surface temperatures: Comparison of Meteosat and Heimann data. KNMI, Scientific Reports WR 90-03, 52 pp.

Munn, R.E., 1966: Descriptive micrometeorology. Academic press New York etc., 245 pp.

Noilhan, J and Planton, S., 1989: A simple parameterization of land surface processes for meteorological models. Mont.Weather Rev. 117, 536-549.

Obukhov, A.M., 1946: Turbulence in an atmosphere with a non-uniform temperature. Trudy Instit. Teoret. Geofiz, AN-S.S.S.R., No.1 (English translation: 1971: Bound.Layer Meteor. 2, 7-29).

Oke, T.R., 1987: Boundary Layer Climates, 2nd edition. Methuen, New York, 435 pp.

Oliver, H.R. and Wright, I.R., 1990: Corrections of errors associated with measurement of net all-wave radiation with double-domed radiometers. Bound.Layer Meteor. 53, 401-407.

Overgaard-Mogensen, V., 1970: The calibration factor of heat flux meters in relation to the thermal conductivity of the surrounding medium. Agric.Forest Meteor. 7, 401-410.

Panofsky, H.A. and Dutton, J.A., 1984: Atmospheric turbulence, models and methods for engineering applications. Wiley Interscience, John Wiley&Sons New York, 397 pp.

Paulson, C.A., 1970: The mathematical representation of wind speed and temperature profiles in the unstable atmospheric surface layer. J.Appl.Meteor. 9, 857-861.

Peterson, E.W., Taylor, P.A., Höjstrup, J., Jensen, N.O., Kristensen, L. and Petersen, E.L., 1980: RISO 1978: Further investigations into the effects of local terrain irregularities on tower-measured wind profiles. Bound.Layer Meteor. 19, 303-313.

Philip, J.R., 1959: The theory of local advection. J.Meteorology 16, 535-547.

Philip, J.R., 1961: The theory of heat flux meters. J.Geophys.Res. 66, 571-579.

Philip, J.R., 1987: Advection, evaporation and surface resistance. Irrig.Sci. 8, 101-114.

Priestley, C.H.B., 1959: Turbulent transfer in the lower atmosphere. Chicago Univ.Press Chicago, Illinois, 130 pp.

Rao, K.S., 1975: Effect of thermal stratification on the grow of the internal boundary layer. Bound.Layer Meteor. 8, 227-234.

Rao, K.S., Wyngaard, J.C. and Cote, O.R., 1974a: The structure of the two-dimensional internal boundary over a sudden change of surface roughness. J.Atmos.Sci. 31, 738-746.

Rao, K.S., Wyngaard, J.S. and Cote, O.R., 1974b: Local advection of momentum, heat and moisture in micrometeorology. Bound.Layer Meteor. 7, 331-348.

Raupach, M.R., 1977: Atmospheric flux measurement by eddy correlation. Flinders Inst.Atm.Mar.Sci. Ph.D.Thesis, Research Report No. 27, 207pp.

Raupach, M.R., 1983: Experimental tests of higher-order closure assumptions for scalar transport. Proc.Eighth Aus.Fluid Mech.Conf., Newcastle, N.S.W. 28 Nov. - 2 Dec. 1983, 1A.1-1A.4.

Raupach, M.R. and Legg, B.J., 1983: Turbulent dispersion from an elevated line source: measurements of wind-concentration moments and budgets. J.Fluid.Mech. 136, 111-137.

Rider, N.E., Philip, J.R. and Bradley, E.F., 1963: The horizontal transport of heat and moisture - a micrometeorological study. Q.J.R.Meteorol.Soc. 89, 507-531.

Rosenberg, N.J., Blad, B.L. and Verma, S.B., 1983: Microclimate, the biological environment, 2nd edition. John Wiley and Sons New York etc., 495 pp.

Schotanus, P., Nieuwstadt, F.T.M., and de Bruin, H.A.R., 1983: Temperature measurement with a sonic anemometer and its application to heat and moisture fluxes. Bound.Layer Meteor. 26, 81-93.

Shao, Y. and Hacker, J.M., 1990: Local similarity relationships in a horizontally inhomogeneous boundary layer. Bound.Layer Meteor. 52, 17-40.

Smith, M., 1992: CROPWAT: a computer program for irrigation planning. FAO Irrigation and Drainage paper 26, 126 pp.

Stull, R.B., 1988: An introduction to boundary layer meteorology. Kluwer Academic Publishers Dordrecht, 666 pp.

Tennekes, H. 1970: Free convection in the turbulent Ekman layer of the atmosphere. J.Atmos.Sci.27, 1027-1034.

Tennekes, H. and Lumley, J.L., 1972: A first course in turbulence. MIT Press Cambridge, 300 pp.

Thom, A.S., 1975: Momentum, mass and heat exchange of plant communities. In: Monteith, J.L. (ed.), Vegetation and Atmosphere Vol.1, Principles, Academic Press, Inc. London Ltd., 57-109.

Tillman, J.E., 1972: The indirect determination of stability, heat and momentum fluxes in the atmospheric boundary layer from simple scalar variables during dry unstable conditions. J.Appl.Meteor. 11, 783-792.

Tillman, J.E., 1991: In situ water vapour measurements in the Lyman-alpha and Infrared spectrum: theory and components. In: Schmugge, T.J. and André, J.C. (eds.), Land surface evaporation, measurement and parameterization, 313-335.

Van Asselt, C.J., Jacobs, A.F.G., Van Boxel, J.H. and Jansen, A.E., 1991: A rigid fast-response thermometer for atmospheric research. Meas.Sci.Technol., 26-31.

Van Boxel, J.H., 1986: Heat balance investigations in tidal areas. Ph.D.Thesis Vrije Universiteit Amsterdam, 137 pp.

Van der Hurk, B.J.J.M. (1990): Numerieke oplossing van de bodemtemperatuur en bodemwarmteflux: een vergelijking tussen de droge Crau en een oplossing met behulp van het Crank-Nicholson schema. Interne publikatie, Vakgroep Meteorologie, Wageningen Agricultural University (in Dutch).

Van Wijk, W.R. and de Vries, D.A., 1966: Periodic temperature variations in a homogeneous soil. In: Van Wijk, W.R. (ed.), Physics of plant environment 2nd ed, North Holland Publishing Company, Amsterdam, 102-143.

Verma, S.B., Rosenberg, N.J. and Blad, B.L., 1978: Turbulent exchange coefficients for sensible heat and water vapor under advective conditions. J.Appl.Meteor. 17, 330-338.

Vugts, H.F., Cannemeijer, F. and Tesselaar, F., 1988: The Crau experiment. Parameterization of the surface fluxes. Internal report Free University Amsterdam, Department of Meteorology.

Walmsley, J.L., 1989: Internal boundary layer height - a comparison with atmospheric data. Bound.Layer Meteor. 47, 251-262.

Warhaft, Z., 1976: Heat and moisture flux in the stratified boundary layer. Q.J.R.Meteorol.Soc. 102, 703-707.

Webb, E.K., Pearman, G.I. and Leuning, R., 1981: Correction of flux measurements for density effects due to heat and water vapour transfer. Q.J.R.Meteorol.Soc. 106, 85-100.

Webster and Wilson, 1980: Agriculture in the tropics, 2nd ed. Longman London, 640 pp.

Wesely, M.L., 1988: Use of variance techniques to measure dry air-surface exchange rates. Bound.Layer Meteor. 44, 13-31.

Wichmann, M. and Schaller, E., 1986: On the determination of the closure parameters in higher-order closure models. Bound.Layer Meteor. 37, 323-341.

Wieringa, J., 1980: A revaluation of the Kansas mast influence on measurements of stress and cup anemometer overspeeding. Bound.Layer Meteor. 18, 411-430.

Wieringa, J., 1993: Representative roughness parameters for homogeneous terrain. Bound.Layer Meteor. 63, 323-363.

Wyngaard, J.C., 1975: Modeling the planetary boundary layer - extension to the stable case. Bound.Layer Meteor. 9, 441-460.

Wyngaard, J.C., 1982: Boundary-layer modelling. In: Nieuwstadt, F.T.M. and Van Dop, H. (eds.), Atmospheric turbulence and air pollution modelling. Reidel Publishing Co., Dordrecht, The Netherlands, 69-106.

Wyngaard, J.C., 1988: Convective processes in the lower atmosphere. In: Steffen, W.L. and Denmead, O.T. (eds.), Flow and transport in the natural environment: advances and applications Springer-Verlag, Berlin etc., 240-260.

Wyngaard, J.C., 1991: On the maintenance and measurement of scalar fluxes. In: Schmugge, T.J. and Andre, J.C. (eds.), Land surface evaporation, measurement and parameterization, 199-230.

Wyngaard, J.C. and Coté, O.R., 1971: The budgets of turbulent kinetic energy and temperature variance in the atmospheric surface layer. J.Atmos.Sci. 28, 190-201.

Wyngaard, J.C., Coté, O.R. and Izumi, Y., 1971: Local free convection, similarity, and the budgets of shear stress and heat flux. J.Atmos.Sci. 28, 1171-1182.

Wyngaard, J.C., Coté, O.R. and Rao, K.S., 1974: Modeling the atmospheric boundary layer. Adv. in Geoph. 18A, Academic Press, New York, 193-210.

Wyngaard, J.C., Pennell, W.T., Lenschow, D.H. and LeMone, M.A., 1978: The temperature-humidity covariance budget in the convective boundary layer. J.Atmos.Sci. 35, 47-58.

Yaglom, A.M., 1977: Comments on wind and temperature flux-profile relationships. Bound.Layer Meteor. 11, 89-102.

A1 THE SECOND-ORDER CLOSURE MODEL

In this appendix an overview of the second-order closure model is given. The governing equations are given together with the parameterizations. The complete set of equations which is solved in the model can also be found in Kroon (1985) and in Rao *et al.*, (1974b). However, the parameterizations contain many 'constants' and the origin of these constants is not always clear, a matter also discussed at length in literature (e.g. Wichman and Schaller, 1985). The calculation of some of these constants is given here. The set of equations which is solved in the second-order closure model can be written in non-dimensional form to obtain expressions for the values for the various 'constants' used in the second-order model. First, the equations for a incompressible flow but with a temperature dependent density (Boussinesq approximation) and for the steady-state, two-dimensional field are given. An overview of the assumptions and concepts which are used to arrive at a suitable set of equations for the flow in the ABL was given by Businger (1982).

A1.1 The equations

The equations for the mean flow are **the conservation equations** for $S = \Theta$, Q or U,

$$\overline{U}\frac{\partial \overline{S}}{\partial x} + \overline{W}\frac{\partial \overline{S}}{\partial z} = \frac{\partial}{\partial z}\overline{sw} \qquad \text{A1.1}$$

and **the continuity equation**

$$\frac{\partial \overline{U}}{\partial x} + \frac{\partial \overline{W}}{\partial z} = 0. \qquad \text{A1.2}$$

Next, there are the second-order variance and covariance equations for Θ, Q and U.

The **Reynolds stress equations** for $\overline{u_i u_k}$ are

$$\overline{U}_j\frac{\partial}{\partial x_j}\overline{u_i u_k} = -\overline{u_j u_k}\frac{\partial \overline{U}_i}{\partial x_j} - \overline{u_j u_i}\frac{\partial \overline{U}_k}{\partial x_j} - \frac{\partial}{\partial x_j}\overline{(u_i u_j u_k)} - \left(\overline{u_k\frac{\partial p}{\partial x_i}} + \overline{u_i\frac{\partial p}{\partial x_k}}\right) - 2\varepsilon\frac{\delta_{ik}}{3}, \qquad \text{A1.3}$$

where repeated indices denote summation. The terms are, from left to right, advection, production (2x), turbulent transport, pressure-velocity covariance and dissipation of $\overline{u_i u_k}$.

The model carries only the equations for $\overline{u^2}$, $\overline{v^2}, \overline{w^2}$ and $\overline{uw}$ since $\overline{uv} = \overline{vw} = 0$.

The **transport equations** for Θ and Q are

$$\overline{U}_j \frac{\partial \overline{u_i s}}{\partial x_j} = -\overline{u_i u_j} \frac{\partial \overline{S}}{\partial x_j} - \overline{u_j s} \frac{\partial \overline{U}_i}{\partial x_j} - \frac{\partial}{\partial x_j}(\overline{u_i u_j s}) - \frac{1}{\rho}\overline{s\frac{\partial p}{\partial x_i}} + g_i \frac{\overline{s\theta_v}}{T_r} \qquad \text{A1.4}$$

with from left to right advection, gradient-S and gradient-U_i production, turbulent transport, pressure-scalar covariance destruction and buoyancy production of $\overline{u_i s}$ with $g = (0,0,-g)$.

The **equations for the (co-)variances** of Θ and Q,

$$+\overline{U}_j \frac{\partial \overline{s_1 s_2}}{\partial x_j} = -\overline{u_j s_1}\frac{\partial \overline{S}_2}{\partial x_j} - \overline{u_j s_2}\frac{\partial \overline{S}_1}{\partial x_j} - \frac{\partial \overline{s_1 s_2 u_j}}{\partial x_j} - 2N_{s_1 s_2} \qquad \text{A1.5}$$

are given as the balance between $\overline{s_1 s_2}$-advection on the left hand side, and production, transport and dissipation of $\overline{s_1 s_2}$ on the right hand side.

The model also carries an equation for **the dissipation of turbulence** $\overline{\varepsilon}$,

$$\overline{U}_j \frac{\partial \overline{\varepsilon}}{\partial x_j} = -\frac{\partial}{\partial x_j}(\overline{u_j \varepsilon}) - 4\frac{\overline{\varepsilon}^2}{\overline{u_i u_i}} + 4a\overline{\varepsilon}\frac{P}{\overline{u_i u_i}} \qquad \text{A1.6}$$

in which $\overline{u_i u_i}$ is twice the kinetic energy of the flow, P is the production of kinetic energy and $a = 0.5$.

A1.2 Parameterizations

Second-order closure implies that turbulent transport (a third order term), covariances with pressure fluctuations and dissipation in the second-order equations need to be parameterized. An important ingredient for the parameterization is the turbulent time scale

$$\tau_\varepsilon = \frac{\overline{u_i u_i}}{\overline{\varepsilon}}, \qquad \text{A1.7}$$

the ratio of TKE and turbulence dissipation. The parameterizations are given for each of the second-order equations which were given in section A1.1.

The Reynolds stress equations (Eq.A1.3)

For pressure-covariance in the Reynolds stress equations the model applies

$$-\left(\overline{u_k \frac{\partial p}{\partial x_i}} + \overline{u_i \frac{\partial p}{\partial u_k}} - \frac{2}{3}\delta_{ik}\frac{\partial}{\partial x_j}\overline{p u_j}\right) = -\left(\overline{u_i u_k} - \overline{u_i u_i}\frac{\delta_{ik}}{3}\right)\frac{C_{ik}}{\tau_\varepsilon}$$

A1.8

where C_{ik} can be considered as the ratio of τ_ε and some time scale specific to the pressure-velocity covariances. Note that the contribution of buoyancy and strain effects in this parameterization was not included in the version of the model used for this thesis.

The third moment in the turbulent transport term is modelled as

$$\overline{\left(u_i u_j + \frac{2}{3}\delta_{ik}p\right)u_k} = a_t \frac{\partial\overline{(-u_i u_j)}}{\partial x_m}\overline{u_m u_k}\tau_\varepsilon.$$

A1.9

where $a_t = 0.15$.

The transport equations for $\overline{u_i s}$ (Eq.A1.4)

The pressure-scalar covariance terms are estimated to be

$$\overline{s\frac{\partial p}{\partial x_i}} = d_i \frac{\overline{\theta u_i}}{\tau_\varepsilon} + a_1 \frac{g_i}{T_r}\overline{s\theta_v} + a_2 \frac{\partial\overline{U}_i}{\partial x_j}\overline{s u_j}$$

A1.10

in which $a_1 = 0.5$ and $a_2 = -0.5$.

The third moment in the transport term is modelled using

$$\overline{u_i u_j s} = -a_t \frac{\partial\overline{u_i s}}{\partial x_j}\overline{u_i u_j}\tau_\varepsilon.$$

A1.11

The scalar (co-)variance equations (Eq.A1.5)

In these equations turbulent transport and dissipation need to be parameterized. The dissipation of $\overline{s_1 s_2}$ becomes

$$N_{s_1 s_2} = b\frac{\overline{s_1 s_2}}{\tau_\varepsilon}$$

A1.12

and the third-order term in transport term is calculated using

$$\overline{s_1 s_2 u_i} = -a_t \frac{\partial\overline{s_1 s_2}}{\partial x_j}\overline{u_i u_j}\tau_\varepsilon.$$

A1.13

The dissipation equation (Eq.A1.6)

The third-order term appearing in the turbulent transport term is modelled as

$$\overline{\varepsilon u_j} = -a_{t,\varepsilon} \frac{\partial \overline{u_k \varepsilon}}{\partial u_k}.$$

A1.14

A1.3 Non-dimensional relations

The equations from section A1.1 are given below in their non-dimensional form. The constants appearing in the parameterizations are given as explicit functions of the ϕ and φ functions defined in section 2.2. To this purpose the transport terms were neglected, $\partial/\partial x = 0$ and $\overline{W} = 0$, furthermore we define

$$\phi_\varepsilon = \frac{\overline{\varepsilon} k z}{u_*^3},$$

A1.15

$$\phi_E = \varphi_u^2 + \varphi_v^2 + \varphi_w^2$$

A1.16

and

$$\phi_\tau = \frac{\phi_E}{\phi_\varepsilon}.$$

A1.17

Then the relations, given in Table A1.1 are obtained.

Non-dimensional relation	Using:	
$C_{11} = \dfrac{\left(2\phi_m - \frac{2}{3}\phi_\varepsilon\right)\phi_\tau}{\left(\varphi_u^2 - \frac{1}{3}\phi_E\right)}$	(Eqs.A1.3,A1.8)	A1.18
$C_{22} = \dfrac{-\frac{2}{3}\phi_\varepsilon\phi_\tau}{\varphi_v^2 - \frac{1}{3}\phi_E}$	(Eqs.A1.3,A1.8)	A1.19
$C_{33} = \dfrac{-\frac{2}{3}\phi_\varepsilon\phi_\tau}{\varphi_w^2 - \frac{1}{3}\phi_E}$	(Eqs.A1.3,A1.8)	A1.20
$C_{13} = \varphi_w^2\phi_m\phi_\tau$	(Eqs.A1.3,A1.8)	A1.21
$d_1 = \dfrac{(\phi_m(1+a_2)+\phi_c)\phi_\tau}{4\phi_m\phi_c}$	(Eqs.A1.4,A1.10)	A1.22
$d_3 = \varphi_w^2\phi_c\phi_\tau$	(Eqs.A1.4,A1.10)	A1.23
$b = \dfrac{\phi_\tau\phi_c}{\varphi_c^2}$	(Eqs.A1.5,A1.12)	A1.24

Table A1.1 Non-dimensional modelling equations written as explicit functions for the modelling constants

The constants, given in Table A1.1 are calculated using the lower boundary conditions

$$\phi_m(0) = \phi_\theta(0) = \phi_q(0) = \phi_\varepsilon(0) = 1 \qquad \text{A1.25}$$

$$\varphi_q(0) = \varphi_\theta(0) = 2.3$$

$$\varphi_w = 1.25, \varphi_v = 1.39, \varphi_u = 2$$

$$\phi_E(0) = 7.5$$

resulting in $C_{11} = 6.7, C_{22} = 8.9, C_{33} = 5.3, C_{13} = 11.7, d_1 = 2.8, d_3 = 11.7,$ and $b = 1.4$.

For $a_{1,\varepsilon}$ a different procedure was used. Eq.A1.6 can be written, also using Eq.A1.15, as

$$\frac{\partial}{\partial z}\left(\overline{w\varepsilon}\right) = \frac{\partial}{\partial z}\left(-a_{t,\varepsilon}\frac{\partial\bar{\varepsilon}}{\partial z}\overline{w^2}\frac{\overline{u_i u_i}}{\varepsilon}\right) = -\frac{4\bar{\varepsilon}^2}{\overline{u_i u_i}} + \frac{4a\bar{\varepsilon}P}{\overline{u_i u_i}} \qquad\qquad \text{A1.26}$$

which, close to the surface, can be approximated as

$$a_{t,\varepsilon} = \left(\frac{4\bar{\varepsilon}^2 - 4a\bar{\varepsilon}P}{\overline{w^2 u_i u_i}\,\overline{u_i u_i}}\right)z^2 = \frac{4 - 4a}{k^2\phi_E^2\phi_w^2} = 0.12 \qquad\qquad \text{A1.27}$$

A2 MEASUREMENT PHYSICS

The analysis of the turbulence data is performed by means of statistics based upon the mathematical theory of stationary random processes. This appendix gives a mathematical basis, which was also used to calculate the corrections, given in section 3.5.4. For the analysis, ergodicity, and therefore stationarity, are assumed (Bendat and Piersol, 1971). Ergodicity is the requirement that the time average approaches the "stochastic average" as the integration time increases.

The signals used in the following outline are $W(t)$ and $S(t)$. The effect of sensor separation and high frequency loss on the covariance $\overline{ws}$ will be calculated.

In the analysis the Fourier transform pair, defined by

$$\mathcal{F}_x(\omega) = \int_{-\infty}^{\infty} x(t)e^{-i\omega t}dt$$

A2.28

$$x(t) = \frac{1}{2\pi}\int_{-\infty}^{\infty} \mathcal{F}_x(\omega)e^{i\omega t}d\omega$$

is used where ω is angular frequency. The complex conjugate of $\mathcal{F}_x$ is $\mathcal{F}_x^*$.

The correlation function of $W(t)$ and $S(t)$ in a stationary flow is

$$r_{ws}(\tau) = \overline{w(t)s(t+\tau)} = \frac{1}{T}\int_{-T/2}^{T/2} w(t)s(t+\tau)dt,$$

A2.29

where T denotes the averaging period and the covariance $\overline{ws} = r_{ws}(0)$.

The Fourier transform of the correlation function

$$\mathcal{F}_{r_{ws}} = \Phi_{ws}(\omega) = \int_{-\infty}^{\infty} r_{ws}e^{-i\omega t}dt$$

A2.30

is known as the cross spectral density and it can be seen that

$$\Phi_{ws} = \frac{\mathcal{F}_w^* \mathcal{F}_s}{T}. \qquad \text{A2.31}$$

The cross spectrum is a two-sided function as it is defined for $(-\infty, \infty)$. In practice, only the one-sided spectrum can be measured which is defined as

$$\phi_{ws}(\omega) = 2\Phi_{ws}(\omega) \text{ for } 0 \le \omega < \infty \text{ otherwise } 0. \qquad \text{A2.32}$$

It is custom to split the cross spectrum according to

$$\phi_{ws}(\omega) = C_{ws}(\omega) - iQ_{ws}(\omega) \qquad \text{A2.33}$$

in which the real part is known as the co-spectrum and the imaginary part is the quadrature spectrum. Furthermore,

$$\tan \alpha_{ws}(\omega) = \frac{Q}{C} \qquad \text{A2.34}$$

defines the phase angle between W and S at frequency ω.

The co-spectrum gives the contribution to the covariance $\overline{ws}$ at each frequency,

$$\overline{ws} = \int_0^\infty C_{ws}(\omega)d\omega. \qquad \text{A2.35}$$

The measured co-spectrum, $\hat{C}_{ws}$ is different from the actual co-spectrum because W and S are measured with sensors with different response characteristics and at different positions in the flow.

The limited response of a sensor acts as a low pass filter on the input signal and the relation between the input and output signal is written as

$$\hat{W}(t) = \int_{-\infty}^\infty W(\tau)h_w(t-\tau)d\tau, \qquad \text{A2.36}$$

$$\hat{S}(t) = \int_{-\infty}^\infty S(\tau)h_s(t-\tau)d\tau$$

which is the convolution in the time domain of the signals $W(t)$ and $S(t)$ and the responses functions $h_w(t)$ and $h_s(t)$ of the sensors measuring W and S. Convolution in the time domain is equal to multiplication in the frequency domain, so

$$\hat{\mathcal{F}}_w = \mathcal{F}_{h_w}\mathcal{F}_w$$

$$\hat{\mathcal{F}}_s = \mathcal{F}_{h_s}\mathcal{F}_s$$

A2.37

where the transfer functions $\mathcal{F}_{h_w}(\omega)$ and $\mathcal{F}_{h_s}(\omega)$ are the Fourier transforms of $h_w(t)$ and $h_s(t)$.

The correlation function calculated from observations is

$$\hat{r}_{ws}(\tau) = \overline{\hat{w}(t - d/U)\hat{s}(t+\tau)} = \overline{\hat{w}(t)\hat{s}(t+\tau+d/U)}$$

A2.38

differs from the real correlation function (Eq.A2.2) because of the combined effect of alongwind sensor separation d at wind speed U, where both W and S are measured at a fixed point in space with W measured downwind of S, and the low pass filtering of the signals indicated by the '^'. The Fourier transform of Eq.A2.11 can be written as

$$\hat{\phi}_{ws} = \mathcal{F}_{h_w}^* \mathcal{F}_{h_s} \phi_{ws} e^{i\frac{\omega d}{U}}.$$

A2.39

The product $\mathcal{F}_{h_w}^* \mathcal{F}_{h_s}$ is the joint transfer function which is split into real and imaginary parts through

$$\mathcal{F}_{h_w}^* \mathcal{F}_{h_s} = J_1 + iJ_2.$$

A2.40

Now, inserting A2.6 and A2.13 in A2.12 and also using A2.7, it is found that

$$\frac{\hat{C}_{ws}}{C_{ws}} = J_1 \cos\beta - J_2 \sin\beta + (J_2 \cos\beta + J_1 \sin\beta)\tan\alpha$$

A2.41

where $\beta = \omega d/U$.

For the error analysis it is assumed that all instruments have a first-order, linear response. The response length of a sensor is $L_r = \tau_r \overline{U}$ which also defines the time constant τ_r. The transfer functions are then

$$\mathcal{F}_{h_w}(\omega) = \frac{1}{1 + i\omega\tau_w} = \frac{1}{1 + i2\pi f L_w/z},$$ A2.42

$$\mathcal{F}_{h_s}(\omega) = \frac{1}{1 + i\omega\tau_s} = \frac{1}{1 + i2\pi f L_s/z},$$

where the non-dimensional frequency $f = nz/\overline{U}$ with $n = \omega/2\pi$, the natural frequency in cycles/time or Hz.

The real and imaginary part of the joined transfer function (Eq.A2.13) become, using A2.14,

$$J_1 = \frac{1 + \omega^2\tau_w\tau_s}{(1 + \omega^2\tau_w^2)(1 + \omega^2\tau_s^2)} = \frac{1 + 4\pi^2 f^2 L_w L_s/z^2}{(1 + (2\pi f L_w/z)^2)(1 + (2\pi f L_s/z)^2)}$$ A2.43

$$J_2 = \frac{\omega(\tau_w - \tau_s)}{(1 + \omega^2\tau_w^2)(1 + \omega^2\tau_s^2)} = \frac{2\pi f(L_w - L_s)/z}{(1 + (2\pi f L_w/z)^2)(1 + (2\pi f L_s/z)^2)}$$

It can be seen that J_2 becomes zero for instruments with equal time constants.

A2.1 High frequency loss of the thermocouple-sonic system

As an example, the response correction for the sensible heat flux measured with the thermocouple and the sonic anemometer is given.

The response length L_θ of the thermocouple was obtained using a method given by Van Asselt *et al.*, 1991. The thermocouple wire has a width of $w = 0.4$ mm and a thickness of $\mu = 0.02$ mm. The Reynolds number for the flow around the thermocouple is $Re = \overline{U}w/\nu$ with the kinematic viscosity of air, $\nu = 1.5 \times 10^{-5}$ m^{2}s^{-1}. The time constant τ_θ can be calculated using

$$\tau_\theta = \frac{c_{cu}\mu w}{2(\mu + w)} \frac{1}{h},$$ A2.44

where the volumetric heat capacity of copper, $c_{cu} = 3.42 \times 10^6$ Jm^{-3}K^{-1}. The 2-sided heat exchange coefficient h is calculated using $h = \text{Nu}2\lambda_{air}/w$ in which $\text{Nu} = 0.6Re^{0.5}$ for $Re < 2 \times 10^4$ (Van Asselt *et al.*, 1991) and the conductivity of still air, $\lambda_{air} = 0.025$ W m^{-1}K^{-1}.

Note that L_θ increases with the square root of wind speed because of the square root dependence of the Nusselt number on wind speed. The response length of the sonic anemometer is neglected.

The high frequency loss

$$hf = \frac{\int_0^\infty \hat{C}_{w\theta}}{\int_0^\infty C_{w\theta}}$$

A2.45

is calculated using a model of co-spectra for $\overline{w\theta}$ for the homogeneous and neutral surface layer (Kaimal *et al.*, 1972),

$$C_{w\theta}(f) = \frac{11f}{(1 + 13.3f)^{1.75}} \quad \text{for } f =< 1$$

A2.46

$$C_{w\theta}(f) = \frac{4.4f}{(1 + 3.8f)^{2.4}} \quad \text{for } f > 1.$$

with $0.005 \leq f \leq 5$ for which

$$\int_0^\infty C_{w\theta} = 0.99.$$

Using Eqs.A2.14 and A2.16, and assuming $\tan \alpha = 0$, hf is calculated and given as a function of L_θ/z and d/z in Fig.A2.1.
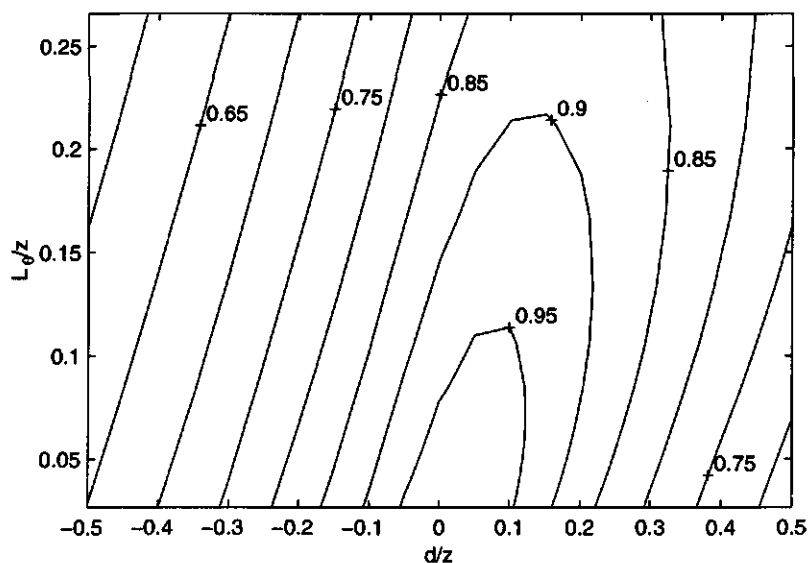
Fig.A2.1 The high frequency loss (Eq.A2.18) of the sonic - thermocouple system for neutral conditions as a function of non-dimensional sensor separation and response length.

A typical L_θ is 0.25 m, so $L_\theta/z \approx 0.06$ at EC1 where $d/z \approx -0.07$ which gives a correction of about 10%. For $d > 0$, the thermocouple is situated upwind of the sonic and it can be seen that upwind placement of the sensor with the slower response (the thermocouple in this case) would be advantageous where it concerns high frequency losses. Other considerations, like the effect on flow distortion, makes such a set-up not attractive and for sufficiently small d/z the difference is small.

A3 TOP-DOWN, BOTTOM-UP DECOMPOSITION OF SCALAR FIELDS

A study of statistics of conservative scalars in the CBL (Moeng and Wyngaard, 1984) was used to do some calculations of $R_{\theta q}$ as a function of z/z_i. In the top-down bottom-up (TD-BU) approach it is assumed that the scalar has two sources, the entrainment flux at the top of the Planetary Boundary Layer (PBL) and the surface flux at the bottom. A scalar mixing ratio field can be decomposed as (Wyngaard, 1982)

$$C = \overline{C}_b + \overline{C}_t + c_b + c_t \qquad\qquad \text{A3.1}$$

where the subscript 'b' is for the surface flux driven, BU-field and 't' for the entrainment flux driven, TD-field of C. An overbar indicates an ensemble mean and the lower case denotes fluctuations.

Applying CBL-scaling the scalar variances in the CBL can be written as

$$\overline{c_b^2} = \left(\frac{\overline{wc_b}}{w_*} \right)^2 f_b, \qquad\qquad \text{A3.2}$$

$$\overline{c_t^2} = \left(\frac{\overline{wc_t}}{w_*} \right)^2 f_t,$$

$$\overline{c_b c_t} = \frac{\overline{wc_b}\,\overline{wc_t}}{w_*^2} f_{tb},$$

w_* is the convective velocity scale and f_b, f_t and f_{tb} are functions of z/z_i.

The covariance $\overline{c_b c_t}$ between top-down and bottom-up fluctuations needs some consideration. A value other than zero for this term indicates that the two scalar fields are correlated. It was found (Moeng and Wyngaard, 1984) for the CBL that indeed they are (positively) correlated and that the correlation reaches a maximum in the mid-CBL.

Using Eq.A3.1 the following products can be assembled to describe the interaction of the temperature field and the humidity field:

$$\overline{\theta^2} = \overline{\theta_t^2} + 2\overline{\theta_t\theta_b} + \overline{\theta_b^2} \tag{A3.3}$$

$$\overline{q^2} = \overline{q_t^2} + 2\overline{q_tq_b} + \overline{q_b^2}$$

$$\overline{\theta q} = \overline{\theta_tq_t} + \overline{\theta_bq_t} + \overline{\theta_tq_b} + \overline{\theta_bq_b}.$$

It is assumed that

$$\frac{\overline{\theta_tq_t}}{\sigma_{\theta_t}\sigma_{q_t}} = \frac{\overline{\theta_bq_b}}{\sigma_{\theta_b}\sigma_{q_b}} = 1 \tag{A3.4}$$

and

$$\overline{\theta_bq_t} = \overline{\theta_tq_b}. \tag{A3.5}$$

With A3.2 it is found that

$$w_*^2\overline{\theta q} = \overline{wq_b}\,\overline{w\theta_b}f_b + \overline{w\theta_b}\,\overline{wq}_t f_{tb} + \overline{w\theta_t}\,\overline{wq_b}f_{tb} + \overline{w\theta_t}\,\overline{wq}_t f_t \tag{A3.6}$$

$$w_*^2\overline{\theta^2}_b = \overline{w\theta_b^2}f_b; \quad w_*^2\overline{\theta^2}_t = \overline{w\theta_t^2}f_t;$$

$$w_*^2\overline{q^2}_b = \overline{wq_b^2}f_b; \quad w_*^2\overline{q^2}_t = \overline{wq_t^2}f_t.$$

Now, the correlation between temperature and humidity in top-down, bottom-up form can be written as

$$R_{\theta q} = \frac{\overline{\theta q}}{\sigma_q\sigma_\theta} = \frac{\overline{\theta_tq_t} + \overline{\theta_tq_b} + \overline{\theta_bq_t} + \overline{\theta_bq_b}}{\{(\overline{\theta^2}_t + 2\overline{\theta_t\theta_b} + \overline{\theta_b^2})(\overline{q^2}_t + 2\overline{q_tq_b} + \overline{q_b^2})\}^{0.5}}$$

$$= \frac{\left(1 + (\xi_\theta + \xi_q)\frac{f_{tb}}{f_b} + \xi_q\xi_\theta\frac{f_t}{f_b}\right)}{\left\{\left(\xi_\theta^2\frac{f_t}{f_b} + 2\xi_\theta\frac{f_{tb}}{f_b} + 1\right)\left(\xi_q^2\frac{f_t}{f_b} + 2\xi_q\frac{f_{tb}}{f_b} + 1\right)\right\}^{0.5}} \tag{A3.7}$$

where $\xi_c = \overline{wc}_t/\overline{wc}_b$, the ratio of the entrainment and the surface flux of C.

To actually calculate $R_{\theta q}$, expressions for f_b and f_t were taken from Moeng and Wyngaard (1984) who found, using Large Eddy Simulation, that

$$f_b = 1.8 \left(\frac{z}{z_i} \right)^{-2/3}$$ A3.8

$$f_t = 2.1 \left(1 - \frac{z}{z_i} \right)^{-3/2}$$

and where Moeng and Wyngaard (1984) used $f_{tb} = 1$ we use

$$f_{tb} = -4 \left(\frac{z}{z_i} \right)^2 + 4 \frac{z}{z_i}.$$ A3.9

so that f_{tb} reaches a maximum in the mid-CBL and is zero at the top and the bottom.

With this function and Eq.A3.7, $R_{\theta q}$ was calculated as function of a fixed ξ_θ of -0.4 and a range of ξ_q-values. The result is given in Fig.4.9 and discussed in section 4.1.

A4 SELECTED RUNS FOR COMPARISON WITH THE MODEL

Table A4.1 gives the input parameters, used to initialize the model, for the selected data set of 45 runs. The upwind Obukhov length, given in the last column, was calculated using the sensible heat flux and the friction velocity also given in this table and the temperature from P0 at $z = 3$m.

Run	Time (decimal)	H Wm^{-2}	λE Wm^{-2}	u_* ms^{-1}	$T(z_{o,2})$ $^\circ C$	$Q(z_{o,2})$ gm^{-3}	r_s sm^{-1}	dd $^\bullet$	L m
	June 20								
1	9.50	160	138	0.53	22.0	7.4	40.0	332	-81
2	10.00	259	169	0.55	23.8	7.5	37.4	343	-57
3	10.50	199	99	0.54	23.5	6.8	39.5	342	-68
4	11.00	223	142	0.61	23.8	6.8	44.8	335	-89
5	11.50	167	115	0.62	22.9	6.7	42.1	344	-126
6	12.00	212	116	0.59	23.5	6.7	39.3	342	-86
7	12.50	158	101	0.60	22.3	6.7	37.5	354	-122
8	13.00	244	99	0.66	23.7	6.6	40.9	338	-104
9	13.50	149	79	0.61	22.4	6.6	42.0	340	-133
	June 21								
19	9.50	307	65	0.81	23.2	8.1	46.2	333	-149
20	10.00	338	97	0.71	24.3	8.3	45.5	337	-91
21	10.50	338	68	0.70	24.8	8.1	52.4	340	-90
22	11.00	337	49	0.65	25.5	7.9	45.0	346	-73
23	11.50	366	72	0.64	26.4	8.1	46.3	341	-63
24	12.00	342	77	0.64	26.2	7.6	49.3	342	-68
25	12.50	406	115	0.63	27.5	7.4	42.4	341	-54
26	13.00	358	87	0.66	27.0	7.0	46.4	352	-70
27	13.50	307	77	0.67	26.8	6.8	46.4	347	-85
	June 22								
38	9.50	329	63	0.66	25.5	8.3	44.8	348	-78
39	10.00	335	68	0.61	26.5	8.4	58.6	349	-59
40	10.50	389	88	0.59	27.4	8.7	62.3	343	-46
41	11.00	376	79	0.55	28.3	8.6	56.2	333	-39
42	11.50	362	72	0.63	28.1	8.2	46.9	346	-61
43	12.00	342	44	0.62	28.1	7.9	52.2	355	-62
44	12.50	372	71	0.65	28.5	8.0	52.7	347	-65
45	13.00	384	79	0.62	29.5	8.2	55.7	350	-54
46	13.50	332	48	0.58	28.9	8.1	48.9	345	-51
	June 23								
55	9.50	309	71	0.32	30.5	9.4	48.9	359	-10
56	10.00	351	74	0.39	31.2	9.2	53.9	350	-15
57	10.50	389	76	0.36	32.5	9.3	59.1	342	-11
58	11.00	419	101	0.40	33.2	9.4	46.3	351	-13
59	11.50	410	85	0.37	33.4	9.5	51.7	351	-11
60	12.00	384	84	0.36	33.5	9.9	48.5	347	-11
61	12.50	389	80	0.38	33.61	0.0	53.9	355	-12
62	13.00	368	72	0.45	33.01	0.4	51.2	352	-22
63	13.50	342	71	0.45	32.71	0.7	53.3	335	-24
	June 24								
73	9.50	349	82	0.44	29.71	1.8	44.1	345	-22
74	10.00	322	62	0.41	30.21	1.9	40.9	345	-19
75	10.50	346	71	0.42	30.81	1.9	39.6	339	-19
76	11.00	434	122	0.57	31.41	2.0	46.2	333	-37
77	11.50	379	100	0.42	32.31	2.0	37.4	338	-17
78	12.00	410	87	0.42	32.81	1.5	47.5	330	-16
79	12.50	367	76	0.46	32.31	1.3	41.8	329	-23
80	13.00	446	112	0.45	33.61	1.8	45.3	331	-19
81	13.50	359	83	0.45	32.51	1.3	49.2	337	-23

Table A4.1 Initialization parameters for the second-order model (45 runs). From left to right: run number, decimal time, the upwind surface sensible and latent heat flux, the upwind friction velocity and the temperature and absolute humidity at $x = 0$, $z = z_{o2}$, the downwind surface resistance, the wind direction and the Obukhov length.

LIST OF SYMBOLS

In this thesis Universal Time (UTC) is used.

Alphanumeric

A	Net available energy	Wm^{-2}
A	Surface area of soil heat flux plate (section 3.4.4)	m^2
A_c	Constant in parameterization of variance dissipation (Eq.2.38)	
$A_{c,x}$	Advection of $\overline{c^2}$ in the x-direction	
A_T	Amplitude of the daily cycle of air temperature	K
A_z	Amplitude soil temperature wave at depth z	K
a	Thermal diffusity (section 3.4.4.1);	m^2s^{-1}
a	Calibration factor Lyman-α (section 3.5.2.1)	
a	Constant in parameterized dissipation equation (Appendix A1)	
$a_{1,2}$	Constants in the parameterization of the pressure term in the scalar flux equation (Appendix A1)	
a_c	Magnitude of φ_c^2 for $\zeta = 0$	
a_t	Constant in second order model	
$a_{t,\varepsilon}$	Constant in second order model	
B	Constant in expression for the height of the IBL	
b	Constant in Eq.3.12	
b	Constant in parameterization of scalar variance dissipation (Appendix A1)	
b_c	Constant in MO flux-variance relation φ_c	
C	Concentration (Θ or Q)	
$\overline{C}$	Mean concentration ($\overline{\Theta}$ or $\overline{Q}$)	
C_s	Specific volumetric heat capacity of the soil	$Jm^{-3}K^{-1}$
C_{ik}	Constants in closure parameterization in the Reynolds stress equations	
c	$C - \overline{C}$	
c	Speed of sound (section 3.5.1.2)	ms^{-1}
c_p	Specific heat capacity of air at constant pressure	$Jkg^{-1}K^{-1}$
c_x	Specific heat capacity of quartz and clay material ($x = q,c$); of water ($x = w$)	$Jkg^{-1}K^{-1}$
c_w	Specific heat capacity of water	$Jkg^{-1}K^{-1}$
c_o	Constant in expression for overspeeding correction	
D	Saturation deficit of specific humidity	$kgkg^{-1}$
D_d	Damping depth	m
D_H	Sensible heat flux difference between two heights	Wm^{-2}
D_r	First order response length	m
d	Sensor separation	
d_i	Constants in the closure parameterization of the scalar flux equations ($i = 1,3$).	
d_o	Constant in expression for overspeeding correction	
d_p	Thickness of the soil heat flux plate	m
day	Time from sunrise to sunset	
dd	Wind direction	°
E_c	Transpiration	$kgm^{-2}s^{-1}$
E	Evapotranspiration (positive when directed away from the surface)	$kgm^{-2}s^{-1}$
$e_s(T)$	Saturation water vapour pressure at temperature T	Pa
e	Water vapour pressure	Pa
F	Flux density	

$\mathcal{F}_x$	Fourier transform of x	
$\hat{F}_c$	Normalized flux of $C = \Theta, Q$	
F_1	Factor which expresses the influence of photosynthetic active radiation on the surface resistance	
F_2	Factor which expresses the influence of soil water status on the surface resistance	
F_3	Factor which expresses the influence of saturation deficit on the surface resistance	
F_4	Factor which expresses the influence of air temperature on the surface resistance	
f_o	Dimensionless peak frequency of the horizontal velocity variance spectrum	
$f(z,x)$	Function to correct 'bulk' advection to the local value	
G	Soil heat flux (positive when directed away from the surface)	Wm^{-2}
G_p	Heat flux trough plate (positive when directed away from the surface)	Wm^{-2}
g	Acceleration due to gravity	ms^{-2}
H	Sensible heat flux density (positive when directed away from the surface)	Wm^{-2}
H_o	Sensible heat flux density calculated using the variance method	Wm^{-2}
h	Thickness of soil layer above soil heat flux transducer (section 3.4.4)	m
h_x	Response function of X	
h_{ial}	Height of the IAL specific to some quantity or observed	m
h_{ibl}	Height of the IBL specific to some quantity or observed	m
I_K	Ratio of the eddy diffusivities of sensible and latent heat	
I_R	Ratio of the transfer efficiencies of sensible and latent heat	
J_o	Dimensionless factor in the equation for overspeeding of cup anemometers	
$K_{M,\theta,q,c}$	Eddy diffusivity of M, Θ, q or C	m^2s^{-1}
k	Von Karman constant	
k	Thermal conductivity (section 3.4.4.1)	$WK^{-1}m^{-1}$
L	Obukhov length	m
L_r	Response length of a sensor	m
L_{in}	Incoming long wave radiation	Wm^{-2}
L_{out}	Outgoing long wave radiation	Wm^{-2}
M	$\overline{\theta q}, \overline{\theta\theta}$ or $\overline{qq}$ or $\overline{u_i s}, s = \theta, q$ in section 2.5	
M_d	Molecular mass of dry air	$kg\,kmol^{-1}$
M_w	Molecular mass of water	$kg\,kmol^{-1}$
N_c	Dissipation of $\overline{c^2}$	K^2s^{-1}
n_o	The natural peak frequency of the horizontal velocity variance spectrum	s^{-1}
P	Air pressure	Pa
P_s	Porosity	
P_t	Seconds in a day	s
$P_{\theta,z}$	Vertical gradient production in temperature variance equation	
Q	Specific humidity	$kgkg^{-1}$
q	$Q - \overline{Q}$	$kgkg^{-1}$
$Q_s(\Theta)$	Saturated specific humidity at temperature Θ	
q_*	Humidity scale for the ASL	
R	Universal gas constant	$J\,kmol^{-1}\,K^{-1}$
R_n	Net radiation (positive towards the surface)	Wm^{-2}
$R_{w\theta}$	Transfer efficiency of sensible heat; Correlation between vertical wind and temperature	

R_{wq}	Transfer efficiency of water vapour; Correlation between vertical wind and specific humidity	
R_{xy}	Correlation between two variables x and y	
r_a	Aerodynamic resistance	sm^{-1}
r_i	Isothermal resistance	sm^{-1}
r_s	Surface or canopy resistance	sm^{-1}
$r_s, \min$	Minimum canopy resistance for some crop	sm^{-1}
r_{ws}	Correlation function	
Ri_f	Flux Richardson number	
S	Electric signal (section 3.5.2.1)	
S	Θ or Q	
$\hat{S}$	Low pass filtered signal of S	
S_s	Heat storage in the soil	Wm^{-2}
S_{in}	Incoming shortwave radiation	Wm^{-2}
S_{out}	Outgoing shortwave radiation	Wm^{-2}
t	Time elapsed since sunrise	s
T	Averaging period (Appendix A2)	s
T_a	Air temperature	°C
T_{dry}	Dry bulb temperature	°C
T_s	Surface temperature	°C
$T_{\theta,z}$	Transport term in variance equation for temperature	°C
T_{wet}	Wet bulb temperature	°C
U	Horizontal wind speed in the x–direction	ms^{-1}
$\bar{U}$	Mean wind speed between z and z_o	ms^{-1}
U_1	U	ms^{-1}
U_2	V	
U_3	W	
u	$U - \bar{U}$	ms^{-1}
u_*	Friciton velocity	ms^{-1}
V	Horizontal wind speed in the y–direction	
v	$V - \bar{V}$	ms^{-1}
W	Vertical wind speed	ms^{-1}
$\hat{W}$	Low pass filtered signal of W	ms^{-1}
w	$W - \bar{W}$	ms^{-1}
w_*	Convective velocity scale	ms^{-1}
X	Function of ζ appearing in the ψ-functions	
x	Downwind distance from the step-change	m
x	Distance source-detector Lyman-α (Eq.3.23-3.25)	m
x	Constant in flux-profile relation (Eq.2.17)	
x_p	Perpendicular downwind distance from the step-change	m
x_q, c	Fraction of quartz and clay in the soil profile	
x_w	Fraction of water in the soil profile	
y	Constant appearing in the flux-profile relations (Eq.2.17)	
z	Height above the surface	m
z_i	Height of the Planetary Boundary Layer	m
z_m	Geometric mean of two heights	m
z_o	Surface roughness	m
z_r	Reference height	m

Greek symbols

α	Ratio of the latent heat flux and available energy	
α	Distortion angle (section 3.5)	
β	Bowen ratio	
β_g	Bowen ratio calculated from mean gradients	
β_σ	Bowen ratio calculated from standard deviations	
δ_x	Height of the IBL calculated using Eg.2.27 (no subscript); $x = q, \theta$: height of the IBL's for water vapour and temperature respectively.	m
δ_{ik}	Kronecker delta	
Δ	Slope of the temperature-specific saturation humidity function	K^{-1}
Δx	Absolute error in x	
Δz	Absolute error in z	
ε	Dissipation of turbulent kinetic energy	m^2s^{-3}
ε_r	Surface emissivity	
ε_w	Ratio M_w/M_d	
γ	Isenthalpic psychrometer constant	K^{-1}
λ	Latent heat of vaporization	Jkg^{-1}
λ_s	Thermal conductivity of soil	$Wm^{-1}K^{-1}$
λ_p	Thermal conductivity of soil heat flux plate	$Wm^{-1}K^{-1}$
ω	Angular frequency	
ϕ_c	Dimensionless vertical gradient of mean wind speed, temperature or humidity (respectively $c = m, \theta, q$).	
ϕ_E	Dimensionless TKE times two	
ϕ_ε	Dimensionless dissipation of TKE	
ϕ_τ	Dimensionless timescale in second order closure model	
φ_c	Dimensionless standard deviation of C also referred to as the flux variance relation of C where c can be u, v, w, θ, q etc.	
Ψ_{ws}	Fourier transform of the correlation function or cross spectral density (Appendix A2)	
ψ_c	Surface layer stability correction where $c = m, \theta, q$ for respectively wind speed, temperature and specific humidity	
ψ_{ws}	One-sided cross spectral density (Appendix A2)	
$\hat{\psi}_{ws}$	One-sided cross spectral density of low pass filtered signals (Appendix A2)	
ρ_x	Air density (no subscript), $x = v$:absolute humidity; $x = q, c$:quartz, clay; $x = w$:water; $x = s$:soil.	kgm^{-3}
ρ'	$\rho - \bar{\rho}$	kgm^{-3}
σ	Boltzman constant	$Wm^{-2}K^{-4}$
σ_c	Standard deviation of C-signal u, v, w, θ, q etc.	
τ	Momentum flux	$kgm^{-1}s^{-2}$
τ	Time shift (Appendix A2)	s
τ_x	Time response of some instrument which measures x	s
τ_t	Time scale for the dissipation of TKE	s
τ_c	Time scale for the dissipation of $\overline{c^2}$	s
Θ	(Potential) temperature	K
θ	$\Theta - \bar{\Theta}$	K
Θ_s	surface temperature	K
Θ_v	(Potential) virtual temperature	K
$\hat{\Theta}$	Normalized temperature	K
θ_*	Temperature scale for the homogeneous Atmosferic Surface Layer	K

ξ_c	Ratio of the entrainment flux and the surface flux of C
ζ	Monin-Obukhov stability parameter
ζ_l	Local variant of the Monin-Obukhov stability parameter

Subscripts

1	Upwind terrain
2	Downwind terrain
calc	Calculated
m	Measured value
max	Maximum value
obs	Observed
r	Actual value
s	Near surface air quantity
son	Sonic anemometer

Abbreviations

ABL	Atmospheric Boundary Layer
ASL	Atmospheric Surface Layer
ECn	Location of Eddy Correlation measurements where $n=0$ for the upwind station and $n=1,2,3$ for three downwind stations (Table 3.1)
HF	High frequency
IAL	Internal Adapted Layer
IBL	Internal Boundary Layer
LAI	Leaf Area Index
MO	Monin-Obukhov
Pn	Location of Profile measurements where $n=0$ for the upwind station and $n=1,2,3,4$ for the four downwind stations (Table 3.1)
PME	Penman Monteith Equation
SA	Strong Advection
TKE	Turbulent Kinetic Energy
UTC	Universal Time
VUA	Vrije Universiteit Amsterdam
WA	Weak Advection
WAU	Wageningen Agricultural University

Curriculum Vitae

Ik, Nicolaas Johannes Bink, werd op 29 juni 1957 geboren te Vught. In dit dorp doorliep ik de lagere school tot de vierde klas en de rest in Almelo. In 1975 behaalde ik het VWO diploma aan het Rijnlands Lyceum te Oegstgeest en begon in Wageningen de studie Tropische Cultuurtechniek. In 1978 maakte ik deel uit van het bestuur van Unitas Wageningen als penningmeester van de Mensa. Het kandidaatsexamen legde ik af in 1982. In 1983 werd ik erelid van biljartvereniging 't Ketsertje van Unitas. Mijn praktijktijd bracht ik door in Niono, Mali en ik werkte daar mee aan de verbetering van het waterbeheer binnen het Office du Niger in het kader van het G(estion de l')EAU project onder begeleidng van ir.Pieter Raijmakers. Mijn doctoraalpakket bevatte een hoofdvak Irrigatie waarvoor een waterverbruikexperiment van maïs werd uitgevoerd in Mali onder begeleiding van ir.Cees Bastiaansen in het kader van het B(esoins en)EAU- project. In het kader van het tweede hoofdvak, Meteorologie en Klimatologie, testte ik, begeleid door dr.ir.Adri Jacobs, een evaporimeter. Als bijvak volgde ik nog Landbouwcoöperatie en Kredietwezen van de niet-westerse gebieden voordat ik afstudeerde in mei 1985. Vervolgens werd ik door NWO in staat gesteld 4 jaar te werken aan het onderzoek dat ten grondslag ligt aan dit proefschrift tot 1 juni 1989. De eerste 18 maanden van deze periode in vervangende dienst en de resterende tijd volledig in dienst van NWO. Van september 1988 tot maart 1989 verbleef ik als gastmedewerker bij het Centre for Environmental Mechanics in Canberra, Australia. Sinds 1 juli 1989 ben ik universitair docent bij de vakgroep Meteorologie van de Faculteit der Aardwetenschappen van de Vrije Universiteit te Amsterdam.